Combining high-density electrical source imaging and hemodynamic responses to epileptic discharges

By

Tanguy Hedrich

Department of Biological & Biomedical Engineering
McGill University

January 2020

A thesis submitted to McGill University in partial fulfillment
of the requirements of the degree of
Doctor of Philosophy.

Força. Equilibri. Valor. Seny.
Strength. Balance. Courage. Common sense.

These four words are the motto of the castellers, who have been building Catalan human towers for more than 300 years. The same adage can be applied to scientific research.

This thesis is dedicated to the *castellers de Montréal*. Gràcies per tot.

Acknowledgements

I would like to extend my deepest gratitude to Dr. Christophe Grova, my supervisor, for his patient guidance, enthusiastic encouragement and useful critiques of this research work. The completion of this project was not easy every day and I would not have achieved it without his guidance and moral support.

I also want to express my great appreciation to my PhD committee: Dr. Eliane Koyashi, Dr. Jean Gotman and Dr. Sylvain Baillet. This project would not be the same without their assistance and their valuable comments. My sincere thanks to Dr. Jean-Marc Lina for guiding me through all the methodological aspects of the MEM framework, and for his tremendous help in the design and writing of my articles.

I cannot express in strong enough terms the gratitude I feel for my former and current colleagues for their constant help, their advice and their friendship. Without you, the laboratory would only be a gloomy, lifeless, bunker-like dungeon. Special thanks to Dr. Chifaou Abdallah and Dr. Makoto Uji for correcting my thesis and to Dr. Rasheda Chowdhury, Dr. Alexis "Peluche" Machado, Dr. Kangjoo Lee, Dr. Marcel Heers, Dr. Giovanni Pellegrino, Zhengchen Cai, Aude Jegou, Dr. Ümit Aydın, Fatemeh Razavipoor, Obaï Bin Ka'b Ali, Jawata Afnan, Amanda Spilkin, Dr. Thomas Vincent and everyone whom I forget and participated in the joyful atmosphere of the multifunkim laboratory.

I am grateful to all my friends who supported me throughout all these years. I would like to address my special thanks to Perrine Clement, Jonathan Benilan, Audrée Alarie, the MacBussche family, Dr. Lauren Fromont, Manon Rolland, and my roommates, Jean-Baptiste Gatineau and Rachael Hardies (thank you for proof-reading my thesis).

I wish to thank my family for their unfailing support, especially my parents, Denise and Jean-Paul, my grand-mother, Vérène (thank you for tirelessly connecting me with the rest of the family), as well as my brother Thomas, my sister-in-law Lucie (congratulations on your medical doctorate!) and my lovely nephew Charlie.

Finally, I would like to thank all the patients and healthy volunteers who participated in this research. Thank you to all the the technicians at McGill and Concordia who assisted me for the recording of EEG, MEG and fMRI.

Table of Contents

Abstract

Electrical source imaging (ESI) and simultaneous electroencephalography and functional magnetic resonance imaging (EEG-fMRI) are two imaging techniques that are useful for the localization of the epileptogenic focus during the pre-surgical evaluation of patients with drug-resistant epilepsy. Whereas ESI and EEG-fMRI are usually employed separately, EEG recorded in the MRI scanner can, in theory, be used to perform ESI. The purpose of this thesis was to assess the performance of joint ESI and EEG-fMRI analysis in the context of epilepsy. The thesis is organized around three contributions, forming the three manuscripts of this document.

The goal of the first study was to evaluate and compare the spatial resolution of four source localization methods, based on high density EEG (hdEEG) or magnetoencephalography (MEG) data. The intrinsic spatial properties of the methods were studied through the analysis of their resolution matrices. Overall, the study showed that the method developed by our group, entitled coherent maximum entropy on the mean (cMEM), exhibited excellent performance in terms of localization error and spatial dispersion. Moreover, we obtained similar levels of spatial accuracy on MEG and hdEEG, further confirmed by real data EEG/MEG acquisitions of electrical median nerve stimulation. Our overall findings indicated that cMEM was a reliable and robust source localization technique, and was therefore a suitable candidate for the analysis of EEG inside the MRI scanner.

In the second study, we specifically evaluated the performance of the source reconstruction of two ESI methods during a visual stimulation paradigm in two conditions: using hdEEG data acquired inside and outside the MRI scanner. We found that, even if EEG signals were distorted when acquired in the presence of a high magnetic field, ESI using cMEM performed inside the scanner remained accurate, exhibiting similar performance to ESI applied on EEG data acquired outside the scanner. This study demonstrated the feasibility of using ESI jointly with EEG-fMRI analysis.

Finally, for the last study, we evaluated how ESI could be applied with simultaneous EEG-fMRI to guide fMRI analysis. Considering eight patients with epilepsy who underwent EEG-fMRI recordings, we used hdEEG reconstructions to automatically classify interictal

epileptic discharges, to propose better regressors for fMRI statistical analyses. The classes of epileptic discharges identified with the automatic clustering from ESI analysis were used to build regressors for the fMRI analysis and compared to regressors obtained with the manual classification of epileptic discharges. We found that ESI results were overall spatially concordant with fMRI responses, and that the automatic classification of epileptic discharges provided similar results to the manual classification. This result opens the door for less operator-dependent approach for EEG-fMRI investigations in epilepsy.

To summarize, we demonstrated in this thesis that cMEM was a source imaging technique exhibiting excellent spatial resolution, even in noisy environments such as EEG data acquired in the MRI scanner. This technique was used on a visual protocol inside the scanner and was proven to be robust to MR-related noise. Finally, when applied on epilepsy data, cMEM exhibited an excellent concordance with the fMRI clusters and was able to classify epileptic discharges in function of their source localization results, providing relevant information to propose a more accurate regression model for fMRI analysis.

Abrégé

L'imagerie de sources électriques (ISE) et l'acquisition simultanée de l'électroencéphalographie et l'imagerie par résonance magnétique (EEG-IRMf) sont deux techniques d'imagerie utiles à la localisation du foyer épileptogène pendant l'évaluation pré-chirurgicale des patients présentant une épilepsie réfractaire aux médicaments. Bien que l'ISE et l'EEG-IRMf soient généralement employées séparément, l'EEG enregistrée dans le scanner IRM peut en théorie être utilisée pour effectuer l'ISE. L'objectif de cette thèse a été de tester la faisabilité et la performance de l'analyse jointe de l'ISE et de l'EEG-IRMf dans le contexte de l'épilepsie. Cette thèse s'organise autour de trois contributions, formant les trois manuscrits de ce document.

Le but de la première étude a été d'évaluer et de comparer la résolution spatiale de quatre méthodes de localisation de sources, basées sur des données d'EEG haute densité (EEGhd) ou de magnétoencéphalographie (MEG). Les propriétés spatiales intrinsèques des méthodes ont été étudiées à travers l'analyse de leurs matrices de résolution. Globalement, l'étude a montré que la méthode développée par notre groupe, intitulée maximum d'entropie sur la moyenne cohérent (MEMc), présentait d'excellentes performances en termes d'erreur de localisation et de dispersion spatiale. Nos observations ont indiqué que MEMc était une technique de localisation de sources fiable et robuste, et qu'il était ainsi un candidat adapté pour l'analyse de l'EEG à l'intérieur du scanner IRM.

Dans la deuxième étude, nous avons évalué spécifiquement la performance de la reconstruction de sources de deux méthodes d'ISE pendant une expérience de stimulation visuelle dans deux conditions: en utilisant les données EEGhd à l'intérieur ou à l'extérieur du scanner IRM. Nous avons trouvé que, même si les signaux EEG ont été déformés dans l'environnement de haut champ magnétique, l'ISE utilisant MEMc effectuée à l'intérieur du scanner demeurait précise, présentant des performances similaires à l'ISE appliquée à des données EEG à l'extérieur du scanner. L'étude a démontré la faisabilité de l'utilisation de l'ISE conjointement avec l'analyse EEG-IRMf.

Finalement, dans la dernière étude, nous avons évalué comment l'ISE pourrait être appliquée avec l'EEGhd-IRMf pour guider l'analyse IRMf. En considérant huit patients

atteints d'épilepsie qui ont réalisé des enregistrements EEG-IRMf, nous avons utilisé les reconstructions ISE pour classifier automatiquement les décharges épileptiques intericales dans le but de proposer de meilleurs régresseurs pour l'analyse statistique IRMf. Les classes de décharges épileptiques identifiées avec le clustering automatique ont été utilisées pour construire des régresseurs pour l'analyse IRMf et ont été comparées aux régresseurs obtenus avec la classification manuelle des décharges épileptiques. Nous avons trouvé que les résultats ISE étaient spatialement concordant avec les réponses IRMf, et que la classification automatique des décharges épileptiques apportait des résultats similaires à la classification manuelle. Il s'agit d'un résultat important permettant de considérer une approche moins dépendante de l'opérateur pour les analyses EEG-IRMf en épilepsie.

Pour résumer, nous avons démontré dans cette thèse que le MEMc était une technique d'imagerie de sources présentant une excellente résolution spatiale, même dans un environnement bruité tel que les données EEG acquises dans le scanner IRM. Cette technique a été utilisée avec un protocole de stimulation visuelle à l'intérieur du scanner et a démontré sa robustesse au bruit lié aux forts champs magnétiques. Finalement, avec des données d'épilepsie, MEMc a présenté une excellente concordance avec les clusters IRMf et a pu classifier les décharges épileptiques en fonction de leurs résultats de localisation de sources, apportant des informations pertinentes afin de proposer un modèle de régression plus précis pour l'analyse IRMf.

Contributions of Authors

All the work presented in this thesis was authored by myself, in collaboration with my supervisor **Dr. Christophe Grova**, PhD. Together we designed the studies, developed and performed the analyses, interpreted the results and wrote the manuscripts. This thesis consists in three studies, in which the contributions of each co-author other than myself and my supervisor are summarized below.

Manuscript 1: Comparison of the spatial resolution of source imaging techniques in high-density EEG and MEG

Published in Neuroimage vol. 157, pp 531-544, 2017

Authors: Hedrich T., Pellegrino G., Kobayashi E., Lina J.M., and Grova C.

- **Dr. Giovanni Pellegrino** assisted with the design and acquisition of the median nerve stimulation protocol. He also significantly helped with reviewing and writing the manuscript.
- **Dr. Eliane Kobayashi** provided useful advice in the design of the study. She also reviewed the manuscript.
- **Dr. Jean-Marc Lina** was involved with the design of the study, the interpretation of the results and writing and reviewing the manuscript.

Manuscript 2: Effect of MR-related noise on the quality of electrical source imaging reconstructions of visual evoked potentials

Under review in Human Brain Mapping

Authors: Hedrich T., Aydin Ü., Grimault S., Benali H., Lina J.M., and Grova C.

- **Dr. Ümit Aydin** assisted with the design and acquisition of the visual protocol. He was significantly involved in interpreting the results and in writing and reviewing the manuscript.

- **Dr. Stephan Grimault** helped with the design and acquisition of simultaneous hdEEG-fMRI data.
- **Dr. Habib Benali** assisted with the design of the analysis and reviewed the manuscript.
- **Dr. Jean-Marc Lina** was involved with the design of the study, the interpretation of the results and writing and reviewing the manuscript.

Manuscript 3: Automatic classification of interictal epileptic discharges based on electrical source imaging for the EEG-fMRI analysis of patients with partial epilepsy.

In preparation

Authors: Hedrich T., Khoo H. M., Koupparis A., Abdallah C., Gotman J., and Grova C.

- **Dr. Hui Ming Khoo** contributed to patient recruitment and EEG-fMRI data acquisition. She was involved in EEG preprocessing as well as visual detection and classification of epileptic discharges. She was also involved in the clinical interpretation of the results.
- **Dr. Andreas Koupparis** assisted with the interpretation of the data and helped in the recollection of the patients' history.
- **Dr. Chiafou Abdallah** assisted with the interpretation of the data and helped in the recollection of the patients' history.
- **Dr. Jean Gotman** was involved in the design of the study and helped in the interpretation of the data.

Statement of Originality

This PhD thesis was based on the realization of three studies, each consisting of a research manuscript. Here are the statements of originality corresponding with each of those three studies.

Manuscript 1: Comparison of the spatial resolution of source imaging techniques in high-density EEG and MEG

- We proposed a method to compare the intrinsic spatial properties of a source imaging method developed by our group, cMEM, to other standard source imaging techniques in a noise-free condition using the resolution matrix analysis.
- We compared the intrinsic spatial resolution of source imaging techniques when considering either high-density EEG or MEG with a similar number of sensors (256 vs 272) which demonstrated that both modalities obtained a similar level of performance.
- We further evaluated our findings considering real hdEEG and MEG data acquired during an electrical median nerve stimulation paradigm.

Manuscript 2: Effect of MR-related noise on the quality of electrical source imaging reconstructions of visual evoked potentials

- We evaluated the impact of the high magnetic environment in the performance of hdEEG source imaging reconstructions.
- We demonstrated in a visual stimulation paradigm that even if the EEG signals were distorted when acquired simultaneously with fMRI, the source imaging techniques provided accurate localization results.
- We compared ESI results from hdEEG data acquired inside and outside the MRI scanner, using the same visual paradigm.

- We demonstrated the robustness of cMEM in presence of MR-related noise.

Manuscript 3: Automatic classification of interictal epileptic discharges based on electrical source imaging for the EEG-fMRI analysis of patients with partial epilepsy.

- We proposed a new approach for the analysis of simultaneous EEG-fMRI data in patients with epilepsy, using automatic classification of electrical source imaging of epileptic discharges to guide fMRI analysis.
- When comparing fMRI regressors obtained from our proposed automatic classification of epileptic discharges to standard manual classification, we obtained similar fMRI responses, allowing a more objective analysis of EEG-fMRI data.
- We demonstrated that ESI applied from data acquired in the scanner was accurate and could be considered to guide fMRI analysis.
- From a clinical perspective, we have shown that the spatial agreement between ESI localization and fMRI response to the same epileptic discharges provided an accurate and reliable identification of the presumed epileptogenic zone.

List of Tables

List of Figures

List of Abbreviations

4-ExSo-MUSIC	4^{th} order Extended Source Multiple Signal Classification
AAS	Artifact Average Subtraction
ANOVA	Analysis of Variance
AP	Action Potential
AR	Autoregressive
AUC	Area Under the receiver operating Curve
BCG	BallistoCardioGram
BEM	Boundary Element Method
BOLD	Blood Oxygenation Level Dependent
CBF	Cerebral Blood Flow
CBV	Cerebral Blood Volume
CI	Confidence Interval
cMEM	coherent Maximum Entropy on the Mean
$CMRO_2$	Cerebral Metabolic Rate of Oxygen consumption
CSF	CerebroSpinal Fluid
CT	Computed Tomography
CT	Crosstalk functions (Chapter 5)
CWL	Carbon Wire Loop
DICS	Dynamic Imaging of Coherent Sources
DLE	Dipole Localization Error
dSPM	dynamic Statistical Parametric Mapping
ECD	Equivalent Current Dipole
ECD	Equivalent Current Dipoles
ECG	Electrocardiography
ECoG	ElectroCorticoGraphy
EEG	Electroencephalography
EEG-fMRI	ElectroEncephaloGraphy and functional Magnetic Resonance Imaging
EMD	Earth's mover distance

EOG	electrooculogram
EPI	Echo Planar Imaging
EPSP	Excitatory PostSynaptic Potential
EPSP	Inhibitory PostSynaptic Potential
ERP	Evoked Response Potentials
ESI	Electrical Source Imaging
FCD	Focal Cortical Dysplasia
FEM	Finite element method
fMRI	functional Magnetic Resonance Imaging
fNIRS	functional Near-InfraRed Spectroscopy
GLM	General Linear Method
GPS	Geodesic Photogrammetry System
hdEEG	High-density Electroencephalography
HFO	High-frequency oscillations
HRF	Hemodynamic Response Function
ICA	Independent Component Analysis
IED	Interictal Epileptic Discharge
iEEG	intracranial EEG
ILAE	International League against Epilepsy
LAURA	Local Auto-Regressive Average
LCMV	Linearly Constrained Minimum Variance
LORETA	Low Resolution brain Electromagnetic Tomography
MEG	MagnetoEncephaloGraphy
MEM	Maximum Entropy on the Mean
MNE	Minimum norm estimate
MNI	Montreal Neurological Institute
MNS	Median Nerve Stimulation
MR	Magnetic Resonance
MRI	Magnetic Resonance Imaging
MSI	Magnetic Source Imaging
MSP	Multivariate Source Pre-localization
MUSIC	Multiple Signal Classification
NMR	Nuclear Magnetic Resonance
OBS	Optimal Basis Sets
PET	Position Emission Topography
PSF	Point Spread Functions

PSP	PostSynaptic Potential
RAP-MUSIC	recursively applied and projected MUSIC
rMEM	ridge MEM
RSA	Ratio of Spurious Activity
$S1_{HAND}$	primary sensory hand region
SD	Spatial Dispersion
sEEG	stereotactic EEG
sLORETA	standardized Low Resolution brain Electromagnetic Tomography
SNR	Signal-to-Noise Ratio
SOZ	Seizure Onset Zone
SPECT	Single-Photon Emission Computed Tomography
SQUID	Superconducting Quantum Interference Device
wMEM	wavelet-based MEM

CHAPTER 1

Introduction

Epilepsy is a neurological disorder characterized by the occurrence of repetitive, unexpected and unpredictable seizures. For nearly 70 % of patients, medication is able to control the seizures. However the remaining 30 % are refractory to any drugs; therefore other therapeutic approaches should be investigated. In the case of focal epilepsy, i.e. when the onset of the seizure is located in a small portion of the brain, brain surgery may be an option. Candidates for epilepsy surgery undergo an extensive pre-surgical evaluation, which aims at localizing the areas in the brain triggering the seizures called "the epileptogenic focus". The evaluation also helps to precisely identify important structures in the brain, so that epileptogenic focus may be removed while avoiding significant loss of functional abilities.

During pre-surgical evaluation, a large number of techniques, such as seizure semiology, electrophysiology monitoring, neuropsychology, or anatomical and functional imaging, provide useful and complementary information to circumscribe the patient-specific epileptogenic focus (Engel and Pedley, 2008). In the present PhD dissertation, we focused on pre-surgical evaluation involving two noninvasive neuroimaging techniques: Electrical Source Imaging (ESI) which localizes the brain generator of bioelectrical potentials recorded on the scalp using Electroencephalography (EEG), and simultaneous EEG and functional Magnetic Resonance Imaging (EEG-fMRI) which aims at detecting the changes in blood flow associated with a pathological manifestation of epileptic discharges detected on scalp electrodes.

Both ESI and EEG-fMRI have typically been used as a way to localize brain regions involved in the generation of Interictal Epileptic Discharges (IEDs). IEDs are abnormal transient brain activities typical of epilepsy occurring between seizures with no clinical manifestations, but are detectable on EEG. The localization of the brain generator of

the IEDs, the so-called irritative zone, is therefore facilitated for neuroimaging techniques for which immobility is required (e.g. EEG-fMRI), when compared to the localization of seizures. To be distinguishable from EEG ongoing background activity, the irritative zone should be synchronized over a spatially extended region of several square centimeters (von Ellenrieder et al., 2014). The irritative zone is known to significantly overlap with the presumed epileptogenic focus. Consequently, the source localization of IEDs is widely used as a marker of epilepsy (Ebersole, 1997; Rampp et al., 2019; Mouthaan et al., 2019).

ESI is an imaging technique aiming at localizing the cortical generator of recorded scalp EEG signals. EEG is mainly sensitive to the brain activity of the pyramidal cells which are mainly located along the cerebral cortex. A traditional EEG system contains 19 to 64 electrodes. New high-density EEG (hdEEG) systems, with 128 or 256 electrodes, have been recently proposed, thus increasing the spatial resolution of the modality (Lantz et al., 2003a). ESI results provide useful and non-redundant information during pre-surgical evaluation, especially when applied to hdEEG (Brodbeck et al., 2011). It is also possible to record MagnetoEncephaloGraphy (MEG) which is sensitive to the magnetic fields elicited by abnormal neuronal bioelectrical discharges. From MEG data, it is possible to apply Magnetic Source Imaging (MSI) which provides complementary information to ESI.

ESI and MSI are challenging techniques since they both rely on the resolution of an ill-posed inverse problem: the problem admits no unique solution unless prior knowledge is added to guide the choice of a particular solution. Over the past decades, several models have been proposed to solve ESI or MSI (Baillet et al., 2009; He et al., 2018; Michel and Brunet, 2019). Our laboratory developed the Maximum Entropy on the Mean (MEM) framework which is a Bayesian strategy which solves ESI by estimating the solution exhibiting the largest relative entropy (i.e. minimizing the added information, or the Kullback-Liebler divergence) when compared to chosen prior information (Amblard et al., 2004; Grova et al., 2006b). Within this framework, the coherent MEM (cMEM) technique was used in this manuscript. cMEM uses a prior model based on the data-driven partition of the cortical surface. For each parcel, spatial smoothness is applied and cMEM estimates a hidden parameter indicating whether each parcel is active or not (Chowdhury et al., 2013). Our laboratory demonstrated that cMEM was a source localization technique able to recover the spatial extent of the underlying generators and was tested both using realistic simulations (Grova et al., 2006b; Chowdhury et al., 2013) and clinical data (Heers et al., 2015; Chowdhury et al., 2016, 2018; Pellegrino et al., 2018).

On the other hand, fMRI is an imaging technique which is sensitive to local fluctuations of hemodynamic activity within the whole brain. In the context of epilepsy, fMRI is often recorded simultaneously with EEG. The aim is to measure the hemodynamic changes associated with

IED, detected on scalp EEG. Simultaneous EEG-fMRI investigation is therefore an efficient imaging approach to localize the irritative zone. fMRI is sensitive to the Blood Oxygenation Level Dependent (BOLD) response, which is inversely correlated with the local concentration in deoxyhemoglobin in the brain. An increase in neuronal activity is often associated with an increase of BOLD signal, mainly due to a large increase of regional blood flow elicited by neuronal activity followed by the vasodilatation of local vessels (Shmuel, 2010).

Both ESI and EEG-fMRI have their weaknesses: ESI has relatively poor spatial resolution, and is mainly able to localize superficial cortical sources. On the other hand, fMRI provides an indirect measure of neuronal activity, through hemodynamic processes with a temporal resolution of the order of 1 second. Consequently, EEG-fMRI is incapable of differentiating the initial focus of epileptic activity from possible propagating regions. Moreover, the relationship between neuronal firing and neurovascular activity is still not completely understood, especially in pathological contexts (Wan et al., 2006). Recording EEG during an fMRI analysis is a challenging task because the EEG signal is distorted by high magnetic field environments (De Munck et al., 2013). However, MR-related artifacts can significantly be reduced using either software-based (Allen et al., 1998; Vanderperren et al., 2010) or hardware-based solutions (van der Meer et al., 2016b; Abbott et al., 2015).

Despite the inherent difficulty of recording good quality EEG in the MRI scanner, few previous studies suggested that it was feasible to consider ESI along fMRI analysis (Vulliemoz et al., 2010a; Centeno et al., 2017). However, little has been done to verify the validity of ESI when applied to EEG data acquired in the MRI scanner.

The purpose of this PhD dissertation is to carefully validate the accuracy of ESI using high-density EEG recording in the MRI scanner, and to propose a new strategy combining ESI and simultaneous hdEEG-fMRI analyses to improve the localization of the generator of epileptic activity.

We hypothesized that, by considering the most appropriate MR-related artifacts correction methods and ESI techniques, it would be possible to consider ESI of IEDs detected on hdEEG in the scanner to guide and improve the performance of fMRI analyses.

This thesis is organized in the following way. Chapters 2 to 4 provide the necessary background information for this PhD thesis. Chapter 2 presents the fundamental mechanisms of electrophysiology and introduces the technical and biological aspects of EEG and MEG source localization. This chapter starts by reviewing the history of EEG and MEG and then discusses the physiological generators of electromagnetic activities. The technical aspects of EEG and MEG source localization are then presented, with a summary of the estimation

of the solution of the forward problem and then the inverse problem. We present here the different source localization methods, with an emphasis on the MEM framework, which is the specificity of our group. Chapter 3 focuses on the EEG-fMRI recording. This chapter starts by presenting the historical aspects of magnetic resonance imaging before introducing the physical fundamentals of MRI. The particular sequence of fMRI is then described and the technical difficulties of recording simultaneous EEG and fMRI are discussed. In Chapter 4, the reader is introduced to the fundamental mechanisms underlying epilepsy and pre-surgical evaluation of epilepsy. It consists in a brief introduction to epilepsy, including its different types and its treatments. The concept of pre-surgical investigation, with specific interest on the role of ESI and EEG-fMRI in this context, is also introduced. The three manuscripts composing the core content of this PhD Thesis are presented in Chapters 5 to 7. Chapter 5 presents the first published manuscript (Hedrich et al., 2017), which compared the intrinsic spatial resolution of source imaging techniques in high-density EEG and MEG using their resolution matrices. The intrinisic spatial properties of different source localization methods evaluated using noise free simulations were then further validated with real hdEEG and MEG data on healthy subjects using an electrical median nerve stimulation protocol. In Chapter 6, our second manuscript (Hedrich et al., Under Review) is presented. It assesses the quality of electrical source imaging inside the MR scanner on healthy subjects using visual evoked potentials. In this chapter, we compared the quality of EEG signal and ESI reconstruction under two conditions: during an fMRI experiment, or outside the MR scanner. Chapter 7 presents our third manuscript (Hedrich et al., In Preparation) introducing an automatic clustering techniques which aimed at classifying IEDs using ESI results in order to guide the construction of the regressors used for the fMRI analysis. Finally, Chapter 8 concludes this PhD thesis with a discussion of our main findings and contributions, possible limitations, and the future perspectives of our proposed studies.

Notations

Throughout this thesis, all vectors and matrices are denoted in bold characters, vectors being denoted with lower case (e.g. $\boldsymbol{r}$ or $\boldsymbol{\lambda}$), and matrices with upper case (e.g. $\boldsymbol{M}$ or $\boldsymbol{\Sigma}$). The matrix $\boldsymbol{I}$ stands for the identity matrix. The estimator of $\boldsymbol{a}$ is denoted $\hat{\boldsymbol{a}}$. The transpose of a matrix $\boldsymbol{A}$ is indicated by $\boldsymbol{A}^t$. ∇ is the nabla operator: for a real function f, ∇f is the gradient of f; for a vector field $\boldsymbol{A}$, $\nabla \cdot \boldsymbol{A}$ is the divergence of $\boldsymbol{A}$, and $\nabla \times \boldsymbol{A}$ is the curl of $\boldsymbol{A}$.

CHAPTER 2

Principles of electrophysiology and source localization

This chapter will present the technical aspects of non-invasive EEG and MEG recordings and will discuss the different approaches proposed to perform EEG/MEG source localization and source imaging.

After a historical introduction of EEG and MEG, we will present the physiological aspects describing the brain generators of EEG and MEG signals. Then we will briefly introduce the physical principles describing the distribution of electrical potentials and magnetic fields within the head, before introducing different methods to solve the EEG-MEG source localization, with an emphasis on a source imaging framework developed in our laboratory: the "maximum entropy on the mean" framework.

2.1 History of electroencephalography and magnetoencephalography

2.1.1 Electroencephalography

Whereas first studies reporting electrophysiology recordings in animals were performed in Italy by Dr. Luigi Galvani and Dr. Alessandro Volta, the first measurement of electroencephalography performed on animals was reported by the British physiologist, Richard Caton, in 1875 (Haas, 2003). In his works, Caton recorded electrical activity on the head surface or on the cortical surface of monkeys and rabbits (Caton, 1875). He showed that the recorded

electrical currents were sensitive to sleep, anoxia and anesthesia and were abolished by the death of the animal. He also discovered current variations elicited by visual and sensory stimulations. Caton's study on brain electrophysiology was then extended by many others. Among them, Adolf Beck described spontaneous and evoked electrical activity in the brain of dogs and rabbits in 1890 (Coenen et al., 2014). In the meantime, the first electrical stimulation of the human cortex was performed in 1870 by G. Fritsch and Julius Eduard Hitzig, showing for the first time that brain regions were associated with different functions (Niedermeyer, 2005).

In 1924, the German neuropsychiatrist Hans Berger performed the first human electroencephalography (EEG), coining the name (Berger, 1929), in an attempt to discover the physiological basis of "psychic energy". Instead, he recorded the electric propagation of electric potentials elicited by neuronal activity (see Section 2.2). He was the first to recognize the importance of brain oscillations in the interpretation of EEG recordings, and described different physiological and pathological brain waves. He discovered what he then named alpha and beta waves (Figure 2.1). His works also focussed on the nature of EEG alterations in brain diseases such as epilepsy.

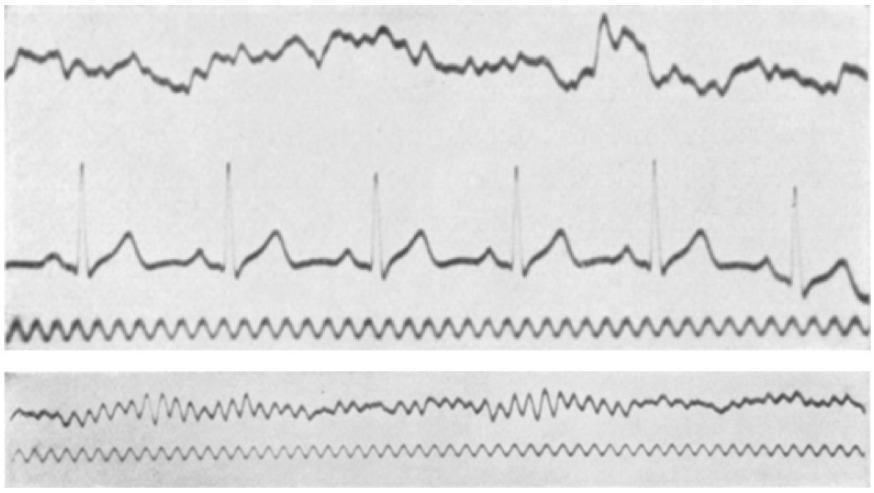

Figure 2.1: One of the first reports of the human EEG from Hans Berger's first publication. **Top:** top line represents beta wave activity (typically 12-30 Hz), related to normal waking consciousness; the middle tracing is the electrocardiogram and the lowest tracing is a generated 10 Hz sine wave. **Bottom:** top line shows what is known now as alpha rhythm (typically 8-12 Hz) which happens when the subject's eyes are closed. The lowest tracing is a generated 10 Hz sine wave. Taken from Berger (1929)

Electroencephalography was first welcomed in the scientific community with high skepticism, and Berger's discovery was really accepted only a few years later when his study was replicated in England by the physiologist Lord Adrian in 1934 (Adrian, 1934) and almost at the same time in the United States by the group of Hallowell Davis (Davis, 1992). EEG

then rapidly became an important tool for clinical and research purposes, especially in the domain of epilepsy where EEG was progressively accepted as a diagnosis tool. Thus, the first tracing of epileptic abnormality was shown by Berger in his early reports (Berger, 1933) and was first carefully investigated in 1934 (Fischer and Lowenback, 1934). In 1935, the *petit mal* seizures, now known as absence seizures and characterized by bursts of spike and wave discharges, of 12 children were recorded (Figure 2.2) (Gibbs et al., 1935).

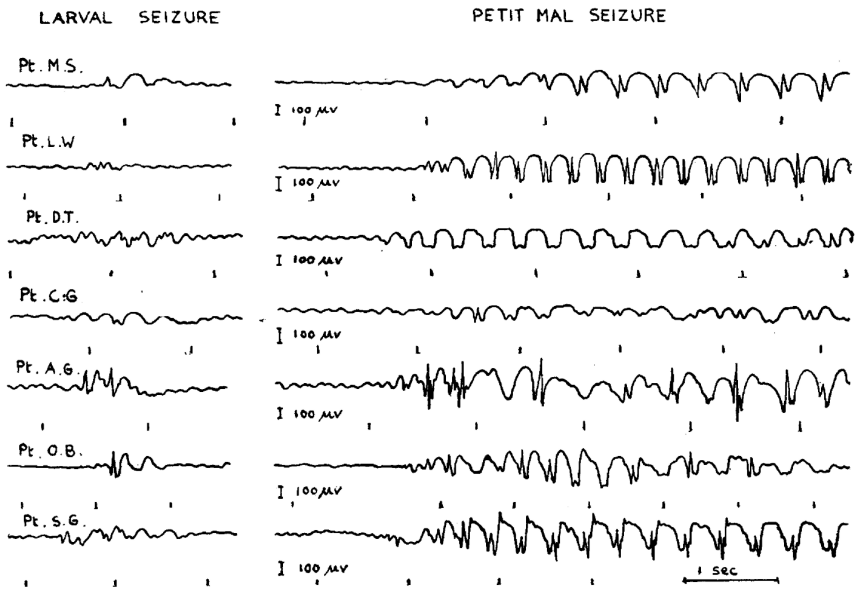

Figure 2.2: Examples of EEGs from petit mal (absence) seizure patients. Taken from Gibbs et al. (1935)

Over the next decades EEG technique became largely popularized and the instrumentation was improved and refined (Collura, 1993). In 1937 the electrophysiologist Herbert Jasper joined the Montreal Neurological Institute (MNI), a neurological center founded in 1934 by the neurosurgeon Wilder Penfield (Feindel, 1992), and developed EEG techniques in Montreal. He notably introduced the international 10-20 system (Jasper, 1958) that was adopted as the standard electrode placement method (see Section 2.3.1). Invasive human EEG recordings, such as implanted intracerebral electrodes (Meyers et al., 1949) and microelectrodes, appeared in the 1950s and allowed the measurement of the activity of a single neuron (Davis, 1992). In the 1970s and 1980s, the invention of the computed tomography and magnetic resonance imaging offered the possibility to have structural images of the brain, and opened the development of EEG brain mapping (Duffy et al., 1979).

2.1.2 Magnetoencephalography

The history of magnetoencephalography (MEG) is more recent. Indeed, the magnetic field induced by the bioelectrical current of the neuronal activity is more difficult to measure than the corresponding electrical potentials. The reason for this is that the magnetic fields generated by human neuronal activity have very low amplitude (in the order of 10^{-15} to 10^{-12} T): much weaker than the Earth magnetic field (in the order of 10^{-5} T) or other magnetic fields generated by electrical devices. The first recording of MEG signals was performed by David Cohen, a physicist at the University of Illinois, in a magnetically shielded room using a copper induction coil as the detector (Cohen, 1968). Later, Cohen improved his technique with the help of James Zimmerman at the Massachusetts Institute of Technology with the development of SQUIDs (Superconducting Quantum Interference Devices) detectors, which are still used today. While first studies involved one or very few MEG sensors, the first whole head MEG system was introduced in the 1990s (Ahonen et al., 1993; Vrba et al., 1993). Most of today's MEG devices consist of whole head systems equipped with around 300 SQUIDs connected to sensor coils. However, recent works on MEG instrumentation seem to have developed a promising new type of sensor: the optically-pumped magnetometers, which do not require cryogenic conditions as opposed to SQUIDs (Boto et al., 2017). The new technology offers the possibility to place MEG sensors directly on the subject scalp, thus increasing the data sensitivity.

2.2 Generators of EEG and MEG signals

The signals recorded on EEG and MEG are mostly generated by neuronal activity located on the cortical surface of the brain. There are about 50-100 billions neurons but not all neurons contribute equally to the EEG/MEG signals. Neurons are brain cells that convey information via electrical or chemical signals. As depicted in Figure 2.3, a neuron is typically composed of dendrites which receive information from other neurons, the soma where the electrical inputs are processed, and one or several axons which represent the output structure of the cell. Very often, the axon is covered by a myelin sheath which facilitates the transmission of the electrical signal.

The main contributors of those electrophysiological (EEG or MEG) signals are the pyramidal cells (Buzsáki and Draguhn, 2004; Nunez and Srinivasan, 2006), which are neurons located within the layer V of the cortical surface (i.e. a few millimeters from the cortical surface), as well as in the hippocampus and in the amygdala. Pyramidal neurons are composed of multiple dendrites and a single axon: both dendrites and axons branch extensively. They

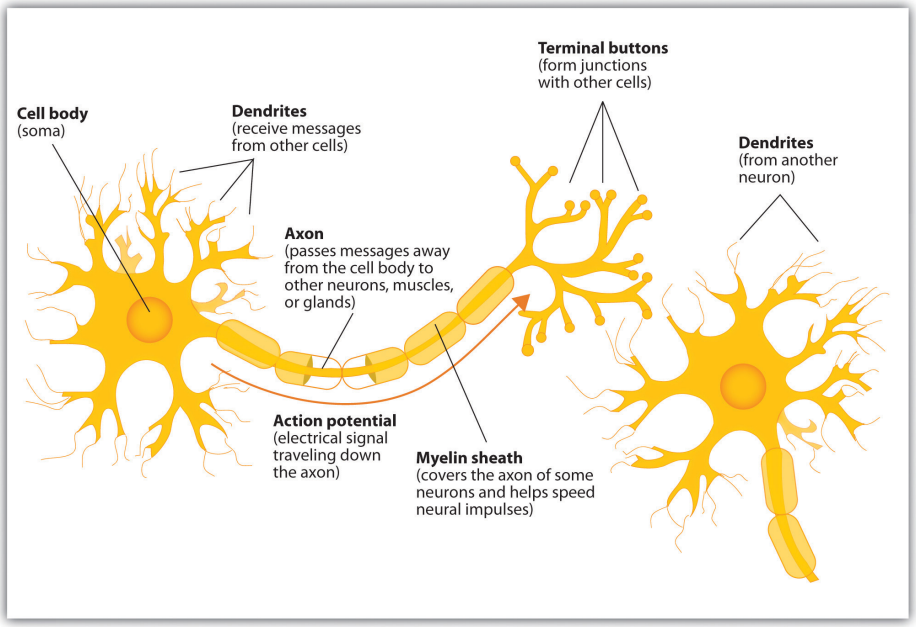

Figure 2.3: Components of a neuron. Taken from Stangor and Walinga (2017).

are typically excitatory, i.e. when activated they provoke a depolarization in efferent neurons.

Information transfer between neurons is ensured through the synapses. A synapse is a junction between two neurons, most of the time from an axon to a dendrite. In the brain there are roughly 100 trillion synaptic connections. The communication is unidirectional: the information only flows from the so-called presynaptic neuron to the postsynaptic neuron. In most cases, the transmission of information within a synapse is ensured by chemical messengers called neurotransmitters. The principle of a synapse activation is explained in Figure 2.4. A synapse is composed of a presynaptic terminal, the end of the axon of the presynaptic neuron; the postsynaptic terminal, where the afferent neuron receives the neurotransmitters; and a gap between the two, called the synaptic cleft. The neurotransmitters are stored in the presynaptic terminal, in vesicles inside the cell, and are released when the presynaptic terminal is depolarized. The change of polarity of the membrane cell causes the opening of the voltage-gated calcium ion Ca^{2+} channels. This results in a movement of calcium ions into the neuron. The Ca^{2+} inside the presynaptic terminal induces the fusion of the vesicles with the neuron membrane – the neurotransmitters are then released into the synaptic cleft. These chemical agents bind with the receptor molecules on the postsynaptic membrane, which causes the opening and closing of different ion channels (mainly Na^+, Cl^- and K^+ ions). This process creates a displacement of charges: the so-called PostSynaptic Potential (PSP). A PSP can be either excitatory or inhibitory, depending on whether the exchange of ions between the cell and the extracellular medium creates a depolarization (for excitatory neurons) or

a hyperpolarization (for inhibitory neurons) of the membrane cell. The neurotransmitters which did not bind to the postsynaptic neuron are taken up by the presynaptic cell and surrounding glial cells, and new vesicles are then created.

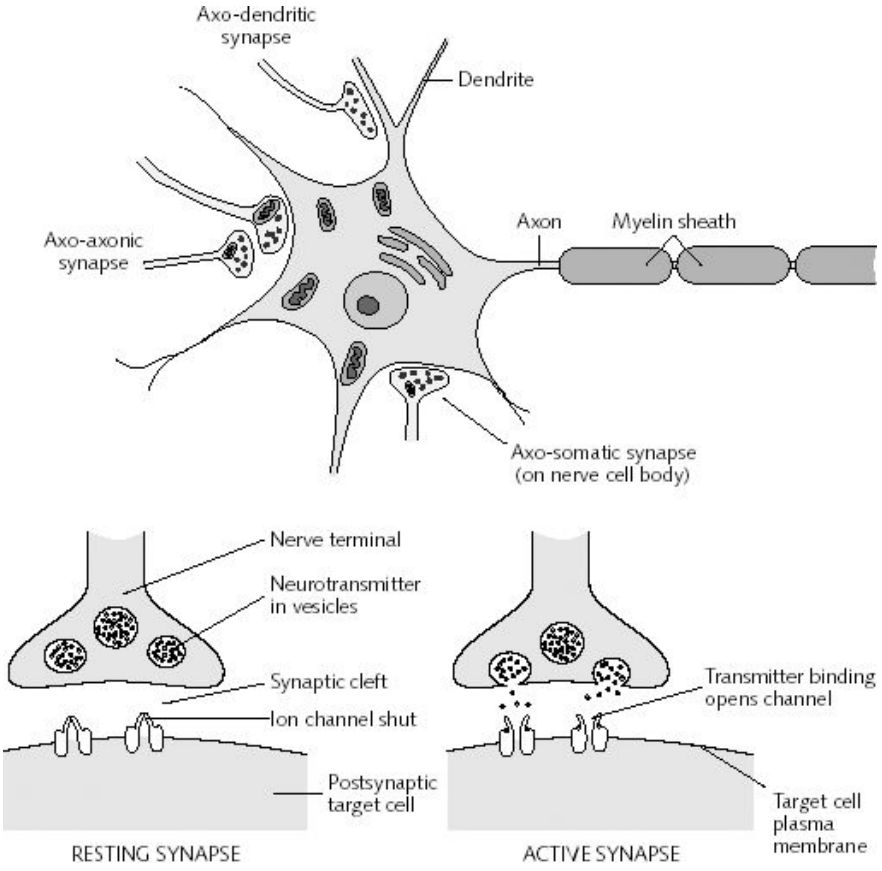

Figure 2.4: Functioning of a synapse. Taken from http://www.answers.com/topic/synapse.

PSPs generally last from tens to a few hundred milliseconds. For this reason, if several PSPs are produced in a short period of time, they could sum up and produce a larger depolarization or hyperpolarization. This phenomenon is reinforced by spatial summation, i.e. a summation of PSPs from synapses that are spatially close, thus increasing overall excitation or inhibition.

The resting membrane potential is -70 mV. If enough Excitatory PSPs (EPSPs) are engaged, and the membrane potential reaches a threshold around -55 mV, an Action Potential (AP) is created in the soma. An AP[1] is an event of high amplitude lasting a few milliseconds which moves along the axon. The propagation of an AP to the axon terminal causes a depolarization of the local membrane, which induces the release of neurotransmitters in the

[1]Action potentials are sometimes called "spikes" but should not be confused with interictal epileptic potentials, which could also be called spikes.

synaptic cleft. Conversely, an Inhibitory PSP (IPSP) provokes a hyperpolarization of the membrane below -70 mV, therefore hindering the production of action potentials.

The PSPs elicit a difference of electric potentials between the apical dendrite and the soma of the cell. This induces a movement of ions within the dendrite trunk, and therefore a current, which is called the primary current. To ensure the conservation of electric charges, the primary current elicits the production of other currents which flow in the opposite direction, in the conductive extracellular medium. Those are called secondary currents or volume conduction currents. EEG electrodes are sensitive to the change of currents in the extracellular medium, i.e. the secondary currents whereas MEG sensors are mainly sensitive to the magnetic field induced by the primary current.

In order to be detected by non-invasive sensors placed on the scalp, the primary currents (for MEG) and the volume conduction currents (for EEG) need to be large enough. This can only be achieved when an sufficient number of neurons in the same region are active together, i.e. by synchronization in time and in space of several PSPs. The particular geometry of the pyramidal cells, which are all aligned perpendicularly to the cortical surface, allows the summation of the currents produced by spatially synchronized neurons. EEG needs an active source of at least 4 to 8 cm^2 to be visually distinguishable from the ongoing background activity (Tao et al., 2007; von Ellenrieder et al., 2014), whereas MEG only needs a source size of 3 to 4 cm^2 to result in a detectable signal (Oishi et al., 2002). To achieve detection, all active neurons should be also synchronized in time. This is one of the reasons why action potentials are usually not detectable on EEG or MEG as opposed to PSPs: the temporal duration of action potential is too short to allow a good time synchronization with all the active neural cells[2].

2.3 EEG and MEG recordings

2.3.1 EEG recordings

EEG acquisition consists of placing electrodes on the scalp of the participant. The number of used electrodes depends on the experimental design, ranging from a few sensors up to 512 electrodes. The electrodes are either glued directly on the scalp of the participant or placed on the head with a special cap. In either case, special care is used to ensure a good electrical conductivity between the skin and the electrodes by using abrasive gel to clean the

[2]Another reason why action potentials are difficult to detect from EEG/MEG scalp recordings is that they behave as quadripoles. The electric potentials and magnetic fields of action potentials are more attenuated when propagating to the scalp

skin and by using a good conductive medium (conductive gel, or sponges imbibed with a saline solution for systems from Philips Neuro).

Electrodes record small bioelectrical potentials which are amplified and converted to digital signals in a device commonly called an amplifier. The output of the amplifier is then stored in a computer. One important feature of the amplifier is the sampling frequency, which is the number of samples recorded in one second. A high sampling frequency is crucial for the detection of fast events (from 50 Hz to around 500 Hz) (Nariai et al., 2019). The active range of the analog-to-digital converter is also a important feature because it is needed to obtain the best resolution of EEG without taking the risk of saturation wherein the EEG data would be unusable. During EEG acquisition simultaneously with fMRI data, special care is brought to the dynamic range of the amplifier, as the MRI-related artifacts present in the EEG have high amplitude leading to an increased risk of saturation of the EEG signal (Abreu et al., 2018a). For the same reason, to allow accurate correction of MR-related artifacts, larger frequency sampling, typically up to 5 kHz, is usually required.

It is worth noting that the amplification and analog-to-digital conversion could be done at the level of the electrodes, on the head of the participant. This particular system, called "active electrodes", has the advantage of reducing the noise induced by the wires (Xu et al., 2017).

A reference electrode, with which every difference of electrical potentials will be measured, is always needed in an EEG experiment. The position of the reference electrode depends on the location of the function of study. Electrodes close to the reference could suffer from a decrease in resolution (Yao et al., 2019), therefore the reference electrode is usually placed far from the region of interest. Classical positions for the reference electrode include, the vertex of the head (Cz), the mastoids (either one of the mastoids or both of them using a linked reference), the ears or the tip of the nose. Moreover, another electrode should be placed on the patient: the ground electrode to perform common mode rejection.

The quality of contact between the electrodes and the skin is measured with the impedance. High impedance can lead to distortions which can be difficult to clean from the signals. Therefore it is important to make sure the impedance is as low as possible (typically below 5 kΩ) before starting an EEG experiment.

The electrode configuration is called a montage. Depending on the number of electrodes and the region of interest in a EEG recording, montages can vary. To obtain a international standard on the position on the electrode on the head, the 10-20 system was introduced in 1958 by Dr Jasper at the Montreal Neurological Institute (Jasper, 1958). This system established a universal set of EEG positions with respect to anatomical landmarks, namely the nasion (the bridge between the nose and the forehead), the inion (the highest point

of the external protuberance of the occipital bone at the back of the head), and the two peri-auricular points (close to the ears, at the superior junction of the tragus). The distance from the anatomical landmark to the electrode positions are set at 10 % of the total distance between landmarks (nasion to inion, or left peri-auricular to right peri-auricular) whereas the distance between electrodes is 20 % of the total distance between landmarks, as illustrated in Figure 2.5(1.). Each electrode position is assigned a letter (or letters) related to the brain areas underlying the position of the electrode (Frontopolar – Fp; Frontal – F; Temporal – T; Central – C; Occipital – O; Parietal – P) and a number showing the position relative to the midline (z for midline, even numbers for right hemisphere and odd numbers for left hemisphere; the larger the number, the further the position is from the midline). The 10-20 montage is composed of 19 electrodes. When the number of electrodes used in an experiment increased, new international montages with higher resolutions appeared, such as the 10-10 system (81 electrodes, interelectrode distance: 10 %) (Chatrian et al., 1985), or even 10-5 system (329 electrodes, interelectrode distance: 5 %) (Jurcak et al., 2007). In this manuscript, we use a EEG system from Philips Neuro (Eugene, Oregon) which does not follow the international standards. In Figure 2.5 the 10-20 system proposed by Dr. Jasper, the 10-5 system and the EGI 256-electrode montage are illustrated.

2.3.2 MEG recordings

The goal of MEG is to record magnetic signals coming from the brain at the order of 50-500 femto Tesla (10^{-15} T). This is challenging because all electronic devices produce a magnetic field with higher strength than the brain magnetic signal; even the Earth produces a magnetic field ranging from 22 to 67 micro Tesla (10^{-6} T) (Chilliat et al., 2015).

For these reasons, recording MEG data from brain activity requires the use of ultrasensitive detectors; the superconducting quantum interference devices (SQUID). A SQUID consists of two superconductors separated by thin insulating layers. Such a structure can be used to convert magnetic flux into an electrical voltage (Josephson, 1962). To allow superconductivity, the SQUIDs are immersed in liquid helium (at the temperature of 4 K = - 269 °C).

The simplest type of magnetic flux detector is the magnetometer, which consists of a single coil located close to the head of the participant. Magnetometers are highly sensitive to the brain magnetic flux, but they are also highly affected by environmental noise. Another type of magnetic sensor is the gradiometer, which consist of two oppositely-wound coils. The coils in gradiometers can either be one above the other radially to the head (axial gradiometers) or next to each other tangentially to the head (planar gradiometers). The designs of the magnetometer and both types of gradiometers are illustrated in Figure 2.6. Gradiometers

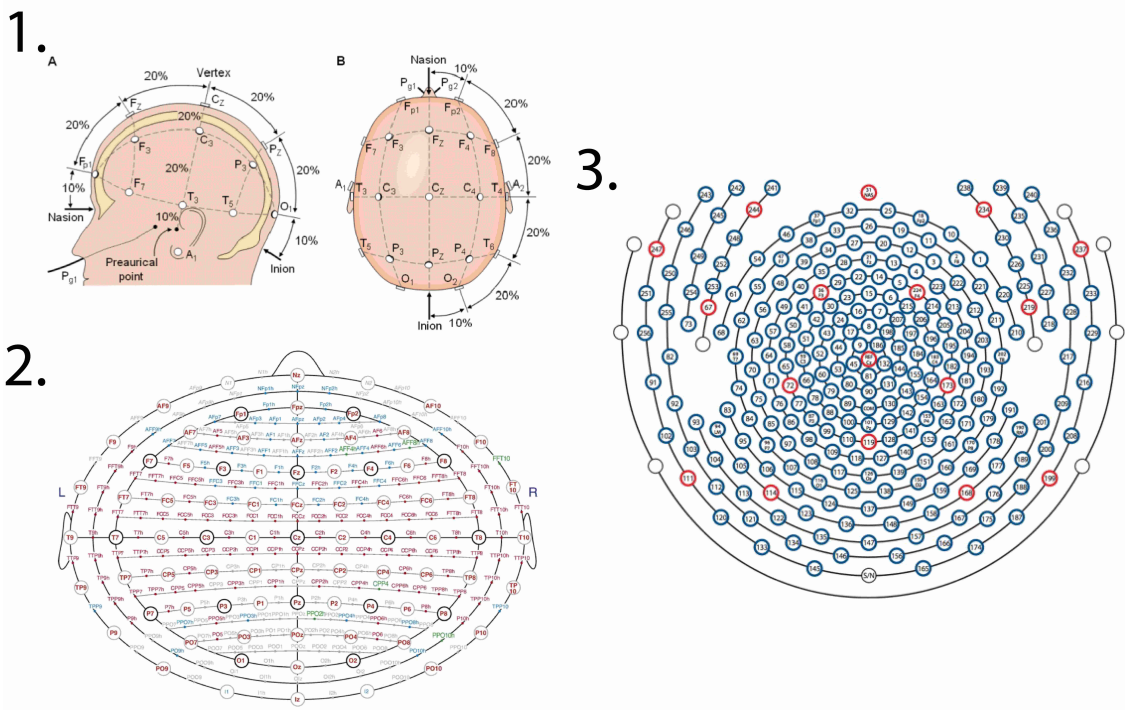

Figure 2.5: Examples of EEG montages. **1.** The international 10-20 system composed of 19 electrodes seen from (A) left and (B) above the head. *A = Ear lobe, C = central, T = temporal, P = parietal, F = frontal, Fp = frontopolar, O = occipital.* Modified from Sharbrough et al. (1991) **2.** The 10-5 system composed of 329 electrodes proposed by Jurcak et al. (2007) **3.** EEG montage for the Philips neuro 256-electrode system

measure a local gradient of magnetic flux. Magnetic interferences from distant sources are relatively uniform across the two coils, thus resulting in dampening of this disturbance. Conversely, nearby cerebral sources produce different fields on the two coil sites and brain signals are therefore preserved.

The MEG device should be placed in a magnetically shielded room to reduce the contribution of environmental magnetic fields. The shielding is composed of several layers of aluminum and mu-metal, a nickel-iron alloy, which distort incoming magnetic fields. However, sources of interference are still present in the room, such as residual environmental noise, instrumental noise and activity coming from the participant (for example, the heart produces a magnetic field a thousand times stronger than the brain). To remove this noise, some MEG devices are equipped with reference sensors composed of magnetometers and gradiometers located far from the head of subject, in order to specifically measure noise. The signals of the reference sensors are then used by the recording software to further clean MEG data.

Since SQUIDs need to be constantly immersed in liquid helium, MEG sensors are placed inside a helmet which is not attached to the head of the participant. Consequently, each head movement changes the relative position of the sensors to the head, and to the brain, which

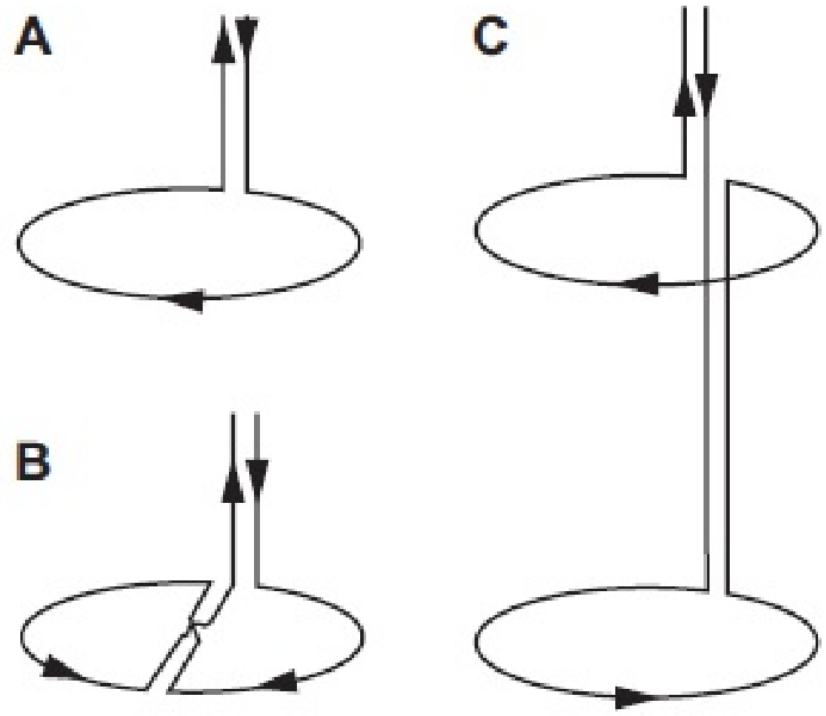

Figure 2.6: Common pick up coil geometries. (A) magnetometer, (B) planar gradiometer, (C) axial gradiometer. Modified from (Hämäläinen et al., 1993).

can lead to spatial inaccuracy. For this reason, participants are asked not to move during MEG recordings and head movements are tracked with head position coils which are fixed on the scalp in known anatomical landmarks.

2.3.3 Coregistration with anatomy

In order to perform source imaging, the positions of the EEG or MEG sensors should be coregistered with the source model, i.e. the segmentation of the subect's cortical surface modeled using anatomical T1-weighted MRI images. Coregistration is an essential step to ensure accurate source localization (Gross et al., 2013). Several techniques exist and aim at finding the position of the EEG and MEG sensors relatively to the fiducial points (nasion, left and right peri-auricular point) using a digitalization device. Since the fiducial points can also be marked on the MRI images, a coregistration using these three points can then be performed. However, this approach is highly sensitive to errors associated with the identification of these landmarks on each modality. To counter this, some studies sample the shape of the head using a 3D digitalization device and coregister the points with the scalp segmentation derived from the MRI images, which usually results in a more accurate and robust coregistration (Whalen

et al., 2008). In this thesis, the EEG sensor digitalization was done using the Geodesic Photogrammetry System developed by EGI, which consists of 11 cameras mounted in a structure permitting simultaneous pictures of the EEG electrodes from different angles to be taken. The location of the sensors was then determined using semi-automated software with machine vision technology. For MEG, a 3D digitalization of the head was performed conjointly with the position of the localization coils using the electromagnetic Polhemus Fastrak 3D localizer (Colchester, NH). For both modalities, the sensors were coregistred with the scalp segmentation from anatomical MRI using the iterative closest point algorithm (Besl and McKay, 1992).

2.4 The EEG/MEG forward problem

2.4.1 Quasi-static approximation of Maxwell's equations

To perform source localization, one should first solve the so-called forward problem, which consists in describing the physical phenomena responsible for the propagation of the electric potentials and magnetic fields within the head. The objective is to model all of the structure inside the head to estimate the EEG or MEG response to a source that is produced by a known configuration of generators.

The forward model is solved using Maxwell's equations of the propagation of electromagnetic fields. Maxwell's equation are a system of four differential equations which permit calculating the electric field $\boldsymbol{E}$, the magnetic field $\boldsymbol{B}$ with the charge density ρ, the current density $\boldsymbol{J}$, and ϵ and μ which are respectively the electrical permittivity and the magnetic permeability of the medium:

$$\begin{cases} \nabla \cdot \boldsymbol{E} = \frac{\rho}{\epsilon} \\ \nabla \times \boldsymbol{E} = -\frac{\partial \boldsymbol{B}}{\partial t} \\ \nabla \cdot \boldsymbol{B} = 0 \\ \nabla \times \boldsymbol{B} = \mu \left(\boldsymbol{J} + \epsilon \frac{\partial \boldsymbol{E}}{\partial t} \right) \end{cases} \tag{2.1}$$

The useful frequency spectrum of MEG or EEG data is typically below 1 kHz, which is slow compared to the propagation of the electromagnetic fields (electromagnetic waves propagating roughly at the speed of light). For this reason, it is possible to simplify Maxwell's equations by considering the quasi-static approximation. In the quasi-static approximation, the time derivatives can therefore be neglected. Moreover, the electric field $\boldsymbol{E}$ could be written as the negative gradient of the electric potential V:

$$\boldsymbol{E} = -\nabla V; \tag{2.2}$$

One can also observe that the current generators $\boldsymbol{J}$ can be written as the combination of the primary current flow $\boldsymbol{J}^p$ related to the actual neural activity and a volume current flow $\boldsymbol{J}^v$ (see Section 2.2):

$$\boldsymbol{J} = \boldsymbol{J}^p + \boldsymbol{J}^v = \boldsymbol{J}^p + \sigma\boldsymbol{E} = \boldsymbol{J}^p - \sigma\nabla V \tag{2.3}$$

where σ is the conductivity of the medium. From the quasi-static approximation, one can derive that $\nabla\cdot\boldsymbol{J} = 0$ (conservation of the charges), and therefore:

$$\nabla\cdot(\boldsymbol{J}^p - \sigma\nabla V) = 0 \implies \nabla\cdot(\sigma\nabla V) = \nabla\cdot\boldsymbol{J}^p \tag{2.4}$$

For the calculation of $\boldsymbol{B}$, the derivation of the above equations leads to the Biot-Savart law, the magnetic field at location $\boldsymbol{r}$ can be written:

$$\boldsymbol{B}(\boldsymbol{r}) = \frac{\mu}{4\pi}\int_{\mathbb{R}^3} \boldsymbol{J}(\boldsymbol{r}') \times \frac{\boldsymbol{r}-\boldsymbol{r}'}{\|\boldsymbol{r}-\boldsymbol{r}'\|^3} d\boldsymbol{r}' \tag{2.5}$$

It is worth noting that, contrary to the conductivity σ, which is highly dependent on the medium and on the frequency, the magnetic permeability μ does not vary between the different head tissues.

2.4.2 Source and head models

The solution to the forward problem in EEG and MEG can be obtained by solving Equations (2.4) and (2.5) respectively. The computational load for the solving of these equations depends on the chosen source and head models. Indeed, the model can be simplified if we assume that either the current generator is only composed of one dipolar source (the single dipole approach), that the geometry of the head can be modeled using spheres (spherical head models), or that the different tissues in the head can be associated to homogeneous conductivity values (boundary element method). Otherwise, the forward solution can also be solved computationally by using a detailed discretization of the whole volume of the head (finite element method).

2.4.2.1 Dipolar source model

We can assume that a local generator of EEG/MEG signals can be modeled by a current dipole at a specific position $\boldsymbol{r}_0$. The primary current $\boldsymbol{J}^p$ elicited by this dipole can then be written:

$$\boldsymbol{J}^p(\boldsymbol{r}) = \boldsymbol{q}\delta(\boldsymbol{r} - \boldsymbol{r}_0) \tag{2.6}$$

where δ is the Dirac distribution and $\boldsymbol{q}$ is the moment of the current dipole (in A.m). Within a uniform medium characterized by the conductivity σ and the magnetic permeability μ, Equations (2.4) and (2.5) can then be written as:

$$V(\boldsymbol{r}) = \frac{1}{4\pi\sigma}\boldsymbol{q}\cdot\frac{\boldsymbol{r} - \boldsymbol{r}_0}{\|\boldsymbol{r} - \boldsymbol{r}_0\|^3} \tag{2.7}$$

$$\boldsymbol{B}(\boldsymbol{r}) = \frac{\mu}{4\pi}\boldsymbol{q}\times\frac{\boldsymbol{r} - \boldsymbol{r}_0}{\|\boldsymbol{r} - \boldsymbol{r}_0\|^3} \tag{2.8}$$

2.4.2.2 Spherical head models

One of the simplest head models is the spherical model, which assumes that the head can be represented as one or a series of homogeneous concentric spheres representing the major structures of the head. This simple geometry allows one to find an analytic solution for the electric potentials generated by a current dipole within the head (Rush and Driscoll, 1969).

The first spherical models considered only one sphere to represent the head for both EEG and MEG (Frank, 1952). This model was greatly inaccurate especially when modeling the EEG forward problem because it failed to take into account the drop in conductivity of the skull compared to the surrounding tissues. In this thesis, a model consisting of three concentric spheres representing the scalp, the skull and the brain, was introduced (de Munck and Peters, 1993).

For MEG on the other hand, since we can assume that the magnetic permeability is constant throughout all parts of the head and that the volume conduction current within the skull has very little impact on the generation of the magnetic field $\boldsymbol{B}$, a single sphere model can usually be considered . This model was later improved to better reflect the actual geometry of the human head. The overlapping spherical model, instead of using only one sphere for all the sensors, uses the best fitting sphere to model the head for each individual sensor (Huang et al., 1999).

2.4.2.3 Boundary element method (BEM)

In the Boundary Element Method (BEM), it is assumed that all different tissues of the head (scalp, cerebrospinal fluid, brain) have homogeneous and isotropic conductivity values. Consequently, only the surfaces representing the boundaries between the different tissues need to be modeled to solve the forward problem. For the BEM model, the geometry of those surfaces are discretized into surface elements using MRI segmentation. The solution

of the forward solution is then solved iteratively for each surface element. Compared to spherical head models, BEM is computationally costly but offers a more realistic model of the generation of the electrical and magnetic fields (Mosher et al., 1999a).

However, BEM assumes that the boundary surfaces should be closed and non overlapping in order to avoid numerical instabilities, which can be problematic for patients with holes in their skull (von Ellenrieder et al., 2014). Moreover, the assumption of isotropy within the medium does not hold in brain structure. Despite the limitations, BEM models are quite accurate (Henson et al., 2009) and were used in the manuscripts of this thesis (Henson et al., 2009). In this PhD thesis, we used the algorithm named "Symmetric BEM method" (Kybic et al., 2006), implemented in OpenMEEG4 (`http://openmeeg.github.io/`) (Gramfort et al., 2010) which has been shown to be the most accurate and robust to numerical instabilities when compared to other implementations of BEM.

2.4.2.4 Finite element method (FEM)

Unlike BEM, finite element method aims at calculating the electrical potentials and magnetic field inside the whole head volume, thus permitting to take into account the anisotropy and non-homogeneity of the tissues (Wolters, 2007). It is therefore the most realistic solution to the forward model but requires a large amount of computational power. FEM also offers the possibility to incorporate a larger variety of tissues (such as soft and hard bones, grey matter and white matter) (Vorwerk et al., 2014).

2.4.2.5 Estimation of electrical conductivities

As mentioned in Section 2.4.1, the magnetic permeability does not vary much in biological tissues and can be approximated with the magnetic permeability of free space: $\mu(\boldsymbol{r}) = \mu_0 \approx 12.57 \,.\, 10^{-7}$ H/m.

However, it is important to note that electrical conductivity does vary to some degree with the nature of the tissue being measured, and uncertainties in assigning conductivity values can lead to significant errors when solving the inverse problem (Vorwerk et al., 2019).

Because of this, estimating the exact value of conductivity values within head tissues is a challenging task. Several studies have developed experiments to estimate those values, either using electrical impedance tomography, comparing intracranial and scalp recordings, or using post-mortem measurements. A literature review on the question has been made in Aydin et al. (2014) and summarized in a table in Vorwerk et al. (2019), which is reproduced in Table 2.1.

Table 2.1: Tissue conductivity ranges [mS/m]. Taken from Vorwerk et al. (2019).

Tissue	Min.	Max.	Standard	References
Skin	280.0	870.0	430.0	(Haueisen et al., 1997; Ramon et al., 2004)
Skull	1.6	33.0	10.0	(Akhtari et al., 2002; Hoekema et al., 2003; Dannhauer et al., 2011)
CSF	1769.6	1810.4	1790.0	(Baumann et al., 1997)
Grey matter	220.0	670.0	330.0	(Haueisen et al., 1997; Ramon et al., 2004)
White matter	90.0	290.0	140.0	(Haueisen et al., 1997; Ramon et al., 2004)

One important parameter to consider is the brain-to-skull conductivity ratio. It has been estimated to be 1:80 in 1969 (Rush and Driscoll, 1969) and this value has been used as a reference since then. However, most recent papers suggest that the ratio should rather range between 1:10 and 1:50 (Lai et al., 2005). For the manuscripts presented in this thesis, the conductivity values for scalp, skull and brain were set to 330.0 mS/m, 16.5 mS/m and 330.0 mS/m respectively, resulting in a brain-to-skull conductivity ratio of 1:20.

2.5 The EEG/MEG inverse problem

EEG and MEG source localization is an inverse problem because the goal is to infer from a set of observations (MEG fields or EEG potentials measured on the scalp) the generators within the brain that produced them. The problem is ill-posed, meaning that a unique solution cannot be found unless further assumptions or constraints are added to the problem.

The first category of assumptions that can be made is to restrict the number of active generators: this is the so-called localization approach. By assuming that the data can be explained by one or a few active dipolar sources, the problem becomes well-posed and consists of estimating the best positions, orientations and amplitude of a small set of dipolar sources. This is the so-called Equivalent Current Dipole localization approach (ECD, see Section 2.5.1). An extension of this approach consists of assessing on every position of a grid how likely an ECD would be localized at this position: these are the so-called dipole scanning methods (see Section 2.5.2). The alternative to the localization approach is the imaging approach. In such models, brain activity is assumed to be generated from a spatially extended brain region, where the source space is assumed to be a large set of dipolar sources for which the positions, and sometimes the orientations, have been fixed. Solving the EEG/MEG inverse problem then consists of estimating the amplitudes of the dipolar sources. These methods are denoted distributed source imaging methods (see Section 2.5.3).

2.5.1 Equivalent Current Dipoles (ECD)

In order to solve the inverse problem, the most straight-forward approach is to assume that the data can be explained by a set of N_s dipolar sources whose positions and orientations need to be estimated in the presence of additive noise:

$$\boldsymbol{m} = \sum_{i=1}^{N_s} \boldsymbol{G}(\boldsymbol{r}_i)\boldsymbol{q}(\boldsymbol{r}_i) + \boldsymbol{e} \tag{2.9}$$

where $\boldsymbol{G}$ is the gain matrix providing an estimate of the forward model assessing the contribution on all the EEG or MEG sensors of a dipolar source located in $\boldsymbol{r}_i$ in a specific orientation. $\boldsymbol{r}_i$ and $\boldsymbol{q}$ are respectively the vector of position, and the vector of amplitude (therefore encoding the magnitude and the orientation) of the ith dipolar source to be estimated, and $\boldsymbol{e}$ is the additive noise.

Those parameters can be estimated using the least square solution. The cost function that needs to be minimized is the square of the Frobenius norm of the residuals. The solution to the least square solution is then given by:

$$\{\hat{\boldsymbol{r}}, \hat{\boldsymbol{q}}\} = \arg\min_{\{\boldsymbol{r},\boldsymbol{q}\}} \left\| \boldsymbol{m} - \sum_{i=1}^{N_s} \boldsymbol{G}(\boldsymbol{r}_i)\boldsymbol{q}(\boldsymbol{r}_i) \right\|_F^2 \tag{2.10}$$

To solve this equation, one can observe that for any estimated $\hat{\boldsymbol{r}}$, the estimated amplitude $\boldsymbol{q}$ that minimizes the cost function is always:

$$\hat{\boldsymbol{q}} = \boldsymbol{G}^{+}\boldsymbol{m} \tag{2.11}$$

where $\boldsymbol{G}^{+}$ is the pseudoinverse of $\boldsymbol{G}$. If $\boldsymbol{G}$ is of full column rank, the pseudoinverse has an explicit expression: $\boldsymbol{G}^{+} = (\boldsymbol{G}^t\boldsymbol{G})^{-1}\boldsymbol{G}^t\boldsymbol{m}$. The cost function to minimize $\boldsymbol{r}$ then becomes:

$$\begin{aligned}
\hat{\boldsymbol{r}} &= \arg\min_{\boldsymbol{r}} \|\boldsymbol{m} - \boldsymbol{G}\hat{\boldsymbol{q}}\|_F^2 \\
&= \arg\min_{\boldsymbol{r}} \left\|\boldsymbol{m} - \boldsymbol{G}\boldsymbol{G}^{+}\boldsymbol{m}\right\|_F^2 \\
&= \arg\min_{\boldsymbol{r}} \left\|(\boldsymbol{I} - \boldsymbol{G}\boldsymbol{G}^{+})\boldsymbol{m}\right\|_F^2 \\
&= \arg\min_{\boldsymbol{r}} \left\|\boldsymbol{P}_{\boldsymbol{G}}^{\perp}\boldsymbol{m}\right\|_F^2
\end{aligned} \tag{2.12}$$

where $\boldsymbol{P}_{\boldsymbol{G}}^{\perp} = (\boldsymbol{I} - \boldsymbol{G}\boldsymbol{G}^{+})$ is the projection matrix onto the orthogonal sub-space of $\boldsymbol{G}$. Several iterative approach may be used to minimize this cost function. Gradient descent, Gauss-Newton or Lavenberg-Marquardt approaches can be considered.

This minimization can be performed for each time instant (using the equations shown here), which is called the moving dipole approach (Cuffin, 1985), and the dipole can be fixed over the whole time window (Wood, 1982).

The main limitations of the ECD localization approach are that the total number of dipoles has to be fixed a priori. Choosing the right number of dipoles can be challenging and can lead to overfitting the data. Moreover, the results of the dipole fitting approaches might be inaccurate in low Signal-to-Noise Ratio (SNR) conditions or when the source generator is spatially extended (Hara et al., 2007; Alarcon et al., 1994).

2.5.2 Dipole scanning models

Dipole scanning models have been proposed as an interesting alternative to handle the difficult question of fixing a priori the number of ECD sources to be considered. Indeed, the dipole scanning approach consists of assessing the relevance of fitting a dipolar source sequentially to each position of a 3D grid inside the brain by estimating a statistical score on how likely such a dipolar source could contribute to the recorded data. Different dipole scanning approaches have been proposed, such as beamforming approaches or the Multiple Signal Classification (MUSIC) approach and its variants: recursive, R-MUSIC, and recursively applied and projected MUSIC, RAP-MUSIC.

2.5.2.1 Beamforming techniques

Beamforming techniques use a linear spatial filter of the data to estimate the contribution coming from a particular position on a 3D grid, while reducing the influence of every other possible location. A specific filter needs to be estimated for every position on a 3D grid, satisfying the following constraints:

$$\boldsymbol{q_r} = \boldsymbol{W_r^t m} \tag{2.13}$$

where $\boldsymbol{q_r}$ is the moment's amplitude of the source at location $\boldsymbol{r}$ and $\boldsymbol{W_r}$ is the corresponding spatial filter. The goal of the Beamforming techniques is to estimate the best spatial filter $\boldsymbol{W_r}$. A widely used technique, called Linearly Constrained Minimum Variance (LCMV) (Van Veen et al., 1997), estimates the spatial filter by minimizing the source variance $\boldsymbol{\Sigma_q}$:

$$\boldsymbol{\Sigma_q}(\boldsymbol{r}) = \mathbb{E}\left[\boldsymbol{q_r q_r^t}\right] = \boldsymbol{W_r^t \Sigma_m W_r} \tag{2.14}$$

where $\boldsymbol{\Sigma_m} = \mathbb{E}\left[\boldsymbol{m m^t}\right]$ is the data covariance matrix.

The estimated of the spatial filter can then be found as:

$$\boldsymbol{W}^t_{\text{LCMV},\boldsymbol{r}} = \left(\boldsymbol{G}^t_{\boldsymbol{r}}\boldsymbol{\Sigma}^{-1}_{\boldsymbol{m}}\boldsymbol{G}_{\boldsymbol{r}}\right)^{-1}\boldsymbol{G}^t_{\boldsymbol{r}}\boldsymbol{\Sigma}^{-1}_{\boldsymbol{m}} \tag{2.15}$$

where $\boldsymbol{G}_{\boldsymbol{r}}$ is the gain matrix at location $\boldsymbol{r}$ considering the three orientations.

The estimated strength of the source is usually normalized with the noise covariance matrix $\boldsymbol{\Sigma}_{\boldsymbol{e}}$ (estimated at the sensor level using background or baseline activity) to obtain a pseudo-Z score:

$$\boldsymbol{Z}_{\text{LCMV},\boldsymbol{r}} = \frac{\text{trace}\left((\boldsymbol{W}^t_{\text{LCMV},\boldsymbol{r}}\boldsymbol{\Sigma}^{-1}_{\boldsymbol{m}}\boldsymbol{W}_{\text{LCMV},\boldsymbol{r}})^{-1}\right)}{\text{trace}\left((\boldsymbol{W}^t_{\text{LCMV},\boldsymbol{r}}\boldsymbol{\Sigma}^{-1}_{\boldsymbol{e}}\boldsymbol{W}_{\text{LCMV},\boldsymbol{r}})^{-1}\right)} = \frac{\text{trace}\left((\boldsymbol{G}^t_{\boldsymbol{r}}\boldsymbol{\Sigma}^{-1}_{\boldsymbol{m}}\boldsymbol{G}_{\boldsymbol{r}})^{-1}\right)}{\text{trace}\left((\boldsymbol{G}^t_{\boldsymbol{r}}\boldsymbol{\Sigma}^{-1}_{\boldsymbol{e}}\boldsymbol{G}_{\boldsymbol{r}})^{-1}\right)} \tag{2.16}$$

$\boldsymbol{\Sigma}_{\boldsymbol{e}}$ needs then to be estimated with background activity.

A frequency domain extension of LCMV, entitled Dynamic Imaging of Coherent Sources (DICS), was also developed (Gross et al., 2001). DICS actually consists of estimating a spatial filter matrix optimized for some specific frequency band, by minimizing the cross-spectral density matrix at a particular frequency band instead of the data covariance matrix.

2.5.2.2 MUSIC approaches

Another well-known dipole scanning approach is the MUSIC method (Mosher et al., 1999b), based on signal classification between signal and noise via signal sub-spaces. If we consider the singular value decomposition of the data $\boldsymbol{m} = \boldsymbol{USV}^t$, the solution to MUSIC consists of minimizing the orthogonal projection onto the noise subspace, estimated by the linear operator $(\boldsymbol{I} - \boldsymbol{U}_d\boldsymbol{U}^t_d)$, where $\boldsymbol{U}_d$ is the d first columns of $\boldsymbol{U}$, d being the estimated rank of the signal space. The estimated MUSIC cost function to minimize for a dipolar source located in $\boldsymbol{r}$ is then given by:

$$\frac{\|(\boldsymbol{I} - \boldsymbol{U}_d\boldsymbol{U}^t_d)\boldsymbol{G}_{\boldsymbol{r}}\|^2}{\|\boldsymbol{G}_{\boldsymbol{r}}\|^2} \tag{2.17}$$

A variant to MUSIC is the Recursively Applied MUSIC (RAP MUSIC) (Mosher and Leahy, 1997), which consists of applying the MUSIC cost function successively after removing the contribution of the previously identified sources as an interesting approach to specifically assess the number of ECD sources contributing significantly to the solution.

2.5.3 Distributed source imaging models

Distributed source imaging models are imaging approaches, attempting to estimate the current density of a set of dipoles, for which the position in space is fixed a priori, doing so at every time sample from the recorded EEG or MEG data. Those dipoles can either be assumed to be sampled in a volumetric source space, typically a 3D grid, or evenly distributed along a

tessellated mesh of the cortical surface (Dale and Sereno, 1993). Solving the inverse method with the distributed source imaging approach is further discussed in Section 2.6, where the Maximum Entropy on the Mean (MEM) framework is introduced. We show that all the well-known linear distributed methods can be defined within this framework. Moreover, we present here the source imaging technique entitled coherent MEM (cMEM), which is widely used in this thesis.

In distributed models, the vector data $\boldsymbol{m}$ of size N_s, the number of sensors can be expressed as the linear combination between the gain matrix $\boldsymbol{G}$, the $N_s \times N_d$ matrix solving the forward problem, where N_d is the number of dipolar sources, and the vector source $\boldsymbol{j}$ of size N_d:

$$\boldsymbol{m} = \boldsymbol{G}\boldsymbol{j} + \boldsymbol{\epsilon} \tag{2.18}$$

where the $N_s \times 1$ vector $\boldsymbol{\epsilon}$ is the additive instrumental noise.

2.6 Solving the inverse problem using the Maximum Entropy on the Mean framework

The inverse problem of the distributed model can be solved within the MEM framework. The MEM framework uses a Bayesian probabilistic approach, where the source $\boldsymbol{j}$ is considered as an observation of the continuous random variable $\boldsymbol{J}$ that describes the dipole current intensities. MEM uses a reference or a prior distribution μ and solves the inverse problem by finding a trade-off between prior information and data fit, i.e. by maximizing the relative entropy (i.e. minimizing the Kullback-Leibler divergence) between the source distribution and the reference distribution, under the constraint of explaining the data.

The source $\boldsymbol{J}$ can be decomposed into the expectation of $\boldsymbol{J}$, corresponding to the source of interest, and a zero-mean additive physiological noise $\boldsymbol{n}$: $\boldsymbol{J} = \mathbb{E}[\boldsymbol{J}] + \boldsymbol{n}$. Equation (2.18) can be then written:

$$\boldsymbol{m} = \boldsymbol{G}(\mathbb{E}[\boldsymbol{J}] + \boldsymbol{n}) + \boldsymbol{\epsilon} = \boldsymbol{G}\mathbb{E}[\boldsymbol{J}] + \boldsymbol{G}\boldsymbol{n} + \boldsymbol{\epsilon} = \boldsymbol{G}\mathbb{E}[\boldsymbol{J}] + \boldsymbol{e} \tag{2.19}$$

where $\boldsymbol{e}$ is the combination between the physiological and instrumental noise.

To solve this equation, the MEM framework regularizes the inverse problem by incorporating prior on $\boldsymbol{J}$ in the form of a reference distribution $\mu(\boldsymbol{j})$. The relative entropy, also known as Shannon entropy or mu-entropy, can then be used to quantify the divergence between the reference μ and the probability distribution p of the random variable $\boldsymbol{J}$:

$$S_\mu(p) = -\int p(\boldsymbol{j}) \ln \frac{p(\boldsymbol{j})}{\mu(\boldsymbol{j})} d\boldsymbol{j} \tag{2.20}$$

The relative entropy measures the difference between the two probabilities, and the positive variant of Equation (2.20) is the Kullback-Leibler divergence between μ and p. In other words, it calculates the amount of information that is needed to be added to the reference distribution μ to explain p, i.e. it measures the amount of "surprise" (new information) received from the distribution p with regards to the prior μ. This measure is negative, and $S_\mu(p)$ is equal to 0 when p is equal to μ.

The objective of the MEM framework is to find the distribution p explaining the data that maximizes the entropy. The corresponding distribution $\hat{p}$ is defined as:

$$\hat{p} = \arg\max_p S_\mu(p), \text{ given } \boldsymbol{m} = \boldsymbol{G}\int_{\mathbb{R}} \boldsymbol{j}p(\boldsymbol{j})d\boldsymbol{j} + \boldsymbol{e} \tag{2.21}$$

In practice one does not need to calculate $\hat{p}$ explicitly. Indeed the solution of the inverse problem, i.e. the current density $\hat{\boldsymbol{j}}$, is obtained as the expected value of $\hat{p}$:

$$\hat{\boldsymbol{j}} = \int_{\mathbb{R}} \boldsymbol{j}\hat{p}(\boldsymbol{j})d\boldsymbol{j} \tag{2.22}$$

The solution of this equation can be solved using the free energy function associated with the reference distribution μ:

$$F_\mu(\boldsymbol{s}) = \ln \int \exp(\boldsymbol{s}\boldsymbol{x})\mu(\boldsymbol{x})d\boldsymbol{x} \tag{2.23}$$

Solving Equation (2.22) consists then of maximizing the cost function $D(\boldsymbol{\lambda})$ (Demoment, 1989; Amblard et al., 2004):

$$\boldsymbol{\lambda}^* = \arg\max_{\boldsymbol{\lambda}} D(\boldsymbol{\lambda}) \text{ with } D(\boldsymbol{\lambda}) = \boldsymbol{\lambda}\boldsymbol{m} - F_\mu(\boldsymbol{G}\boldsymbol{\lambda}) - \frac{1}{2}\boldsymbol{\lambda}^t\boldsymbol{\Sigma}_{\boldsymbol{e}}\boldsymbol{\lambda} \tag{2.24}$$

Where $\boldsymbol{\Sigma}_{\boldsymbol{e}}$ is the noise covariance matrix. $\boldsymbol{\Sigma}_{\boldsymbol{e}}$ is often estimated from segments of ongoing background activity. To avoid numerical instability, the off-diagonal elements of $\boldsymbol{\Sigma}_{\boldsymbol{e}}$ are usually set to zero, and only the diagonal elements are estimated.

It can be shown that in this equation, the function $D(\boldsymbol{\lambda})$ to maximize is a strictly convex function, which means that the maximum value is unique and it is not possible to fall into a local maximum. Once the optimal lambda is found, the current density source solution $\hat{\boldsymbol{j}}$ can be obtained by:

$$\hat{\boldsymbol{j}} = \nabla_{\boldsymbol{s}} F_\mu(\boldsymbol{s})|_{\boldsymbol{s}=\boldsymbol{G}^t\boldsymbol{\lambda}^*} \tag{2.25}$$

The main originality of MEM framework is the degree of flexibility offered in the definition of prior information through the so-called reference distribution, μ. It is possible to obtain solutions that are widely known in the literature with the right choice of μ. Different source

imaging techniques could then be obtained within the MEM framework. Moreover it is worth noting that in practice, the optimization problem of MEM depends only on the parameter $\boldsymbol{\lambda}$ which is the same dimension as the number of sensors N_s, thus reducing the computational load compared to methods which need to solve an optimization problem of the dimension of the number of dipolar sources N_d.

2.6.1 Minimum norm estimate

If the reference distribution is defined as a Gaussian distribution with zero mean and a covariance matrix $\boldsymbol{\Sigma_j}$, the MEM optimization problem can be solved analytically. Equation (2.23) becomes:

$$F_\mu(\boldsymbol{s}) = \frac{1}{2}\boldsymbol{s}^t\boldsymbol{\Sigma_j}\boldsymbol{s} \tag{2.26}$$

Therefore the cost function $D(\boldsymbol{\lambda})$ can be written as:

$$\begin{aligned} D(\boldsymbol{\lambda}) &= \boldsymbol{\lambda}^t m - \frac{1}{2}(\boldsymbol{G}^t\boldsymbol{\lambda})^t\boldsymbol{\Sigma_j}(\boldsymbol{G}^t\boldsymbol{\lambda}) - \frac{\alpha}{2}\boldsymbol{\lambda}^t\boldsymbol{\Sigma_e}\boldsymbol{\lambda} \\ &= \boldsymbol{\lambda}^t\boldsymbol{m} - \frac{1}{2}\boldsymbol{\lambda}^t\left(\boldsymbol{G}\boldsymbol{\Sigma_j}\boldsymbol{G}^t + \alpha\boldsymbol{\Sigma_e}\right)\boldsymbol{\lambda} \end{aligned} \tag{2.27}$$

To solve Equation (2.24), one can observe that $D(\boldsymbol{\lambda})$ is convex. Therefore, the maximum of $D(\boldsymbol{\lambda})$ can be found by solving the equation $\frac{dD}{d\boldsymbol{\lambda}} = 0$:

$$\begin{aligned} \frac{dD(\boldsymbol{\lambda}^*)}{d\boldsymbol{\lambda}} = 0 &\iff \boldsymbol{m} - (\boldsymbol{G}\boldsymbol{\Sigma_j}\boldsymbol{G}^t + \alpha\boldsymbol{\Sigma_e})\boldsymbol{\lambda}^* = 0 \\ &\iff \boldsymbol{\lambda}^* = (\boldsymbol{G}\boldsymbol{\Sigma_j}\boldsymbol{G}^t + \alpha\boldsymbol{\Sigma_e})^{-1}\boldsymbol{m} \end{aligned} \tag{2.28}$$

Therefore, once the optimal $\boldsymbol{\lambda}^*$ is found, the corresponding current density solution within the MEM framework Equation (2.25) can be solved:

$$\begin{aligned} \hat{\boldsymbol{j}}_{\text{MNE}} &= \nabla_{\boldsymbol{s}} F_\mu(\boldsymbol{s})|_{\boldsymbol{s}=\boldsymbol{G}^t\boldsymbol{\lambda}^*} \\ &= \boldsymbol{\Sigma_j}\boldsymbol{s}|_{\boldsymbol{s}=\boldsymbol{G}^t\boldsymbol{\lambda}^*} \\ &= \boldsymbol{\Sigma_j}\boldsymbol{G}^t(\boldsymbol{G}\boldsymbol{\Sigma_j}\boldsymbol{G}^t + \alpha\boldsymbol{\Sigma_e})^{-1}\boldsymbol{m} \\ &= \boldsymbol{W}_{\text{MNE}}\,\boldsymbol{m} \end{aligned} \tag{2.29}$$

where $\boldsymbol{W}_{\text{MNE}}$ is defined as the resolution kernel. This solution is called the Tikhonov regularization of Equation (2.19) which is more known in the source imaging community as the Minimum Norm Estimate (MNE), as first proposed in Hämäläinen and Ilmoniemi (1994).

As indicated by the name of the technique, MNE will exhibit the solution with the lowest ℓ_2-norm with the constraint of the data fit. The MNE solution is still widely used in the community, and noise-normalized version of MNE exist, as explain in Section 2.6.1.1 and in Chapter 5.

In practice, since the a priori variance of the currents is unknown, a hyperparameter α controlling the proportion between the contribution of the noise and source of interest to the data is often introduced. The source covariance matrix can be written as $\boldsymbol{\Sigma_j} = \frac{\boldsymbol{\Sigma'_j}}{\alpha}$. The MNE solution of Equation (2.29) then becomes:

$$\hat{\boldsymbol{j}}_{\text{MNE}} = \boldsymbol{\Sigma'_j} \boldsymbol{G}^t (\boldsymbol{G} \boldsymbol{\Sigma'_j} \boldsymbol{G}^t + \alpha \boldsymbol{\Sigma_e})^{-1} \boldsymbol{m} \tag{2.30}$$

A high value of α indicates that noise is an important contributor to the data, which tends to reduce the amplitude of source current. In some circumstances, α can be approximated as the inverse of the signal-to-noise ratio[3].

A good estimation of α is crucial, as different values of α can lead to different source imaging reconstructions. Different methods in the literature have been presented to estimate this hyperparameter. One of the common methods is the L-curve technique (Hansen, 1992), which uses graphical interpretation to define α as the point with the highest curvature when plotting the curve of ℓ_2-norm of the inverse solution against its residuals, parametrized by α. Indeed it can be shown that the MNE solution can be solved by minimizing the cost function (Gramfort, 2009):

$$\hat{\boldsymbol{j}}_{\text{MNE}} = \arg\min_{\boldsymbol{j}} \|\boldsymbol{m} - \boldsymbol{G}\boldsymbol{j}\|^2_{\boldsymbol{\Sigma_e}} + \alpha \|\boldsymbol{j}\|^2_{\boldsymbol{\Sigma_j}} \tag{2.31}$$

where $\|\boldsymbol{X}\|_{\boldsymbol{\Sigma}} = \text{trace}(\boldsymbol{X}^t \boldsymbol{\Sigma}^{-1} \boldsymbol{X})$. The solution to the L-curve is then the point of highest curvature of $\|\hat{\boldsymbol{j}}\|^2_{\boldsymbol{\Sigma_j}}$ against $\|\boldsymbol{m} - \boldsymbol{G}\hat{\boldsymbol{j}}\|^2_{\boldsymbol{\Sigma_e}}$ by varying the values of α. A graphical illustration of an L-Curve can be found in Figure 2.7. Other methods exist to estimate α such as Morozov discrepancy approach (Morozov, 1966), generalized cross-validation (Golub et al., 1979) or the restricted maximum likelihood (Daunizeau et al., 2007).

In the present manuscript, the MNE technique has been used in the first two manuscripts of this thesis (Chapters 5 and 6) and the α parameter has been set arbitrarily to $1/3$ using whitened gain matrices, indicating that the SNR was estimated to be 3.

MNE results tend to be biased towards more superficial sources. This tendency can be alleviated by adjusting the source covariance matrix $\boldsymbol{\Sigma_j}$ to counterbalance this bias. One way of solving this issue is to set all the diagonal elements of $\boldsymbol{\Sigma_j}$ as the norm of the columns

[3] see https://mne.tools/dev/overview/implementation.html#the-minimum-norm-current-estimates for further explanation

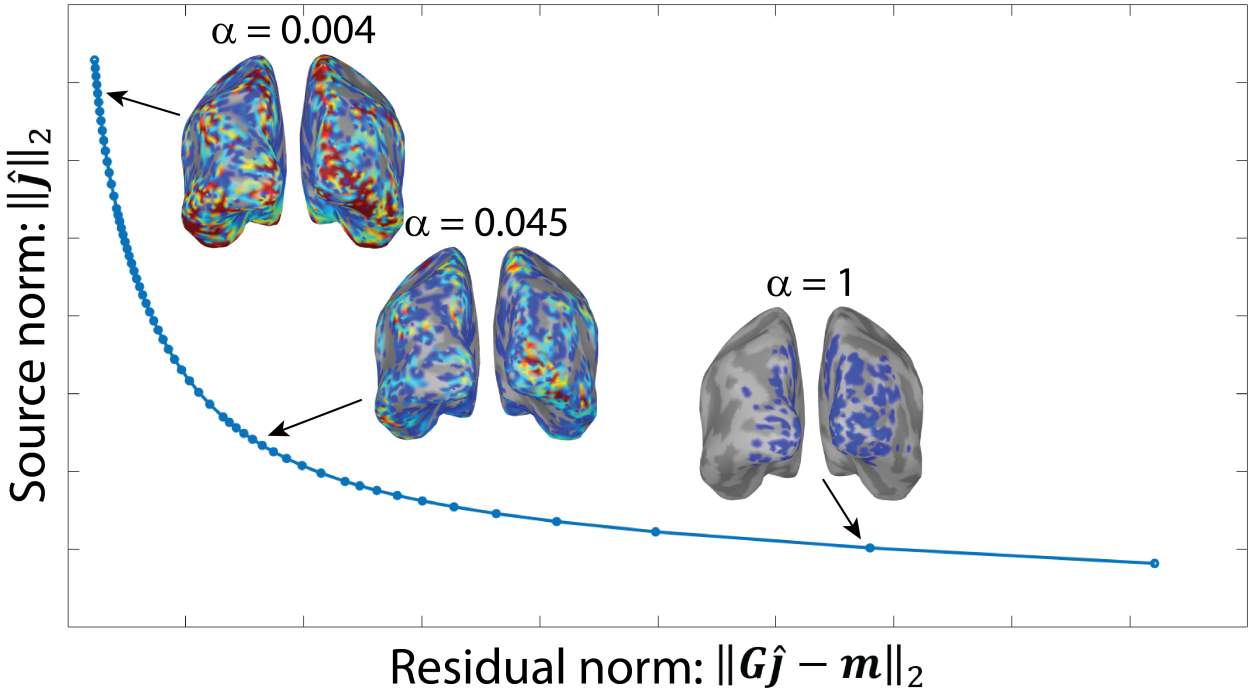

Figure 2.7: Illustration of the L-curve technique on EEG data for the localization using MNE of an average visual evoked potential induced by the visual stimulation of the left hemifield. When the parameter α was too large (here when $\alpha = 1$), the source reconstruction had low amplitude and was spatially spread. Conversely, when α is too small ($\alpha = 0.004$), the maximum of localization was too sensitive to noise. When α was chosen at the elbow of the L-curve, the source was focal and located on the right occipital region, which is expected from the visual stimulation of the left hemifield.

of the gain matrix $\boldsymbol{G}$ (Lin et al., 2006). A similar approach could be used to enhance the contribution of other modalities, such as fMRI-constrained source localization (Liu et al., 1998).

2.6.1.1 Noise-normalized MNE: dSPM and sLORETA

As further explored in the first manuscript (Chapter 5), different variants of the MNE solution, defined as noise-normalized versions of MNE method, have been introduced in the literature. The aim of these approaches is to convert the inverse solution into a dimensionless statistical quantity which is normalized with respect to a reference level (typically, baseline activity). Z-transformation is often used on MNE maps to convert the current density values to a score that represents the number of standard deviations with respect to background activity. To obtain a Z-map, the variance $\boldsymbol{\Sigma}_e$ of the sources of the background activity is computed. Then we transform the data $\hat{\boldsymbol{j}}_{\text{MNE}}$ by dividing the baseline standard deviation: $\boldsymbol{z} = \boldsymbol{\Sigma}_e^{-1/2}\hat{\boldsymbol{j}}_{\text{MNE}}$.

Other methods of noise normalization exist, such as dynamic Statistical Parametric Mapping (dSPM) (Dale et al., 2000) and standardized Low Resolution brain Electromagnetic

Tomography (sLORETA) (Pascual-Marqui, 2002). The goal of these two approaches is to normalize the MNE solution using the empirical standard deviation $\boldsymbol{S}_{\hat{\boldsymbol{j}}}^{1/2}$ of the effect in order to derive a t-statistic:

$$\hat{\boldsymbol{t}} = \boldsymbol{S}_{\hat{\boldsymbol{j}}}{}^{-1/2}\, \hat{\boldsymbol{j}}_{\text{MNE}} \tag{2.32}$$

The difference between dSPM and sLORETA lies in the definition of the empirical variance $\boldsymbol{S}_{\hat{\boldsymbol{j}}}$.

dSPM In dSPM method, the variability of the inverse solution is assumed to come only from the additive noise $\boldsymbol{e}$. For this reason, the source $\boldsymbol{j}$ is not assumed to be a random variable (which, in practice, is in contradiction with the MEM framework). This additive noise is supposed to follow a Gaussian distribution with zero mean and covariance matrix $\boldsymbol{\Sigma_e}$. Consequently, the empirical variance $\boldsymbol{S}_{\hat{\boldsymbol{j}},\text{dSPM}}$ is given by:

$$\boldsymbol{S}_{\hat{\boldsymbol{j}},\text{dSPM}} = \text{diag}(\boldsymbol{W}_{\text{MNE}} \boldsymbol{\Sigma_e} \boldsymbol{W}_{\text{MNE}}^t) \tag{2.33}$$

and the dSPM method is therefore:

$$\boldsymbol{t}_{\text{dSPM}} = \sqrt{\text{diag}(\boldsymbol{W}_{\text{MNE}} \boldsymbol{\Sigma_e} \boldsymbol{W}_{\text{MNE}}^t)}^{-1}\, \hat{\boldsymbol{j}}_{MNE} \tag{2.34}$$

$\boldsymbol{t}_{\text{dSPM}}$ is then a dimensionless, normalized statistic that follows a Student t-distribution, where the null hypothesis is the absence of source activity. If the number of time samples used to calculate the noise covariance matrix $\boldsymbol{\Sigma_e}$ is large enough, then the empirical variance approaches the true variance and $\boldsymbol{t}_{\text{dSPM}}$ can be then considered as a z-score (Dale et al., 2000).

sLORETA This method is similar to dSPM but also considers that the source also contributes to the variance. The empirical variance is then given by:

$$\boldsymbol{S}_{\hat{\boldsymbol{j}},\text{sLORETA}} = \text{diag}(\boldsymbol{W}_{\text{MNE}} (\boldsymbol{G} \boldsymbol{\Sigma_j} \boldsymbol{G}^t + \lambda \boldsymbol{\Sigma_e}) \boldsymbol{W}_{\text{MNE}}^t) = diag(\boldsymbol{R}_{\text{MNE}}) \tag{2.35}$$

where $\boldsymbol{R}_{\text{MNE}}$ is the resolution matrix. The sLORETA solution can be then written:

$$\boldsymbol{t}_{\text{sLORETA}} = \sqrt{\text{diag}(\boldsymbol{W}_{\text{MNE}} (\boldsymbol{G} \boldsymbol{\Sigma_j} \boldsymbol{G}^t + \lambda \boldsymbol{\Sigma_e}) \boldsymbol{W}_{\text{MNE}}^t)}^{-1}\, \hat{\boldsymbol{j}}_{\text{MNE}} \tag{2.36}$$

As discussed in Chapter 5, sLORETA is often called the "zero-localization error method" since, in a noiseless case when only one dipolar source is active, the sLORETA method has no localization bias (Pascual-Marqui, 2002).

The same statistical properties of dSPM hold for sLORETA.

2.6.2 LORETA

Apart from the depth-weighted minimum norm, other types of constraints can be added to the MEM solution. The spatial smoothness within the cortical surface, controlled by the Laplacian-weighted minimum norm, can be used as one of these contraints. This method is an equivalent to the method called Low Resolution brain Electromagnetic Tomography (LORETA – Pascual-Marqui et al., 1995). Laplacian-weighted minimum norm tends to find a solution which is spatially smooth by adding a Laplacian operator $\boldsymbol{L}$ in the source prior ($\boldsymbol{\Sigma_j}_{,\text{LORETA}} = \boldsymbol{L\Sigma_j}$). Each source is then correlated with its neighbors, resulting in a spatially smooth localization source map with larger patches of activity. The method was originally introduced for volumetric source localization, but a LORETA solution constrained to the cortical surface, cLORETA (cortical LORETA) was then proposed by Wagner et al. (1996). However, the computation of a discrete Laplacian on a complex closed cortical surface can lead to numeric instabilities and requires additional level of regularization (David and Garnero, 2002).

Even if LORETA comes from the physiologically plausible assumption that the neuronal activity of a population of neurons is affected by its connecting neighbors, LORETA is often criticized because spatially close regions of the brain might not be directly connected, such as the medial parts between the two hemispheres and the two walls of a gyrus. This can lead to additional blur and misleading reconstructions (Michel et al., 2004).

2.6.3 coherent Maximum Entropy on the Mean (cMEM)

One of the inverse methods developed in our laboratory is entitled coherent Maximum Entropy on the Mean (cMEM). It was designed within the MEM framework and uses a data-driven approach based on the prelocalization of the source to define the reference. It was validated multiple times with realistic simulations but also with real data acquisitions on healthy subjects and patients with epilepsy.

2.6.3.1 Definition of the reference distribution

The main idea behind cMEM reference distribution is to consider that brain electrical activity is organized within non-overlapping parcels with homogeneous activity within each parcel (Amblard et al., 2004). The parcellization of the brain is based on a data-driven approach called Multivariate Source Pre-localization (MSP) (Mattout et al., 2005). MSP uses the information of the EEG/MEG data and the solution to the forward model to estimate an index for each of the source. This index, which varies between 0 and 1, assesses the contribution of every dipolar source of the distributed model to the scalp recording and can

be interpreted as the probability that a given dipolar source is active given the data. Cortex parcellization is then obtained using a region-growing algorithm, where the seed points are defined as the sources exhibiting the local maxima of the MSP score. The size of the parcels is defined a priori and usually is of the same order of magnitude as the number of sensors. However, we have demonstrated that the size of the parcels was not an issue. Chowdhury and colleagues investigated how cMEM was robust to the spatial scale of such parcellization, regardless of the spatial extent of the underlying generator (Chowdhury et al., 2013).

Each of the cortical parcels is then considered to follow either an active or inactive reference distribution. The probability for a certain parcel k to be active is defined as α_k and the reference distribution of this parcel μ^k_{cMEM} can then be written as:

$$\begin{aligned}\mu^k_{\text{cMEM}}(\boldsymbol{j}_k) &= \alpha_k\, \mu^k_{\text{act.}}(\boldsymbol{j}_k) + (1-\alpha_k)\, \mu^k_{\text{inact.}}(\boldsymbol{j}_k) \\ &= \alpha_k\, \mathcal{N}(0, \boldsymbol{\Sigma}_k)(\boldsymbol{j}_k) + (1-\alpha_k)\, \delta(\boldsymbol{j}_k)\end{aligned} \tag{2.37}$$

where $\mu^k_{\text{act.}}$ and $\mu^k_{\text{inact.}}$ correspond respectively to the reference distributions in the active and inactive state of the cortical parcel k. Whereas an active parcel is assumed to follow a normal distribution of zero mean and variance $\boldsymbol{\Sigma}_k$, the reference distribution of a parcel in a inactive state is a dirac distribution, thus "shutting down" all the sources in the corresponding parcel when inactive.

In our standard implementation, the parcels are considered independent to each other[4]. The reference distribution of all the sources μ_{MEM} is then defined as:

$$\mu_{\text{cMEM}}(\boldsymbol{j}) = \prod_{k=1}^{K} \mu^k_{\text{cMEM}}(\boldsymbol{j}_k) = \prod_{k=1}^{K} \left[\alpha_k\, \mathcal{N}(0, \boldsymbol{\Sigma}_k)(\boldsymbol{j}_k) + (1-\alpha_k)\, \delta(\boldsymbol{j}_k)\right] \tag{2.38}$$

where K is the total number of parcels.

The formula for the estimated cMEM source can then be derived from Equations (2.25) and (2.38). The cMEM estimate for each parcel $\hat{\boldsymbol{j}}^k_{\text{cMEM}}$ can be written:

$$\hat{\boldsymbol{j}}^k_{\text{cMEM}} = \frac{\alpha_k}{(1-\alpha_k)\, \exp\left(-F^k_{\text{act.}}(\boldsymbol{G}_k^t \boldsymbol{\lambda}^\star)\right)} \left[\boldsymbol{\Sigma}_k \boldsymbol{G}_k^t \boldsymbol{\lambda}^\star\right] \tag{2.39}$$

where $\boldsymbol{G}_k$ is the subset of the lead field matrix $\boldsymbol{G}$ for dipolar sources belonging in parcel k, and $F^k_{\text{act.}}$ is the free energy function for parcel k when it is active. Therefore, we have:

$$F^k_{\text{act.}}(\boldsymbol{G}_k^t \boldsymbol{\lambda}^\star) = \frac{1}{2} \boldsymbol{\lambda}^{\star t} \boldsymbol{G}_k \boldsymbol{\Sigma}_k \boldsymbol{G}_k^t \boldsymbol{\lambda}^\star \tag{2.40}$$

Contrary to the previous inverse methods, cMEM has no analytical solution since the estimation of $\boldsymbol{\lambda}^\star$ still need to be done to obtain $\hat{\boldsymbol{j}}_{\text{cMEM}}$.

[4]The use of a connected graph to describe the relationship between parcels has been already introduced from the theoretical point of view in Amblard et al. (2004).

2.6.3.2 Initialization of α_k and $\mathbf{\Sigma}_k$

Two parameters need to be initialized for the estimation of cMEM: the probability for parcel k to be active α_k, and the covariance matrix of the active reference distribution for the kth parcel $\mathbf{\Sigma}_k$. α_k is usually initialized as the median MSP score from all the sources within the parcels.

$\mathbf{\Sigma}_k$ is defined as:

$$\mathbf{\Sigma}_k = \boldsymbol{\eta} \boldsymbol{W}_k(\sigma)^t \boldsymbol{W}_k(\sigma) \tag{2.41}$$

where $\boldsymbol{\eta} = 0.05 \frac{1}{\#P_k} \sum_{i \in P_k} \hat{\boldsymbol{j}}^2_{\text{MNE}}(i)$ is used as a scaling factor. P_k is the set of all the sources in parcel k and $\#P_k$ is its cardinal.

$\boldsymbol{W}_k(\sigma)$ is a smoothing operator for parcel k. It is based on the diffusion-based spatial prior, proposed by Harrison et al. (2007), which is an extension of the discrete Laplacian operator along a geodesic cortical surface. σ is an index of smoothness, indicating the strength of the spatial smoothness. For this manuscript, σ is set to 0.6. The calculation of $\boldsymbol{W}_k(\sigma)$ was originally proposed by Friston et al. (2008):

$$\boldsymbol{W}_k(\sigma) = \sum_{i=1}^{8} \frac{\sigma^i}{i!} \boldsymbol{S}^i \approx \exp(\sigma \boldsymbol{S}) \tag{2.42}$$

Similarly to LORETA, the $\boldsymbol{W}_k$ matrix allows us to add local smoothness, therefore allowing a more physiologically plausible solution.

2.6.3.3 Detailed evaluation of cMEM methodology

Numerous studies have used cMEM as an inverse source localization method, either to validate the method or to use it as a source localization procedure of interest. An initial version of cMEM (without spatial smoothing) was first introduced in Amblard et al. (2004) using the MEM framework proposed in Clarke and Janday (1989). In Amblard et al. (2004), the method was validated using synthetic data and compared to other techniques, namely LORETA and S-MAP (Baillet and Garnero, 1997), a Bayesian approach using anatomical and temporal a priori information to solve the inverse problem. cMEM technique outperformed the latter techniques in terms of localization accuracy thanks to its ability to "shut down" cortical parcels which do not contribute to the data.

In Grova et al. (2006a), cMEM was further validated using realistic simulations of interictal epileptic discharges (IEDs) contaminated by background EEG noise recorded from a patient. cMEM and LORETA-like inverse methods were tested within different level of signal-to-noise ratios and spatial extensions of the generator. Good performance of cMEM was confirmed

and this study proved that cMEM was sensitive to the spatial extent of the underlying source. This was the first time spatial extents of source maps were carefully evaluated, using the receiver operating curve analysis and its Area Under the Curve (AUC). A specific AUC metric was introduced for this purpose.

The comparison of inverse methods in the localization of IEDs of 15 patients was performed in Heers et al. (2015). The performance of cMEM was compared to Bayesian methods similar to MNE and LORETA. cMEM was shown to outperform the other techniques in terms of concordance with intracranial results and spatial spread of the reconstruction.

In Chowdhury et al. (2016), cMEM was compared to the 4^{th} order Extended Source Multiple Signal Classification (4-ExSo-MUSIC), another inverse method which is sensitive to the spatial extent of the source, using realistic simulations generated using a biophysical computational model. While both methods exhibited excellent performance in the reconstruction of the simulated source, cMEM was the only one able to reconstruct several simultaneous sources.

Pellegrino et al. (2018) aimed at comparing the performance of cMEM with the ECD technique in the localization of interictal epileptic discharges. This study is of particular interest since ECD is the only localizing technique which is approved by the Food and Drug Administration for the localization of epileptic events. On a study on 49 epilepsy patients, cMEM was shown to exhibit a better accuracy and was more sensitive to the spatial extent of the sources than the ECD solution.

cMEM was also used to compare electrical or magnetic brain activity to the hemodynamic response recorded with fMRI during similar epileptic discharges recorded either using EEG/MEG or simultaneous EEG-fMRI. In Grova et al. (2008), cMEM source localization of IEDs in EEG was compared to the fMRI BOLD clusters of the same events. On this study involving 9 patients, for most of the patients, BOLD clusters were highly concordant with the cMEM reconstruction indicating a spatial relationship between the distributed source imaging technique and the hemodynamic response elicited by fMRI. This finding was further confirmed in Heers et al. (2014), where each of the BOLD cluster was compared to the localization of the average IEDs in 21 patients, this time considering source localization obtained from both EEG and MEG recordings. Again, it was proved that ESI and MSI were concordant with the hemodynamic response (see Figure 2.8). In addition, the study demonstrated that the fMRI clusters which were the most concordant to ESI or MSI were the ones displaying the most significant t-value.

In Grimault et al. (2014), cMEM was used as the inverse solution in a short-term memory task and helped to prove that the brain activates more parts of the frontal, temporal and parietal regions as the number of items stored in memory increases. cMEM allowed having a

fine localization of the recruited regions, thus it helped understanding of the physiological processing of short-term memory.

In Grova et al. (2016), cMEM was used to estimate intracranial EEG (iEEG) tracing based on MEG data. To do so, cMEM was applied to IED recorded in MEG, and the source reconstruction was projected on the iEEG contacts using the iEEG forward model. The comparison between the MEG-estimated iEEG traces and the actual recorded iEEG signals was used to assess the concordance between both modalities, iEEG being considered as the clinical gold standard. The study demonstrated an excellent correspondence between MEG and iEEG in 4 out of 5 patients, the generator being too deep for the last patient. It notably exhibited an excellent concordance between the number of iEEG contacts involved during IEDs in both approaches. This study was our first attempt at a quantitative evaluation of the ability of cMEM to recover the spatial extent of the generators using clinical data. See Figure 2.9 for an illustration.

Another use of cMEM can be using the reconstruction as prior for functional Near-InfraRed Spectroscopy (fNIRS). Specifically, in Pellegrino et al. (2016b), cMEM was used to help determine a optical montage for the placing of fNIRS sources and optode detectors.

cMEM was also used as a potential candidate to perform EEG or MEG functional conductivity. Hassan et al. (2016) tested source imaging techniques, one of them being cMEM, with different connectivity measures, to test the performance of source connectivity using these methods. This study indicated that MNE was preferable to the other tested techniques. It is possible that cMEM did not perform well in the detection of distant networks because of its ability to cancel the parcels which are distant from the region contributing the most to the data.

Source imaging using fusion between EEG and MEG has been performed using cMEM in Chowdhury et al. (2015). The fusion was obtained by combining the MSP score from both modalities using a logical OR operator, resulting in a reference distribution using the complementary information of EEG and MEG. Using realistic simulations, the result of the fusion method was proved to be more accurate than cMEM when applied to either EEG or MEG (see Figure 4.3). This finding was further validated using epilepsy data (Chowdhury et al., 2018). In a study with 26 patients, the sources using the fusion technique were found to be more concordant with the known epileptogenic focus than the EEG or MEG source imaging. This study also introduced the concept of consensus maps, which allow for more robust and more reliable results than simple averages. Consensus maps were very similar to the automatic IED clustering technique introduced in Chapter 7.

2.6.4 Wavelet-based Maximum Entropy on the Mean (wMEM) and ridge MEM (rMEM)

Other reference distributions, derived from cMEM, can be used for particular cases.

The wavelet-based MEM (wMEM) uses the same reference distribution of cMEM, but instead of applying the MEM framework for each time sample, the technique was applied to every coefficient of a wavelet-based time-frequency decomposition. This method, introduced in Lina et al. (2014), uses a discrete wavelet representation to transform the EEG/MEG temporal signal into time-frequency bins. Each of the bin contains a wavelet coefficient indicating the strength of the signal at a particular time and frequency. The use of discrete wavelets allows an efficient sparse representation of the recorded signal, in a non-redundant manner, offering interesting denoising properties. The MEM framework was performed on the frequency decomposition using a reference distribution similar to cMEM. The reconstruction source is then a set of wavelet coefficients. An inverse wavelet transform is needed to reconstruct the time course signals in the source space, using either the full frequency band or a more specific one, which allows the study of the localization of specific brain oscillations. This technique is useful for the localization of oscillatory patterns such as bursts of rhythmic activity, commonly found in some patients with epilepsy.

wMEM was used to localize the generators involved in the onset of the epileptic seizures. In Pellegrino et al. (2016a), the authors localized the onset of seizures of 13 patients and tested the concordance with the clinically defined Seizure Onset Zone (SOZ) for these patients (see Figure 4.4). The study proved that wMEM was concordant with the SOZ for 81 % of the seizures (increasing to 90 % when considered only MEG localizations) and was therefore a useful tool for the presurgical investigation.

Moreover, wMEM was also used to localize fast oscillations (40-160 Hz) (von Ellenrieder et al., 2016) and High-Frequency Oscillations (HFO) (80-500 Hz) (Papadelis et al., 2016) in MEG and EEG. The authors in von Ellenrieder et al. (2016) developed a method to semi-automatically find pathological rhythmic events between 40 Hz and 160 Hz and used wMEM to localized these events. wMEM reconstructions of fast oscillations overall showed excellent concordance with the proven epileptogenic zone, thus proving that wMEM was a suitable method in the detection of rapid oscillations. In Papadelis et al. (2016), the authors used the same detector proposed in von Ellenrieder et al. (2016) to localize HFO from pediatric epilepsy patients . Again, wMEM showed good concordance with the seizure onset zone.

Another variant of wMEM, named ridge MEM or rMEM, was introduced in Zerouali et al. (2014) to study the time-frequency properties of sleep spindles. Ridges are the curves formed

by the local maxima of the time-frequency plane and are of particular interest to detect frequency-locked events that change over time and space. Source imaging using wMEM can be performed on each element of the ridge curve in order to only localize the generators of frequency-locked activity. rMEM was used in Zerouali et al. (2014) to show that earlier synchrony during sleep spindles was associated with mainly intra-hemispheric connectivity whereas later synchrony was associated with global long-range connectivity.

2.6.5 Other inverse solutions

Several other source localization have been proposed to solve the distributed inverse problem and the list provided in this Chapter is not exhaustive: we refer the interested reader to these reviews of the field (Baillet et al., 2009; He et al., 2018; Michel and Brunet, 2019).

LAURA

It is worth citing the Local Auto-Regressive Average (LAURA) model which has been largely used (Grave de Peralta Menendez et al., 2001). LAURA is similar to the MNE approach but differs in the definition of the source covariance matrix $\boldsymbol{\Sigma_j}$. In LAURA, the covariance matrix is written as:

$$\boldsymbol{\Sigma_j} = \boldsymbol{M}^t\boldsymbol{M}, \text{ where } \boldsymbol{M} = \boldsymbol{W}\boldsymbol{A} \tag{2.43}$$

where $\boldsymbol{W}$ is a matrix whose diagonal elements correspond to the norm of the column of the lead field matrix $\boldsymbol{G}$ and $\boldsymbol{A}$ is a matrix related to the spatial distance to the neighbor sources.

Sparse Solutions

While MNE corresponds to solving the inverse problem with an ℓ_2 regularization, sparse solutions have also been used in electrical and magnetic source imaging. One of the solution using sparse constraint is the minimum current estimate, or LASSO regularization, which is a solution that imposes sparsity directly on the sources by using ℓ_1-norm regularization.

Note that these kinds of estimates usually provide unrealistic estimates of the time course of the sources. To overcome this issue, combination of ℓ_1 prior in space and ℓ_2 prior in time have been proposed (Gramfort et al., 2012).

2.7 Conclusion

In this chapter, the basic principles of EEG and MEG, from the physiology of their generators to the technical aspects of source localization, were introduced. First, a summary of the functioning of a neuron, especially the pyramidal cells, which are the main contributors of EEG and MEG, was presented. Then, the technical aspects of EEG or MEG recording were introduced, with a discussion on the different type of EEG and MEG sensors. Finally, the different techniques used to perform source imaging were widely discussed. Source localization in EEG and MEG can be used in a variety of applications, and have been applied in the manuscripts of this thesis either on evoked potentials or on epileptic discharges.

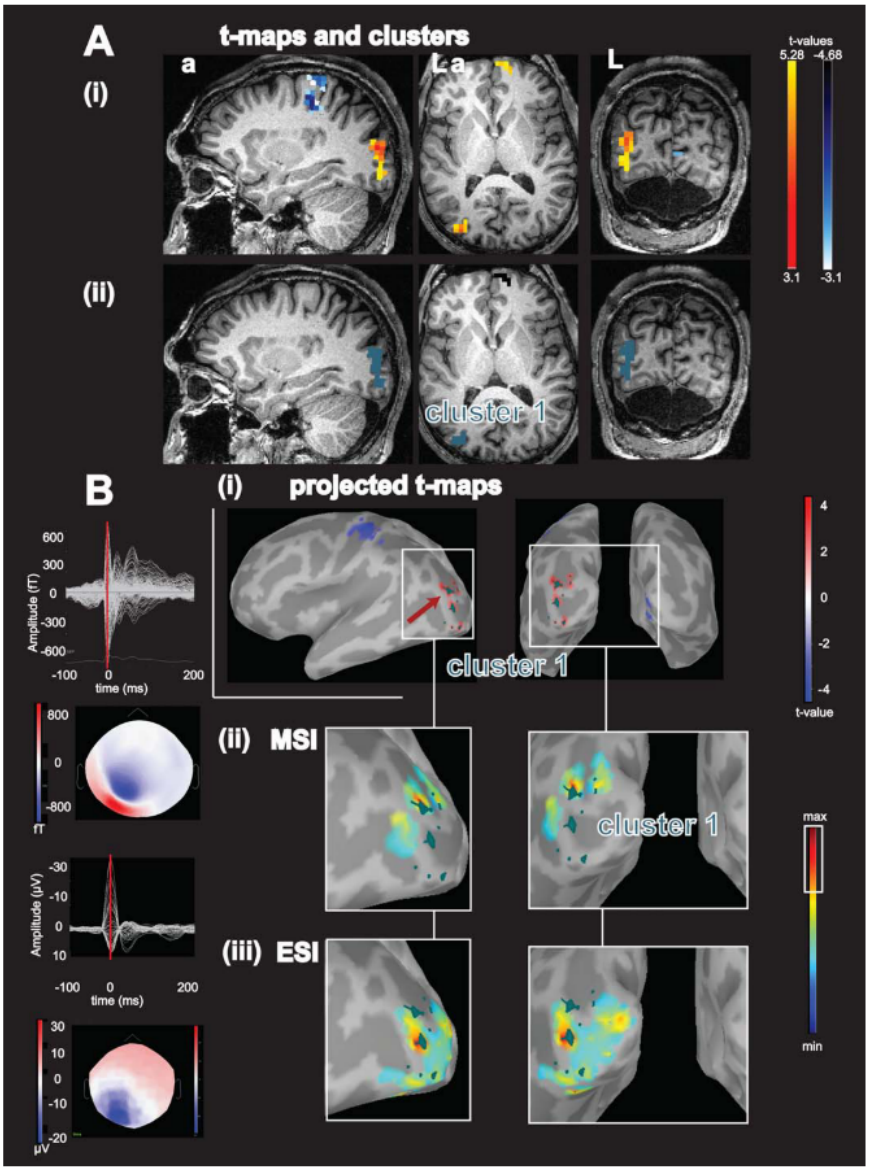

Figure 2.8: Illustration of a concordance of BOLD activation with ESI/MSI on a patient with occipital lobe epilepsy. **A**: (1): Activations (red) and deactivations (blue) of the BOLD response of the interictal discharges (IEDs) (ii) corresponding BOLD clusters. **B**:(i): Combined BOLD t-map (red: activation, blue: deactivation, green: most significant BOLD cluster) projected over the cortical surface. (iii): MEG signals and corresponding MSI results of the averaged IEDs with the superimposition of the most significant project BOLD cluster. **C**: Same as in **B** for EEG and ESI. This figure nicely illustrates the different characteristics of ESI and MSI: The ESI peak is found on top of the gyration, whereas the peaks of the MSI findings are localized over the borders of the sulci, which are most often the generators of tangential sources. Please note that ESI and MSI are concordant with different parts of the BOLD cluster. Taken from Heers et al. (2014).

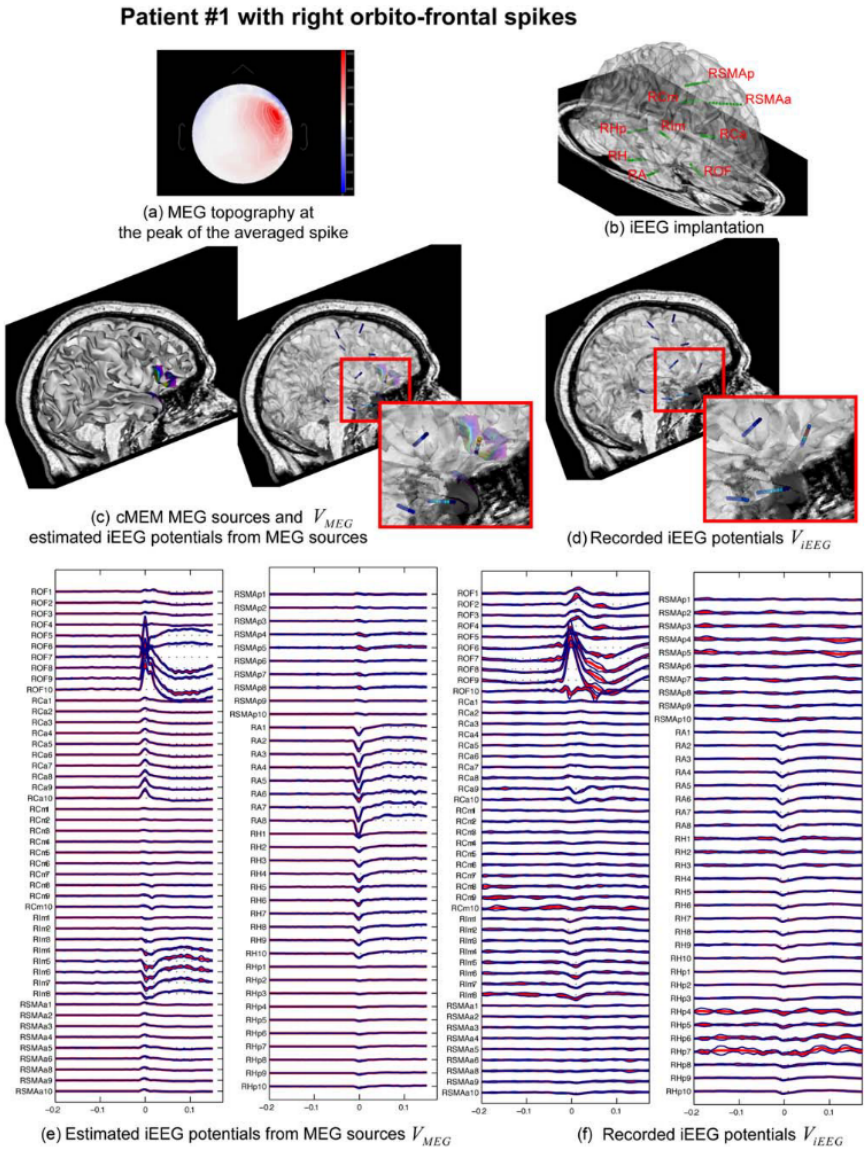

Figure 2.9: Illustration of a correlation between MEG and iEEG for a patient with right orbitofrontal epileptic discharges. (**a**) MEG topography at the peak of the averaged epileptic spike. (**b**) iEEG implantation overview where each iEEG contact is represented in 3D as a green sphere. (**c**) cMEM source localization results and corresponding V_{MEG} iEEG potentials estimated from MSI at the peak of the averaged epileptic spike. (**d**) Actual iEEG recording V_{iEEG} (**e**) Time courses of the estimated iEEG V_{MEG} potentials estimated over all contacts obtained for all epileptic spikes (average time course in red, ±standard deviation in blue). (**f**) Time courses of the actual V_{iEEG} potentials recorded over all contacts for all epileptic spikes.
This figures shows an excellent spatial concordance between cMEM sources, estimated V_{MEG} potentials and recorded V_{iEEG} involving mainly a lateral right orbitofrontal generator. A secondary right temporal source involving the deepest contacts of RA electrodes was also found with V_{MEG} and confirmed with V_{iEEG}. Taken from Grova et al. (2016).

Chapter 3

Simultaneous recording of EEG and fMRI

This chapter will introduce the technique of functional magnetic resonance imaging (fMRI) and how it can be combined with a simultaneous electroencephalography recording (EEG) to explore brain activity.

After briefly describing the history of MRI and functional MRI, this chapter will present the technical aspects associated with the recording and analysis of MRI and fMRI data, before focusing on the specificity of the simultaneous EEG-fMRI recording.

In this chapter and the following, anatomical MRI imaging is presented extensively, therefore before we start it is important to clarify important vocabulary used when dealing with the orientation of the MRI images. Figure 3.1 presents the three standard orientations of a brain MRI image (axial, sagittal, coronal), as well as the corresponding directiodens of the orientation.

3.1 History of magnetic resonance imaging

The origin of MRI comes with the discovery of a magnetic property of the nuclei of atoms composed with an odd number of nucleons (protons and/or neutrons) called the Nuclear Magnetic Resonance, or NMR (Rinck, 2018). This phenomenon was described independently in 1946 by two scientists, Felix Bloch and Edward M. Purcell, who were later awarded the Nobel Prize in Physics in 1952.

A few years later, the Swedish scientist and doctor Erik Odeblad found the potential of this technique in medicine and was a precursor of MRI in bioimaging. With the help of the

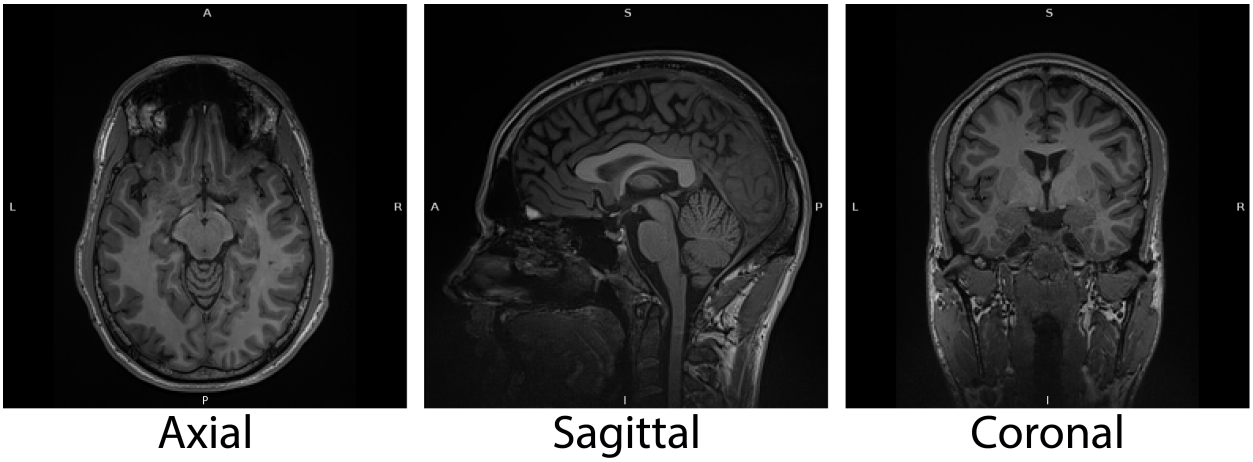

Figure 3.1: MRI orientation of the slices with axial (or transversal), sagittal and coronal orientation of a T1-weighted MRI. The respective directions are: Superior (S) to Inferior (I); Left (L) to Right (R) and Anterior (A) to Posterior (P).

physicist Gunnar Lindström, he submitted the first works on NMR data on biological data in 1954.

In the 50s and 60s, significant progress was made in the context of instrumentation and fundamental knowledge of NMR properties, when applied to either animal or human participants. In the early 70s, Paul C. Lauterbur, a professor of chemistry, produced the first images based on NMR signals and was the first to publish scholarly articles about them (Lauterbur, 1974). He called these images *Zeugmatograms* (see Figure 3.2). The term *zeugmatogram*, unlike the technique, did not stand the test of time, and was later replaced by NMR imaging and then MRI. Lauterbur's imaging technique was improved in 1975 by the Swiss physical chemist Richard Ernst who had the idea of performing image reconstruction in the Fourier domain, which is the fundamental process which is still in use in today's MRI reconstructions. Ernst's study on MRI development was awarded a Nobel prize in Chemistry in 1991. In the same period, Peter Mansfield developed the use of gradients of magnetic fields during the image acquisition, thus reducing the recording time from several hours to just a few minutes. This important breakthrough permitted a new way of imaging in vivo subjects, and notably soft tissue, in full complementarity with X-ray-based computed tomography. MRI was therefore at the origin of a new state of the art approach and practice in medical imaging. Both Lauterbur and Mansfield received the Nobel prize in Physiology or Medicine in 2003 for their significant work in the development of MRI. In the following decades, MR imaging acquisition techniques were greatly improved and became a valuable clinical tool.

The first functional MRI findings were reported in 1990 by Ogawa and colleagues (Ogawa et al., 1990), using the paramagnetic properties of deoxyhemoglobin as an intrinsic contrast agent for MRI. The authors coined the term Blood Oxygenation Level-Dependent (BOLD)

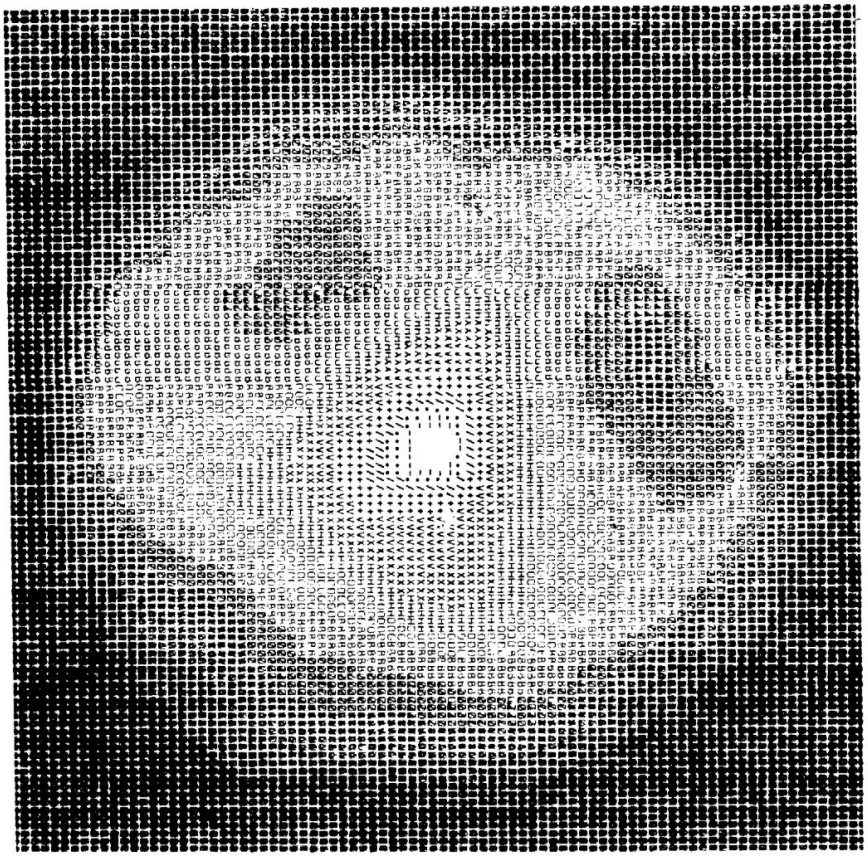

Figure 3.2: First zeugmatogram of animal MR images. Proton density map of the thoracic cavity of a live mouse. Taken from Lauterbur (1974)

response, which is still in use today. The first human fMRI images were acquired a few years later (Kwong et al., 1992).

The first study introducing MRI-compatible electrodes in the MR scanner during an fMRI experiment was performed in 1993 by Ives and colleagues (Ives et al., 1993). While fMRI experiments can recorded using a wide variety of imaging techniques, the current most commonly used technique is the single-shot Echo Planar Imaging (EPI). EPI was proposed in the 70s by Mansfield, but it is only since the mid 1990s that this technique has become widely available (Schmitt et al., 2012). Moreover, several sequences of multiband EPI have been proposed by the community, leading to increased EPI sequence speeds by a factor of 30 (Moeller et al., 2010; Feinberg and Setsompop, 2013).

3.2 Fundamentals of magnetic resonance imaging

Magnetic Resonance Imaging requires the use of a large static magnetic field B_0 (typically from 1 T up to more than 10 T). In the human body, some atoms, including hydrogen ^1H

(i.e. single protons) have a small magnetic dipole moment that aligns with this magnetic field, in a similar fashion to a compass needle pointing to the direction of the Earth's magnetic north. The magnetic moments of the Hydrogen atoms add up, and give rise to a macroscopic magnetization vector parallel to the magnetic field.

The magnetization vector can be tilted from the orientation of the static field by applying a radiofrequency magnetic pulse B_1, rotating at the so-called Larmor frequency, which is the frequency which provokes a change in the orientation of the magnetization vector. This physical phenomenon is called the Larmor precession. Once the excitation is over, the net magnetization gradually returns to its original state. This effect is called relaxation and is characterized by two time constants: the return of the longitudinal component of magnetization vector along the axis of the static magnetic field B_0 which follows an increasing exponential with time constant T1, and the decay of the transverse magnetization following a decreased exponential with time constant T2.

T1 and T2 depend on the strength of the magnetic field, and the type of tissue in which the hydrogen atom is located. In the human brain, in a 3-T scanner, the T1 values vary roughly between 850 ms (in the white matter) to 4500 ms (in the cerebrospinal fluid – CSF) and T2 values range between 80 ms (white matter) to 2000 ms (CSF) (Wansapura et al., 1999). Considering that the MRI signal is most sensitive to the density of hydrogen ^1H, it is possible to develop MRI acquisition sequences that exploit whether T1 or T2 contrasts, which is why MRI as an imaging technique is so well adapted to study soft tissues within the body. T1-weighted techniques are commonly used to visualize and quantify brain morphology, whereas T2-weighted acquisition are often used to detect lesions (Nishimura, 2010).

Another additional source of signal decay of the transverse magnetization components is due to local inhomogeneity of the static magnetic field B_0, provoking a desynchronization of the magnetization of the atoms. Such decay, combined with the T2 related decreased of magnetization in the transverse plane, is characterized by the time constant T2*, which is much shorter than the T2 constant. The T2* constant is influenced by local field inhomogeneities created by local artifacts (e.g. local influence of dental work on the MRI signal), but also importantly by the local amount of deoxyhemoglobin molecules, which act as an intrinsic contrast agent and locally distort the static magnetic field because of its paramagnetic characteristics. Consequently, T2*-weighted images are sensitive to local change in deoxyhemoglobin. This is the main physical principle used to track the hemodynamic response of the brain to a specific event by measuring the so-called Blood Oxygenation-Level Dependent (BOLD) signal.

Although in some rare cases 3D acquisition is used, in general MRI acquisition consists of acquiring a series of 2D slices of the brain in any of the three standard directions. To

do so, gradient magnetic fields are used in addition to the main field. These gradient fields slightly modify the overall magnetic field which allows the Larmor frequency of hydrogen ^1H to vary slightly as a function of their position in space. By tuning the frequency of the radiofrequency pulse B_1, the signal becomes excited and can be imaged from one specific slice of the head, in any orientation. MRI scanners are quite versatile and offer several ways to explore brain anatomy and function, through the tuning of appropriate sequences. While T1- and T2-weighted MRI can be used for anatomical imaging, diffusion MRI measure the local anisotropy of the water in the white matter to generate images of the fiber tracks within the white matter (Wu and Miller, 2017). Magnetic resonance angiography is used to accurately map blood vessels vessels (Lim and Koktzoglou, 2015). Magnetic resonance spectrography measures the local concentrations of some metabolites instead (Lim and Koktzoglou, 2015). The final two techniques worth mentioning in this non-exhaustive list of advanced MRI sequences are perfusion MRI, which measures the delivery of oxygen and other nutrients to organs and tissue (Günther, 2014), and myelin water imaging, which measures and quantifies the local myelin loss in patients with multiple sclerosis (Kolind et al., 2012).

3.3 Functional Magnetic Resonance Imaging

MRI can be used to explore the brain functions of a living subject using functional MRI (fMRI). As mentioned previously, an fMRI signal is obtained by recording T2*-weighted images, and is sensitive to local distortion of the magnetic field induced by the presence of de-oxygenated hemoglobin (or deoxyhemoglobin). The signal recorded by the fMRI, the so-called blood oxygenation-level dependent (BOLD) signal, is inversely proportional to the local content of deoxyhemoglobin (Ogawa et al., 1990), and therefore depends on local changes in cerebral blood volume and cerebral blood flow.

BOLD response is then indirectly related to the underlying neuronal activity through the so-called neurovascular coupling process. Although, the relationship between activity of the neurons and the corresponding hemodynamic response is still not fully understood (Wan et al., 2006), several theoretical models have been suggested to define the neurovascular coupling (Buxton et al., 1998; Friston et al., 2000; Sotero and Trujillo-Barreto, 2008; Phillips et al., 2015; Iadecola, 2017). An illustration of a typical hemodynamic response to a transient increase in neuronal activity is presented in Figure 3.3. The relation between neural response and the BOLD response is then defined using different parameters of the hemodynamic response, namely the Cerebral Blood Flow (CBF), the Cerebral Blood Volume (CBV), and the Cerebral Metabolic Rate of Oxygen consumption ($CMRO_2$), i.e. the proportion of oxygen consumed by the tissue. During neuronal activity, the first observed physiological phenomenon

is an increased of $CMRO_2$ due to the demand for oxygen by the active neurons. This process creates a short and fast initial decrease in BOLD response corresponding to a local increase in deoxy-hemoglobin concentration: the so-called initial dip (Buxton, 2001). The physiological response to the increase of oxygen consumption is the local vasodilatation of the arterioles, inducing a large local increase of CBF. Increasing CBF reduces the local concentration of deoxyhemoglobin by dilution, thus increasing the BOLD response. On the other hand, due to the compliance structure of the membrane of the veins, CBV increases as well, which has the effect of increasing the local amount of deoxyhemoglobin, thus reducing the BOLD response. However, during the first 5-10 s following the initial dip, the effect of CBF is stronger than the increase in $CMRO_2$ and CBV, thus inducing a large increase in the BOLD response. This is called the "washout effect" (Hoge et al., 1999). After the response, the levels of $CMRO_2$, CBF, and CBV progressively returns to their baseline levels. However, CBV takes more time to reach its physiological level, resulting in $CMRO_2$ and CBF inducing a late decrease in BOLD response called the undershoot.

It is worth mentioning that in some cases, neuronal activity, especially epileptic discharges, are associated with negative BOLD responses instead of positive responses (Mullinger et al., 2014; Mayhew et al., 2016). The physiological interpretation of the deactivation patterns remains unclear possibly, reflecting an active neuronal inhibition, an inadequate perfusion of tissue or the shunting of blood flow (Kobayashi et al., 2006; Sten et al., 2017).

3.4 Simultaneous EEG-fMRI recording

As mentioned in Section 2.3, EEG is a direct measure of neuronal activity with a good temporal resolution (around 1 ms) but suffers from a poor spatial resolution and a relative incapacity to detect deep seated generators (Mulert and Lemieux, 2010). On the other hand, fMRI is a technique which allows the monitoring of brain activity within the whole head with an excellent spatial resolution but has a temporal resolution of 1 s and is an indirect measure of neuronal activity. Combining both EEG and fMRI simultaneously was first utilized in the 1990s and the complementary nature of both modalities offers a larger picture and a better understanding of some brain mechanisms. However, recording EEG in the presence of a high magnetic field is a challenging task because of the inherent artifacts induced by the presence of metal electrodes in the MR scanner, as described in Section 3.4.1.

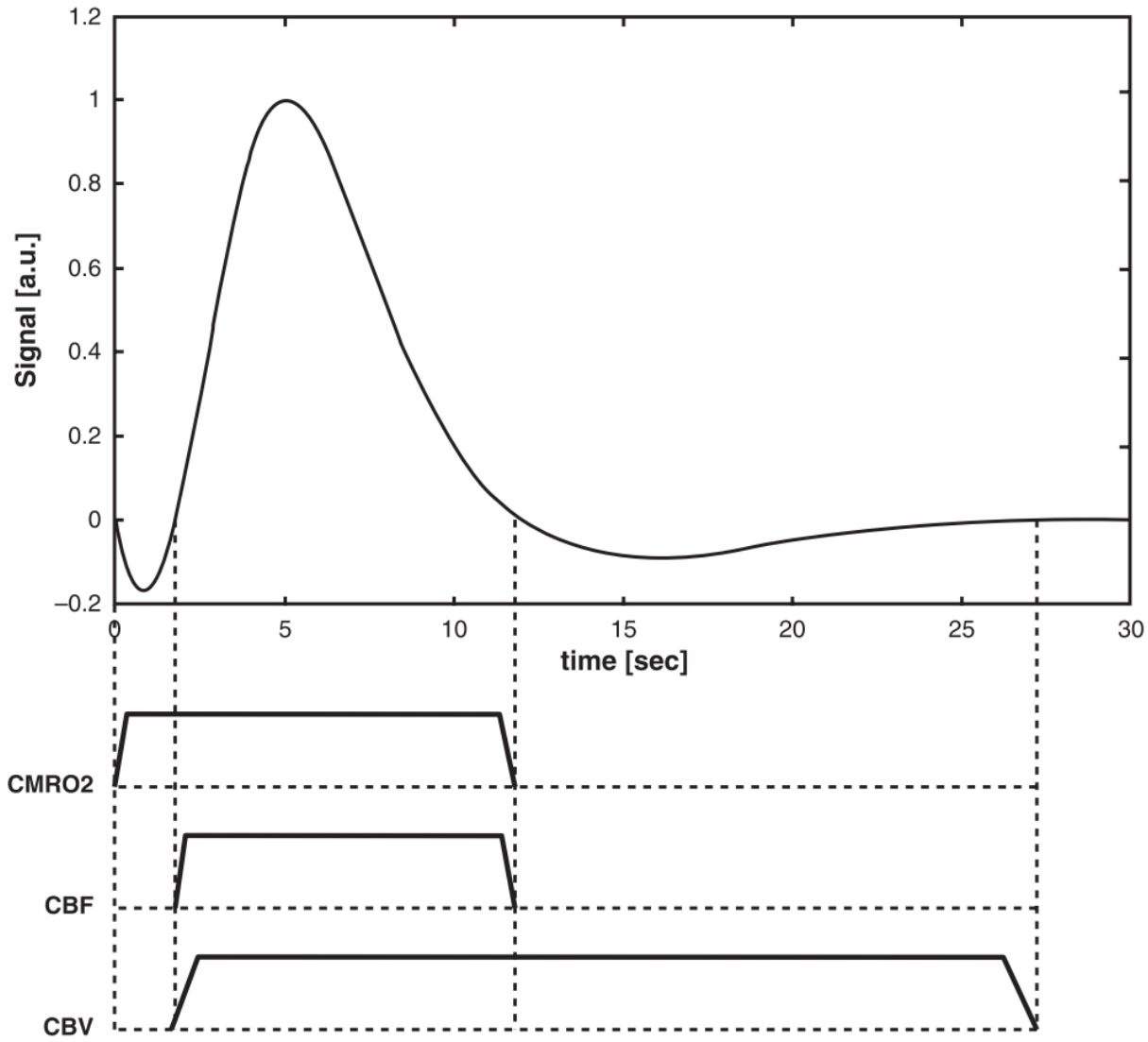

Figure 3.3: A typical haemodynamic response function following a stimulus, showing a negative initial dip, a strong positive BOLD response, and a subsequent negative undershoot. These phenomena can be explained by the different time constants of the underlying physiological parameters: the metabolic rate of oxygen consumption ($CMRO_2$), the cerebral blood flow (CBF), and the cerebral blood volume (CBV). Taken from Deichmann et al. (2010).

3.4.1 MR-related EEG artifacts

Recording EEG in the MR scanner is a challenging task.The EEG signal is affected by different kinds of artifacts, which impacts the validity of the ESI results. Any movement of electric wire in the presence of a high magnetic field will induce currents that will contribute to the ongoing EEG signal. This is the reason why electric wires should be immobilized with sand bags and the patient's head should be kept still, ideally with vacuum cushions, during simultaneous EEG-fMRI recordings (Benar et al., 2006).

Changes of the magnetic gradients, which are required during the fMRI acquisition, will also induce an artifact in the EEG of a far larger amplitude than background EEG activity: the so-called gradient artifact. Consequently, in order to successfully correct the data from the gradient artifact, the EEG amplifier used for the EEG-fMRI analysis should be characterized by a large dynamic range and sampling rate. Several methods have been proposed to remove this artifact (De Munck et al., 2013; Grouiller et al., 2007). The most popular method is the Artifact Average Subtraction (AAS) (Allen et al., 2000), which is based on averaging a large number of occurrences of the gradient artifact, followed by a subtraction of this artifact model to the EEG data. Thanks to the reproducibility and stability of the gradient artifact, this method is able to remove most of the artifact without altering the signal of interest (Grouiller et al., 2007). AAS can perform even more efficiently when the clocks of the fMRI and the EEG amplifier are synchronized, which result in a better modelling of the gradient artifact (Mandelkow et al., 2006; Mullinger et al., 2008b). It is worth noting that the gradient artifact is sensitive to how the subject and the EEG equipment are installed in the MRI, and it is possible to reduce the effect of gradient artifact on the EEG signal with a careful adjustment of the subject's axial position (Mullinger et al., 2011) and with a optimizing EEG cap-cabling configuration (Chowdhury et al., 2019). It is also possible to avoid the occurrence of gradient artifacts by creating small quiet periods without fMRI acquisition. In other words, during these periods of time, the gradient magnetic fields are not active, and therefore prevents the appearance of an artifact. The so-called sparse fMRI sequences have been proposed in multiple studies (Mulert and Lemieux, 2010; Scheeringa et al., 2011; Leicht et al., 2016), even in multiband fast fMRI sequences (Uji et al., 2018).

Another phenomenon, called the BallistoCardioGram (BCG) or pulse artifact, also greatly affects the EEG quality. This artifact appears 100–200 ms after each heartbeat. The main contributors of the artifact are small pulse-related head rotations of the subject (Yan et al., 2010; Mullinger et al., 2013a). Contrary to the gradient artifact, the shape and amplitude of this artifact vary over time, following heart beat variability. As a result, this artifact is more difficult to characterize. Several BCG artifact removal algorithms have been proposed: Allen et al. (1998) developed a method very similar to AAS, consisting of estimating the averaged artifact obtained from several consecutive heartbeats before subtracting this artifact template from the data after each heartbeat detected on ECG (see Figure 3.4 for a diagram explaining the method) or using a more sophisticated measure of the heart activity, the vectorcardiogram (Mullinger et al., 2008b). Nakamura et al. (2006) proposed using ICA and discarded components contaminated by the BCG artifact. Niazy et al. (2005) considered Optimal Basis Sets (OBS) by applying a principal component analysis on all the artifact occurrences for each channel independently, a process which can model the average effect as

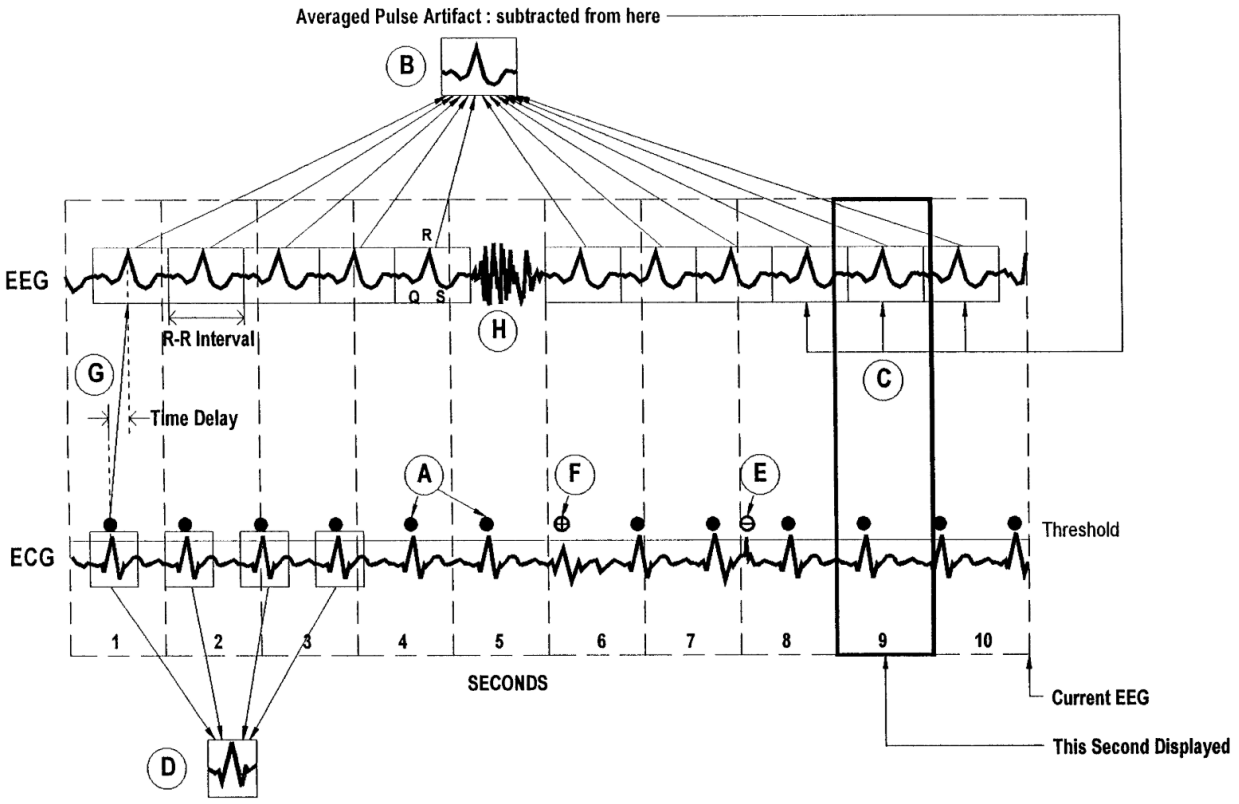

Figure 3.4: A diagram representing the AAS method for BCG correction. (**A**) The QRS complexes are identified on the ECG recorded during the fMRI analysis. (**B**) The BCG artifact waveforms in the EEG channels, following the ECG peaks, are averaged. (**C**) The averaged BCG artifact signal for each channel is subtracted from the EEG signals at times corresponding to the ECG peaks. (**D**) QRS complexes are then averaged and cross-creelated with the ECG signal to detect false ECG peaks, as in (**E**). (**F**) QRS complexes which are not detected by threshold crossing are identified by detecting an "R-R" interval between successive ECG peaks. (**G**) The time delay between the ECG peaks and the BCG peaks is calculated automatically. (**H**) Artifactual ECG segments are discarded. Taken from Allen et al. (1998).

well as some degrees of temporal variability in the occurrence of the artifact. Then, the authors proposed removing the first three OBS components which were assumed to contain only BCG artifacts. Ferdowsi et al. (2013) modeled the BCG artifact with an autoregressive model which predicted the amplitude of the artifact at a particular time point based on the previous time samples and the artifact of the previous heartbeat. Grouiller and colleagues (Grouiller et al., 2007) compared four BCG artifact correction methods (AAS, PCA, ICA and an adaptive filtering technique) on simulated and real data (spontaneous alpha rhythm and epileptic discharges). They concluded that the AAS method was the most accurate, by correcting the artifact without deteriorating too much ongoing EEG brain activity. Using simulated data, they showed that the BCG artifact affected EEG signals mainly below 12 Hz. Consequently, they claimed that, when looking at higher frequencies, the BCG artifact removal techniques

were not useful and tended to deteriorate the data. Another group proposed a comparison of OBS and ICA methods when using a Go/NoGo task (Vanderperren et al., 2010). The authors concluded that both methods showed similar results but advised OBS method since it had fewer parameters to tune.

In addition to software solutions, BCG artifacts could be solved using hardware techniques. LeVan et al. (2013) used video recordings to track small head movements and used these measurements as a confound to model the artifact. Luo et al. (2014) and Xia et al. (2014) introduced a hardware solution where they insulated some electrodes of an high-density EEG system. Those electrodes, which were still placed on the scalp, recorded only artifactual data, in particular gradient and BCG artifacts, and no brain activity. The signal was then cleaned from gradient artifact and was used as a regressor to remove the BCG artifact from the non-insulated EEG electrodes. Moreover, loops made of carbon wire could also be considered as an hardware-based approach to monitor BCG artifacts. Using this approach, the data can then be regressed out from the EEG data using the Carbon Wire Loop (CWL) data recorded during the fMRI experiment (van der Meer et al., 2016b; Abbott et al., 2015; van der Meer et al., 2016a). In van der Meer et al. (2016b), the authors showed that the CWL correction produced EEG data more comparable to EEG obtained outside the scan, compared to conventional post-processing methods.

Other types of interference can have a negative effect on the quality of the EEG recorded in the MR-scanner, such as the internal ventilation system (Nierhaus et al., 2013), or the cryogenic pump (Rothlübbers et al., 2014; Kim et al., 2015). The best way to avoid these artifacts is to turn off ventilation and helium pumping during the fMRI analysis, but it might not always be possible to do so, due to the subject's discomfort or hospital policy.

It is also worth mentioning that EEG electrodes, wires and equipment inside the MR scanner can create a distortion in the magnetic field that can result in a drop of signal in corresponding MRI images (Stevens et al., 2007; Mullinger et al., 2008a). Whereas the impact on anatomical scans can be problematic (Mullinger et al., 2008a), fMRI images (T2*-weighted scans) were shown to be less sensitive to these decrease in MRI signal quality caused by the metallic equipment in the scanner (Krakow et al., 2000).

3.4.2 EEG-fMRI integration strategy

In this section, we will clarify the rationale of combining EEG and fMRI, and explain their impact on analysis approaches and the main limitations and difficulties associated to those approaches. Firstly, since EEG and fMRI measure two different processes, it is worth

mentioning that we do not expect a one-by-one correspondence between EEG and fMRI signal contributors. Indeed, some neural activity detected on EEG might not be associated with a BOLD response, corresponding for instance to an hemodynamic response with an amplitude that is too small to be detected, or a pathological deficit (Song et al., 2016). Conversely, BOLD signal changes are sometimes not associated with EEG signals. Indeed, synchronization of neuronal activity in time and space is required to generate detectable EEG signals (because for instance of geometry favorable to signal cancellation, or deep generators) whereas the BOLD response reflects a metabolic process that does not require synchronization (Nunez and Silberstein, 2000).

Different methods have been proposed to integrate EEG and fMRI data. They can be classified according to the three following categories (Jorge et al., 2013): fMRI-informed EEG (Kiebel et al., 2008), symmetrical approaches (Valdes-Sosa et al., 2009; Daunizeau et al., 2010), and EEG-informed fMRI (Abreu et al., 2018a).

3.4.2.1 fMRI-informed EEG

The fMRI-informed EEG approach uses fMRI results as spatial priors or constraints to solve EEG source localization for either equivalent current dipoles method (Daunizeau et al., 2010; Kiebel et al., 2008) or distributed models (Babiloni et al., 2004; Grova et al., 2008). In this approach, EEG and fMRI do not need to be recorded simultaneously and, most of the time, EEG is recorded outside the MR scanner to avoid the potential loss in quality when cleaning EEG data from MR-related artifacts. One disadvantage of the fMRI-based constraint is that EEG and fMRI generators are not always concordant, and can lead to false positive if the constraint is too strong. To alleviate this problem, Bayesian techniques have been used to reduce the contribution to the fMRI-informed prior if it is not relevant (Kiebel et al., 2008).

3.4.2.2 EEG-fMRI symmetrical approaches

EEG-fMRI symmetrical approaches propose a multimodal generative model where EEG and fMRI data could be used jointly within a fusion process to infer underlying brain activity. Different methods have been proposed in this context, and key approaches are presented here. First of all, Bayesian framework can be used to obtain a source map reflecting the results of a ESI approach as well as the BOLD response (Daunizeau et al., 2007; Luessi et al., 2011). Another use of the Bayesian model was found in (Lei et al., 2011) to detect the common findings between EEG and fMRI in the detection of brain networks involved during cognitive tasks or during resting state.

Joint Independent Component Analysis (ICA) was also proposed as a fusion approach, where the EEG independent temporal components and fMRI independent spatial components were combined to determine a fused BOLD and ERP response (Calhoun et al., 2005, 2009).

Ostwald et al. (2010) proposed a method analyzing the concordance between different features in EEG and fMRI using information theory, notably the mutual information (Ostwald and Bagshaw, 2011).

Finally, (Yang et al., 2010) presented a reciprocal approach combining EEG-based fMRI prediction with fMRI-driven EEG estimation. EEG data were initially decomposed with ICA, and the time courses of the independent components were used for fMRI GLM analysis. Each of the resulting statistical maps was then used as a prior to reconstruct the EEG sources originating the corresponding independent component, yielding a final source distribution with improved spatiotemporal resolution. The authors validated their methods on the study of alpha-band EEG modulations during a eyes-open-eyes-closed resting state experiment and successfully found an increase in alpha power and alpha-band phase-synchronization in eyes-closed condition versus eyes-open condition.

3.4.2.3 EEG-informed fMRI

EEG-informed fMRI analysis is the most common strategy considered when analyzing simultaneous EEG-fMRI recordings. EEG can be used as a marker of neuronal activity or to quantify specific properties of the EEG response, whereas fMRI is then used to study the corresponding hemodynamic response elicited by such activity within the whole brain.

An overview of all the proposed methods using EEG-informed fMRI is presented in Table 3.1. The most common method of EEG-informed fMRI is the General Linear Method (GLM) (Friston et al., 1998), where events or signals of interest detected on EEG are used to detect BOLD changes on the fMRI (see Section 3.4.2.4). The method presented in the following chapters uses Dirac and boxcar functions to model neural activity elicited by interictal epileptic discharges (IED) (Gotman and Pittau, 2011) or ERP (Debener et al., 2005; Bénar et al., 2007; Fuglø et al., 2012; Nguyen and Cunnington, 2014; Wirsich et al., 2014). This method consists of taking into account only the time of occurrence and potentially the duration of the events, but is blind to other features of the IED. Other characteristics of the IED (or ERP) have been used to help the fMRI analysis. In a study on independent component analysis (ICA) of the BOLD signals, LeVan et al. (2010) showed a significant correlation between the HRF and IED amplitudes, and then proved that the amplitudes of the IEDs could be used to modulate the regressors in the GLM analysis to increase the specificity of EEG-fMRI studies in epilepsy. Moreover, several studies have shown the importance of modeling the stimulus onset (Debener et al., 2005; Wirsich et al., 2014; Nguyen

Table 3.1: List of EEG features predictive of BOLD signal fluctuations of interest. Modified from (Abreu et al., 2018a).

Type of features	Name	Reference
Temporal events	Dirac and boxcar functions	(Lemieux et al., 2001; Bagshaw et al., 2005; Jacobs et al., 2009; Thornton et al., 2010)
	IED amplitude, energy and width	(Bénar et al., 2002; LeVan et al., 2010)
	IED amplitude width, slope of the rising phase, energy and spatial extent (icEEG)	(Murta et al., 2016)
	ERP amplitude and response latency	(Debener et al., 2005; Wan et al., 2006; Bénar et al., 2007; Fuglø et al., 2012; Nguyen and Cunnington, 2014; Wirsich et al., 2014)
Spectral features	EEG power across frequency bands	(Goldman et al., 2002; Mantini et al., 2007; Tyvaert et al., 2008; de Munck et al., 2009; Meir-Hasson et al., 2014; Marecek et al., 2016)
	Phase-amplitude coupling (icEEG)	(Murta et al., 2017)
Spatial correlation features	Spatial template from separate EEG recordings	(Grouiller et al., 2011)
	EEG microstates	(Britz et al., 2010; Yuan et al., 2012; Schwab et al., 2015)
	Continuous ESI	(Vulliemoz et al., 2010a)
Functional connectivity	Partial directed coherence	(Biazoli et al., 2013)
	Phase synchronization index	(Mizuhara et al., 2005; Kottlow et al., 2012; Abreu et al., 2018b)

and Cunnington, 2014), the amplitude of the ERPs (Bénar et al., 2007; Fuglø et al., 2012; Nguyen and Cunnington, 2014), and the latency of the ERPs (Bénar et al., 2007; Fuglø et al., 2012). The articles presented studies in various fields, such as auditory stimulation (Bénar et al., 2007), visual stimulation (Fuglø et al., 2012), face recognition (Nguyen and Cunnington, 2014; Wirsich et al., 2014) and monitoring task performance (Debener et al., 2005). A study on IEDs in intracranial EEG (iEEG) tested how different features of the epileptic events (namely, the amplitude, the width (i.e. duration), the slope of the rising phase, the energy and the spatial extent of the sharp wave) accounted for the variance of the BOLD response. The authors showed that only the width of the IEDs had a significant effect on the BOLD response, suggesting that the amplitude of the BOLD signal depends more on the duration of the epileptic events than on the degree of neuronal activity synchrony (Murta et al., 2016).

Other studies studies aimed at investigating the BOLD correlates of specific frequency

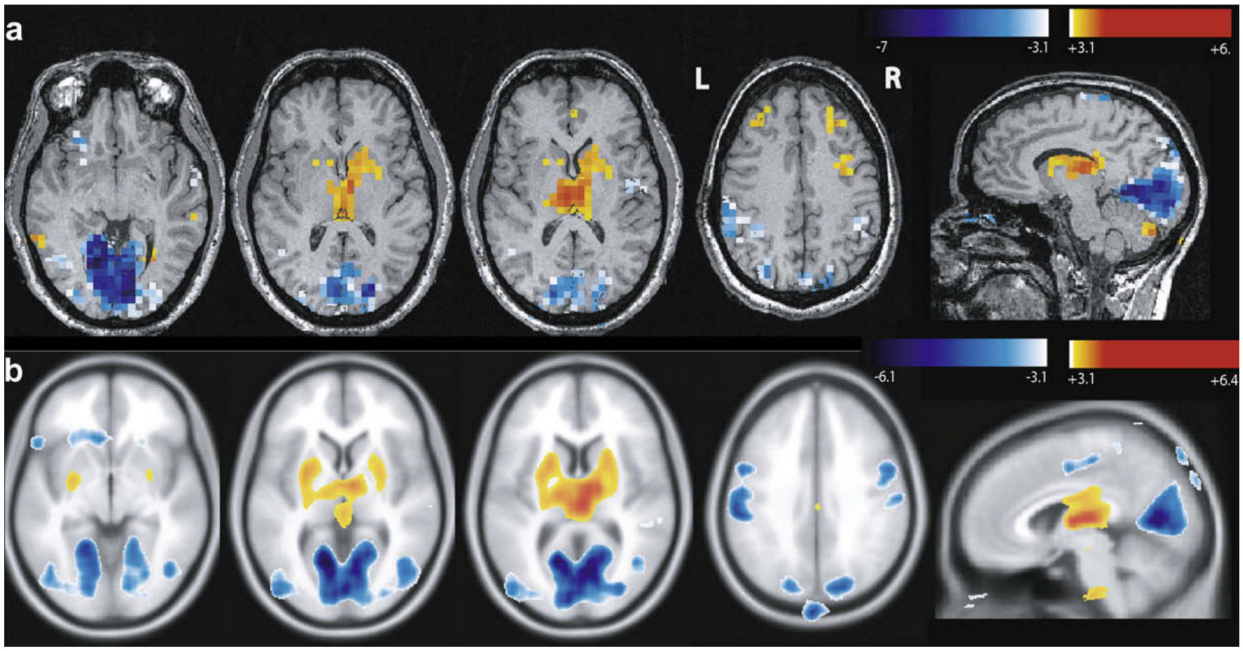

Figure 3.5: Correlation between BOLD and alpha power of a individual patient (**a**) and on the group analysis (**b**). Alpha power is associated with an activation in the thalami and putamen and a deactivation in the occipital lobe, inferior parietal lobule, precentral gyrus, inferior frontal gyrus and middle frontal gyrus, bilaterally. Taken from Tyvaert et al. (2008).

bands, especially the alpha band (usually 8–10 Hz) (Goldman et al., 2002; Scheeringa et al., 2012; Wilson et al., 2019) and the gamma band (30–100 Hz) (Castelhano et al., 2014; Green et al., 2017; Leicht et al., 2016; Mantini et al., 2007; Michels et al., 2010; Mulert and Lemieux, 2010; Rosa et al., 2010; Scheeringa et al., 2011), which were sometimes studied with other frequency bands of interest, such as delta (0.1–4 Hz), theta (4–8 Hz), and beta (12–30 Hz) bands (Tyvaert et al., 2008; de Munck et al., 2009; Uji et al., 2018). To do so, the power variations of each frequency band were convolved with the canonical HRF and used as regressors in a GLM analysis (Goldman et al., 2002; Tyvaert et al., 2008; de Munck et al., 2009; Scheeringa et al., 2012). The illustration of the fMRI response correlated to the alpha band is illustrated in Figure 3.5. Another study (Murta et al., 2017) used as regressors not only the power of the alpha, beta and gamma, but also the phase-amplitude coupling. Phase-amplitude coupling is a measure of the influence of the phase of activity at a low frequency band in the amplitude of high-frequency activity, which was proven to be a good model of neural functional mechanisms (see review in Hyafil et al., 2015). In the article (Murta et al., 2017) the regressor reflecting the phase-amplitude coupling strength explained the variance of the amplitude of the fMRI BOLD signal that had not been explained by the band-power-related regressors alone.

Other continuous regressors can also be used to compare EEG and fMRI, such as continuous

ESI (See review Vulliemoz et al., 2010b), which is further described in Section 4.3.3 and in Chapter 6.

When none or few IEDs were found in EEG recorded with the fMRI, Grouiller et al. (2011) proposed a technique to use the information of EEG recorded outside the scanner to localize the hemodynamic response elicited by the fMRI signals. To do so, the authors proposed a method to measure the correlation between the spatial topography of IEDs detected outside the scanner and the EEG data recorded during an fMRI analysis. The correlation is then convolved with an HRF and used as a regressor for a GLM analysis. The BOLD changes detected by the GLM analysis were found to be concordant with invasive findings or with surgical resection.

Functional connectivity, which is a measure of how different regions of the brain communicate with each other, is of particular interest, both in the fields of EEG and fMRI. Different markers of functional connectivity were convolved with the canonical HRF to construct regressors for the fMRI analysis, such as the partial directed coherence (Biazoli et al., 2013), and the phase synchronization index (Mizuhara et al., 2005; Kottlow et al., 2012; Abreu et al., 2018b). These studies permitted to better understand and to identify brain networks during resting state (Biazoli et al., 2013), or during cognitive tasks such as an arithmetic task (Mizuhara et al., 2005), a face recognition task (Kottlow et al., 2012) or to help identifying the brain networks involved during IEDs (Abreu et al., 2018b).

Another important feature of EEG is the brain microstates which corresponds with several stable brain states (usually four), lasting around 100 ms, which structure the spontaneous EEG (Michel and Koenig, 2018). In resting-state studies of healthy volunteers, the fMRI response to the EEG microstates has been studied based on the hypothesis that resting-state networks are reflected in both EEG and fMRI. Predictors of spontaneous BOLD fluctuations occurring during rest have been obtained by spatially correlating the concurrent EEG topographies at each time point with the previously identified EEG microstates (Britz et al., 2010; Yuan et al., 2012).

EEG-fMRI has been used to better understand the mechanisms of sleep (Picchioni et al., 2013) and EEG has been used to define and characterize the different brain states that occur during sleep (Berry et al., 2013). While EEG can detect the different stages of sleep, fMRI can be used to measure the brain networks involved during each stage using functional connectivity (Kaufmann et al., 2006). EEG-fMRI can also be used to detect the structures involved in the production of different frequency bands related to sleep such as the alpha, delta, and sub-delta bands (Czisch et al., 2004) and to further understand the function of sleep-specific event recorded on EEG during sleep, such as K-complexes and spindles (Schabus et al., 2007).

3.4.2.4 EEG-informed fMRI using GLM analysis

Since GLM analysis is the most common method used in an EEG-fMRI analysis, it is important to introduce here the basics of fMRI analysis through GLM. The GLM model introduced here only considers the neural activity detected on EEG as timing events, modeled by Dirac and boxcar functions. For finer GLM models, taking into account specific parameters such as the amplitude or the latency of the response, the reader is invited to refer to: Mayhew et al. (2010); Mullinger et al. (2013b). A illustration of the GLM analysis in the context of epilepsy is presented in Figure 3.6.

The GLM analysis is a mass-univariate approach for voxel-wise statistical analysis of the hemodynamic response to events detected on EEG (Friston et al., 1995; Worsley et al., 1996; Monti, 2011). In this framework, the BOLD signals measured at N_T time points on N_V voxels $\boldsymbol{Y}$ ($N_T \times N_V$ matrix) can be expressed as a linear combination of regressors, consisting of the expected effect of the task stimulus or other known effects that may confound the results. All the concatenated N_r regressors used for the model form the so-called design matrix $\boldsymbol{X}$ ($N_T \times N_r$ matrix). The relationship between the BOLD signal at a voxel i, denoted $\boldsymbol{y}_i$, and the design matrix $\boldsymbol{X}$ is then as follows:

$$\boldsymbol{y}_i = \boldsymbol{X}\boldsymbol{\beta}_i + \boldsymbol{\epsilon}_i \tag{3.1}$$

where $\boldsymbol{\epsilon}_i \in \mathbb{R}^{N_T}$ is additive noise. The vector $\boldsymbol{\beta}_i$ of size N_r is the unknown regression coefficients that needs to be estimated. The design matrix $\boldsymbol{X}$ is usually constructed with two parts:

The regressors of interest consist of the expected effect of the events of interest (usually ERPs or IEDs). These regressors of interest are usually constructed with the convolution of the timing of events of interest (often estimated by Dirac and boxcar functions) with the canonical Hemodynamic Response Function (HRF) (Glover, 1999), which is the expected neurovascular response to neural activity (Friston et al., 1998). However, the shape and the delay of the HRF vary as a function of both task and brain region (Birn et al., 2001; Marrelec et al., 2003). Moreover, pathological activity, such as epileptic discharges, can also affect the hemodynamic response. For instance, studies have reported HRF occurring a few seconds before the detected scalp discharge (Pittau et al., 2011; Hawco et al., 2007). Therefore, using the same canonical for every voxel and for every task might lead to imprecision in the model. Several methods have been proposed in the literature to overcome this issue (Lindquist et al., 2009). A popular choice is to use a combination of the canonical HRF and its derivatives with respect to time and dispersion (Friston et al., 1998; Henson et al., 2002). In this thesis, a different

approach was chosen, in which four different GLM analyses are performed, wherein the peak of the HFR varies from 3 s to 9 s after the stimulus (Bagshaw et al., 2004).

Nuisance regressors are experimental factors confounding the analysis (such as head motion or signal drifts). The nuisance regressors may be empirically determined (e.g. actual measurements of head translations and rotations obtained during the experiment) or modeled (e.g. by a linear trend or oscillating basis functions). In this thesis, the nuisance regressors include motion trends measured during the experiment and signal drifts estimated by cubic splines designed to model a polynomial trend of degree 3.

To perform a GLM analysis, the error $\boldsymbol{\epsilon}_i$ should be a sequence of independent and identically distributed normal random variables with zero mean (i.e. white noise). This assumption is usually not true in actual fMRI recordings. To alleviate this issue, $\boldsymbol{\epsilon}_i$ is often modeled with the first order autoregressive model, AR(1) (Worsley et al., 2002). In the AR(1), the error at time instant t depends on the amplitude of the error from the previous time instant $t-1$: $\boldsymbol{\epsilon}_i(t) = \rho\boldsymbol{\epsilon}_i(t-1) + \boldsymbol{\xi}_i(t)$, where $|\rho| < 1$ and $\boldsymbol{\xi}_i$ follows a white noise distribution of variance $\boldsymbol{\sigma}_{\xi_i}\boldsymbol{I}$: $\boldsymbol{\xi}_i \sim \mathcal{N}(0, \boldsymbol{\sigma}_{\xi_i}\boldsymbol{I})$. The autocorrelation parameter ρ is estimated from the residuals of the GLM model without an autoregressive model of the noise. The estimated AR(1) parameters $\hat{\rho}$ can then be used to prewhiten the data $\boldsymbol{Y}(t)$ and the design matrix $\boldsymbol{X}(t)$ at time instant t:

$$\begin{aligned} \tilde{\boldsymbol{Y}}(1) &= \boldsymbol{Y}(1), \;\; \tilde{\boldsymbol{Y}}(t) = \left(\boldsymbol{Y}(t) - \hat{\rho}\boldsymbol{Y}(t-1)\right) / \sqrt{1-\hat{\rho}^2} \\ \tilde{\boldsymbol{X}}(1) &= \boldsymbol{X}(1), \;\; \tilde{\boldsymbol{X}}(t) = \left(\boldsymbol{X}(t) - \hat{\rho}\boldsymbol{X}(t-1)\right) / \sqrt{1-\hat{\rho}^2} \end{aligned} \tag{3.2}$$

With the prewhitened matrices, the GLM in Equation (3.1) becomes:

$$\tilde{\boldsymbol{y}}_i = \tilde{\boldsymbol{X}}\boldsymbol{\beta}_i + \boldsymbol{\xi}_i \tag{3.3}$$

The parameters $\boldsymbol{\beta}_i$ for voxel i can then be estimated by the ordinary least-squares estimates that find the solution $\hat{\boldsymbol{\beta}}_i$ minimizing the sum of squared errors $\|\boldsymbol{\xi}\|^2$ as follows:

$$\hat{\boldsymbol{\beta}}_i = \left(\tilde{\boldsymbol{X}}^t\tilde{\boldsymbol{X}}\right)^{-1}\tilde{\boldsymbol{X}}\tilde{\boldsymbol{y}}_i \tag{3.4}$$

Usually, a parametric statistical test is needed to infer whether the measured signals exhibit a specific effect of interest or not. Often, this is tested by examining whether a linear combination of regressor coefficients controlled by a contrast vector $\boldsymbol{c}$ of length N_r, $\boldsymbol{c}^t\boldsymbol{\beta}_i$, has a non-null effect. To do so, a null hypothesis H_0: $\boldsymbol{c}^t\boldsymbol{\beta}_i = 0$ is tested against an alternative hypothesis H_1: $\boldsymbol{c}^t\boldsymbol{\beta}_i \neq 0$. One can show that under the H_0 hypothesis, a t statistic can be

constructed with the estimated contrast effect $\boldsymbol{c}^t\hat{\boldsymbol{\beta}}_i$ and the estimated variance of the noise $\hat{\boldsymbol{\sigma}_{\boldsymbol{\xi_i}}}^2$ as:

$$\hat{\boldsymbol{\sigma}_{\boldsymbol{\xi_i}}}^2 = \frac{\boldsymbol{r}_i^t \boldsymbol{r}_i}{\nu} \tag{3.5}$$

where $\boldsymbol{r}$ is the vector of residuals: $\boldsymbol{r}_i = \tilde{\boldsymbol{y}}_i - \tilde{\boldsymbol{X}}\hat{\boldsymbol{\beta}}_i$, and $\nu = N_t - \text{rank}(\tilde{\boldsymbol{X}})$ is the degrees of freedom.

The test statistic can then be defined as:

$$t = \frac{\boldsymbol{c}^t\hat{\boldsymbol{\beta}}_i}{\sqrt{\hat{\boldsymbol{\sigma}_{\boldsymbol{\xi}}}^2 \boldsymbol{c}^t \left(\tilde{\boldsymbol{X}}^t \tilde{\boldsymbol{X}}\right)^{-1} \boldsymbol{c}}} \tag{3.6}$$

which follows an approximate Student's t distribution with ν degrees of freedom. For each voxel, the null hypothesis H_0 is then rejected if $t > u_\alpha$ for a significant level $\alpha = p(t > u_\alpha | H_0)$.

The statistical inference is performed for every voxel in the brain, i.e. in the order of 100,000 times. Therefore, this approach suffers from the multiple comparison problem (Nichols, 2012). Because of the massive number of tests, a standard significant level α of 5 % would lead to about 5,000 false positives, potentially provoking spurious results. Several methods have been suggested to correct for multiple comparisons by controlling the family-wise error rate (FWE; the chance of one or more false positives), such as the Bonferroni correction (Nichols and Hayasaka, 2003) or the random field theory (Worsley et al., 1996). Other studies suggested controlling the false discovery rate (FDR; the expected proportion of rejected hypotheses that are false positives) (Benjamini and Hochberg, 1995).

3.5 Conclusion

This chapter presented the principles of MRI and fMRI, and the strategies and challenges of recording EEG inside the MRI scanner. A focus was set in the correction of MR-related EEG artifacts as it is in important aspect of the proposed manuscripts 2 and 3 (Chapters 6 and 7). In this manuscript, we used the AAS to remove the gradient and the ballistocardiogram artifacts (Allen et al., 1998, 2000). An overview of the use of EEG-fMRI in the literature was presented, but the use of this imaging technique in epilepsy is further explained in the next chapter.

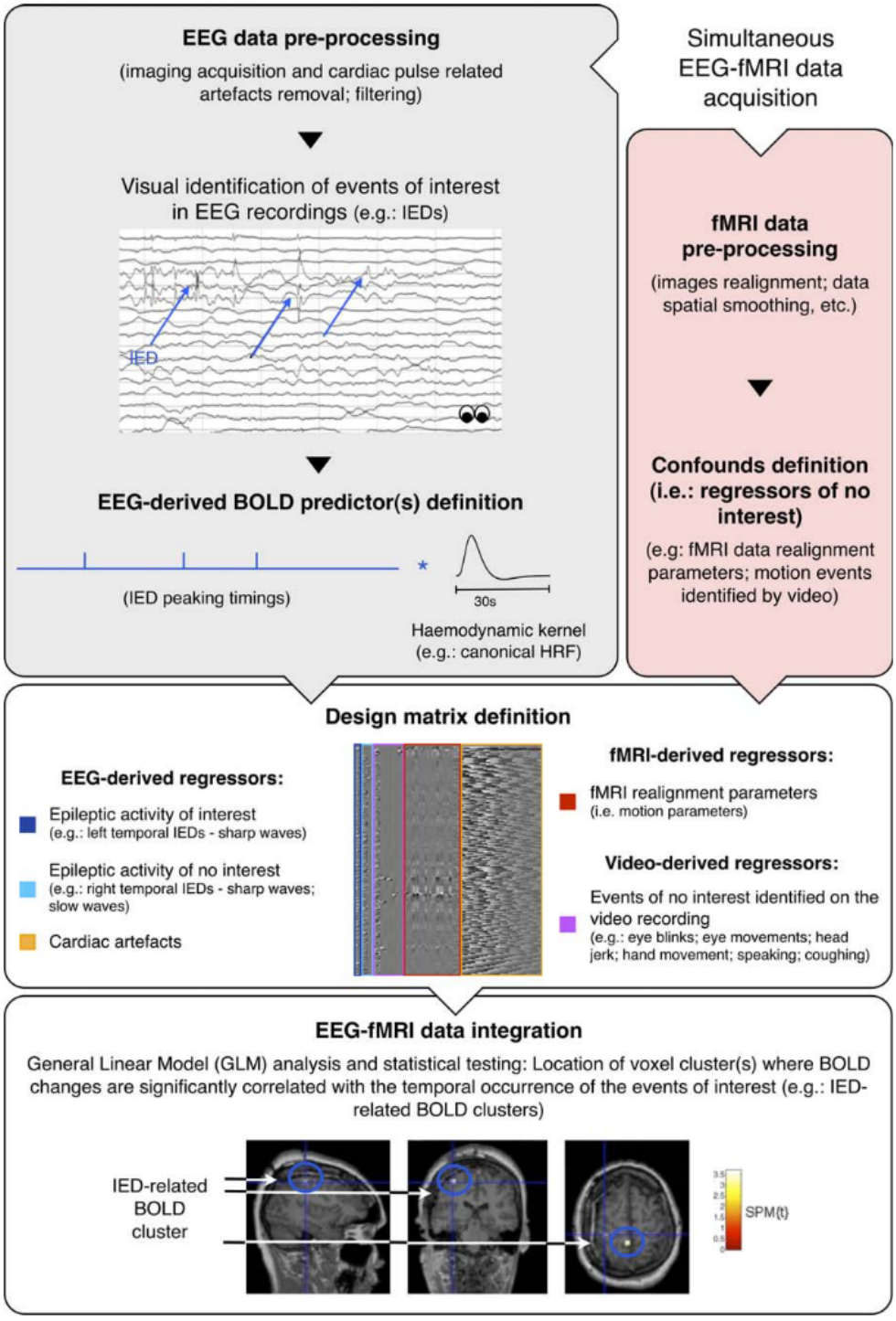

Figure 3.6: Common pipeline of EEG-informed fMRI in epilepsy. Taken from Murta et al. (2015).

Chapter 4

Presurgical investigation of epilepsy

4.1 Definition of epilepsy

The International League against Epilepsy (ILAE) and the International Bureau for Epilepsy define epilepsy as "a disorder of the brain characterized by an enduring predisposition to generate epileptic seizures and by the neurobiological, cognitive, psychological, and social consequences of this condition. The definition of epilepsy requires the occurrence of at least one epileptic seizure" (Fisher et al., 2005).

Epilepsy is not a disease per se since the causes of the seizures are multiple, but rather a condition of the brain where a sudden and abnormal neuronal discharge could occur, provoking a seizure. This disorder can be caused by different factors. For example, the presence of anatomical abnormalities may result in the occurrence of seizures, as for instance malformation during cortical development, brain lesions, tumors, central nervous system diseases, post-traumatic scars or other abnormalities (whose cause may not be known or identified) (Engel and Pedley, 2008).

Epilepsy affects 1 % of the population in Canada (Wiebe et al., 1999). Seizures can be controlled through long-term drug therapy. Medication does not cure epilepsy but rather helps reduce or stop the occurrence of seizures. The type of medication prescribed to the patients depends on the type of seizures and the patient's age, sex and health condition. However, 30 % of the patients are drug-resistant, meaning that medication has no or little effect on the reduction of the occurrence of seizures. For those patients, other forms of treatments are considered. Patients with focal epilepsy may undergo surgery to resect the brain region responsible for the generation of the the seizures while avoiding any important functional

loss (Stippich, 2007).

4.2 Epileptic seizures and interictal epileptic discharges

Seizures and interictal epileptic discharges (IEDs) are both important markers for the diagnostic and treatment of epilepsy. An epileptic seizure, as described by the ILEA, is "a transient occurrence of signs and/or symptoms due to abnormal excessive or synchronous neuronal activity in the brain" (Fisher et al., 2005). In rare cases, IEDs are defined as spontaneous abnormal paroxysmal events of short duration (a few hundred milliseconds) occurring in between the seizures. IEDs are not associated with any clinical manifestation, as patients are unaware of having them.

4.2.1 Classification of epileptic seizures

There are three main features that characterize an epileptic seizure (Fisher et al., 2005):

1. A seizure is demarcated in time, delimited by a clear onset and termination. Typically, a seizure lasts a few minutes, but can be as short as a few seconds. On the other hand, a long-duration case of epileptic seizures, called *status epilepticus*, can last days or weeks.

2. A seizure provokes clinical manifestations. Those clinical signs are various, depending on the location of the brain areas involved during the generation and propagation of the seizure. Epileptic seizures can involve loss of consciousness; interruption of memory; sensory, visual or auditory hallucinations; motor automatisms such as jerking; and changes of emotional state, among other symptoms. Not all seizures affect all of these factors and patients can experience seizures causing different clinical signs.

3. A seizure is caused by abnormal synchrony of overexcited neurons in a region of brain. This excessive and unpredictable discharge is often due to a decrease in local inhibition on a population of pyramidal neurons. These abnormal neuronal discharges give rise to changes in electro-magnetic activity in the neurons, that can most of the time be detected remotely by measuring differences of electrical potentials using scalp EEG and variations in magnetic field using MEG. It is worth noting here that some epileptic events provoke long-lasting (several seconds) abnormal discharges detectable in EEG, but without causing any clinical manifestations. These types of events are called electrographic seizures.

In 2017, the ILAE presented their latest classification of seizure types, based on the type of onset. The basic and extended versions were introduced. The basic version of the classification is presented in Figure 4.1.

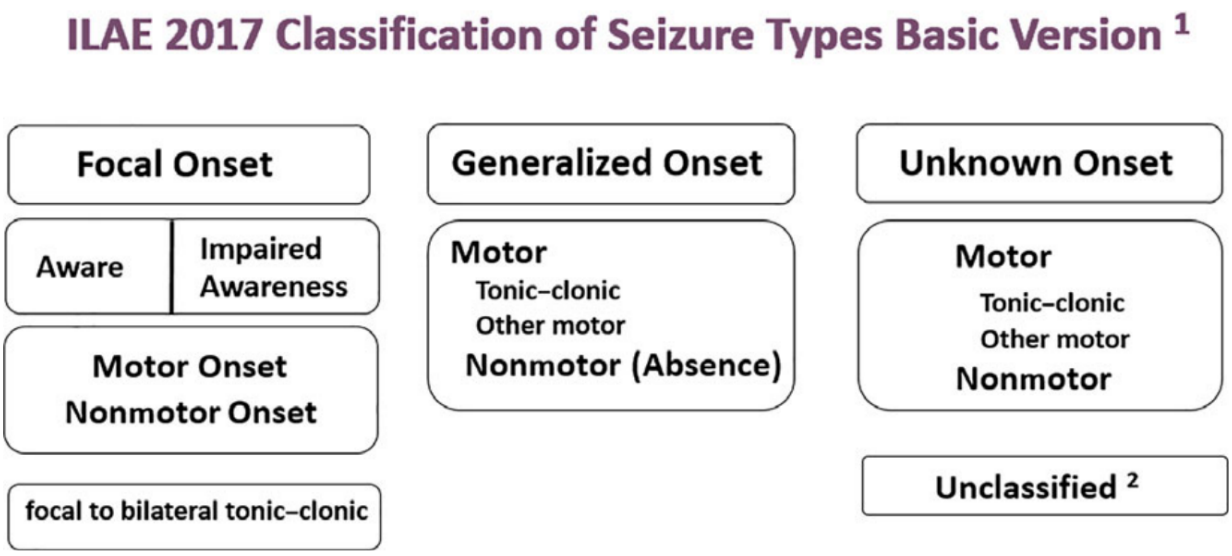

Figure 4.1: The basic ILAE 2017 operational classification of seizure types. "**1** Definitions, other seizure types and descriptors are listed in the accompanying paper and glossary of terms. **2** Due to inadequate information or inability to place in other categories." Taken from Fisher et al. (2017).

The first two classifications of basic seizure types focus on characterizing seizures on whether their onset is focal or generalized. Seizures have a focal onset if the generator of the seizure is a delimited brain region. Comparatively, the onset of generalized seizures involves an extended network of brain regions, covering both hemispheres.

Focal onset seizures can be sub-classified by whether or not the seizures are associated with cognitive impairment (Fisher and Saul, 2010). They can be further characterized by the type of clinical manifestations that appear at the onset of the seizures, such as motor onset (e.g. automatisms, tonic, atonic or clonic postures) or nonmotor onset (emotional, such as fear, anxiety or joy, sensory, cognitive impairments, or behaviors) symptoms. Finally, some focal seizures can evolve into bilateral tonic-clonic motor activity, which are reported as focal seizure with secondary generalization in the previous classifications. Focal seizures account for about 60 % of all seizures (Hauser et al., 1991; Keränen et al., 1988). The onset of focal seizures can be localized anywhere in the brain. However, seizures with an onset in the temporal lobe are more frequent (60 % of all focal seizures), whereas seizure onset localized in the forntal lobe account for 30 % of all focal seizures. Finally, seizures onset localized in the parietal and occipital lobes account for the remaining 10 % (Shorvon, 2009).

Generalized onset seizures involve extended brain regions covering both hemispheres. They can further be characterized by the description of seizures, whether it is associated

with motor (tonic-clonic, or other types of motor manifestations) or nonmotor manifestations (absence seizures).

When the classification of seizures into focal or generalized-onset categories is not possible, seizures are then referred to the category entitled "unknown onset". However they may still be characterized with some evidence of motor or non-motor characteristics.

4.2.2 Classification of epilepsy types

The ILAE also proposed a classification of the patient's type of epilepsy (Scheffer et al., 2017). The epilepsy types include four different groups:

Focal epilepsies include unifocal and multifocal disorders. They are characterized by seizures with focal onset and are often associated with focal interictal discharges detected on EEG.

Generalized epilepsies are characterized by seizures with generalized onset such as absence, myoclonic, atonic, tonic or tonic-clonic seizures. Interictal findings usually include generalized spike and wave activity on EEG.

Combined generalized epilepsies and focal epilepsies are characteristic of patients presenting both generalized and focal seizures. They are characterized by ictal recordings, but also interictal EEG tracings, usually with the presence of both characteristic generalized spike and wave discharges and more focal epileptiform events.

Unknown epilepsies is a category used when the diagnosis of epilepsy could be made but it is not possible to determine if the epilepsy type is focal or generalized.

Once the type of epilepsy is known, it is sometimes possible to define an epilepsy syndrome associated with the disease. An epilepsy syndrome refers to "a cluster of features incorporating seizure types, EEG, and imaging features that tend to occur together" (Scheffer et al., 2017). The diagnostic of an epilepsy syndrome permits a broader classification than only the seizure type. Indeed epilepsy syndromes also include information about the clinical features of the patient, such as the severity, the prognosis and the treatment implications. They are characterized by several age-dependent features, i.e. age at onset and remission (where applicable), seizure triggers and diurnal variation, but also characteristic intellectual and psychiatric dysfunction, EEG findings and imaging studies.

4.2.3 Interictal epileptic discharges

Interictal epileptic discharges (IEDs) are abnormal EEG activity which occur without the manifestation of seizures. IEDs are the EEG byproduct of the summation of postsynaptic potentials from pathologically synchronized firing neurons. They usually occur sporadically, isolated or in short rhythmic bursts and without clinical manifestations. IEDs can have different characteristics and are often described as either sharp waves, spikes, or polyspikes (see Figure 4.2). Sharp waves and spikes are both transient events with a duration between 70-200 ms for sharp waves and 20-70 ms for spikes, whose amplitudes detach from physiological EEG background. Polyspikes are characterized by a fast series of spikes. Spikes and polyspikes can sometimes be followed by a slow wave, usually of higher amplitude and lasting longer than the spike (Noachtar and Rémi, 2009). IEDs are sometimes associated with rhythmic activity, such as high-frequency oscillations (Frauscher et al., 2017) or slower activity, like paroxysmal slow activity. The identification of IEDs from physiologic or artifactual sharp transients usually requires the expertise of a trained epileptologist (Zijlmans et al., 2002).

These events are generated by the brain without clinical manifestations. They do not induce patient movement and occur more frequently than the seizures. For these reason, they are a excellent marker used in EEG and MEG source imaging for the pre-surgical evaluation of patients who are candidates for epilepsy surgery (Pittau et al., 2014; Habibabadi et al., 2019).

4.3 Treatment of epilepsy

The goal of the treatment of epilepsy is to achieve seizure freedom with minimal side-effects. The first method of treatment is anti-epileptic medication, which aims to reduce or abolish the occurrence of seizures by altering the neuronal excitation and inhibition balance in the region triggering the seizures. For approximately 60-80 % of the patients, anti-epileplic drugs successfully control the seizures (Kwan et al., 2010). When the medication is not able to reduce the occurrence of seizures, the epilepsy of those patients is then referred to as drug-resistant epilepsy. For drug-resistant patients with focal epilepsy, surgery may be considered.

The principle of epilepsy surgery is to resect the so-called epileptogenic zone, i.e. “the minimum amount of cortex that must be resected (inactivated or completely disconnected) to produce seizure freedom” (Lüders et al., 2006). Surgery successfully achieves seizure freedom in 30 % to 85 % of the patients (Téllez-Zenteno et al., 2005), depending on the epilepsy syndrome and the ability to clearly define and completely resect the epileptogenic zone. It

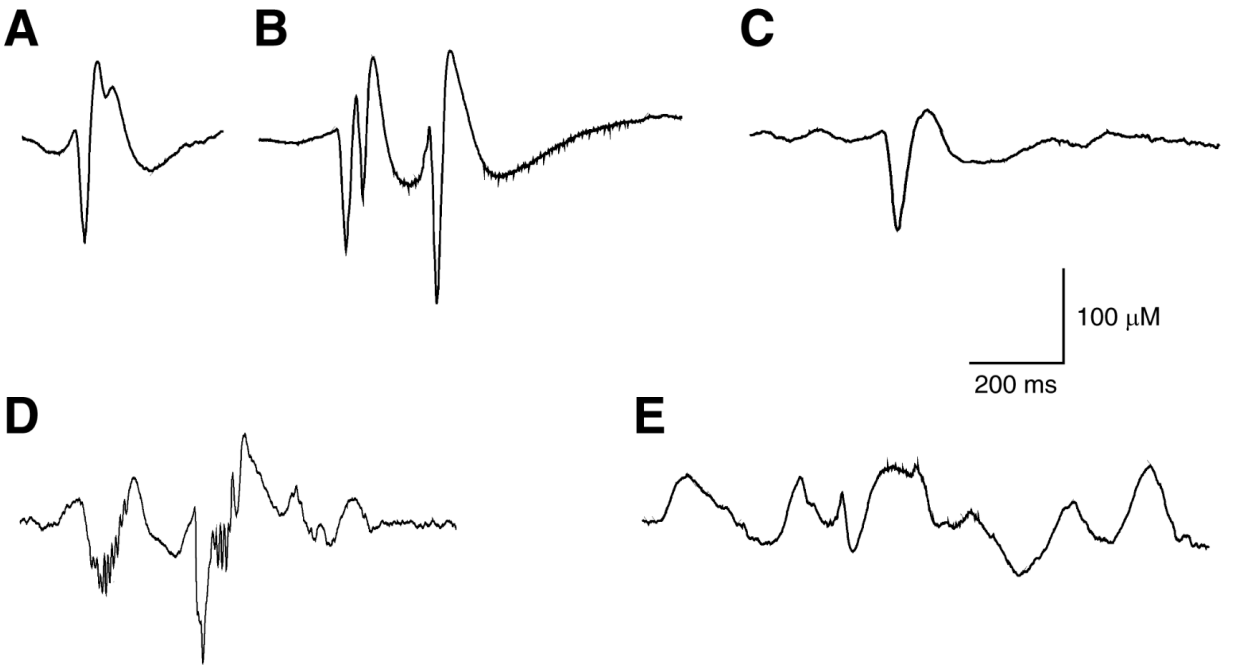

Figure 4.2: Interictal epileptic discharge patterns recorded with intracranial electrodes. **A.** Spike; **B.** Polyspike; **C.** Sharp wave; **D.** fast activity (brushes) riding on a spike; **E.** paroxysmal slow activity superimposed to slow spikes. Taken from Curtis et al. (2012).

is therefore very important to perform a comprehensive presurgical evaluation, in order to precisely localize the epileptogenic zone.

4.3.1 Presurgical evaluation

The presurgical evaluation aims at localizing the zone of the brain triggering the seizures. To do so, a large variety of measures could be used. Different aspects of epilepsy can be investigated to gain information about the localization of the epileptogenic zone, such as the seizure semiology, the study of cognitive deficit produced by the epilepsy, the potential presence of anatomical brain lesions, the electrophysiological patterns associated with epileptic discharges, or finally the corresponding hemodynamic and metabolic patterns associated with epilepsy.

Each of the measures have advantages and disadvantages, and none of the techniques can provide a perfect marker of the *epileptogenic zone*. In reality, each of the techniques helps localize different brain areas which are related to the epileptogenic zone, which is a theoretical concept not directly accessible. Table 4.1 reports the definition of all those regions of interest.

EEG and MEG allow the detection and localization of the generators of the IEDs and seizures, defining the irritative zone and the seizure onset zone respectively. The irritative

Table 4.1: Brain areas of interest in partial epilepsy. Modified from (Engel and Pedley, 2008)

Brain area	Definition	Measure
Irritative zone	Area of cortex that generates IEDs	EEG, MEG, EEG-fMRI, iEEG
Seizure onset zone	Area of cortex that initiates or generates seizures	EEG, MEG, EEG-fMRI, iEEG
Epileptogenic lesion	Structure pathology of the brain that is the direct cause of seizures	CT, MRI, tissue pathology
Symptomatogenic zone	Portion of the brain that produces the first clinical symptoms	EEG, behavioral observation
Functional deficit zone	Cortical area producing nonepileptic dysfunction	Neurologic exam, neuropsychology, PET, SPECT
Epileptogenic zone	Total area of the brain that is necessary to generate seizures and that must be removed to abolish seizures	—

zone usually involves a larger region than the ictal onset zone (Hauf et al., 2012). Concordance between the irritative zone or the *seizure onset zone* and the epileptogenic zone has been validated many times (Rampp et al., 2019; Mouthaan et al., 2019). A more precise localization of the irritative and seizure onset zone can be done with invasive recorded, i.e. intracranial electrodes (iEEG). iEEG includes ElectroCorticoGraphy (ECoG) using subdural grid electrodes or stereotactic EEG (sEEG) using depth electrodes (Parvizi and Kastner, 2018).

When epileptic seizures are likely to be elicited by the presence of an underlying lesion, the area of the lesion may be detected with brain imaging techniques such as Magnetic Resonance Imaging (MRI) (Bernasconi et al., 2011; Strandberg et al., 2008) and Computed Tomography (CT), or with the analysis of tissue pathology during biopsy performed before or during resective surgery. These techniques reveal the epileptogenic lesion, whose resection is often sufficient to abolish epileptic seizures (Téllez-Zenteno et al., 2010; De Tisi et al., 2011).

The Symptomatogenic zone is the zone that produces the clinical manifestations occurring at the onset of the seizure. This area is usually determined by the testimony of the patient's relatives or by video-EEG.

Sometimes, patients with epilepsy may also exhibit specific cognitive deficits. The location of the brain region associated with a deficit in a particular cognitive function (the functional

deficit zone) can also help identify the epileptogenic zone. For this purpose, a series of neurological and neuropsychological tests are performed to define the impaired cognitive functions (Baxendale, 2018). The functional deficit may be characterized by a change in local brain metabolism and perfusion than can be elicited by Position Emission Topography (PET) (Juhász and Chugani, 2003) and Single-Photon Emission Computed Tomography (SPECT) (Knowlton and Shih, 2004; Van Paesschen et al., 2007) respectively.

4.3.2 EEG and MEG source localization in epilepsy

Due to the unpredictable and infrequent nature of epileptic seizures, EEG and MEG investigations usually focus on estimating the irritative zone by the analysis of IEDs. When these discharges are recorded with a sufficient number of channels, source localization can be used to increase spatial resolution and localization accuracy (Baillet et al., 2009). Studies have shown performance of dipole fitting (Knowlton et al., 2006), dipole scanning (Mosher et al., 1992), and distributed models (Klamer et al., 2014; Pellegrino et al., 2018). To assess the performance of source localization techniques, the gold standard or reference is either the results of iEEG local measurements or the surgical outcome. As mentioned in Section 2.6.3.3, our group have shown that the distributed model using cMEM might be preferable to dipole fitting for the pre-surgical evaluation of patients with epilepsy (Pellegrino et al., 2018) .

In a meta-analysis, Mouthaan et al. (2019) analyzed the results of 11 studies of interictal source localization in MEG and/or high-density EEG ($\geq$ 64 electrodes), for a total of 264 patients in MEG and 127 patients in EEG. Source localization was performed using a linear source imaging technique for EEG, and dipole fitting methods for MEG. When the concordance with the resected area was compared to seizure outcome, the meta-analysis reported an overall sensitivity of 82 % (Confidence Interval (CI) at 95 %: 75–88%) and specificity of 53 % (95%-CI: 37–68 %). It seems then that EEG and MEG source localization could add valuable information in the presurgical evaluation. Consequently, it seems that EEG and MEG source localization was effectively beneficial to guide the placement of intracranial EEG electrodes (Sutherling et al., 2008; Knowlton et al., 2009).

In the review of Mouthaan et al. (2019), the authors found no statistical difference between patients presenting an epileptogenic lesion detected on anatomical MRI images and patients with no lesions. They also reported no difference in localization performance between temporal lobe and extra-temporal lobe epilepsy. These two results are considered controversial since other studies did show a statistical difference between the diagnostic accuracy between lesional and non-lesional patients (Abdallah et al., 2017; Rampp et al., 2019), and between temporal and extra-temporal lobe epilepsy (Rampp et al., 2019; Vadera

et al., 2013; Abdallah et al., 2017).

Not only can distributed source localization methods give information about the localization of the irritative zone, but also its spatial extent. The spatial extent of the underlying source of IEDs was shown to be helpful in the pre-surgical investigation and several ESI and MSI techniques which were able to recover the source spatial extent have been proposed in the literature (Ding et al., 2007). Specifically, our method cMEM was proven to be sensitive to spatial extent in multiple studies (Chowdhury et al., 2013, 2015; Heers et al., 2015; Chowdhury et al., 2016), and was compared in a study to another technique, 4-ExSo-MUSIC, and both techniques were found accurately sensitive to the location and spatial extent of the sources (Chowdhury et al., 2016).

Most of the studies presented in this section used either EEG or MEG separately. It has been showed that EEG and MEG conveyed complementary information, and several approaches considered the fusion of EEG and MEG data to perform source localization. These fused data sets demonstrated that combined EEG-MEG exhibited a higher accuracy in terms of source localization for the presurgical evaluation than either modality taken separately (Aydin et al., 2015; Chowdhury et al., 2015, 2018). The potential added value of fusion EEG/MEG is illustrated in Figure 4.3. On this patient, combined EEG/MEG identified a source in the inferior part of the left pre-central gyrus which was in perfect concordance with a Focal Cortical Dysplasia (FCD) identified on the anatomical MRI of this patient. Conversely, individual EEG and MEG localizations mainly detected sources in the frontal lobe, which more likely consisted in secondary sources. Another source was found in MEG close to the FCD location, but it was not the source exhibiting the largest amplitude.

Another point of debate in the ESI and MSI community is the ability for those techniques to localize IEDs coming from deep generators, as, for example, mesial temporal structures. While some studies state that sources coming from deep structures are not visible on EEG (Gavaret et al., 2014), others claim being able to localize sources in the mesial temporal region (Carrette et al., 2011). A study comparing intracranial EEG to scalp EEG (Koessler et al., 2014) demonstrated that in mesial temporal lobe epilepsy deep structures can contribute to the EEG data, but with a level of amplitude much lower than the background activity, which means that mesial temporal sources are not spontaneously visible on the scalp. EEG was found to be more sensitive to source propagation coming from the neocortex. Another study on simultaneous iEEG and MEG was able to detect brain activity on MEG of deep structures, such as the hippocampus and amygdala, using the ICA method triggered by IED events detected on iEEG (Pizzo et al., 2019).

IEDs are complex phenomena that could be subject to propagation. Some studies advised performing source localization based on the time period halfway between the onset and the

peak of the spike in order to avoid propagation effect (Ebersole, 1991; Lantz et al., 2003b). A more recent study recommended analyzing both the onset and the peak of the spikes in order to optimize the accuracy of the source imaging (Mălîia et al., 2016).

It is commonly known that epilepsy is a condition affecting the parts of brain involved in the generation of seizures and IEDs, but also the regions which are functionally connected to them. The study of brain networks through EEG or MEG is a promising technique that can help to identify the structures involved in epilepsy and help with pre-surgerical evaluation. However, it still needs to be thoroughly validated (see review in van Mierlo et al., 2019).

Even though seizures are rare events, it is still possible to record them and therefore to localize them using either EEG or MEG data during seizures. Source localization of ictal activity has already been reported and showed good concordance with the presumed epileptogenic zone (Koessler et al., 2010; Pellegrino et al., 2016a; Kuo et al., 2018). In a study from our group (Pellegrino et al., 2016a), the onset of epilepsy seizures of 13 patients was localized using wavelet-based MEM (wMEM) in EEG and MEG, and the relevance of the source imaging results was compared to IED source imaging. The decision to analyze the seizure onset was chosen to avoid contamination from motion and muscle artifacts. As illustrated in Figure 4.4, the analysis of ictal data can provide valuable information to the presurgical evaluation. In this figure, the source localization of the seizure onset zone was localized in the left posterior frontal region, in concordance with intracranial findings, where a focal cortical dysplasia had been detected on the anatomical MRI of this patient. Conversely, ESI and MEG of spikes were located in the more anterior frontal region, suggesting that, for this patient, the localization of ictal activity was more informative than the localization of interictal events. Overall, over the 46 seizures we reported on these 13 patients, one of the largest reported cohorts so far, we found a good level of agreement between seizure and IED source imaging.

4.3.3 Simultaneous EEG-fMRI investigations

For the detection of the epilepleptogenic zone, EEG-fMRI aims to estimate and localize the hemodynamic response associated with transient epileptic discharges detected on scalp EEG. The most common use of EEG-fMRI in studies on epilepsy is the localization of the change in hemodynamic response following IEDs (Mulert and Lemieux, 2010; Gotman et al., 2006; Gotman, 2008).

After carefully denoising EEG data acquired during fMRI acquisition (see Section 3.4.1), each IED detected on scalp EEG is then marked by an expert epileptologist as an event with or without duration, following the nature of the discharge. These events are then usually

convolved with the so-called canonical HRF, which is an estimation of the change in blood flow following an IED, and then used as a regressor in a general linear model (Friston et al., 1998).

The resulting fMRI maps display significant BOLD clusters associated with the neural activity elicited by the IEDs. A significant BOLD cluster can indicate either an increase (activation) or a decrease (deactivation) in BOLD response. In either case, the BOLD cluster can be a marker of the irritative zone (Heers et al., 2014; Pittau et al., 2012). The BOLD clusters are related to either the generation of epileptic discharges (Grova et al., 2008; Heers et al., 2014), their eventual propagation patterns (Vulliemoz et al., 2009) or remote influence, as for instance on the default mode network (Gotman et al., 2005). The region displaying the most significant BOLD cluster has been suggested to be a good indicator of the presumed epileptigenic focus (Heers et al., 2014; Khoo et al., 2017).

The clinical relevance of EEG-fMRI investigations in epilepsy has been extensively evaluated using intracranial data or surgical outcome (Zijlmans et al., 2007; Zhang et al., 2012; An et al., 2013; van Graan et al., 2015). Figure 4.5 is an illustration of the concordance between EEG-fMRI analysis and intracranial EEG data. In this example, the fMRI BOLD cluster was located in the right orbito-frontal region, indicating the location of the generators of the epileptic discharges. This location which was later confirmed by iEEG, and with surgery, the patient being seizure-free after the resection of this region.

One main limitation of EEG-fMRI analysis is the low detection rate of IEDs in EEG. It has been showed that no IED was detected in 40 % of the cases, and for another 30 % of cases, no significant fMRI response was found (Salek-Haddadi et al., 2006). To improve the sensitivity of the technique, Grouiller et al. (2011) proposed a method by which a GLM regressor was constructed based on the correlation between the clean topography of the averaged IEDs recorded outside the scanner and the EEG signals recorded during the fMRI analysis, thus increasing sensitivity to 83 % (Grouiller et al., 2011; Elshoff et al., 2012).

EEG-fMRI analysis shows the effect of IEDs on the full brain, thus allowing the analysis of the network involved during an epileptic event. Indeed, the distributed BOLD clusters detected in fMRI were proven to be functionally synchronized in iEEG (Khoo et al., 2017). IEDs were shown to disturb the brain network, such as the default mode network, both in generalized (Laufs et al., 2006; Gotman et al., 2005) and focal epilepsy (Fahoum et al., 2013).

EEG-fMRI analyses of ictal events, though uncommon, were also verified as being reliable indicators of the epileptogenic zone (Chaudhary et al., 2013).

4.4 Conclusion

To summarize, epilepsy is defined by the presence of recurring seizures. Those seizures are controlled by medication in most of the patients. For the remaining patients, if their epilepsy is focal, i.e. where seizures are triggered in a delimited location in the brain, surgery may be considered. During presurgical evaluation, different approaches are used to define, as precisely as possible, the zone of the brain that is needed to resect in order to abolish the seizures. Two of those approaches are EEG/MEG source localization, which aims at localizing the generator of the seizure onset and other epileptic events detected in EEG and MEG, and EEG-fMRI, an imaging technique which detects the hemodynamic response related to epileptic events. The goal of this thesis is to use both ESI and EEG-fMRI with the same EEG data to perform an EEG-fMRI analysis informed by ESI. To do so, we developed and presented in Chapter 7 a method to automatically classify IEDs on EEG recorded in the MRI scanner, which constructs GLM regressors with a more homogeneous population of IEDs to increase the accuracy of the fMRI analysis.

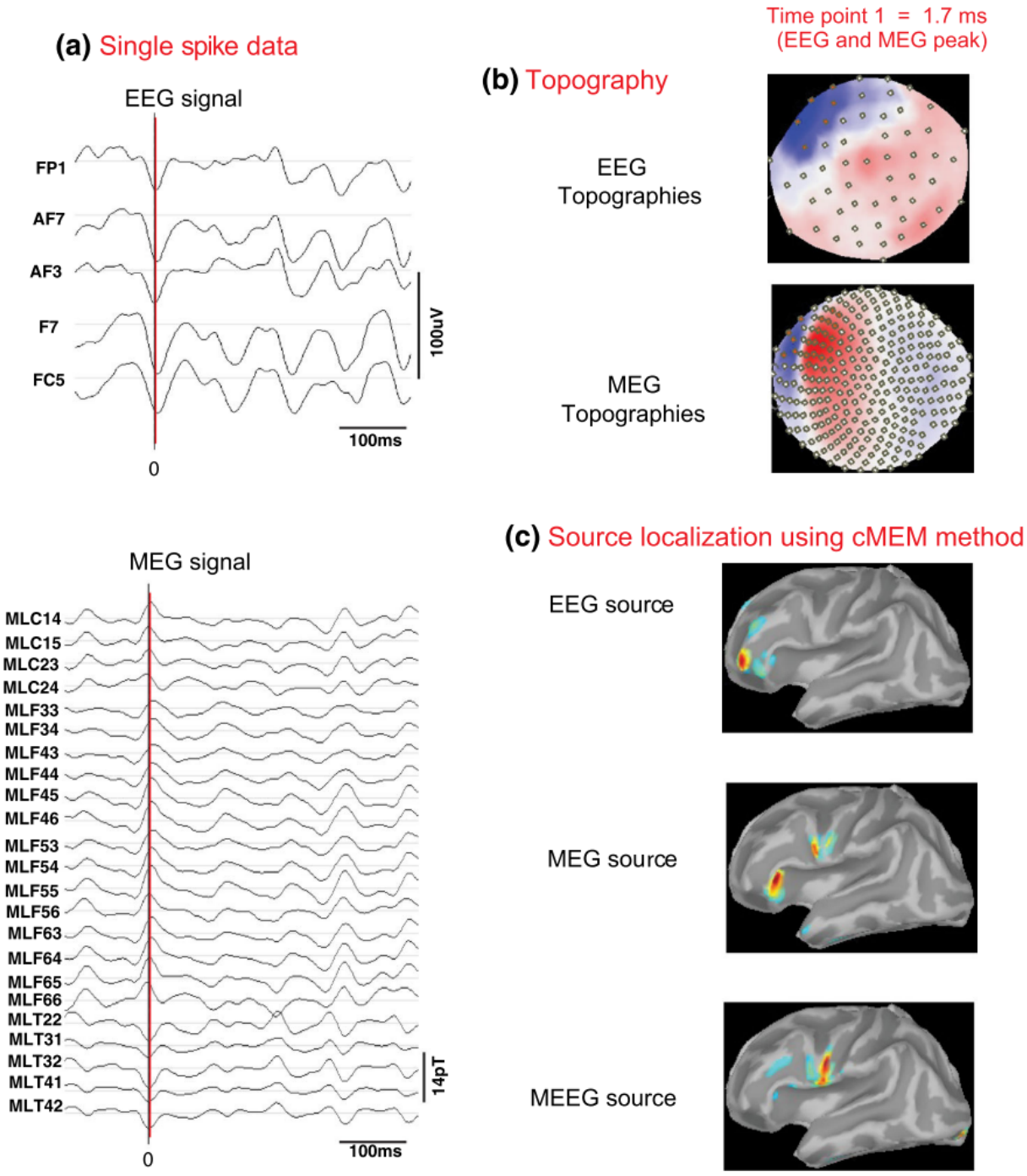

Figure 4.3: Single spike localization of one patient. **(a)** EEG and MEG signal for the respective spike type. **(b)** EEG and MEG topographies at the peak. **(c)** Source localization results using cMEM method for EEG data, MEG data and fusion between EEG and MEG (MEEG). Taken from Chowdhury et al. (2015).

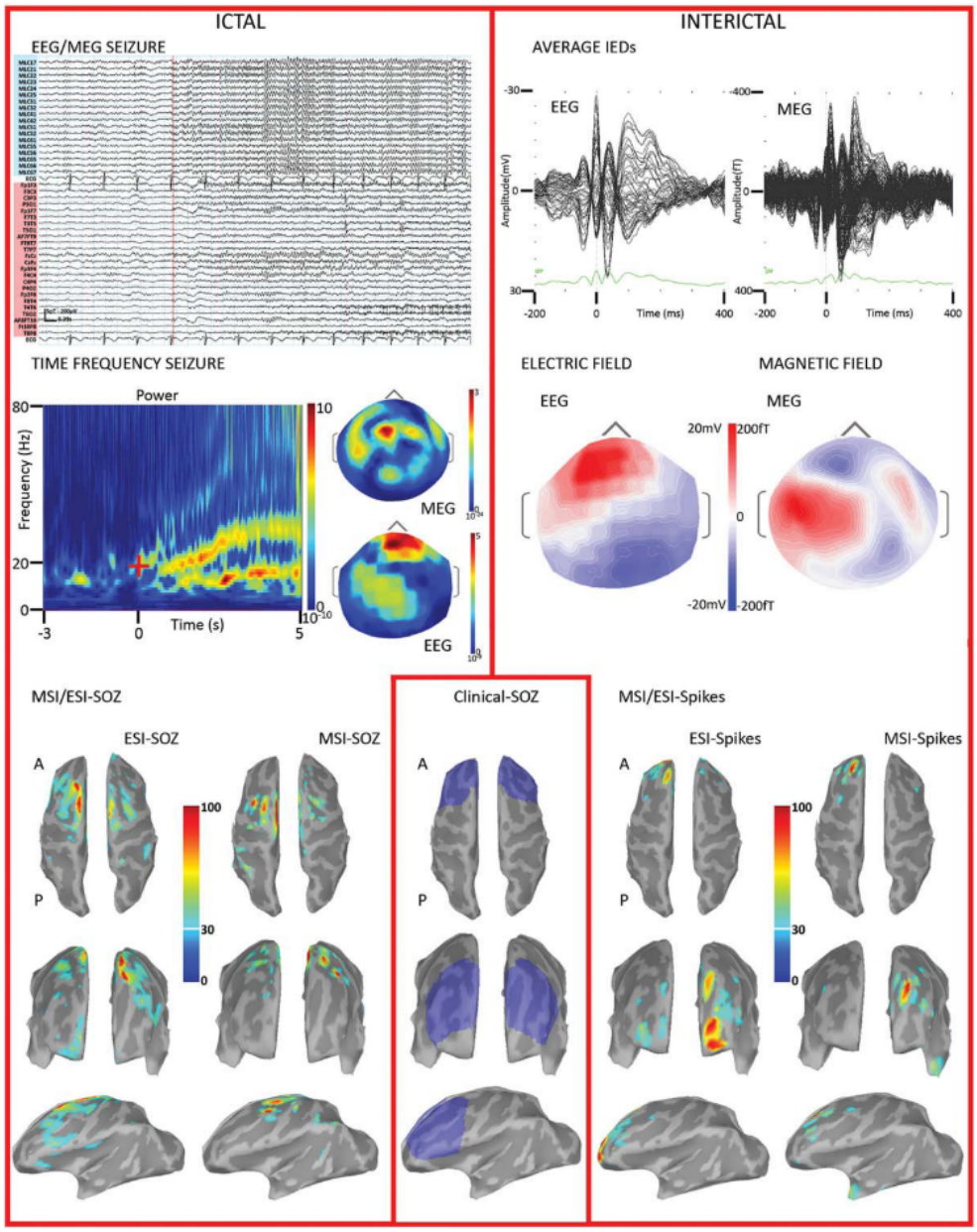

Figure 4.4: Illustration of MSI/ESI source localization of ictal activity. **Left panel:** *top*: MSI/ESI localization of the SOZ. From top to bottom: MEG (cyan) and EEG (pink) traces of the onset of the seizures. The onset is marked by the red line. *center*: Time-frequency decomposition suggesting the involvement of two frequency bands in the alpha–beta range, with the strongest energy change at about 20 Hz. *bottom*: corresponding localization of the onset zone in EEG and MEG. **Right panel:** MSI/ESI localization of the spikes. **Bottom, middle panel:** estimated epileptogenic zone (in blue), confirmed by intracranial EEG. Taken from Pellegrino et al. (2016a).

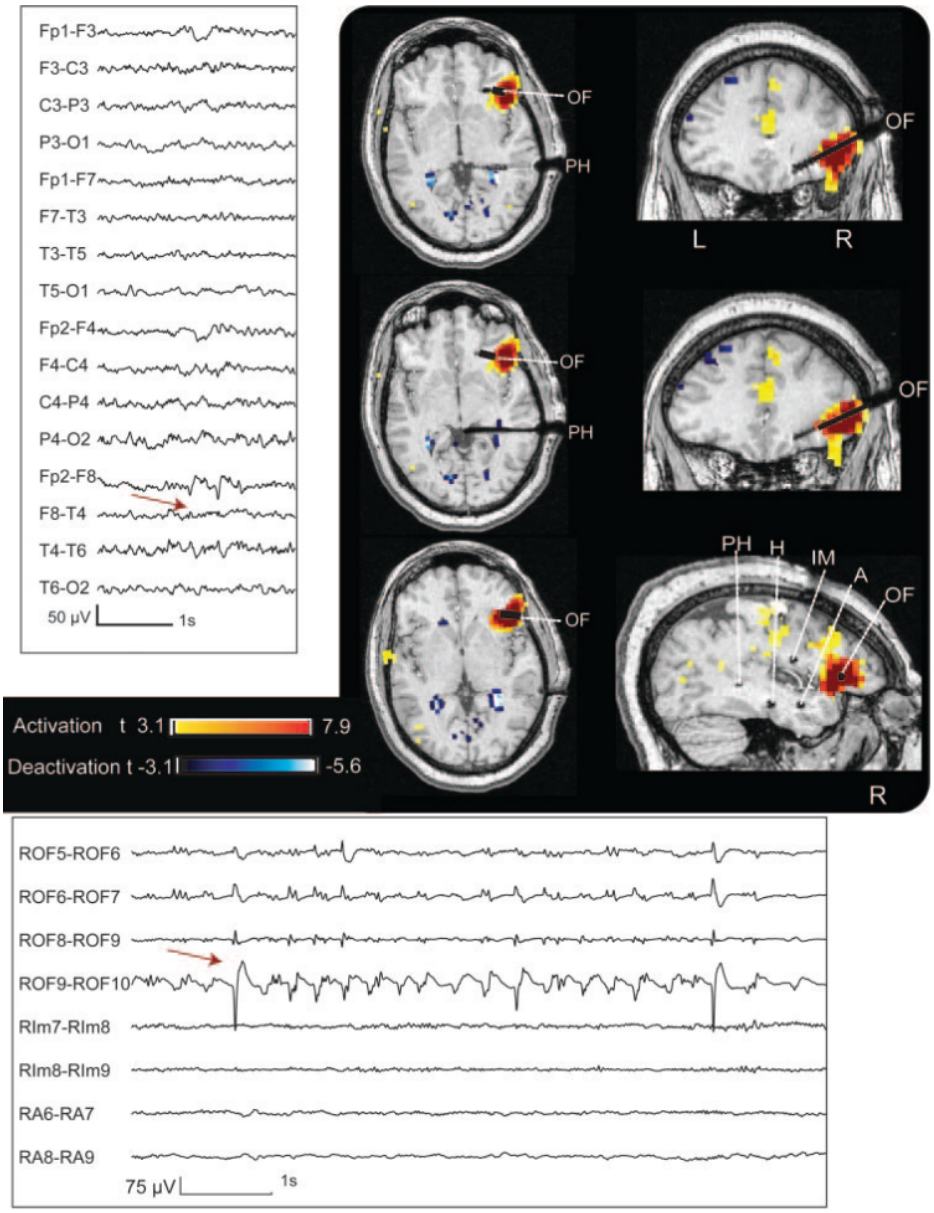

Figure 4.5: Illustration of a EEG-fMRI analysis of a patient with right frontal epilepsy. The BOLD response showed a limited activation in the lateral right orbitofrontal region. The finding was validated with intracranial EEG showing a active epileptic general in the lateral portion of the right orbitofrontal lobe (electrodes ROF6–ROF10). A limited right frontal corticectomy was performed and histology showed focal cortical dysplasia type 1. Taken from Pittau et al. (2012).

Chapter 5

Manuscript 1: Comparison of the spatial resolution of source imaging techniques in high-density EEG and MEG

Authors: Tanguy Hedrich, Giovanni Pellegrino, Eliane Kobayashi, Jean-Marc Lina, Christophe Grova.

Context

Detection and source analysis of IEDs is widely used during the pre-surgical investigation of patients with intractable epilepsy. As outlined in the previous chapters, EEG and MEG record the neuronal dynamics of brain activity with high temporal resolution, but with limited spatial resolution, since recordings are made from the scalp. To alleviate this problem, electrical or magnetic source imaging can be considered to improve the spatial resolution and to obtain a more accurate localization of the generators of IEDs. Several ESI and MSI techniques have been proposed, including some within the framework of distributed source models, meaning that the generators of the EEG/MEG signals can be estimated with a set of fixed dipolar sources distributed along the cortical surface. Source localization then consists of estimating the amplitudes of the dipolar sources that can explain the EEG/MEG data. We have developed such a source imaging technique in our group, cMEM, and have demonstrated in several studies that cMEM was an interesting technique, especially because it is sensitive to the spatial extent of the underlying generators. So far, our group mainly evaluated cMEM using either MEG data or standard EEG montage (56 or 64 electrodes) but not high-density

EEG. Since our overall objective is to consider cMEM-based ESI during an hdEEG-fMRI analysis, we first had to further investigate the spatial resolution of cMEM, and compare it to well-known standard ESI methods: MNE and its noise-normalized variants, dSPM and sLORETA. For this study, we were inspired by the studies from other researchers, especially Molins et al. (2008), to compare the intrinsic spatial resolution of all these source imaging techniques using the analysis of their resolution matrices, as introduced in Chapter 2. We were then able to assess the spatial resolution of these four techniques in ideal conditions, i.e. in the absence of noise, and assuming no errors in the forward solution before comparing the different methods during an electrical median nerve stimulation paradigm.

This study is our first study carefully assessing the behavior of cMEM in presence of focal sources, as opposed to spatially extended generators of IEDs, while providing a detailed comparison of source localization performance of MEG and hdEEG data.

This manuscript was published as: **T. Hedrich, G. Pellegrino, E. Kobayashi, J. M. Lina, and C. Grova. Comparison of the spatial resolution of source imaging techniques in high-density EEG and MEG. *NeuroImage*, 157:531–544, 2017**.

Abstract

Background: The present study aims at evaluating and comparing electrical and magnetic distributed source imaging methods applied to high-density Electroencephalography (hdEEG) and Magnetoencephalography (MEG) data. We used resolution matrices to characterize spatial resolution properties of Minimum Norm Estimate (MNE), dynamic Statistical Parametric Mapping (dSPM), standardized Low-Resolution Electromagnetic Tomography (sLORETA) and coherent Maximum Entropy on the Mean (cMEM, an entropy-based technique). The resolution matrix provides information of the Point Spread Functions (PSF) and of the Crosstalk functions (CT), this latter being also called source leakage, as it reflects the influence of a source on its neighbors.

Methods: The spatial resolution of the inverse operators was first evaluated theoretically and then with real data acquired using electrical median nerve stimulation on five healthy participants. We evaluated the Dipole Localization Error (DLE) and the Spatial Dispersion (SD) of each PSF and CT map.

Results: cMEM showed the smallest spatial spread (SD) for both PSF and CT maps, whereas localization errors (DLE) were similar for all methods. Whereas cMEM SD values were lower in MEG compared to hdEEG, the other methods slightly favored hdEEG over MEG. In real data, cMEM provided similar localization error and significantly less spatial spread than other methods for both MEG and hdEEG. Whereas both MEG and hdEEG

provided very accurate localizations, all the source imaging methods actually performed better in MEG compared to hdEEG according to all evaluation metrics, probably due to the higher signal-to-noise ratio of the data in MEG.

Conclusion: Our overall results show that all investigated methods provide similar localization errors, suggesting very accurate localization for both MEG and hdEEG when similar number of sensors are considered for both modalities. Intrinsic properties of source imaging methods as well as their behavior for well-controlled tasks, suggest an overall better performance of cMEM in regards to spatial resolution and spatial leakage for both hdEEG and MEG. This indicates that cMEM would be a good candidate for studying source localization of focal and extended generators as well as functional connectivity studies.

5.1 Introduction

High-density Electroencephalography (hdEEG), defined here as EEG with 256 electrodes, and Magnetoencephalography (MEG) are two complementary and non-invasive neurophysiology modalities used to depict electromagnetic brain activity (Ebersole and Ebersole, 2010; Ahlfors et al., 2011). Electrical and magnetic source imaging consist in solving a so-called inverse problem, localizing the generators of scalp EEG or MEG signals into the brain (Darvas et al., 2004).

The inverse problem is ill-posed by nature and a unique solution can only be found if specific constraints are added for regularization (Baillet et al., 2009). Multiple inverse solution approaches are nowadays available, including equivalent current dipole fitting, dipole scanning approaches and distributed source models (see Wendel et al., 2009; Klamer et al., 2014).

The spatial accuracy of source imaging techniques is influenced by several factors, including the choice of modality (Pittau et al., 2014), the number of sensors (Sohrabpour et al., 2014), the orientation of the generator (Ahlfors et al., 2010), the conductivity of the biological tissues (Aydin et al., 2014) and the source imaging technique used to solve the inverse problem (Hauk et al., 2011).

The objective of this study was to compare the intrinsic spatial resolutions of different source imaging techniques applied to hdEEG and MEG signals, when considering these two modalities with approximately the same number of sensors. We analyzed the resolution matrix, whose application in the neuroimaging field was originally proposed by Grave de Peralta Menendez (Grave De Peralta Menendez et al., 1997), to characterize the spatial properties of a linear inverse operator. The spatial resolution matrix is a square matrix, whose size is the number of dipolar sources, providing the following two features (Schoffelen and Gross, 2009):

1. The columns of the resolution matrix quantify the Point Spread Functions (PSF) of every dipolar source of the source space. Each PSF is assessing the solution of the source imaging method for the activation a single cortical dipole, when considering noise-free data. Analyzing the localization error and the spatial extent of the PSF provides information about the intrinsic spatial property of a source imaging technique.

2. The rows of the resolution matrix represent the crosstalk functions (CT) which reflect the influence a single dipolar source may have on the estimation of the generators in its neighborhood. Hence, the spatial extent of the CT informs on the amount of "source leakage" and the potential bias in the estimation of functional connectivity patterns leading to spurious local coherence (Schoffelen and Gross, 2009).

An ideal resolution matrix should be the identity matrix. In practice, any source estimate is subject to blurring (if large amplitude values are found in off-diagonal terms in the matrix) and mislocation (if off-diagonal values were higher amplitude than diagonal values).

Once PSF and CT maps are constructed for each dipolar source, one can assess their spatial properties through evaluation metrics such as Dipole Localization Error (DLE) and Spatial Dispersion (SD) (Liu et al., 2002; Molins et al., 2008). DLE measures the Euclidean distance between the maximum of the PSF or CT maps and the true source location, whereas SD quantifies the spatial spread around the true source location.

Beyond the theoretical analysis of the resolution matrix, a validation of the comparison between the intrinsic spatial resolution can be achieved by studying real data acquired under well-controlled paradigms, for which the location of generator is known a priori. To that motive, we measures somatosensory evoked responses measured after electrical stimulation of the median nerve. This paradigm is known to generate evoked response exhibiting the activation of the contralateral primary sensory hand region (Balzamo et al., 2004). In this context, for which the generator is located in a predefined focal brain region, properties of source imaging techniques and comparison between them could also be evaluated using DLE and SD metrics, as proposed by Molins et al. (2008).

We chose to evaluate and compare four distributed sources localization methods. Three of them are well-known linear operators: Minimum Norm Estimate (MNE) (Hämäläinen and Ilmoniemi, 1994), dynamic Statistical Parametric Mapping (dSPM) (Dale and Sereno, 1993) and standardized Low-Resolution Electromagnetic Tomography (sLORETA) (Pascual-Marqui, 2002). The fourth one is the coherent Maximum Entropy on the Mean (cMEM) (Amblard et al., 2004; Grova et al., 2006a), which is a novel non-linear method specifically evaluated for its sensitivity to recover the spatial extent of the underlying cortical generators (Chowdhury et al., 2013; Heers et al., 2015; Grova et al., 2016). Whereas the calculation

of the resolution matrix is straightforward for the linear methods (MNE, sLORETA and dSPM), specific estimation of the resolution matrix for the non-linear method cMEM was performed with the iterative reconstruction of the PSF of every dipolar source.

We proposed a systematic and quantitative assessment of these source imaging techniques based on two strategies: (i) theoretical analysis of the resolution matrix; (ii) study of the source estimated from hdEEG and MEG responses evoked by electrical median nerve stimulation, in the primary somatosensory cortex.

5.2 Material and Methods

5.2.1 Subjects selection

Five right-handed healthy subjects (3 males, mean age ± standard deviation = 26.6 ± 3.21) were selected for this study. The study was approved by the Research Ethics Board of the Montreal Neurological Institute and Hospital and a written informed consent was signed by all participants prior to the procedures.

5.2.2 Electrical Median Nerve Stimulation

Electrical Median Nerve Stimulation (MNS) was performed using a Digitimer system (Digitimer DS7A, Letchworth Garden City, U.K). 600 stimuli were delivered to the left and right median nerves using electrodes placed on the wrist. A 12-minute run was acquired for each stimulation side, using two different modalities, i.e. hdEEG and MEG. The stimulus duration was set to 0.2 ms, the inter stimulus interval was set to 500 ms, with an additional jitter between 0 ms and 500 ms. The stimulation intensity was set just above the motor threshold to cause a small thumb movement. During the whole recording, participants were instructed to focus on a fixation cross in the middle of a black screen.

5.2.3 MEG data acquisition

MEG data were acquired on a 275-gradiometer CTF system (VSM MedTech Systems Inc., Coquitlam, BC, Canada) in a magnetic shielded room at the McConnell Brain Imaging Centre of The Montreal Neurological Institute (McGill University, Montreal, Canada). Electrocardiogram (ECG) and electrooculogram (EOG) were acquired to record potential sources of artifacts contaminating MEG signals. The sampling rate was set to 1200 Hz. Continuous head localization was obtained using three localization coils attached to the nasion and left and right peri-auricular points on each subject. The exact position of the localization coils,

as well as the shape of the head of the subject, were digitized with a 3D Polhemus localizer for subsequent coregistration with the anatomical MRI.

5.2.4 hdEEG data acquisition

hdEEG was recorded using a 256-electrode EGI system (Electrical Geodesics Inc., Eugene, Oregon) with a sampling rate of 1000 Hz. ECG was also recorded using additional electrodes. For safety reasons Since the EEG system we used for this study was actually an MRI-compatible EEG device, each electrode was equipped with an additional 10 $k\Omega$ resistance. Good data quality was achieved by maintaining the EEG impedances below 70 $k\Omega$.

The EEG sensor positions were estimated using the Geodesic Photogrammetry System (GPS, geodesic inc., Eugene, OR). The system consists in 11 cameras mounted in a geodesic structure. The electrodes were then manually labeled on the 11 pictures, and the coordinates were calculated using a triangulation algorithm (Russell et al., 2005).

5.2.5 Anatomical MRI

A high resolution T1-weighted MRI (MPRAGE 1 mm isotropic 3D acquisition, 192 sagittal slices, 256×256 matrix, TE = 9.2 ms, TR = 22 ms, flip angle 30 degrees) was acquired at the McConnell Brain Imaging Centre Siemens Tim Trio 3T scanner. MRI brain segmentation and white/gray matter interface reconstruction were performed using BrainVISA software (http://www.brainvisa.info) (Mangin et al., 1995).

5.2.6 Determination of the primary somatosensory region

Source localization was performed at the peak of the N20 component of the somatosensory evoked response (Balzamo et al., 2004; Molins et al., 2008). Invasive EEG investigations have shown that the generator of the N20 wave is localized in the primary somatosensory region and more precisely in the primary sensory hand region, denoted in this paper as $S1_{HAND}$, located in the postcentral sulcus facing the hand knob region (Maldjian et al., 1999; Eickhoff et al., 2008; Yousry et al., 1997; Rumeau et al., 1994). For evaluation purposes, an expert neurologist (GP) marked on the cortical mesh of each subject the location of $S1_{HAND}$ relying on these anatomical landmarks before any data analysis.

5.2.7 hdEEG and MEG data preprocessing

hdEEG and MEG processing was performed using Brainstorm software (Tadel et al., 2011). Epochs lasting 350 ms (from -100 ms to 250 ms, 0 being the time of the stimulus) were

imported.

Preprocessing included 0.3-300 Hz band-pass filter, 60 Hz and 120 Hz notch filter, DC correction (baseline window from -100 ms to -10 ms) and noisy channels removal. For MEG, the third-order software gradient compensation was also applied. The hdEEG electrodes located on the face and on the neck (76 channels) were excluded for further analysis for each subject before re-referencing all the remaining electrodes to an average reference.

ECG and eye movement artifacts were removed from hdEEG and MEG using Signal Space Projection (SSP) method (Uusitalo and Ilmoniemi, 1997).

5.2.8 Forward model estimation

The coregistration of the hdEEG or MEG sensor positions with the MRI images was performed by fitting the fiducial landmarks and hundreds additional points covering the shape of the head of the subject into the space of the MRI using a rigid geometrical transformation (3 rotations, 3 translations). The source space consisted in a mesh of the cortical surface segmented from the white-gray matter interface, subsampled to around 8000 vertices. The distributed source model consisted in placing dipolar sources on every vertex of the mesh oriented perpendicularly to the cortical surface.

The forward model assessing the contribution of every dipolar source to MEG or hdEEG sensors was computed using the Boundary Element Method (BEM) proposed by Kybic et al. (2006). For hdEEG, the gain matrix was calculated with a 3-layer BEM model consisting in the inner skull, outer skull and scalp surface (respective conductivity: 0.33 S/m, 0.0165 S/m, 0.33 S/m). For MEG, we chose a 1-layer BEM model (inner skull; conductivity: 0.33 S/m). To do so, we used the OpenMEEG implementation (Gramfort et al., 2010) in Brainstorm.

5.2.9 Estimation of the sensor-level noise covariance matrix

A 2-second artifact-free segment of resting-state data was used for noise estimation, i.e. the computation of sensor-level noise covariance matrix (full matrix) $\mathbf{\Sigma_e}$ for MNE, dSPM and sLORETA and baseline data for cMEM. We verified that the choice of this 2-second segment background activity to model the noise covariance matrix had little influence as long as the segment did not contain artifacts. To do so, resolution matrix results were reproduced three times, using three different segments of background activity, showing overall very similar results (data not shown).

5.2.10 Source imaging methods

We assumed the source space to be defined as a set of evenly distributed dipolar sources located on the gray-white matter interface which are normally oriented to the surface. The measurement for each time sample can then be represented as a vector $\mathbf{m}$, which is given by:

$$\mathbf{m} = \mathbf{G}\mathbf{j} + \mathbf{e} \tag{5.1}$$

where $\mathbf{m}$ is the measurement vector of dimension number of sensors n_s. $\mathbf{G}$ is the gain matrix of dimension number of sensors n_s by number of dipolar sources n_d, providing the solution of the forward model. $\mathbf{j}$ (dimension $n_d \times 1$) is the current density of each dipole source and $\mathbf{e}$ (dimension $n_s \times 1$) is the measurement noise.

5.2.10.1 Minimum norm estimate (MNE)

The general solution of the minimum norm estimate can be written as follows:

$$\hat{\mathbf{j}}_{\text{MNE}} = \mathbf{W}\mathbf{m} \tag{5.2}$$

where $\mathbf{W} = \mathbf{G}^T \left(\mathbf{G}\mathbf{G}^T + \lambda \mathbf{\Sigma_e}\right)^{-1}$ is the resolution kernel and λ is a regularization hyper-parameter. Several methods have been proposed to estimate λ: either using the estimate signal-to-noise ratio (SNR) of the data, the L-curve approach (Hansen, 1992; Gorodnitsky et al., 1995) or restricted maximum likelihood estimate within a Bayesian framework (Friston et al., 2008). In our study, we fixed $\lambda = 1/\text{SNR}^2$, with the SNR arbitrary set to 3 (Brainstorm default value). By varying this value from 1 to 5, we observed that this value had very little impact on the estimation of the resolution matrices and its properties (data not shown). $\mathbf{\Sigma_e}$ is the noise covariance.

5.2.10.2 dynamic Statistical Parametric Mapping (dSPM) and standardized Low-Resolution Brain Electromagnetic Tomography (sLORETA)

dSPM is a method aiming at providing a statistical parametric map based on MNE results (Dale et al., 2000). It consists in a noise-normalized version of MNE and can be written with the MNE solution $\hat{\mathbf{j}}_{\text{MNE}}$ as follows:

$$\mathbf{t}_{\text{dSPM}}(i) = \frac{\hat{\mathbf{j}}_{\text{MNE}}(i)}{\mathbf{W}_i(\lambda \mathbf{\Sigma_e})\mathbf{W}_i^T} \tag{5.3}$$

where $\hat{\mathbf{j}}_{\text{MNE}}(i)$ is the ith element of $\hat{\mathbf{j}}_{\text{MNE}}$ and $\mathbf{W}_i$ denotes the ith row of the resolution kernel $\mathbf{W}$ (Dale et al., 2000).

sLORETA, proposed by Pascual-Marqui (Pascual-Marqui, 2002) consists in another normalized version of MNE solution:

$$\mathbf{t}_{\text{sLORETA}}(i) = \frac{\hat{\mathbf{j}}_{\text{MNE}}(i)}{\mathbf{W}_i \left(\mathbf{G}\mathbf{G}^T + \lambda \boldsymbol{\Sigma}_{\mathbf{e}}\right) \mathbf{W}_i^T} \tag{5.4}$$

5.2.10.3 coherent Maximum Entropy on the Mean (cMEM)

We proposed a probabilistic source imaging technique within the MEM framework (Amblard et al., 2004). MEM-based source localization procedure consists in two steps: (i) initialization of a reference distribution summarizing our prior knowledge; (ii) an entropy-based regularization framework allowing to identify a solution explaining the data "on average", by estimating a distribution as close as possible to the reference distribution, according to Kullback-Leibler divergence. In the present implementation, cMEM reference model assumes brain activity to be described by K cortical parcels covering the whole cortical surface, while each parcel is associated to an hidden state variable controlling whether the parcel is active or not. During the regularization step, cMEM is able to switch off the parcels that do not contribute to the solution, while preserving the ability to create a contrast of current intensities within the active parcels. We demonstrated that the use of such parcellation model was the key feature to provide a method sensitive to the spatial extent of the sources (Chowdhury et al., 2013). cMEM also imposes a local spatial smoothness constraint within each parcel. The implementation of cMEM used in this study is available in brainstorm software (we used the default parameters for this study) and a tutorial describing its use has been created: http://neuroimage.usc.edu/brainstorm/Tutorials/TutBEst.

MNE, dSPM and sLORETA were computed in brainstorm using the following settings: constrained orientation of the dipolar sources normal to the cortical surface, no prewhitening using Principal Component Analysis, SNR set to 3 to tune the regularization hyperparameter, regularization of the noise covariance using a value of 0.1, no depth weighting.

5.2.11 Estimation of the resolution matrix

An analytic solution of the resolution matrix for MNE could be obtained by combining Equations (5.1) and (5.2):

$$\hat{\mathbf{j}}_{\text{MNE}} = \mathbf{W}(\mathbf{G}\mathbf{j} + \mathbf{e}) = \mathbf{R}_{\text{MNE}}\mathbf{j} + \mathbf{N} \tag{5.5}$$

where $\mathbf{R}_{\text{MNE}}$ is the resolution matrix of MNE. It characterizes the relation between the source estimate and the actual source distribution. $\mathbf{N}$ is the matrix showing the effect of the source imaging technique on the noise. Therefore, the resolution matrix for MNE is given by:

$$\mathbf{R}_{\text{MNE}} = \mathbf{WG} \tag{5.6}$$

Similarly, analytical expression of the resolution matrix can be found for dSPM and sLORETA, as follows:

$$\mathbf{R}_{\text{dSPM}}(i,j) = \mathbf{R}_{\text{MNE}}(i,j)/\mathbf{S}_{\text{dSPM}}(i,i) \tag{5.7}$$

$$\mathbf{R}_{\text{sLORETA}}(i,j) = \mathbf{R}_{\text{MNE}}(i,j)/\mathbf{S}_{\text{sLORETA}}(i,i) \tag{5.8}$$

where $\mathbf{R}_{\text{dSPM}}(i,j)$ is the element of the ith row and jth column of $\mathbf{R}_{\text{dSPM}}$, $\mathbf{S}_{\text{dSPM}} = \mathbf{W}(\lambda\mathbf{\Sigma_e})\mathbf{W}^T$ and $\mathbf{S}_{\text{sLORETA}} = \mathbf{W}\left(\mathbf{GG}^T + \lambda\mathbf{\Sigma_e}\right)\mathbf{W}^T$.

No analytical formulation of the resolution matrix can be derived for non-linear source imaging techniques such as cMEM. However, one could still provide an estimation of the resolution matrix, by applying iteratively cMEM algorithm on noise-free simulations of single dipolar sources. We could then construct the resolution matrix column by column, by computing the source localization of a simulation including a single activated dipolar source, for each source in the cortical surface.

Indeed, assuming the definition of cMEM resolution matrix to be $\hat{\mathbf{j}}_{\text{cMEM}} = \mathbf{R}_{\text{cMEM}}\mathbf{j}$, then for each $\mathbf{j} = \boldsymbol{\delta}_i$, where $\boldsymbol{\delta}_i$ is a vector with 1 in the ith element and 0 otherwise, $\mathbf{R}_{\text{cMEM}}\boldsymbol{\delta}_i$ provides an estimate of the ith column of $\mathbf{R}_{\text{cMEM}}$:

$$\hat{\mathbf{j}}_{\text{cMEM}}(i) = \mathbf{R}_{\text{cMEM}}\boldsymbol{\delta}_i = \mathbf{R}_{\text{cMEM},i} \tag{5.9}$$

where $\mathbf{R}_{\text{cMEM},i}$ is the ith column of $\mathbf{R}_{\text{cMEM}}$.

5.2.12 Analysis of the intrinsic properties of the resolution matrix

One can easily notice that $\mathbf{R}_{\text{MNE}}$ is symmetrical, meaning that the PSF and CT are equivalent for this source imaging technique. On the contrary, neither $\mathbf{R}_{\text{dSPM}}$ or $\mathbf{R}_{\text{sLORETA}}$ are symmetrical. However, the noise-normalization of MNE methods introduced for both dSPM and sLORETA only impact the PSF maps of the resolution matrix. Therefore, the spatial properties of CT maps for dSPM and sLORETA (i.e. the rows of the corresponding resolution matrices) are identical to those for MNE since they are only multiplied by a scaling factor.

Plus, one can notice from Equation (5.7) that:

$$\mathbf{S}_{\text{sLORETA}} = \mathbf{W}\left(\mathbf{G}\mathbf{G}^T + \lambda\boldsymbol{\Sigma}_\mathbf{e}\right)\mathbf{W}^T = \mathbf{G}^T\left(\mathbf{G}\mathbf{G}^T + \lambda\boldsymbol{\Sigma}_\mathbf{e}\right)^{-1}\mathbf{G} = \mathbf{R}_{\text{MNE}} \tag{5.10}$$

Therefore, $\mathbf{R}_{\text{sLORETA}}(i,j) = \mathbf{R}_{\text{MNE}}(i,j)/\mathbf{R}_{\text{MNE}}(i,i)$, meaning that the maximum value for each column of $\mathbf{R}_{\text{sLORETA}}$ is always found on the diagonal, allowing zero localization error for sLORETA (Pascual-Marqui, 2002).

5.2.13 Reconstruction of a spatially extended generator using the resolution matrix

Based on the resolution matrix, it is possible to compare the source reconstruction of different imaging techniques for an extended source in ideal conditions, i.e. when no noise, no error in the forward model or no channel co-registration error could corrupt the data. We performed the reconstruction of a 11 cm^2 cortical generator, located on the right middle frontal gyrus, by using the sum of the PSF of all the dipolar sources corresponding to the region of interest in MNE, dSPM, sLORETA and cMEM. In addition, another cMEM reconstruction was also done by applying source localization on the extended source as a whole. For linear techniques, sum of the PSF or reconstruction of the whole extended source provide identical results. Since cMEM is a non-linear technique, we were interested in assessing the differences between the two approaches.

All the source reconstructed maps were individually normalized so that their values ranged between 0 and 1. Validation metrics were calculated for the source reconstructions, the simulated source being the ground truth.

5.2.14 Reconstruction of source of different spacial extents

To assess the ability for the source imaging technique to reconstruct spatially extended sources, we extended our evaluation of the resolution matrix, when considering spatially extended generators instead of single dipolar sources. To do so, we first constructed two sets of non-overlapping parcels covering the whole cortical surface: small parcels (300 parcels, average parcel surface: 3.75 cm^2) or large parcels (50 parcels, average parcel surface: 30 cm^2). For each set of spatially extended generators, noise-free hdEEG and MEG data corresponding to generators in each parcel were constructed. These noise free data were localized using the four proposed methods (cMEM, MNE, dSPM and sLORETA) before assessing the performance of each method using DLE and SD metrics, the corresponding simulated parcel being considered as ground truth.

5.2.15 Validation metrics considered for quantitative analysis

5.2.15.1 Resolution matrix analysis

The resolution matrix analysis was performed in MEG and hdEEG considering the sensor configuration and the geometry of one of the five subjects (cortical surface, sensor registration, sensor noise covariance matrix). The metrics of Dipole Localization Error and Spatial Dispersion (Hauk et al., 2011; Molins et al., 2008) were applied to each PSF and CT map:

- Dipole Localization Error (DLE) was estimated as the Euclidean distance between the maximum of every PSF or CT map and the position of the true activated generator. In ideal conditions, a DLE of zero indicates that the maximum amplitude of the source reconstructed map was indeed located on the activated generator.

- The Spatial Dispersion (SD) was estimated for each dipole as follows, for each PSF and CT map:

$$\mathrm{SD}_{\mathrm{PSF}}(i) = \sqrt{\frac{\sum_{j=1}^{n_d} d_{ij}^2 \mathbf{R}_{ij}^2}{\sum_{j=1}^{n_d} \mathbf{R}_{ij}^2}} \tag{5.11}$$

$$\mathrm{SD}_{\mathrm{CT}}(j) = \sqrt{\frac{\sum_{i=1}^{n_d} d_{ij}^2 \mathbf{R}_{ij}^2}{\sum_{i=1}^{n_d} \mathbf{R}_{ij}^2}} \tag{5.12}$$

  with d_{ij} the Euclidean distance between dipolar sources i and j. Notice that the difference between Equation (5.11) and Equation (5.12) is that for $\mathrm{SD}_{\mathrm{PSF}}$, we apply a summation over the columns of $\mathbf{R}$, whereas for $\mathrm{SD}_{\mathrm{CT}}$, we apply a summation over its rows.

  This metric was proposed to characterize the spatial spread of a source imaging method. SD values reflect either a mislocation of the point spread function to the actual source or large overestimation of the spatial extent around the generator (Molins et al., 2008).

  $\mathrm{DLE}_{\mathrm{PSF}}$, $\mathrm{SD}_{\mathrm{PSF}}$ for all the source imaging techniques and $\mathrm{DLE}_{\mathrm{CT}}$ and $\mathrm{SD}_{\mathrm{CT}}$ for cMEM were calculated in all the $n_d = 8003$ dipolar sources distributed along the cortical surface.

5.2.15.2 Evaluation of source localization of somatosensory evoked responses

In the context of median nerve stimulation data, we considered the manually labeled region of interest $\mathrm{S1}_{\mathrm{HAND}}$ as the ground truth to evaluate the localization of the N20 using DLE and SD metrics for all source imaging methods. DLE was defined as the minimum distance between the maximum of source reconstruction and the closest boundary of $\mathrm{S1}_{\mathrm{HAND}}$.

SD was calculated as follows:

$$\mathrm{SD} = \sqrt{\frac{\sum_{i=1}^{n_d} d_{i,\mathrm{S1}}^2 \hat{\mathbf{j}}_i^2(t_{20})}{\sum_{i=1}^{n_d} \hat{\mathbf{j}}_i^2(t_{20})}} \tag{5.13}$$

where $d_{i,\mathrm{S1}}$ is closest Euclidean distance between the dipole i and $\mathrm{S1_{HAND}}$ region border and $\hat{\mathbf{j}}_i^2(t_{20})$ is the energy of the ith dipole of the source reconstruction at the time of the N20 peak. For each participants, the N20 peak was estimated using the local maximum in the global field power around 20 ms.

DLE and SD results may be largely affected by spurious activity located far from the primary sensory region. To avoid taking into account potential source imaging instabilities involving distant and medial structures, activity arising from remote regions were therefore not taken into account for the calculation of these metrics, focusing on the ability of the methods to localize $\mathrm{S1_{HAND}}$ region only at the time of the N20. Dipoles whose shortest paths to S1 along the mesh were larger than 6 vertices along the cortical surface (corresponding approximately to a geodesic distance of about 75 mm) were discarded for DLE and SD. Figure 5.1 shows an example of $\mathrm{S1_{HAND}}$ region of interest and its surrounding area considered to estimate DLE and SD metrics. The set of all distant dipoles, i.e. all the dipolar sources which do not belong to $\mathrm{S1_{HAND}}$ or its surrounding, was defined as Θ.

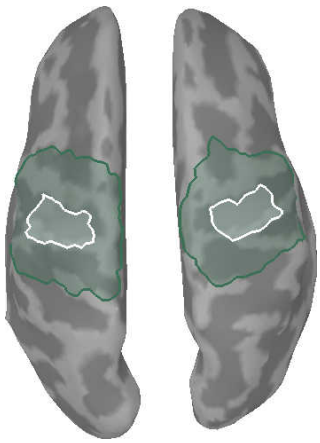

Figure 5.1: Example of the detection of the primary sensory hand region $\mathrm{S1_{HAND}}$ (in white) and the surrounding region (in green) displayed on the inflated cortical surface of one subject. The white region was marked by an expert neurologist. The green region was constructed by taking all vertices belonging to the 6th order neighbors of any vertex in $\mathrm{S1_{HAND}}$. For MNS data, DLE and SD metrics were calculated within the green region only. RSA is defined as the ratio between the energy of the source reconstruction outside the green region and the total energy on the cortex.

To measure the Ratio of distant Spurious Activity (RSA), we measured the ratio between the energy localized for distant sources over the total energy:

$$\text{RSA} = \frac{\sum_{\theta \in \Theta} \hat{\mathbf{j}}^2_\theta(t_{20})}{\sum_{i=1}^{n_d} \hat{\mathbf{j}}^2_i(t_{20})} \tag{5.14}$$

5.2.15.3 Statistical analysis

Using a Kolmogorov-Smirnov test, we observed that the distribution of all metric values did not follow a Gaussian distribution. Therefore, for hdEEG and MEG separately, we computed a Kruskal-Wallis ANOVA test on the inverse operators to assess the effect of the source imaging method on DLE or SD distributions. Comparisons between modalities (hdEEG and MEG) and one-on-one comparisons between inverse operators were performed using a non-parametric Wilcoxon signed rank test. Level of significance was set to $p < 0.05/6 = 0.0083$, in order to take into account multiple comparison through the analysis of four source imaging methods (i.e. 6 comparisons tested) using Bonferroni method.

5.3 Results

5.3.1 Quantitative analysis of the resolution matrices

5.3.1.1 Analysis of DLE and SD distributions

For each source localization technique and each modality, the distributions of DLE and SD metrics over all dipolar sources along the cortical surface are presented in Figure 5.2, using boxplot representations. As expected (see Section 5.2.12), all metrics values for MNE PSF and MNE CT were identical. Similarly, all metrics values for MNE CT, dSPM CT, and sLORETA CT were the same. Moreover DLE values for sLORETA PSF were correctly found to be zero.

The Kruskal-Wallis ANOVA test indicated a significant effect of the source imaging technique for DLE and SD metrics in both hdEEG and MEG ($p < 0.001$).

The difference of median distributions between source imaging techniques and their pairwise comparison tests were presented for PSF in Table 5.1.

In MEG for DLE values, no significant difference was found between cMEM PSF and MNE PSF (Wilcoxon signed rank test, $p = 0.80$), whereas both these methods showed a significantly lower median value than dSPM PSF (5.47 mm and 5.69 mm respectively, Wilcoxon signed rank test, $p < 0.001$).

In hdEEG for DLE values, all pairwise comparisons were found statistically significant (Wilcoxon signed rank test, $p < 0.0083$). However, for each comparison, the effect size was actually very small (median difference being less than 1 mm), except for sLORETA.

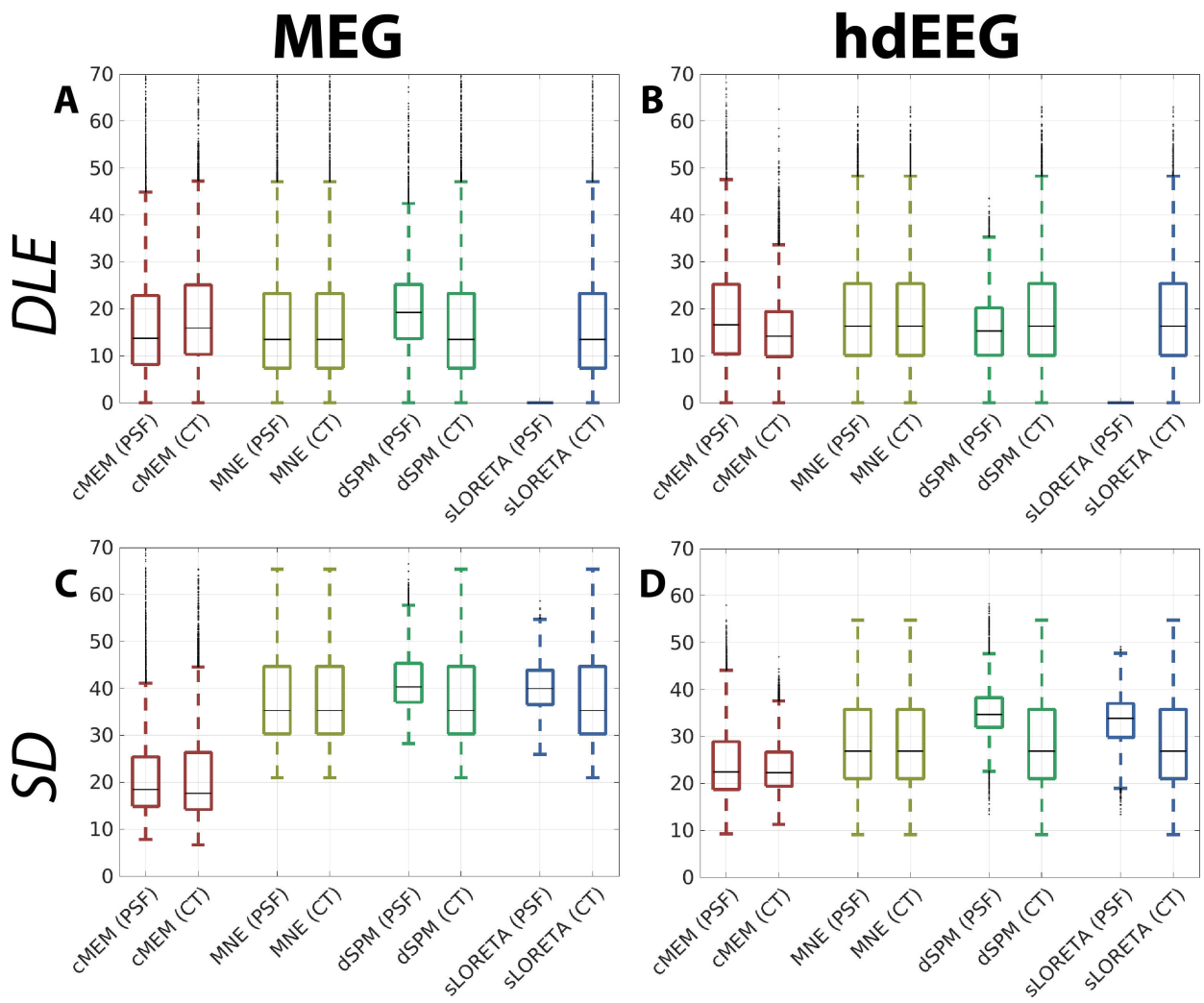

Figure 5.2: Statistical distribution of the evaluation metrics for DLE in MEG (A) and hdEEG (B), and SD in MEG (C), and hdEEG (D) for cMEM, MNE, dSPM and sLORETA using boxplot representations. All values are in mm.

In MEG for SD values, we found that the cMEM PSF median was significantly lower than all the other techniques (differences of medians: 16.82 mm, 21.85 mm and 21.50 mm for MNE, dSPM and sLORETA respectively, Wilcoxon signed rank test, $p < 0.001$).

Similarly in hdEEG for SD values, we found that cMEM PSF median was significantly lower than all the other techniques (differences of medians: 4.53 mm, 12.41 mm and 11.52 mm for MNE, dSPM and sLORETA respectively, Wilcoxon signed rank test, $p < 0.001$).

The comparisons of CT maps were displayed in Table 5.2. The difference between cMEM DLE CT and the other techniques in MEG, although significant (Wilcoxon signed rank test, $p < 0.001$), was found to have a negligeable effect size (median difference being less than 1 mm). We observed that the DLE CT values in hdEEG were significantly lower in cMEM

Table 5.1: Difference between distribution medians of source imaging techniques for DLE and SD in PSF maps. Each cell shows the difference between the distribution median of the source imaging technique in the column against the distribution median of the source imaging technique in the corresponding row. As an example, the second cell of the first row indicates that the median of DLE PSF of dSPM in MEG was 5.47 mm higher than the median of DLE PSF of cMEM. *n.s.*: not significant. * : $p < 0.0083$. **: $p < 0.001$. The effect size of the median distribution differences is color coded as follows: red: difference of median higher than 10 mm. Light red: median difference between 1 mm and 10 mm. Light gray: median difference between -1 mm and 1 mm. Light blue: median difference between -10 mm and -1 mm. Blue: median difference below -10 mm.

		MNE	dSPM	sLORETA
MEG DLE PSF	cMEM	*n.s.*	5.47 **	-13.74 **
	MNE		5.69 **	-13.52 **
	dSPM			-19.21 **
hdEEG DLE PSF	cMEM	-0.3580 *	-0.87 **	-16.65 **
	MNE		-0.51 **	-16.30 **
	dSPM			-15.78 **
MEG SD PSF	cMEM	16.82 **	21.85 **	21.50 **
	MNE		5.03 **	4.68 **
	dSPM			-0.35 **
hdEEG SD PSF	cMEM	4.53 **	12.41 **	11.52 **
	MNE		7.88 **	6.99 **
	dSPM			-0.89 **

Table 5.2: Difference between the distribution medians of linear source imaging techniques against cMEM for DLE and SD on CT maps. As an example, the first cell of the first row indicates that the median of DLE CT of cMEM in MEG was 0.43 mm lower than the median of the other techniques. *n.s.*: not significant. * : $p < 0.0083$. **: $p < 0.001$. The effect size of the median distribution differences is color coded as follows: red: difference of median higher than 10 mm. Light red: median difference between 1 mm and 10 mm. Light gray: median difference between -1 mm and 1 mm. Light blue: median difference between -10 mm and -1 mm. Blue: median difference below -10 mm.

		MNE & dSPM & sLORETA
MEG DLE CT	cMEM	-0.43 **
hdEEG DLE CT	cMEM	2.12 **
MEG SD CT	cMEM	16.13 **
hdEEG SD CT	cMEM	5.69 **

compared to the other techniques (difference of medians: 2.12 mm, Wilcoxon signed rank test, $p < 0.001$).

We found that SD CT values in MEG were significantly lower in cMEM compared to the other techniques (difference of medians: 16.13 mm, Wilcoxon signed rank test, $p < 0.001$). Similarly, we observed that the SD CT values in hdEEG were significantly lower in cMEM compared to the other techniques (difference of medians: 5.69 mm, Wilcoxon signed rank

Table 5.3: Difference between the distribution medians of hdEEG against MEG for DLE and SD. As an example, the first cell of the first row indicates that the median of DLE PSF of cMEM in hdEEG was 2.92 mm higher than the median of DLE PSF of cMEM in MEG. *n.s.*: not significant. * : $p < 0.0083$. **: $p < 0.001$. The effect size of the median distribution differences is color coded as follows: red: difference of median higher than 10 mm. Light red: median difference between 1 mm and 10 mm. Light gray: median difference between -1 mm and 1 mm. Light blue: median difference between -10 mm and -1 mm. Blue: median difference below -10 mm.

		hdEEG				
		cMEM	cMEM (CT)	MNE	dSPM	sLORETA
MEG	DLE	2.92 **	1.80 **	2.78 **	-3.43 **	*n.s.*
	SD	4.04 **	4.67 **	-8.25 **	-5.40 **	-5.95 **

test, $p < 0.001$).

The results for the comparison between hdEEG and MEG are displayed in Table 5.3. cMEM DLE (PSF and CT) as well as MNE DLE values were significantly lower in MEG when compared to hdEEG (difference of medians: 2.92 mm and 1.80 mm, for cMEM DLE PSF and cMEM DLE CT respectively, Wilcoxon signed rank, $p < 0.001$), whereas it was the other way around for dSPM DLE. For SD values, cMEM (PSF and CT) were significantly lower in MEG compared to hdEEG (difference of medians: 4.04 mm and 4.67 mm, for cMEM SD PSF and cMEM SD CT respectively, Wilcoxon signed rank, $p < 0.001$), whereas the opposite behavior was found for MNE, dSPM and sLORETA.

5.3.1.2 Spatial distribution of the metrics

To further characterize the spatial distribution of DLE_{PSF} and SD_{PSF}, we represented the results over the inflated cortical surface (only the left hemisphere is shown) for MEG (Figure 5.3) and in hdEEG (Figure 5.4).

The localization errors were smaller in DLE maps in cMEM and MNE for superficial sources when compared to deeper generators. In contrast, dSPM exhibited excellent DLE values for deeper generators, except for temporo-mesial sources.

A qualitative assessment of SD_{PSF} maps showed that lower SD values were located in more superficial sources for cMEM and MNE, whereas a more homogeneous spatial distribution was found for dSPM and sLORETA.

Overall, for most cortical regions, SD_{PSF} values were smaller for cMEM when compared to other methods, illustrating known intrinsic properties of cMEM to be sensitive to the spatial extent of the underlying generators. The other methods, in contrast, would overestimate such spatial extent.

Despite the statistical differences between DLE and SD when comparing hdEEG and

MEG (Section 5.3.1.1), the spatial distribution of these metrics for both modalities was actually very similar.

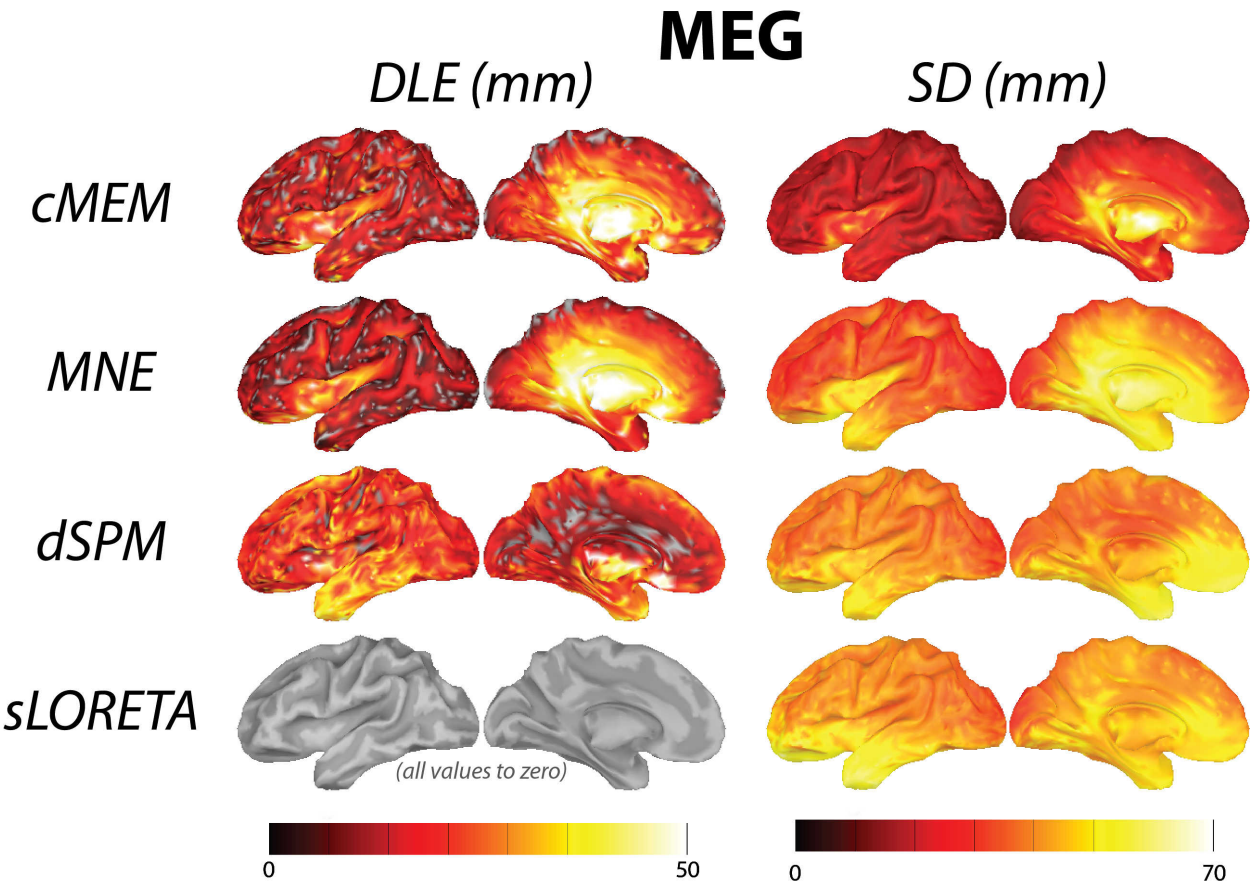

Figure 5.3: Spatial distribution of DLE_{PSF} and SD_{PSF} metrics in MEG. The figure shows the lateral and mesial aspect of the left hemisphere's cortical surface.

5.3.1.3 Illustration of the theoretical ability to recover a spatially extended generator

The reconstruction of the spatially extended source was illustrated in Figure 5.5. For all source imaging techniques, MEG and hdEEG reconstructions were very similar except that, as expected, MEG did not recover the radial aspects of the dipolar source belonging to this spatially extended patch.

DLE values were null for most source reconstructions, indicating that the maximum of the source amplitude was found within the simulated extended source. However, the maxima of the source reconstruction for dSPM in MEG and hdEEG were more than 20 mm away from the ground truth. The maxima were actually located in anterior cingulate region, illustrating the bias of dSPM towards deep structures.

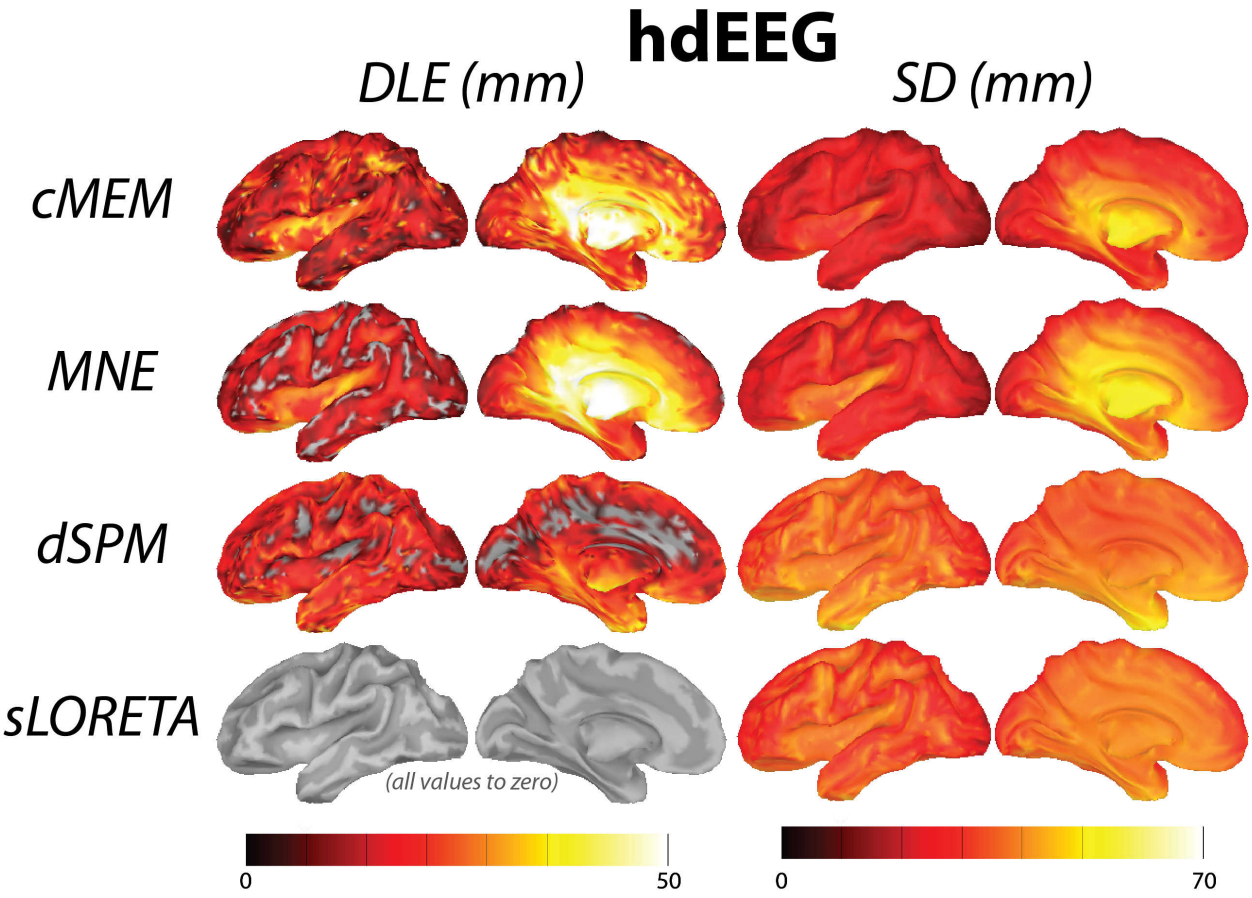

Figure 5.4: Spatial distribution of DLE_{PSF} and SD_{PSF} metrics in hdEEG. The figure shows the lateral and mesial aspect of the left hemisphere's cortical surface.

Among all the source imaging techniques, the lowest SD values were found for cMEM using the "*sum of PSF*" (7.30 mm for MEG, 5.25 mm for hdEEG) or "*source recons.*" map (5.92 mm for MEG, 3.80 mm for hdEEG). Despite the non-linearity nature of cMEM estimation, we overall noticed very little difference in the two approaches indicating that the source localization result of the whole generator is equivalent to the sum of the PSF for each dipolar source composing the generator.

In order to generalize our results on the resolution matrix analysis, Figure 5.6 is reporting performances of the four source imaging methods when considering noise-free simulation of spatially extended generators. Using two sets of parcels covering the whole cortical surface, either large (50 parcels) or small parcels (400 parcels), we assessed the performance of all source imaging techniques using DLE and SD metrics. Overall the results were in agreement with the ones presented in Figure 5.2 for single dipolar sources, i.e. similar DLE values for all methods and smaller SD values for cMEM (except perhaps for DLE metrics when applied to cMEM in MEG when considering small parcels). It is first worth noting than when

considering spatially extended sources, sLORETA is not providing zero-localization error anymore.

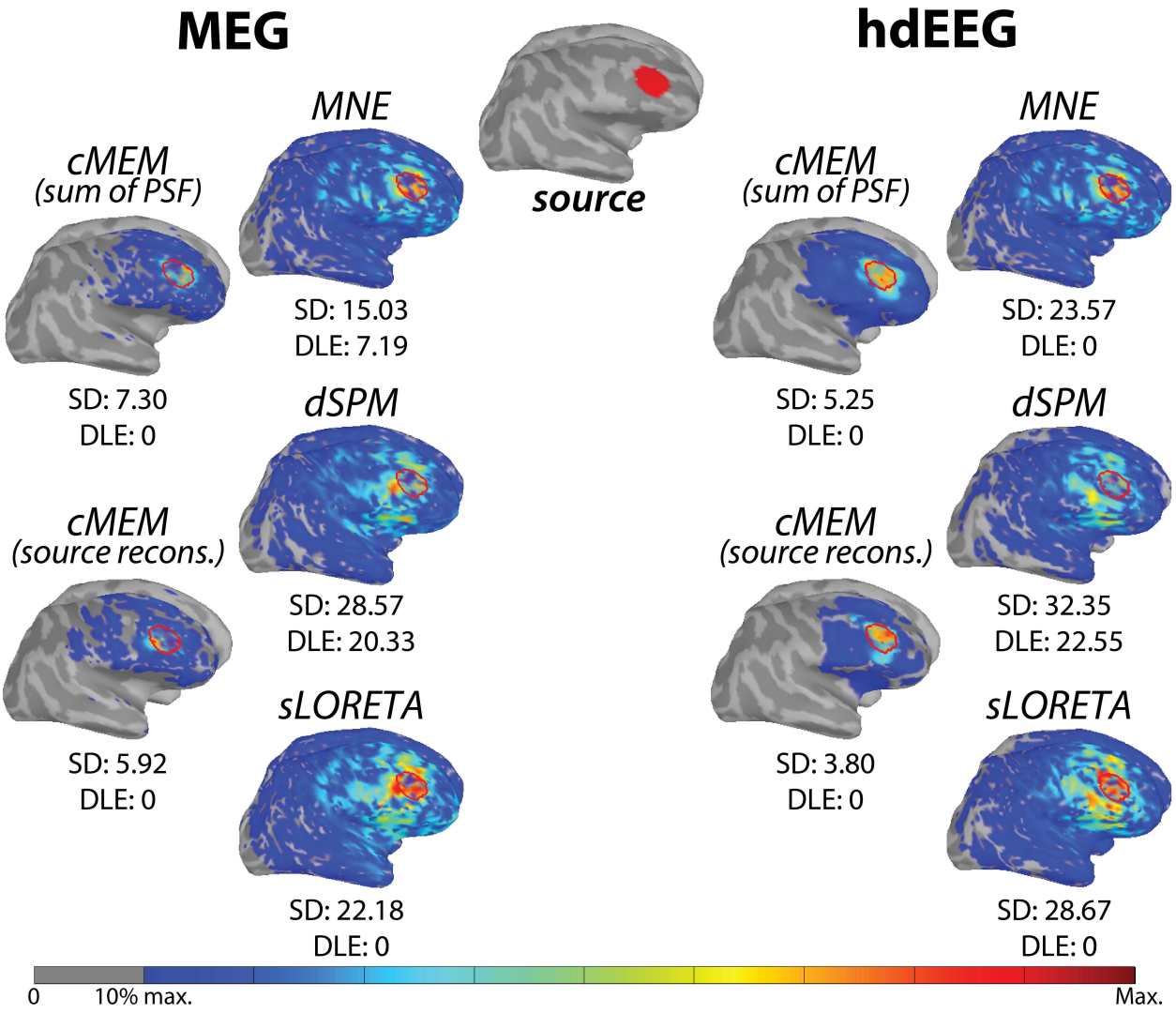

Figure 5.5: Summation of all point spread functions corresponding to the spatially extended red source (cf. the red line in all figures). The source is located in the frontal cortex and is composed by 63 dipolar sources (11 cm^2). Sources with amplitude below 10% of the maximum were displayed in grey. SD and DLE were calculated based on the simulated source, all units in mm.

5.3.2 Evaluation of source localization of somatosensory evoked responses

From 10 recorded runs of MEG and hdEEG, nine were analyzed: one MEG run corresponding to right MNS was contaminated by stimulation artifacts that could not be successfully

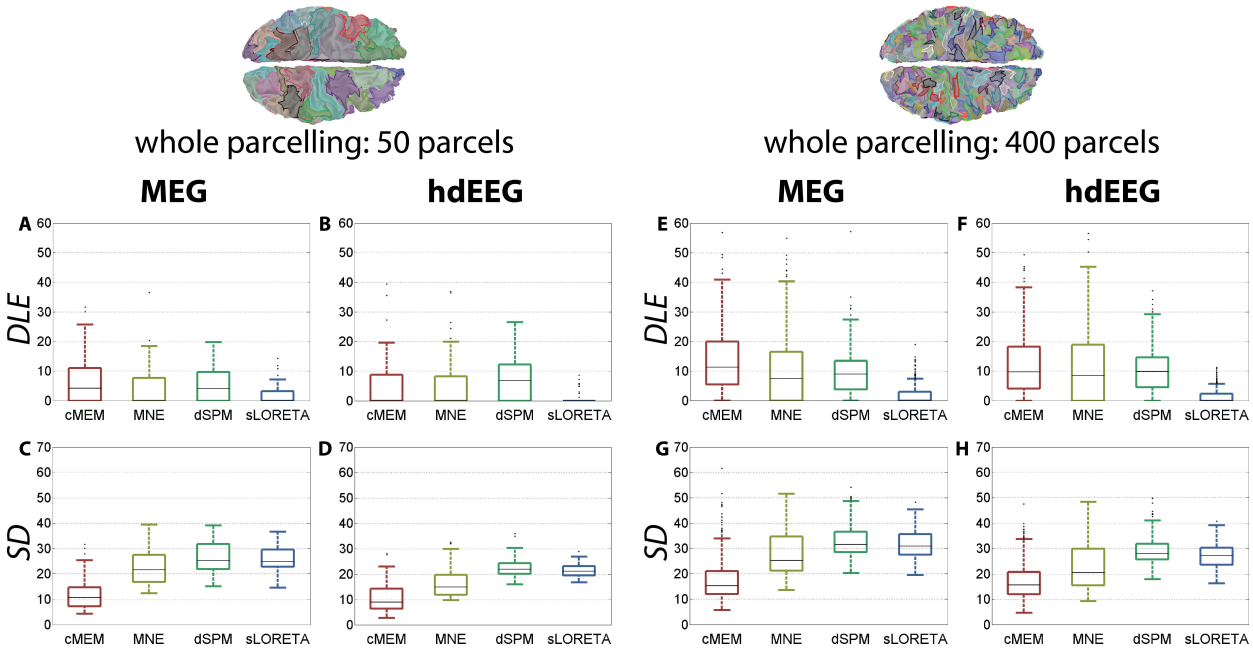

Figure 5.6: Reconstruction of noise-free spatially extended generators. Statistical distribution of the evaluation metrics for DLE in MEG (A - E) and hdEEG (B - F), and SD in MEG (C - G), and hdEEG (D - H) for cMEM, MNE, dSPM and sLORETA using boxplot representations. The metrics are based on source localization in ideal condition obtained from the large parcels (A to D) and from the small parcels (E - H). All values are in mm.

removed, and was therefore discarded. Results for DLE, SD and RSA are displayed in Figure 5.7.

No significant effect of source imaging methods on DLE scores were found for either hdEEG and MEG (Kruskal-Wallis ANOVA test, $p > 0.5$), indicating similar DLE scores for all source imaging methods.

No significant effect was found for SD in hdEEG (Kruskal-Wallis test, $p = 0.084$). However, we observed a significant effect of the source imaging method on SD scores for MEG (Kruskal-Wallis test, $p < 0.05$). Moreover, in MEG, all pairwise tests between source imaging techniques showed a significant difference (Wilcoxon signed rank test, $p < 0.0083$), with a better performance of cMEM (mean for SD: 5.2 mm) over the other techniques (means for SD: 10.1 mm, 9.3 mm and 9.7 mm for MNE, dSPM and sLORETA respectively).

We observed a significant effect of source imaging methods on RSA scores for hdEEG (Kruskal-Wallis test, $p < 0.05$): all the pairwise comparison were significantly different (Wilcoxon signed rank test, $p < 0.0083$), except between dSPM and sLORETA. Overall cMEM showed the lowest RSA score in hdEEG. Similarly, a significant effect of source imaging methods on RSA scores for MEG (Kruskal-Wallis test, $p < 0.05$): all the pairwise comparison were significantly different (Wilcoxon signed rank test, $p < 0.0083$), except between dSPM

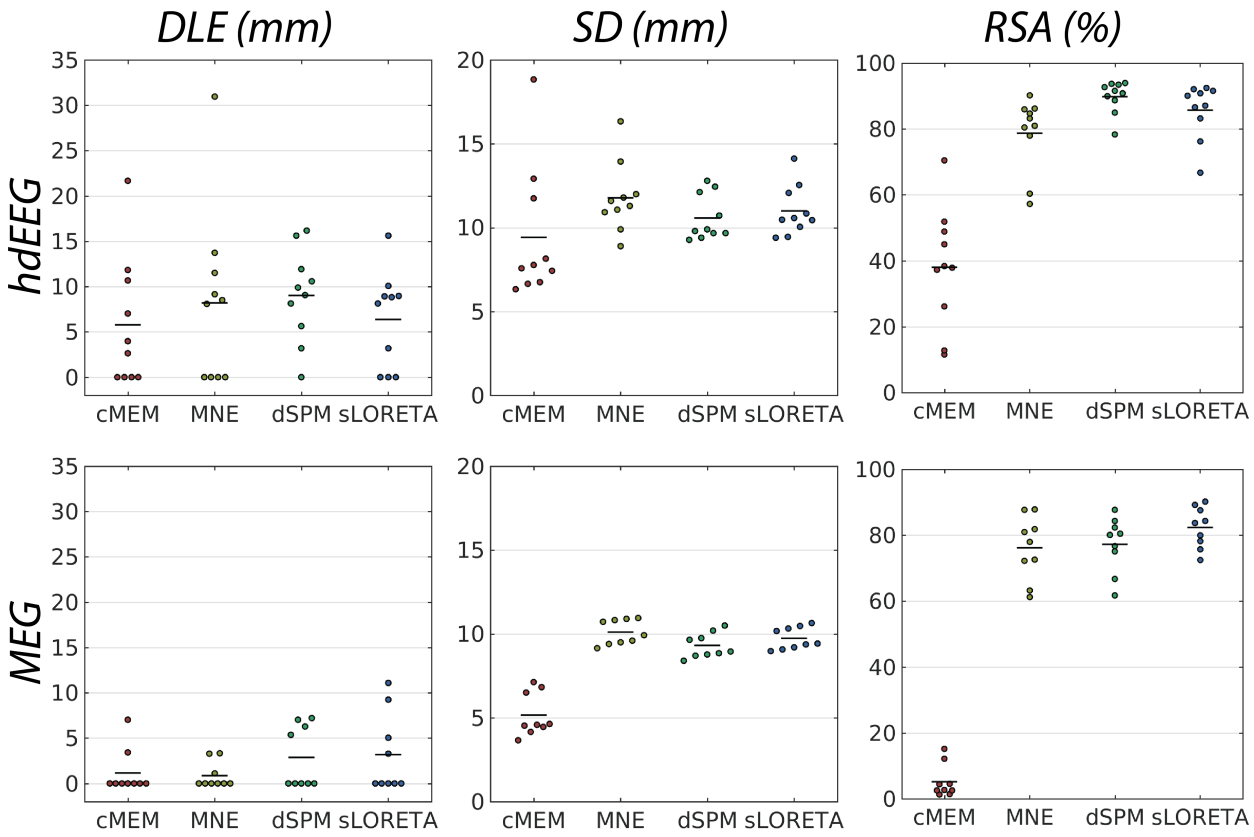

Figure 5.7: Results of the dipole localization error (DLE), spatial dispersion (SD) and ratio of spurious activity (RSA) for left and right median nerve stimulation in MEG and hdEEG. Points represent each individual results ($n = 9$ for MEG and $n = 10$ for hdEEG) and horizontal thick lines represent the mean of the distribution.

and sLORETA and between MNE and dSPM. Overall cMEM showed the lowest RSA score in MEG.

When comparing results between hdEEG and MEG, we observed a significant difference between modalities in DLE and RSA for dSPM and in SD and RSA for cMEM (Wilcoxon signed rank test, $p < 0.05$). with an overall better performance of MEG over hdEEG.

The source group average of the MNS results were obtained by projecting all the individual sources on a template cortical surface within Brainstorm software (Figure 5.8). This figure also displays the distribution of the amplitude for each source reconstruction, as a function of the Euclidean distance to $S1_{HAND}$. When compared to other methods, the results for cMEM appeared less spatially distributed and more accurately focused around $S1_{HAND}$. Moreover, it is worth noting that dSPM and sLORETA tended to generate a large amount of energy in deep structures. The histogram representations further confirmed that cMEM was more focused than the other techniques, in agreement with the SD values reported in Figure 5.7.

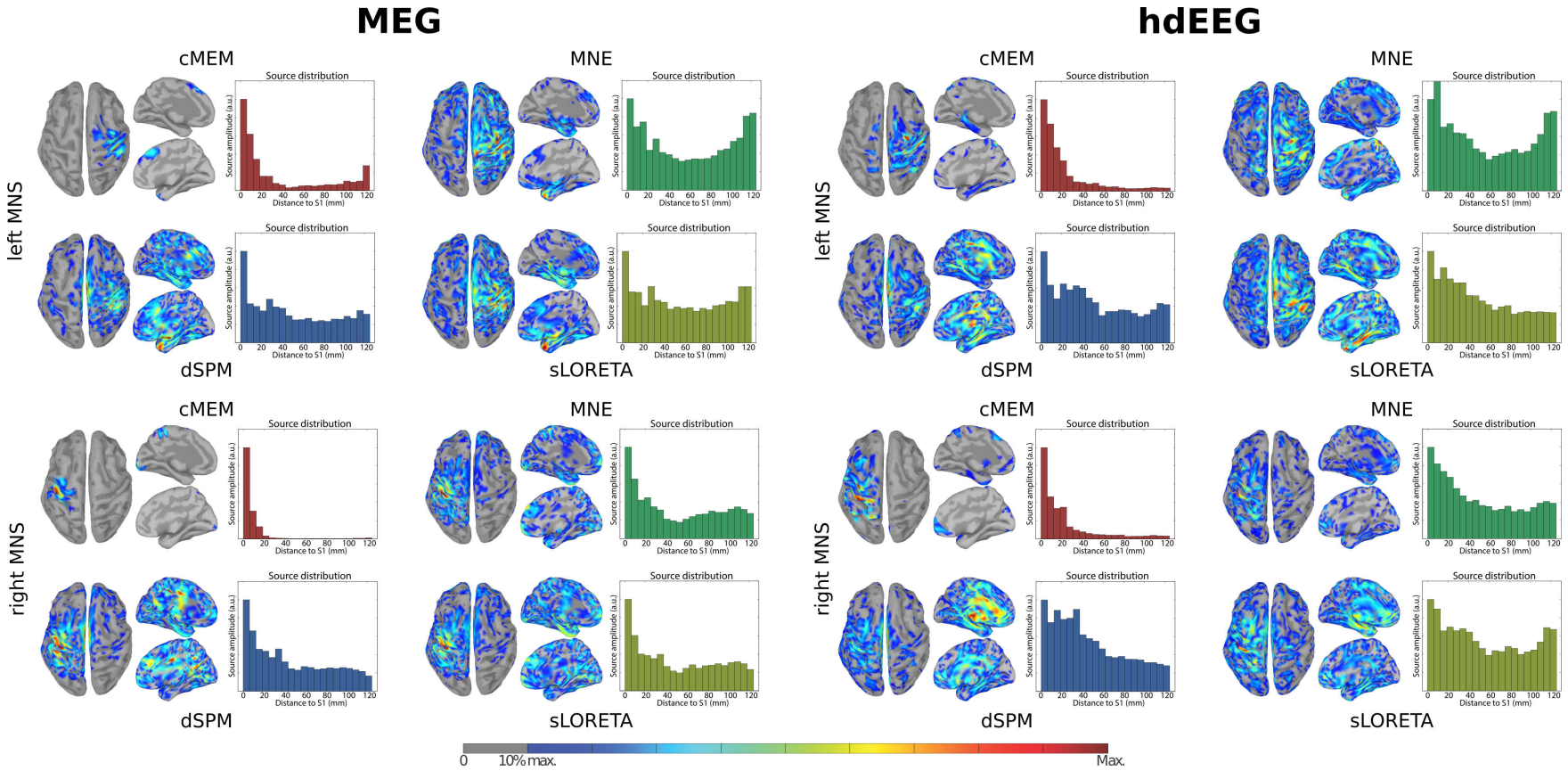

Figure 5.8: Source average of median nerve stimulation in MEG and hdEEG. The results reflect the average of the stimulation of 5 subjects (4 subjects for right MNS in MEG). For each source imaging method, The source results corresponding to the N20 peak were projected on a cortex template, normalized and averaged. Results were illustrated by a view of the cortical surface from the top and the mesial part of the left and right hemispheres. In all the maps, sources whose amplitudes were lower than 30% of the maximum were displayed in gray. The spatial distribution of source amplitudes is further described by reporting the histogram of sources amplitudes as a function of their Euclidean distance to $S1_{HAND}$

5.4 Discussion

In this study, we applied the concept of resolution matrix to compare four source imaging methods, namely MNE, dSPM, sLORETA and cMEM on the basis of spatial accuracy measured with PSF and CT scores. The spatial properties of the imaging techniques were also analyzed by applying source localization of the N20 peak of the somatosensory evoked response to electrical stimulation of the median nerve.

Whereas most methods can reach overall good performance in accurately localizing the main peak of the generator, as measured by DLE, cMEM presented excellent results in term of SD in hdEEG and MEG signals, confirming our previous observations from epilepsy studies (Grova et al., 2006a; Chowdhury et al., 2013; Heers et al., 2015; Grova et al., 2016).

In addition, here we demonstrated for the first time that cMEM was also able to accurately localize focal sources, besides its ability to also recover large extended sources. In the MNS study, cMEM was the source imaging technique which provided the most focal sources within the expected cortical area and which was the most robust to noise, since it exhibited very little distant spurious activity compared to other methods.

Surprisingly even if pairwise comparisons were found statistically different, some of the differences in DLE or SD between source imaging techniques were extremely small. Indeed, several significant differences consisted in differences of distribution median below 1 mm. The unusual shape of the statistical distribution of those metric (e.g. DLE values present a bimodal distribution with values ranging from 0 to 70 mm, and a large number of null values) may be an explanation why significant statistical differences were found despite the negligeable effect size. We added a color code of the effect size in Tables 5.1 to 5.3 to facilitate the interpretation of our results in this regard.

Whereas this present study was focusing on resolution matrix analysis and electrical median nerve stimulation experiments, it is worth mentioning that cMEM has already been studied and compared to other source imaging techniques, in configurations involving more complex source patterns. The behavior for cMEM in presence of realistic simulations of EEG and MEG data has been extensively studied: in Grova et al. (2006a), using realistic simulated EEG data, we first evaluated the ability of cMEM to be sensitive to the spatial extent of the generators. A later study completed this work by extensively studying MEG source imaging in similar contexts (Chowdhury et al., 2013), showing that cMEM was indeed able to reconstruct MEG sources of various sizes with good accuracy and robustness. In a last study comparing cMEM to another method characterized by its ability to recover extended sources (4-ExSo-MUSIC), the ability of cMEM to reconstruct two synchronous or propagated sources was studied (Chowdhury et al., 2013). cMEM was also proven to be a

promising source imaging technique for clinical data, such as epileptic discharges: our group compared the reconstruction of EEG and MEG transient epileptic discharges and assessed concordance with intracranial EEG findings (Heers et al., 2015; Grova et al., 2016). We demonstrated that cMEM was more accurate and did not tend to overestimate the source extent, when compared to the other standard source imaging techniques (Heers et al., 2015). A wavelet-based extension of MEM (Lina et al., 2014) has demonstrated promising results when localizing high-frequency oscillations (von Ellenrieder et al., 2016) or epileptic seizures onset (Pellegrino et al., 2018). Finally it is worth noting that cMEM has been applied in other context than epilepsy by our group or others, as for instance auditory short-term memory task using MEG (Grimault et al., 2014), oscillatory patterns such as epileptic high-frequency oscillations (Papadelis et al. 2016) or sleep spindles (Zerouali et al., 2014), and more recently in functional connectivity studies (Zerouali et al., 2016; Hassan et al., 2016).

5.4.1 Resolution matrix analysis

Resolution matrix is an interesting approach for investigating the intrinsic spatial properties of source localization technique in noise-free conditions. An analytical formula of the resolution matrix exists for linear techniques as MNE, dSPM and sLORETA. However, this is not the case for cMEM since it is a non-linear inverse solver. We assumed here that cMEM spatial properties could be estimated by a reconstruction of the resolution matrix. One important hypothesis behind this is that cMEM reconstruction of a spatially extended generator is given by the additive superposition of the reconstructions of all the dipolar sources, which is true in the linear techniques but not straightforward in a non-linear framework. This assumption was partly confirmed by the comparison of the two approaches, i.e. summing the PSF of every dipole involved in a spatially extended generator or the noise-free localization of the signal generated by the whole patch (Figure 5.5). Moreover, the analysis of source reconstruction of parcels with different spatial extents presented similar results than the ones obtained for the PSF analysis when simulated noise free single dipolar sources (Figure 5.6). Our results indeed suggest that, in noise free conditions, the intrinsic spatial properties of cMEM could be investigated through its estimated resolution matrix.

Best results in DLE in hdEEG and MEG analyzed with cMEM and MNE were found for superficial sources (Figures 5.3 and 5.4). For dSPM, the noise normalization had an effect of depth weighting on the solution. As a consequence, dSPM exhibited good DLE values for deeper sources when compared to other methods, except in the temporo-mesial structures. Overall, the median of DLE of all the techniques never exceeded 20 mm for both MEG and hdEEG (See Figure 5.2 A-B), which was low considering that the mean distance between

two neighbor dipoles along the cortical surface was about 5.5 mm.

It has already been pointing out that the localization error could not be enough to determine the quality of a source imaging technique (Grave de Peralta et al., 2009; Hauk et al., 2011). This is the reason why we added spatial dispersion metric to our analysis. In PSF and CT, cMEM SD values were significantly smaller than all the other methods. cMEM seems to exhibit intrinsic spatial properties to accurately localize focal sources, especially superficial ones. cMEM SD values were indeed quite low in superficial regions, when compared to other methods, whereas the distribution of SD values were more uniform throughout the whole brain for other techniques. Interpretation of SD is more difficult for deeper sources, because it is then influenced by spatial spread and localization error.

A study of the spatial properties of MNE, dSPM and sLORETA in MEG (Hauk et al., 2011) showed similar results in SD for all techniques, with lower DLE values in dSPM compared to MNE. Our study was not able confirm this observation, as we found that DLE values were actually high for dSPM for superficial sources. dSPM tended to be biased towards deep sources, resulting in large amplitude current density estimated in some deep structures (probably due to some numerical instabilities), consequently increasing DLE values for superficial sources. This difference may also be due to the different MEG technology used in (Hauk et al., 2011). Indeed, their study was done on an Elekta Neuromag Vectorview system, with 102 magnetometers and 204 planar gradiometers (Elekta AB, Stockholm, Sweden), whereas the current study uses 275 axial gradiometers.

Other studies used additional metrics to characterize the spatial properties of the resolution matrices. This included the average of all PSF or CT maps reported for each dipolar source suggested by Liu et al. (2002) or the resolution index proposed by Hauk et al. (2011). These metrics did not provide additional information that what we already showed using DLE and SD (data not shown).

CT maps are a marker of characterizing how dipoles could affect surrounding dipole reconstruction, which is also studied as the source leakage caused by volume conduction (Hauk and Stenroos, 2013). Low leakage is important when choosing source imaging techniques for functional connectivity studies (Hassan et al., 2014). Our results showed that resolution matrices had very low values of SD CT for cMEM when compared to other well-established methods. cMEM is therefore a promising relevant method to be considered for functional connectivity studies, and has recently be applied with success in such context (Zerouali et al., 2016).

cMEM results showed significantly lower SD values for MEG when compared to hdEEG whereas the reverse trend was observed for the other techniques. Our results are in agreement with Liu et al. (2002) who also demonstrated that MNE had more crosstalk in MEG when

compared to EEG. However, Molins et al. (2008) reported larger SD values in MNE for EEG when compared to MEG. The difference between these studies may again be explained by the used MEG sensors: Liu's study as well as ours used gradiometers, whereas magnetometers were used in Molins et al. (2008). This difference may explain the higher spatial dispersion reported in MEG in this study.

Here we illustrated, for the first time, the behavior of cMEM in focal source configuration and in noise-free conditions. Out results suggest that the maximum of activity was usually successfully recovered by most methods. However MNE, dSPM and sLORETA were less sensitive to the spatial extent of the source generators, whereas cMEM was able to provide a more accurate representation of the true underlying spatial extent for cMEM.

Some of the differences we observed between hdEEG and MEG analysis could also be caused by the choice of the forward model. In terms of forward modeling, we considered a Boundary Element Model for hdEEG and MEG. We decided to chose such forward models because they are easily available through conventional software packages and source reconstructions were shown to be more accurate than when using single-sphere or overlapping-sphere models (Henson et al., 2009). We notably used OpenMEEG implementation of BEM (Gramfort et al., 2010), a method that was demonstrated to be robust to numerical instabilities that could occur when the source model is getting to close to inner BEM surfaces. Whereas we previously demonstrated that cMEM was quite robust to possible errors related to the brain-to-skull conductivity ratio (Chowdhury et al., 2015, 2016), one should mention that different head modeling affect differently EEG and MEG data, as suggested in Vorwerk et al. (2014). In this study, starting with a 3-compartment Finite Element Method model, the authors measured the effect of adding different compartments (such as cerebrospinal fluid (CSF), skull spongiosa, or skull compacta) on the accuracy of EEG and MEG forward models and concluded that including the CSF and distinction between gray and white matter should be considered in head volume conductor modeling for both EEG and MEG. However, studying specifically the effect of the choice of the forward model on the resolution matrix results, despite being of great interest, was falling out of the scope of the present study.

5.4.2 Evaluation using somatosensory data

MNS was used because it is known to produce a focal activity in the hand region of the primary sensory cortex (Wood et al., 1988; Allison et al., 1995; Barba et al., 2005). Since such a generator is very focal and reliably localized in S1 area, one can consider the same metrics to analyze PSF maps (Molins et al., 2008) using an anatomical landmark as gold standard (Kuo et al., 2014).

Distant spurious activity was not considered in the evaluation of SD and DLE metrics in order to avoid bias evaluation results by remote activity far from the generator, as proposed in Grova et al. (2016). In order to quantify the amount of activity discarded by this approach, the metric RSA was introduced. We showed that when compared to other source imaging methods, cMEM exhibited very little distant spurious activity, probably due to its ability to shut down parcels during the regularization process. This finding is also in agreement with our previous studies investigating the localization of extended epileptic generators (Grova et al., 2016; Heers et al., 2015).

DLE values were similar for all source imaging techniques, whereas cMEM exhibited significantly smaller SD and RSA values when compared to any other methods. This means that while all the techniques often found their maximum in the region of interest, cMEM produced less spatial spread around the main generator, exhibiting very little distant spurious activity, especially in MEG.

The overall results showed that SD and RSA metrics were lower in MEG compared to hdEEG in almost all techniques. The difference between hdEEG and MEG in MNS data could be explained by the difference in signal-to-noise ratio of the average signals, and the difficulty for hdEEG to correctly estimate the conductivity value of the skull. We also verified that the $S1_{HAND}$ regions manually segmented for this study consisted mainly in tangential oriented sources. To do so, we used the measure of cancellation index proposed in Ahlfors et al. (2010) on all regions and showed similar level of cancellation for hdEEG and MEG, suggesting that source orientation may not explain the different results obtained in both modalities.

Molins et al. (2008) also reported DLE and SD metric to compare EEG and MEG for N20 reconstructions. It is important to note that the SD and DLE values found in Molins's study were higher than the ones reported in the present investigation. These differences can be explained mostly by the choice of the ground truth. Molins and colleagues decided to compare the source imaging reconstruction to the equivalent current dipole reconstructions, whereas we opted with the anatomical location of $S1_{HAND}$. Our labeled region representing the ground truth being by construction larger than theirs, DLE and SD values were consequently smaller.

This is the first time we are investigating the behavior of cMEM on real data in controlled experiments to identify focal generators. cMEM results were very accurate and the behavior of the method was in agreement with our previous studies, for both MEG and hdEEG.

5.5 Conclusion

We used the resolution matrix to compare different source imaging techniques (MNE, dSPM, sLORETA, and cMEM) in terms of PSF (related to the intrinsic spatial resolution of the source reconstruction) and CT, an important feature to be characterized before assessing functional connectivity between different regions. In this study combining theoretical analysis of resolution matrices and localization of real somatosensory data, we carefully evaluated both MEG and hdEEG data using similar amount of sensors. We showed that, despite few differences slightly in favor of MEG, both modalities allowed very accurate localization. Moreover, for both MEG and hdEEG, we showed that cMEM outperformed widely used linear operators in term of PSF and CT maps, especially for cortical sources. We concluded that cMEM was the best candidate to correctly reconstruct focal sources and was more robust to noise than other techniques.

CHAPTER 6

Manuscript 2: Effect of MR-related noise on the quality of electrical source imaging reconstructions of visual evoked potentials

Authors: Tanguy Hedrich, Ümit Aydin, Stephan Grimault, Habib Benali, Jean-Mac Lina, Christophe Grova.

Context

In Chapter 5, we have demonstrated the excellent performance of cMEM in terms of spatial resolution, as well as its ability to recover the extent of a source with minimal leakage. We did so providing a detailed evaluation using MEG data but also for the first time with high-density EEG data. Since our overall objective was to apply ESI on EEG data recorded in the MR scanner, this second manuscript aimed at assessing the robustness of different source imaging techniques when applied to EEG data in presence of MR-related noise. As described in Chapter 3, recording EEG inside the MR scanner is a challenging task since MR-related artifacts affect the EEG data and create distortion in the signals. Several techniques have been used to overcome this issue. Despite advanced method to remove those artifacts, remaining residuals could still contaminate the data. To understand the effect of the MR-related noise on the quality of ESI reconstructions, we performed visual stimulation experiments on healthy subjects twice: once outside the scanner, and then during an fMRI experiment. In that way, we were able to obtain a gold standard (data recorded outside) as a comparison reference for a better assessment of the performance of the ESI techniques. Conducting this experiment to

carefully evaluate ESI quality from hdEEG data acquired inside the scanner was necessary before considering ESI from hdEEG inside the scanner to localize IEDs (Chapter 7).

All the acquisitions were realized at the PERFORM centre in Concordia University in Montreal. With this study, we were actually the first group performing an EEG-fMRI experiment in the PERFORM centre and we were able to obtain good quality data and results with the help of our MR physicist Dr. Grimault and the PERFORM scientific director Dr. Benali, as well as all the technicians from the PERFORM centre.

The manuscript was submitted for publication as: **T. Hedrich, Ü. Aydin, S. Grimault, H. Benali, J.-M. Lina, and C. Grova. Effect of MR-related noise on the quality of electrical source imaging for simultaneous EEG-fMRI recordings. *Human Brain Mapping*, Under Review**.

Abstract

Background: Electroencephalography (EEG) recorded simultaneously with functional magnetic resonance imaging (fMRI) suffers from artifacts caused by the high magnetic field environment. The goal of this study was to assess the quality of electrical source imaging (ESI) techniques using EEG data recording in the scanner using a well-controlled visual stimulation paradigm.

Methods: The P100 peak recorded inside and outside the MR scanner was acquired in 14 participants and localized using two ESI techniques: Minimum Norm Estimate (MNE) and coherent Maximum Entropy on the Mean (cMEM). The EEG quality was assessed using: Signal-to-Noise Ratio (SNR) and the correlation with grand average topography (Corr). The ESI accuracy was measured using: Dipole Localization Error (*DLE*), Spatial Dispersion (*SD*) and Ratio of Spurious Activity (*RSA*).

Results: Corr and SNR were affected by the residuals of the MR-related artifacts, as indicated by a significant decrease of those metrics inside the scanner. However, only small effects were found on *DLE* and *SD* indicating the robustness of ESI to MR-related noise. However, ESI from data inside the scanner exhibited a large amount of distant spurious activity. Overall cMEM proved to be more robust to this noisy environment than MNE.

Conclusion: Even if EEG quality decreased in the presence of high-magnetic field, EEG source reconstruction remained accurate, exhibiting similar performance when compared to data acquired outside the scanner, although contaminated with more distant spurious activity. These results strengthen the prospect to compare and combine ESI of neuronal activity and the corresponding hemodynamic response using simultaneously recording.

6.1 Introduction

Functional magnetic source imaging (fMRI) is a largely recognized neuroimaging technique measuring the Blood Oxygen Level Dependent (BOLD) signal in the brain (Kwong et al., 1992; Ogawa et al., 1992). fMRI is an indirect measure of brain activity and relies on the estimation of the blood hemodynamic response elicited by neural activation following neurovascular coupling processes (Logothetis et al., 2001). On the other hand, electroencephalography (EEG) measures directly the brain activity by recording neuronal bioelectrical activity, mostly post-synaptic potentials, with scalp electrodes (Nunez and Srinivasan, 2006). Whereas fMRI provides excellent spatial resolution at a millimetric scale, EEG provides a better temporal resolution, measuring brain neuronal activity at the millisecond scale. Both modalities can be recorded simultaneously (Gotman et al., 2006; Mulert and Lemieux, 2010; Abreu et al., 2018a). However, measuring EEG in the MR scanner is challenging, mainly due to large artifacts produced by the MR scanner on the EEG signals. Main artifacts are: the gradient artifact, caused by rapidly varying magnetic field during gradient switches; the ballistocardiogram artifact, mostly due to small head movements induced by heartbeats; and the vibrations induced by helium pump (Allen et al., 2000; Vanderperren et al., 2010; Mullinger et al., 2013a). There is a growing interest in acquiring EEG simultaneously with fMRI. Indeed, EEG could be used to detect specific brain activity, such as specific oscillations (Tyvaert et al., 2008), epileptic discharges (Gotman et al., 2006), and sleep spindles (Dang-Vu, 2010). fMRI could then localize the hemodynamic changes related to those events with an excellent spatial resolution. In epilepsy, simultaneous EEG-fMRI is a valuable method used to localize brain regions involved during the generation of epileptic discharges, by studying the brain hemodynamic changes related to transient epileptic events detected on scalp EEG (Gotman et al., 2004; Khoo et al., 2017; van Graan et al., 2015)).

In order to improve the spatial resolution of EEG data, Electrical source imaging (ESI) can be considered (Hämäläinen and Ilmoniemi, 1994; Lascano et al., 2015; Michel et al., 2004). ESI consists in solving a so-called inverse problem to localize the generators of scalp EEG signals along the underlying cortical surface (Baillet et al., 2009). The problem is ill-posed in nature, meaning that a unique ESI solution can only be found if additional constraints are added to the model. Several methods providing inverse solution for ESI have been proposed and carefully validated in the literature (He et al., 2018). The forward model, based on realistic individual brain segmentation and a physical model of electric propagation inside the head, should also be carefully addressed to obtain reliable results (Hallez et al., 2007; Mosher et al., 1999a). In this study, we used the distributed inverse solution approach entitled coherent Maximum Entropy on the Mean (cMEM), developed by our group (Amblard et al.,

2004; Grova et al., 2006a; Chowdhury et al., 2013) using boundary element model (BEM) methods as the forward model. cMEM has been carefully evaluated and validated in the context of EEG and magnetoencephalography source imaging for its ability to be sensitive to the underlying spatial extent of the generators (Chowdhury et al., 2018, 2015; Grova et al., 2006b; Pellegrino et al., 2018) and its robustness in the presence of data with low signal to noise ratio (Chowdhury et al., 2016; Hedrich et al., 2017). In a recent study, we demonstrated that, when using high density EEG, cMEM exhibited an excellent spatial resolution when compared to other widely used ESI techniques, namely the minimum norm estimate (MNE) and its noise-normalized variants (dSPM and sLORETA) (Hedrich et al., 2017).

On the other hand, simultaneous EEG-fMRI allows studying the hemodynamic response to electrophysiological signals of spontaneous activity, pathological patterns or cognitive tasks. Simultaneous EEG-fMRI studies have been notably considered to investigate the relationship between the hemodynamic activity and different brain rhythms during rest (Laufs, 2008; Tyvaert et al., 2008), or during sleep (Dang-Vu, 2010; Picchioni et al., 2013). EEG-fMRI has been also used to study well-controlled tasks, for example pain stimulation, cognitive, motor and sensory tasks, where the amplitude, but also several other characteristics of the EEG response such as spectral components, latencies of the evoked response or spatial topographies could be included within the fMRI statistical model to assess their interaction with hemodynamic activities (Arnstein et al., 2011; Bénar et al., 2007; Christmann et al., 2007; Debener et al., 2005; Knyazeva et al., 2006).

However, ESI has been rarely applied to EEG data recorded in the scanner (Boutin et al., 2018; Brookes et al., 2008; Groening et al., 2009; Vulliemoz et al., 2009, 2010a). Most studies aimed at detecting EEG patterns to be analyzed within the fMRI framework (e.g. epileptic discharges, sleep related discharges, specific events); for this reason, only a few electrodes were usually considered for simultaneous EEG-fMRI acquisitions (about 20 electrodes), thus, limiting the possibility to perform reliable and accurate ESI reconstructions. Moreover, even after careful artifact corrections using different approaches (Allen et al., 1998, 2000; Mullinger et al., 2013a; Vanderperren et al., 2010), EEG data within the scanner remains of lower quality when compared to EEG data recorded outside the scanner, whereas ESI procedure would require good EEG quality over the whole spatial topography (Leijten and Huiskamp, 2008). To the best of our knowledge, the effects of the high magnetic field environment on the performance of the ESI reconstruction have never been studied in a dedicated manner. In this study, we carefully investigated the use of high-density EEG (hdEEG), involving 256 electrodes, to evaluate the accuracy of ESI within the context of simultaneous EEG-fMRI acquisitions, using a well-controlled visual task.

One could question the interest of using ESI inside the MRI scanner. Indeed, several

studies compared ESI and fMRI using EEG data recorded outside the scanner (Mayhew et al., 2013), including some studies from our group (Grova et al., 2008; Heers et al., 2014). One advantage of simultaneous recording is that EEG and fMRI hold complementary information. Electrophysiology is sensitive to synchronous post-synaptic potential whereas fMRI records the hemodynamic activity: recording both modalities at the same time allows to better understand the dynamics of the neurovascular coupling and avoids discrepancies that are due to differences in vigilance or in attention during EEG and fMRI acquisitions. In this context, resting state functional connectivity appears as a domain which might greatly benefit from the fusion of the information generated simultaneously from both modalities (Mantini et al., 2007; Meyer et al., 2013).

In the present study, we propose a careful evaluation of ESI using high-density EEG data acquired in the scanner, using a well-controlled visual stimulation task. We evaluated the accuracy of ESI using high-density EEG data acquired either outside or inside the scanner, while varying the number of averaged evoked response trials, hence the level of signal-to-noise ratio (SNR). Our objective was to demonstrate whether ESI can be considered for hdEEG data acquired in the scanner, even in low SNR conditions.

6.2 Material and methods

6.2.1 Subjects

From 20 subjects who were enrolled in the experiment, 6 were excluded because of high movement artifacts and too many eye blinks synchronous with the stimulation (n=5) or high susceptibility artifact (n=1). Thus, fourteen healthy volunteers (eleven females; age range: [21-40]), with normal or corrected-to-normal vision participated in the study. All 14 subjects performed two sessions, EEG only first, then EEG acquired simultaneously with fMRI. The study was approved by the "Comité centrale d'éthique de la recherche" of Quebec ministry of health and a written informed consent was signed by all participants prior to the procedures.

6.2.2 Paradigm design

The visual stimuli consisted in the presentation of radial black and white checkerboard, derived fromPinel et al. (2007), of the left side of screen in a gray background, while the participant was asked to fixate a plus-shaped cross at the center of the screen (Figure 6.1). Each stimulus was presented for one second, with a phase reversal after 500 ms of presentation, with a random interstimulus interval varying between 6 s and 8 s, for a total number of 70 stimuli. To maintain the subject's attention during the experiment, five times randomly

throughout the experiment, the plus-shaped cross target was changed into an 'X'-shaped and the participant was instructed to press a button as soon as possible when such a change occurred.

The diameter of the checkerboard stimuli outside the MR scanner was 33 cm and the distance between the participants and the monitor was set to 75 cm. Inside the MR scanner, a Hyperion MRI digital projection system (PST100984) was used for the stimuli. The diameter of the checkerboard was 60.7 cm, the distance from the mirror to the screen was 128 cm and the distance from the eyes to the mirror was approximately 10 cm.

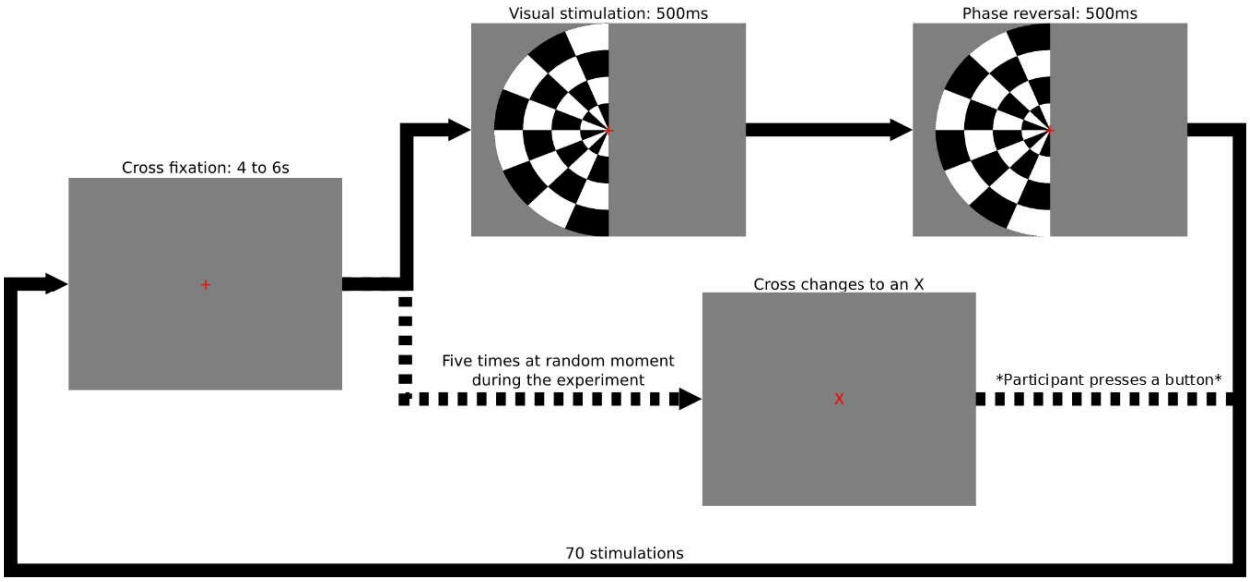

Figure 6.1: Diagram describing the visual stimulation task.

6.2.3 Data acquisition

All acquisitions were conducted at the PERFORM Centre of Concordia University. hdEEG data was recorded using a 256-electrode EGI system (Philips Neuro, Eugene, OR, USA) at a sampling rate of 1000 Hz. Electrocardiography was also recorded using additional electrodes. For safety reasons allowing EEG recording inside the MRI, each electrode was equipped with an additional 10 kΩ resistance. We visually evaluated that good data quality was therefore achieved by maintaining the EEG impedances below 70 kΩ as suggested by the manufacturer.

MRI data were acquired using a 3T GE Discovery MR750 scanner (General Electric, Milwaukee, WI, USA). During the task, the fMRI data acquisition consisted in an EPI sequence ($3.7 \times 3.7 \times 3.7$ mm^3 voxels, 33 slices, 64×64 matrix TE = 25 ms, TR = 1.9 s, flip angle 90°). Additionally, two high-resolution T1-weighted MRIs (1 mm isotropic 3D acquisition, 192 sagittal slices, 256×256 matrix, TE = 2.98 ms, TR = 2.3 s, flip angle 9°)

were acquired after the task, one with the EEG cap and one without the EEG cap for fMRI image co-registration and head modeling for hdEEG source imaging.

The data that support the findings of this study are available from the corresponding author upon reasonable request.

6.2.4 hdEEG data analysis

For data acquired inside the scanner, MR-related artifacts (gradient and pulse artifacts) were corrected using averaged artifact subtraction method (Allen et al., 1998, 2000) using BrainVision BrainAnalyzer2 software (Brain Products, Munich, Germany). The acquired EEG data were then imported in to Brainstorm software (Tadel et al., 2011). A 1-25 Hz band-pass filter was first applied as suggested in Mayhew et al. (2013). Blink artifacts were reduced using the Signal Space Projection method, where we selected the first one or two components to remove, based on their topography, time courses and explained variance (Uusitalo and Ilmoniemi, 1997). The data was then segmented into 700 ms epochs (from -200 ms to 500 ms, 0 being the time of the visual stimulus onset) and DC correction was applied, considering a baseline window from -200 ms to 0 ms. Electrodes located on the face and on the neck (76 channels) as well as any other potential noisy channels were excluded for further analysis. All the remaining electrodes were re-referenced to an average reference. All trials were inspected visually and trials with remaining large artifacts were discarded. For some of the subjects, if ballistocardiogram artifacts were still present in the signal, independent component analysis (Nakamura et al., 2006) was performed to visually remove additional components, based on their topographies and rhythmicity. For each subject and condition, all non-discarded trials were averaged and the exact timing of the P100 peak was estimated as the peak of maximum amplitude of the electrode O2 around 100 ms after the stimulus.

In order to study the effects of the signal-to-noise ratio of the evoked potential of hdEEG data acquired inside and outside the scanner, subaveraged signals were constructed by randomly drawing and averaging n trials, with n = {1,5,10,20,30,40}. For each n, draws with replacement were repeated 20 times. The whole process of hdEEG data analysis is illustrated in Figure 6.2.

6.2.5 Forward model estimation

The EEG sensor positions were estimated using the default EGI positions in Brainstorm software (Tadel et al., 2011), individually adapted for each subject. After this, head segmentation using the MRI of the subjects with the EEG cap on was performed and the position of the EEG electrodes was modified so that each electrode fit to the center of the corresponding MRI

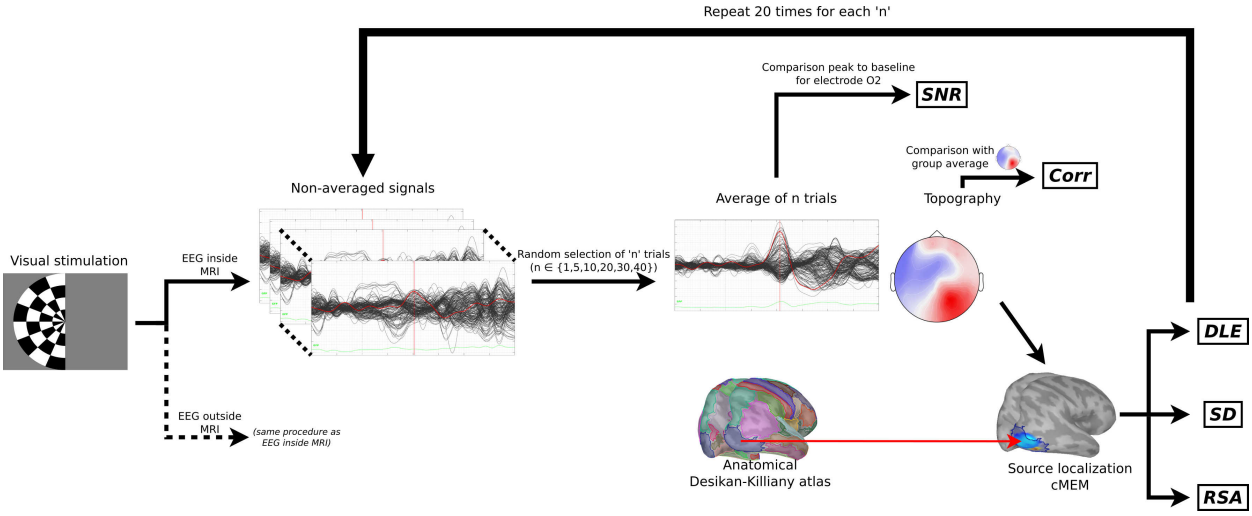

Figure 6.2: Summary of the EEG and ESI analysis pipeline. *SNR*: Signal-to-Noise Ratio; *Corr*: spatial correlation of the EEG topography with grand average; *DLE*: Dipole Localization Error; *RSA*: Ratio of Spurious Activity.

signal attenuation. Another head segmentation, using MRI images of the subject without the EEG cap, was then performed and the position of the EEG electrodes was coregistered to this surface using Brainstorm. The source space consisted in a mesh of the cortical surface segmented based on the mid-line between gray-white matter interface and the pial surface, subsampled to around 8000 vertices, estimated using Freesurfer Fischl (2012) and Brainstorm software. All dipolar sources in the distributed source model were oriented perpendicularly to the cortical surface.

The forward model assessing the contribution of every dipolar source to hdEEG sensors was computed using the Boundary Element Method (BEM) proposed by Kybic et al. (2006). The gain matrix was calculated using a 3-layer BEM model consisting in the inner skull, outer skull and head surface (respective conductivity: 0.33 S/m, 0.0165 S/m, 0.33 S/m). The calculations were done using the OpenMEEG implementation (Gramfort et al., 2010) in Brainstorm software.

6.2.6 Source analysis

Two source imaging techniques were considered in this study. The weighted minimum norm estimate (MNE) (Dale and Sereno, 1993; Hämäläinen and Ilmoniemi, 1994), a widely used linear technique calculating the source solution which explains the measured data assuming a broad distribution of low-amplitude currents in the brain.

The other source imaging technique used was coherent Maximum Entropy on the Mean (cMEM) (Amblard et al., 2004; Chowdhury et al., 2013), a Bayesian approach, in which the

a priori knowledge is given through a parcellation of the cortical surface, whereas data fit and regularization are ensured through entropic approaches. We have carefully evaluated the accuracy of cMEM source imaging method, and notably its ability to recover the underlying spatial extent of the generators in realistic EEG and MEG simulations (Grova et al., 2006a; Chowdhury et al., 2013, 2016) as well as with clinical data (Chowdhury et al., 2018; Grova et al., 2016; Pellegrino et al., 2018). The implementation of cMEM algorithm considered in this study is available as a plug-in in Brainstorm software and a tutorial describing its use is available: http://neuroimage.usc.edu/brainstorm/Tutorials/TutBEst.

6.2.7 fMRI statistical analysis

The EPI data underwent a standard General Linear Method (GLM) analysis using FSL software (http://www.fmrib.ox.ac.uk/fsl/index.html). fMRI preprocessing included non-brain tissue removal, slice timing correction, motion correction using MCFLIRT method (Jenkinson et al., 2002), spatial smoothing (5 mm FWHM) and high-pass filtering (temporal cutoff: 100 s). Regressors for the visual stimulations were based on the timing of each event, convolved with the canonical hemodynamic response function. The six parameters estimated during motion correction were also included in the GLM analysis as confound regressors, in order to account for residual movement artifacts. The significance of every cluster was assessed using a method involving Gaussian random field theory (Z threshold: 2.3, Cluster threshold: $p < 0.001$ (Woo et al., 2014)). The BOLD cluster containing the voxel exhibiting the largest absolute t-value was selected and projected into the EEG source space, i.e. the cortical surface, using a Voronoi based interpolation (Grova et al., 2006a; Heers et al., 2014).

6.2.8 Inter-subject variability

Inter-subject and test-retest reliability of hdEEG source imaging for data recorded outside and inside the scanner were evaluated at the sensors and at the source level using metrics similar to the ones introduced in our previous study (Hedrich et al., 2017).

Our first metrics aimed at assessing the quality of the evoked response within the sensor space. We also used metrics in the source space aiming at assessing specifically source imaging performances. For these latter ones, we considered as "ground truth" an anatomical segmentation outlining the right lateral occipital region. This anatomical region was extracted from the Desikan-Kiliany atlas, estimated on subject specific cortical surface during the Freesurfer surface segmentation. This occipital region was indeed the region where we could expect maximum intensity of our source reconstruction of P100 as suggested in Di Russo et al. (2002).

6.2.8.1 Signal-to-noise ratio on electrode O2 (*SNR*)

The signal-to-noise ratio (*SNR*) was estimated as the ratio between the amplitude of electrode O2 (EGI electrode 150) at the P100 peak and the standard deviation pre-stimulus background estimated in O2 along a period of 200 ms before the visual stimulation.

6.2.8.2 Spatial Correlation of the EEG topography with grand average (*Corr*)

To assess the spatial accuracy of the evoked topography at the P100 peak, we estimated spatial Pearson's correlation (*Corr*) of EEG topographies using as reference the grand average P100 peak topography obtained by averaging all trials recorded outside the scanner from all subjects.

6.2.8.3 Dipole Localization Error (*DLE*)

The Dipole Localization Error (*DLE*) was used to assess the localization error of the source reconstruction. This metric in millimeters was calculated as the minimum Euclidean distance between the location of the reconstructed dipolar source exhibiting maximum amplitude at the P100 peak, and the closest border of the anatomical reference area considered for this study.

6.2.8.4 Spatial dispersion (*SD*)

The spatial dispersion (SD), as originally proposed by Molins et al. (2008), measured the spatial spread around the right lateral occipital region. A low score of *SD* indicates a focal source, whereas a higher score means that the source was either mis-localized when compared to the reference or exhibited a spatially extended pattern around the presumed true location. *SD* was calculated as follows:

$$SD = \sqrt{\frac{\sum_{i=1}^{n_d} d_{i,\phi}^2 \hat{\boldsymbol{j}}_i^2(t_{P100})}{\sum_{i=1}^{n_d} \hat{\boldsymbol{j}}_i^2(t_{P100})}} \tag{6.1}$$

where $d_{i,\phi}$ is the closest Euclidean distance between the dipole i and the anatomical reference ϕ, and $\hat{\boldsymbol{j}}_i^2(t_{P100})$ is the energy of the ith dipole of the source reconstruction at the time of the P100 peak.

6.2.8.5 Ratio of spurious activity (*RSA*)

For the calculation of *DLE* and *SD*, we only selected dipolar sources exhibiting activity at a distance smaller than 40 mm from the anatomical reference. This was done to prevent the

DLE and *SD* metrics to be biased by additional spurious source reconstructions occurring far from the presumed localization. Consequently, we also developed a metric quantifying the amount of activity falsely localized in remote regions from the presumed generator. To do so, we calculated the ratio between the energy far from the studied region, i.e. activity in dipolar sources located at a distance larger than 40 mm from the right lateral occipital reference region, to the total energy. Results were expressed in percentage, where 0 % means that all the activity was localized within a close neighborhood of the anatomical reference and 100 % that all the activity was located far from this region and therefore considered as spurious.

6.3 Results

6.3.1 Sensor based metrics (*SNR* and *Corr*)

Figure 6.3 presents the distribution of the two proposed scalp EEG sensor-based metrics (*SNR* and *Corr*) as a function of the number of trials considered to compute the evoked response, in both conditions: inside (dark line) and outside (light line) the scanner. Group median of the 14 participants is presented on the left side of each figure, whereas results obtained for every individual analysis are presented on the right side. The grand average spatial topography from EEG data recorded outside the scanner, considered as the reference for Corr estimation, is presented in Figure 6.6.

Regarding spatial correlation, Corr, we observed an increase in correlation values as the number of averaged trials increased, ranging from 0.53 for single trial topographies and reaching a plateau at around 0.76 when 20 trials were averaged, for all subjects for EEG data recorded outside the scanner. Similarly, for EEG data recorded inside the scanner, we observed a median Corr value of 0.31 for single trial data, reaching a plateau at 0.68 when for a subaverage of 30 trials. Correlation values were significantly smaller for data acquired inside the scanner when compared to the EEG data acquired outside the scanner (Wilcoxon RankSum test, $p < 0.05$, Bonferroni corrected). We also found a large inter-subject variability, the range of correlation values for 40 averaged trials ranged from 0.20 (S4) to 0.94 (S2) for data acquired outside the scanner, and from 0.28 (S4) to 0.94 (S2) for data acquired inside the scanner.

The SNR levels measured at O2 electrode varied from 2.10 to 8.50 outside the scanner and from 1.64 to 5.32 inside the scanner. Importantly, at the group level, SNR values estimated inside the scanner were statistically larger than SNR values estimated from data recorded outside (Wilcoxon RankSum test, $p < 0.05$, Bonferroni corrected) for all subaverages. Again, a large inter-subject variability was observed, with SNR data ranging from 1.88 (S1) to 26.5

(S2) for data recorded outside and 1.49 (S1) to 15.3 (S2) for data recorded inside the scanner, when considering a subaverage of 40 trials.

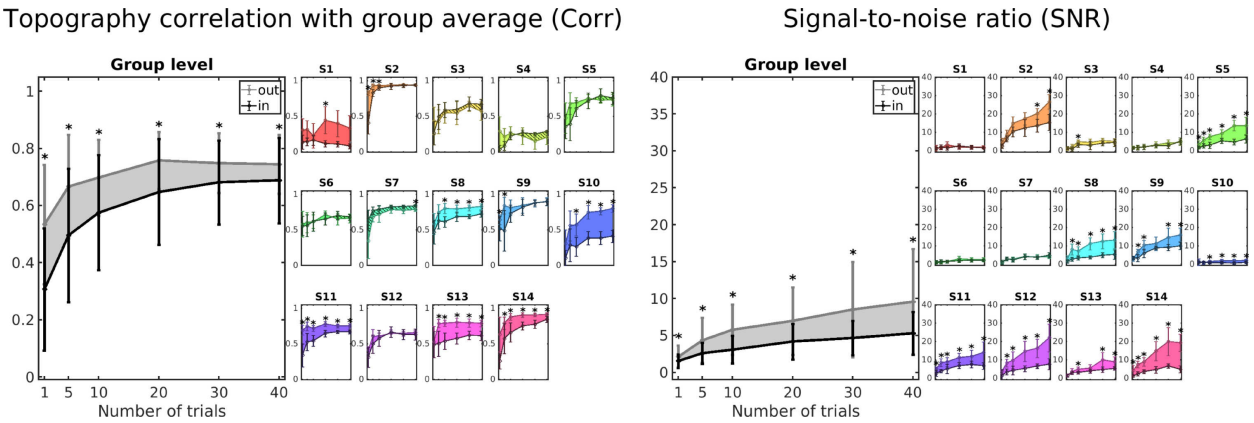

Figure 6.3: (A) Topography spatial correlation (*Corr*) and (B) signal-to-noise ratio (*SNR*) as a function of the number of trials. For each subfigure, the left panel presents the group subject average, whereas the right panel depicts the results for each individual subject. Each sample point represents the median +/- interquartile range over the corresponding distribution. The dark line and light line represent the data inside and outside the scanner, respectively. A plain color was used between the two curves when the corresponding metric exhibited better performance outside versus inside the scanner. On the other hand, hatchings were used between the two curves when the metric exhibited better performance inside versus outside the scanner. For group and single subject and for each level of subaveraging, Wilcoxon RankSum was used to compare metrics obtained inside and outside the scanner. (*: $p < 0.05$, Bonferroni corrected.)

6.3.2 ESI based metrics (*DLE*, *SD*, and *RSA*)

DLE, *SD* and *RSA* metrics after applying cMEM or MNE source localization methods are reported in Figure 6.4. At the group level, *DLE* showed a decrease in localization error when increasing the number of trials used for averaging for both ESI techniques. For single trials, the average *DLE* values was 14 mm for MNE and 20 mm for cMEM, both outside and inside the scanner. Increasing the number of trials averaged inside the scanner decreased the *DLE* values for MNE down to a median value of 0 mm with a subaverage of 10 or higher. Surprisingly, there was a constant, although not significant, bias (∼5 mm) in median *DLE* values between inside and outside the scanner for MNE. *DLE* values for cMEM did not show any significant differences between inside and outside the scanner and the median values in both conditions were 0 mm when the number of averaged trials exceeded n=20. At the single subject level, we could however observe a large discrepancy between the subjects. Some subjects illustrated good results with *DLE* scores rapidly decreasing to 0 or very small *DLE* values (S2, S5 and S9 for both MNE and cMEM, S3 for MNE only, S14 for cMEM only). On the hand, other subjects showed very high localization error, and for some subjects,

localizations were more accurate for data acquired inside when compared to data outside the scanner compared to outside (5 subjects for MNE, 4 subjects for cMEM).

SD values at group level were decreasing when increasing number of trials, starting, for data outside the scanner with median values of 22 mm for single trial data (for both cMEM and MNE), and reaching a plateau at around 14 mm (for cMEM) and 19 mm (for MNE) for a subaverage of 20 trials. The *SD* scores outside the scanner were significantly lower compared to the ones inside the scanner for averages of 5 and 10 trials for cMEM and when averaging more than n=10 trials for MNE (Wilcoxon RankSum test, $p < 0.05$, Bonferroni corrected). The number of averaged trials had little effect on the *SD* scores for MNE, indicating that increasing SNR did not benefit the spatial dispersion of MNE. On the other hand, for cMEM the *SD* decreased from a median of 22 mm to 14 mm as increasing number of trials. At the single subject level, we observed overall the same patterns as for the group level, with little effect of the number of trials seen for MNE, and a progressive decrease for cMEM, suggesting that when increasing the SNR, cMEM was able to recover more accurately the spatial extent of the underlying generators.

Regarding distant spurious localizations at the group level, *RSA* values decreased significantly when increasing the number of trials, for both data acquired inside and outside the scanner, ranging from 87 % to 29 % for data inside and from 72 % to 7.7 % for data outside for cMEM. *RSA* values were ranging from 76 % to 62 % for data inside and from 76 % to 51 % for data outside for MNE. *RSA* values were found significantly higher inside the scanner when compared to data acquired outside for all subaverages in cMEM and for subaverages of 10 and 40 trials for MNE (Wilcoxon RankSum test, $p < 0.05$, Bonferroni corrected). Importantly, we found considerably lower *RSA* scores for cMEM when compared to MNE in all conditions (inside and outside, for all number of trials larger than 10). At the single subject level, one could observe a consistent pattern, i.e. a constant decrease of *RSA* values when increasing the number of trials, for MNE. However, for cMEM, we could observe some larger discrepancies in *RSA* values when comparing data recorded inside and outside the scanner (S6, S8, S10, S12, S13 and S14), suggesting the influence of remaining MR artifacts impacting source localization results. On the other hand, for few other subjects, very low *RSA* scores were found in both conditions (S2, S5, S7, and S9).

6.3.3 Illustration with single subject level analyses

Figure 6.5 provides an illustration of the results obtained for two subjects (S2 and S8), when considering a subaverage of n=20 trials.

In subject S2, EEG signals and the reconstructed sources were similar in both conditions

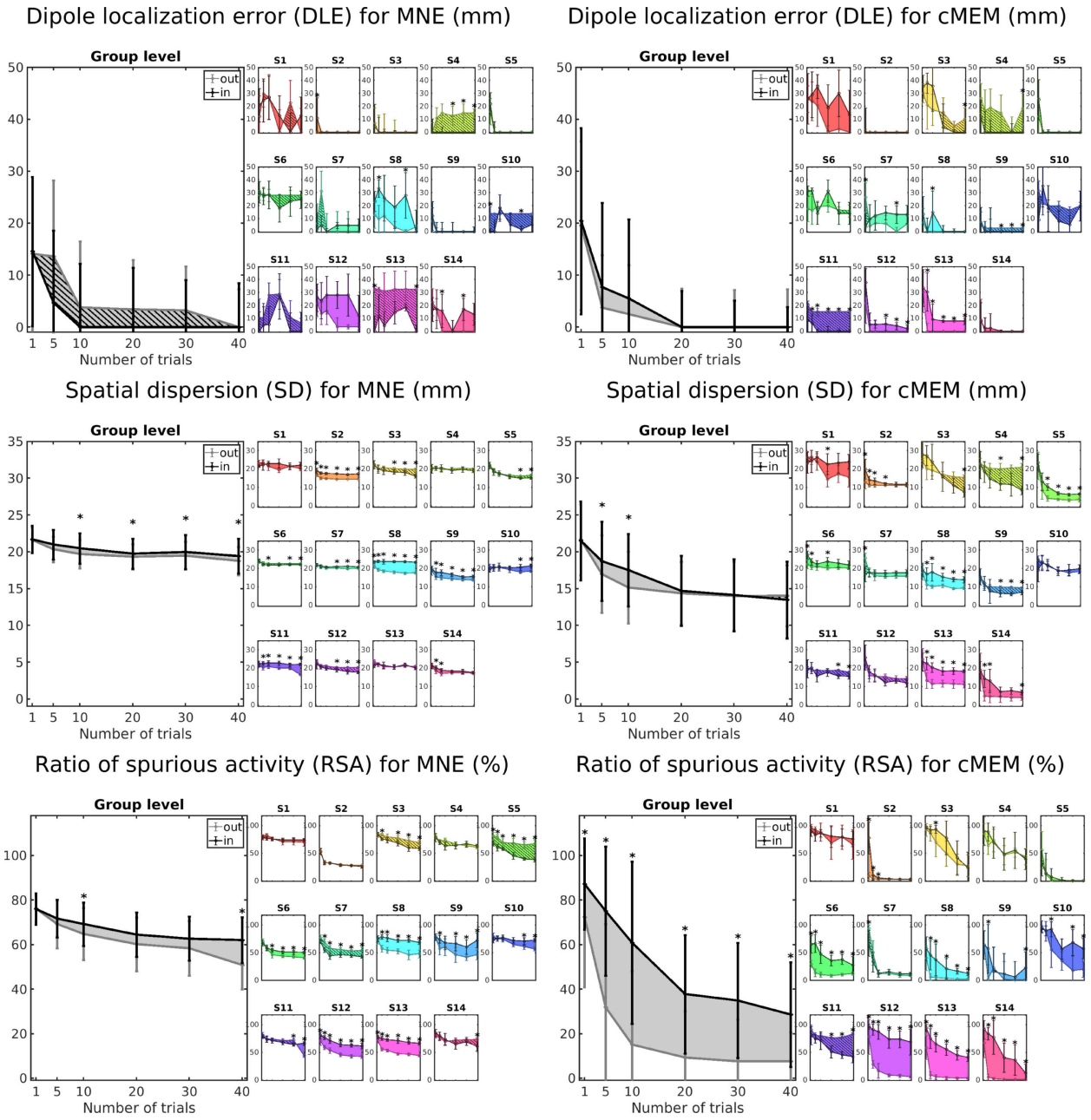

Figure 6.4: (A) Dipole Localization Error (*DLE*), (B) Spatial Dispersion (*SD*) and (C) Ratio of Spurious Activity (*RSA*) as a function of the number of trials for cMEM reconstructions. For each subfigure, the left panel is the subject average whereas the right panel depicts the results for each individual subject. Each sample point represents the median +/- interquartile range. The dark line and light line represent the data inside and outside the scanner, respectively. A plain color was used between the two curves when the corresponding metric exhibited better performance outside versus inside the scanner. On the other hand, hatchings were used between the two curves when the metric exhibited better performance inside versus outside the scanner. For group and single subject and for each level of subaveraging, Wilcoxon RankSum was used to compare metrics obtained inside and outside the scanner. (*: $p<0.05$, Bonferroni corrected.).

(inside and outside the scanner). Indeed, SNR and Corr scores were high for data recorded inside and outside the scanner (SNR: 12.2 outside compared to 16.0 inside; Corr: 0.94 outside compared to 0.86 inside). Source reconstructions were also similar, as illustrated by the small differences in *DLE* and *SD* values between each condition. cMEM exhibited a clear localized focus in the lateral occipital region (with $DLE = 0$ mm in both conditions, and $SD = 12.0$ mm inside and 11.3 mm outside the scanner), whereas MNE presented a more diffuse reconstruction in the same region (with a maximum in the lateral occipital region, as indicated by a zero *DLE* score in both conditions, and *SD* values of 17.4 mm inside and 15.0 mm outside the scanner). However, the *RSA* scores were found slightly higher for data outside the scanner (2.7 % for cMEM and 23 % for MNE for data recorded inside, compared to 3.2 % for cMEM and 32 % for MNE for data recorded outside the scanner). These possible distant spurious sources were more likely generated by the anterior positivity in the topography, which is probably caused by remaining artifacts, as for instance remaining eye blinks artifacts.

Subject S8 was an example that showed highly degraded EEG signals inside the scanner when compared to data acquired outside the scanner, confirmed by the drop in SNR from 12.7 outside to 3.6 inside the scanner. However, the topographies obtained in both conditions were still very similar and characterized by similar levels of spatial correlation with the reference (Corr of 0.79 outside versus 0.72 inside). For data acquired outside the scanner, cMEM found the maximum of activity in the lateral occipital region ($DLE = 0$ mm), while recovering accurately the spatial extent of the generator and exhibiting very little distant spurious activity ($SD = 11.0$ mm and $RSA = 3.2$ %). On the other hand, MNE found the maximum activity slightly outside the region of interest ($DLE = 14.6$ mm). This error in localization also impacted the spatial dispersion measure ($SD = 19.6$ mm), whereas MNE also exhibited distant spurious sources ($RSA = 58$ %). Inside the scanner, cMEM still performed well despite the low quality of the EEG data ($DLE = 0$ mm, $SD = 16.8$ mm, $RSA = 33$ %), and found a source in the lateral occipital region, which is consistent with the EEG topography. In this situation, MNE failed to localize activity in the occipital region ($DLE = 37.4$ mm, $SD = 26.0$ mm, $RSA = 81$ %).

6.3.4 Group level analysis

Figure 6.6 shows the EEG grand average from all the subjects for EEG recorded inside and outside the MRI and the corresponding group level fMRI analysis. The P100 peaks from each subject were realigned and centered at 0 ms (Figure 6.6). Individual source models were coregistered to a template segmentation of the cortex (Colin27) using Freesurfer registered spheres. All the individual subject average EEG signals and their corresponding source

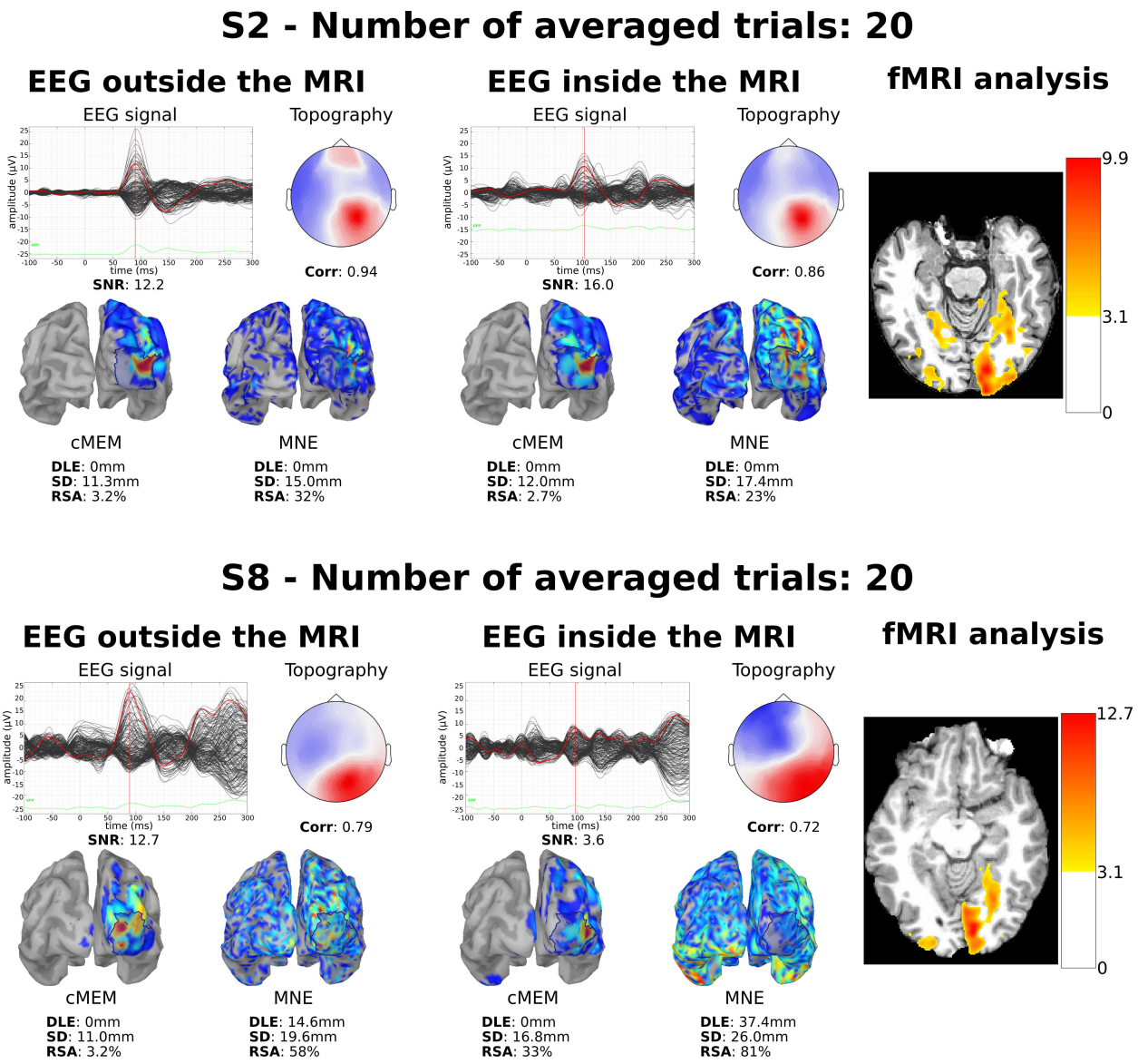

Figure 6.5: Illustration of the EEG signal, topography and source reconstruction using cMEM and MNE of the P100 peak for two subjects for n=20 averaged trials. For all the figures, the blue outline represents the reference lateral occipital region. The EEG signal shows a butterfly plot of all the EEG channels. The tracing highlighted in red corresponds to O2 electrode. All sources were normalized for visualization purposes and sources whose amplitude was found below 10 % of the maximum were discarded. The corresponding fMRI analyses of the subjects are also presented (t map, clusters corrected using Random Field Theory, Z threshold: 2.3, Cluster threshold: $p < 0.001$).

imaging maps were averaged to obtain the sensor-based and source-based grand average data. The EEG source grand averages in both conditions were localized in the right lateral occipital region with both cMEM and MNE. Overall the SNR and topography correlation were excellent (SNR: 46.5 outside versus 24.8 inside; Corr: 1.00 (which was expected as this correlation was the reference) outside versus 0.97 inside). For data acquired outside the

scanner, cMEM found the maximum of activity in the lateral occipital region ($DLE = 0$ mm), while recovering accurately the spatial extent of the generator and however exhibiting some distant spurious activity ($SD = 14.7$ mm and $RSA = 19$ %). MNE found the maximum activity slightly outside the region of interest ($DLE = 5.67$ mm). The spatial dispersion was however similar to cMEM ($SD = 16.1$ mm), but MNE exhibited more distant spurious sources ($RSA = 34$ %). Inside the scanner, cMEM and MNE found their sources inside the region of interest ($DLE = 0$ mm), but cMEM outperformed MNE in term of SD (10.8 mm versus 20.5 mm for MNE) and RSA (20 % versus 53 % for MNE). The group average fMRI analysis, however, showed a maximum activation in the calcarine gyrus in the medial occipital region (V1). The discrepancy between the EEG sources (lateral occipital) and the fMRI results cluster (medial occipital) is further discussed in the next section.

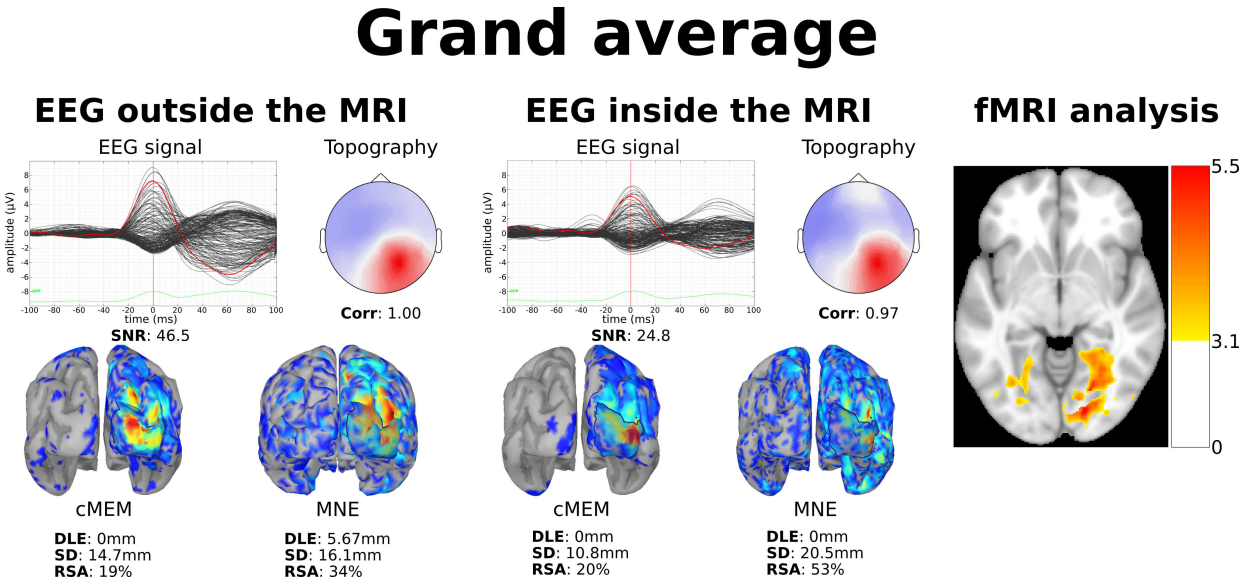

Figure 6.6: Grand average using all non-discarded trials from all subjects of averaged EEG signal, topography and source reconstruction using cMEM and MNE of the P100 peak. All sources were normalized for visualization purposes and sources whose amplitude was found below 10 % of the maximum were discarded. The fMRI analysis represents the group average of the fMRI BOLD response (t map, clusters corrected using Random Field Theory, Z threshold: 2.3, Cluster threshold: $p < 0.001$).

6.4 Discussion

The main objective of this study was to carefully assess the performance of two source imaging techniques, MNE and cMEM, in two conditions, when considering hdEEG data recorded inside and outside the MRI scanner, while varying the SNR level using different levels of partial trial averaging.

The overall results using a well-controlled visual protocol demonstrated that accurate source reconstructions could be achieved from hdEEG acquired inside the scanner, despite the overall decrease in EEG quality. We aimed at studying the effect of the MR-related noise on the accuracy of EEG source reconstruction, while varying the SNR level by assessing ESI for different levels of trial averaging. The effect of the number of trials on the SNR of EEG evoked potentials has been shown in the literature in some early studies (Nakamura et al., 1988; Turetsky et al., 1988), however, to the best of our knowledge this idea was never investigated in the context of simultaneous EEG-fMRI acquisitions. Even after considering several "standard" preprocessing steps to reduce the influence of MR-related artifacts, the EEG inside the scanner was still found degraded, as demonstrated by a drop in SNR and topography correlation when compared to EEG data acquired outside the scanner. This decrease in the overall EEG quality can be explained by the presence of residuals of MR-related artifacts. However, at the group level, we reported almost no significant differences (or little effect) in ESI accuracy, even when using these lower quality EEG data, when considering the location and extent of the main generator, as illustrated by similar *DLE* and *SD* metrics for data recorded outside and inside the scanner. Unlike *DLE* and SD, we did observe an increase in *RSA* scores inside the scanner, which indicated increased activity distant from the presumed occipital generator, when localizing noisier hdEEG data recorded inside the scanner. Therefore, even after careful artifact removal software procedures, MRI related artifacts tend to reduce the SNR and the accuracy of the EEG topography of the evoked response. However, they only slightly affected the localization error and spatial spread around the presumed region of interest, whereas we found an increase level of distant spurious activity in the source reconstruction maps.

Overall MNE and cMEM demonstrated similar values of DLE, whereas cMEM outperformed MNE, effectively reducing spurious activity around the source (*SD* metric) or at distant location (*RSA* metric). These results are in agreement with our previous studies comparing MNE and cMEM on synthetic and real data for EEG and MEG (Grova et al., 2006a; Chowdhury et al., 2013, 2015; Heers et al., 2015; Chowdhury et al., 2016; Hedrich et al., 2017). Therefore, our present study suggests that ESI could indeed be considered for hdEEG data acquired inside the MRI scanner and opened the possibility to study the source imaging results of non-averaged events along with the corresponding BOLD response, as long as the SNR is sufficient large.

It is worth mentioning that residuals from MR-related artifacts were still present and did impacted source localization results, especially through the presence of distant spurious localization. Those artifacts were mainly generated in the temporal regions, therefore probably had lesser impact on the accuracy of ESI for generators located in the occipital cortex. In

other conditions, involving more frontal or temporal generators, these residuals MR related artifacts would more likely influence the accuracy of ESI results. In this context, several efforts have been deployed to improve the accuracy and efficiency of artifact removal procedures, proposing either hardware-based (LeVan et al., 2013; Chowdhury et al., 2014; Abbott et al., 2015; van der Meer et al., 2016b) and software-based solutions (Vanderperren et al., 2010) in the recent years. Studying the impact of these promising approaches on ESI was out of the scope of this study and will be considered in future investigations.

To the best of our knowledge, this work is the first study carefully evaluating the accuracy ESI using hdEEG data recorded inside the MRI scanner, while comparing performances with ESI applied to hdEEG acquired outside the scanner. Few other studies actually investigated the possibility to perform ESI from EEG data acquired inside the scanner, i.e. when considering MR-corrupted EEG data (Brookes et al., 2008; Groening et al., 2009; Vulliemoz et al., 2009; Centeno et al., 2017; Boutin et al., 2018), but without a direct comparison with ESI from good quality EEG recorded outside the scanner. In Brookes et al. (2008), beamformer source localization was applied on 32 channels EEG data recorded simultaneously with fMRI during a visual stimulation protocol. They showed that the spatial filter inherent to beamformer methods was able to filter out the ballistocardiogram and residual gradient artifact efficiently by comparing the power spectra of scalp EEG electrodes and the estimated beamformer virtual electrodes. In Groening et al. (2009), the authors combined ESI and fMRI to study pediatric epilepsy patients, concluding that ESI helped to differentiate BOLD responses corresponding to propagating sources versus early sources during interictal epileptic discharges. They used LAURA (Local autoregressive average) ESI algorithm on EEG data acquired from 30 channels. Although Brookes et al. (2008) and Groening et al. (2009) were providing very interesting and promising results that are also in agreement with our findings, the low number of EEG channels used for ESI and the low numbers of subjects considered in both studies (two subject in Brookes et al. (2008) and four subject in Groening et al. (2009) were a limiting factor. Another study on 53 epileptic pediatric patients showed that spatial concordance between ESI (LAURA method, with 64 electrodes) and fMRI responses to epileptic discharges was a better predictor of postsurgical outcome (Centeno et al., 2017). However, the study focused on the comparison between ESI and fMRI and their clinical relevance, but not on the accuracy of ESI when recorded simultaneously with fMRI. The authors tested the concordance between ESI and fMRI where we focused on the assessment of the accuracy of ESI using the data recorded outside the scanner as reference. We validated the accuracy of ESI technique by varying the level of SNR, i.e. by varying the number of trials averaging. It is therefore difficult to compare the results in Centeno et al. (2017) to the present study. In Vulliemoz et al. (2009), by comparing ESI of interictal epileptic discharges

using LAURA with 32 to 64 EEG channels and fMRI BOLD responses, the authors were able to differentiate the BOLD clusters corresponding to the onset of the epileptic discharges from the BOLD clusters related to propagation of the discharges. These results were in line with our own findings comparing BOLD response to EEG and MEG source imaging from data not simultaneously acquired with MRI (Heers et al., 2014). Moreover, the good concordance between ESI applied inside the scanner and the BOLD cluster indicated a good quality of ESI reconstruction inside the scanner. Furthermore, the same group (Vulliemoz et al., 2010a) used LAURA on the continuous EEG signal recorded during an fMRI analysis and used the source signal in the fMRI analysis. They demonstrated that continuous ESI could help localizing the irritative zone (Vulliemoz et al., 2010a). Finally, Boutin and colleagues (Boutin et al., 2018) performed source imaging on spindles during EEG-fMRI sleep recordings using 64 sensors and MNE as source imaging technique, providing a spectral analysis of deep regions at the time of the spindles. However this study was not able to assessed the performance of the spectral analysis of ESI results in the scanner. All these studies showed the versatile and powerful potential of using ESI at the time as fMRI analysis. It is important to note that except Brookes et al. (2008), all of these studies were investigating spontaneous brain activities with considerably larger amplitudes than evoked potentials, such as interictal epileptic discharges or sleep spindles. Therefore, the effect of SNR on the quality of the localization has not been evaluated in these studies, whereas this validation is one of the main contributions of our present study.

As a controlled experiment for this validation study, we considered a visual stimulus paradigm, using the presentation of a radial checkerboard in the left hemifield. The results for our source reconstructions, when considering hdEEG data acquired inside or outside the scanner, were found located in a dorsal part of the occipital lobe. These activations were not in direct spatial concordance with corresponding fMRI analyses, since BOLD responses were exhibiting the largest activation in the V1 region, close to the calcarine sulcus (see Figures 6.5 and 6.6). As suggested in Souza et al. (2013) and Odom et al. (2004), pattern onset/offset and pattern reversal actually produce different evoked potentials. Pattern reversal elicits N75, P100, and N135 components while pattern onset elicits C1, C2 (also named as P1), and C3 (also named as N1) components. Therefore, the component we analyzed in this study with EEG was actually the P1 component. However, since only 500 ms after the pattern onset there was a pattern reversal, we suspect the slow hemodynamic responses for both pattern onset and pattern reversal were contributing together to fMRI activations, resulting in mainly V1 BOLD response. Furthermore, studies have shown that while the earlier C1 component of the pattern onset, were generated in the medial occipital V1 region, the later components, especially the P1 component, studied here, have been shown to arise from

more ventral occipital regions (Di Russo et al., 2002, 2005; Whittingstall et al., 2008) in agreement with our findings. Therefore, we can conclude that our EEG source localization results and the anatomical reference we considered for ESI evaluation were in agreement with this literature. The topography of the EEG recorded in this study was very similar to the one presented in Mayhew et al. (2013), who performed a similar protocol. Despite this spatial discrepancy we observed between ESI and fMRI results, this visual task proposed within an event-related design was chosen for a better control on the total number of trials to average. To further investigate this issue, for one of the subjects (S14), we also considered another visual paradigm, using a block design experiment. Instead of considering only the onset of the checkerboard stimulation, this block design was focusing on the visual response elicited by the phase reversal of the checkerboard. When considering an average of n = 550 phase reversal trials, the resulting averaged evoked response exhibited an excellent SNR of 32.6 outside the scanner and 16.6 inside the scanner. The corresponding P100 source exhibited source generators located in the ventral occipital region (Figure 6.7), in better agreement with fMRI results and consistent with the literature (Cottereau et al., 2011). These findings confirmed the good localizations of the generators of event-related ERP in this study, reinforcing the claim that it is feasible to perform ESI from hdEEG acquired in the scanner.

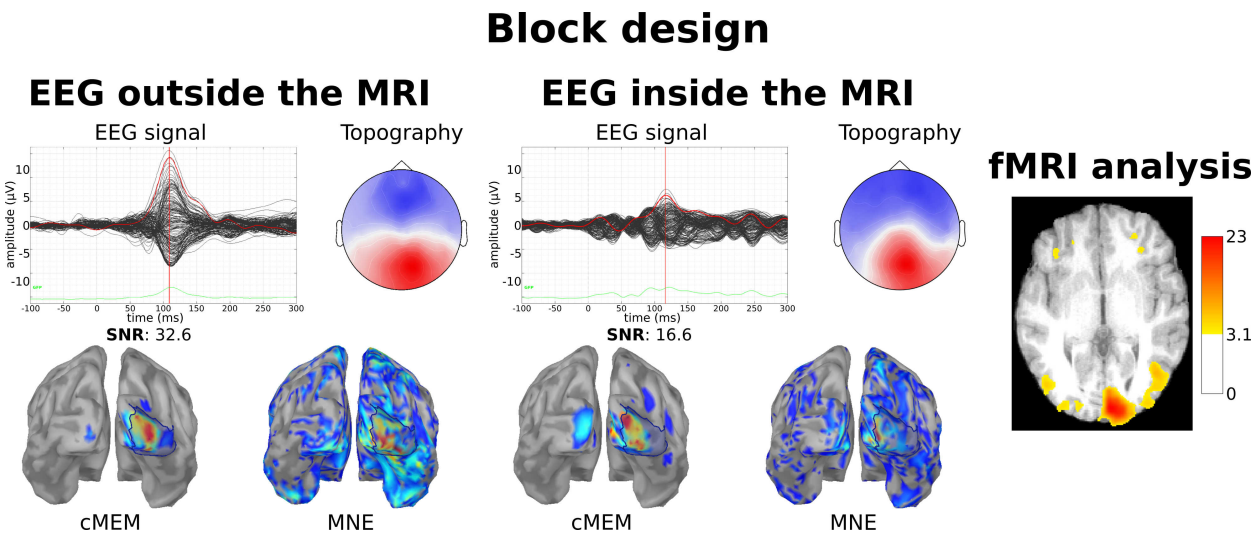

Figure 6.7: Example of a subject (S14) using a visual block design showing EEG signal, topography and source reconstruction using cMEM and MNE of the P100 peak. All sources were normalized for visualization purposes and sources whose amplitude was found below 10 % of the maximum were discarded. The fMRI analysis represents the group average of the fMRI BOLD response (t map, clusters corrected using Random Field Theory, Z threshold: 2.3, Cluster threshold: $p < 0.001$).

6.5 Conclusion

We compared visual evoked potentials inside and outside the scanner with two source imaging techniques (MNE and cMEM). Studying evoked potentials allowed us to control the SNR by varying the number of trials averaged. We assessed the quality of the EEG signal at the scalp level (using SNR and correlation measures) as well as the overall quality of hdEEG source reconstructions, in terms of localization error, spatial dispersion and amount of distant spurious activity. We showed that even if the EEG quality was degraded in the high-magnetic environment, the accuracy of source reconstructions remained similar for data acquired outside and inside the scanner, although more spurious activity was found when localizing hdEEG acquired inside the scanner, resulting in noisier reconstructions. Our study also confirmed the overall excellent performance of cMEM, especially in term of spatial dispersion and sensitivity to distant spurious localization, for hdEEG data acquired inside the scanner. This study proves that source imaging inside the scanner is feasible and accurate, even at relatively low SNR, therefore opening the possibility to compare accurately brain activity localized using EEG and the corresponding hemodynamic response elicited by fMRI analysis during simultaneous hdEEG-fMRI sessions.

Chapter 7

Manuscript 3: Automatic classification of interictal epileptic discharges based on electrical source imaging for the EEG-fMRI analysis of patients with focal epilepsy.

Context

Using well-controlled stimulation paradigms, we demonstrated in Chapter 5 that cMEM had a good spatial resolution and we have shown in Chapter 6 that it was a good candidate to perform ESI on hdEEG data recorded during an fMRI experiment. The goal of this final manuscript is to take advantage of the accuracy of ESI using cMEM in the context of the presurgical evaluation of patients with epilepsy introduced in Chapter 4. To do so, we proposed a method using ESI of IEDs to improve fMRI analysis. We have demonstrated in Chapter 6 that, when the SNR was large enough, source localization of averaged evoked responses was feasible in the scanner. We then assumed that similar level of SNR and therefore similar ESI performance could be obtained when localizing spontaneous IEDs, or at least when considering local averaging of those events to ensure a sufficiently large SNR. To use the additional information brought by the ESI reconstructions, we developed an automatic clustering technique that classified IEDs according to their source maps. Those clusters of IEDs were then used to build the corresponding regressors for fMRI analysis and compared with standard manual classification IEDs, which required a significant amount of time and was operator-dependent. All the acquisitions were performed at the McConnell Brain Imaging

Centre in McGill University, and the patients were recruited thanks to the help of Dr Gotman and his team.

The manuscript is currently in preparation and is soon to be submitted for publication: **T. Hedrich, H. M. Khoo, A. Koupparis, C. Abdallah, J. Gotman, and C. Grova. Automatic classification of interictal epileptic discharges based on electrical source imaging for the EEG-fMRI analysis of patients with partial epilepsy.** ***In preparation.***.

Abstract

Background: Combined electroencephalography (EEG) and functional magnetic resonance imaging (fMRI) is an important method for the pre-surgical investigation of patients with focal epilepsy. Interictal epileptic discharges (IEDs) are usually manually detected and classified on scalp EEG traces, therefore allowing one to study the corresponding fMRI response to every type of discharge. The classification of IEDs is a crucial step in the fMRI analysis, and an incorrect classification can lead to a decrease in sensitivity of the method. This study proposes an automatic IED clustering which groups events based on the results of electrical source imaging (ESI).

Methods: Eight patients were recruited and underwent simultaneous high-density EEG (256 electrodes) and fMRI recordings. IEDs were detected manually and then source imaging was performed using coherent Maximum Entropy on the Mean (cMEM). Source results were then classified using a hierarchical clustering technique with the Earth mover's distance as clustering metric. IED classes detected with the automatic clustering algorithm were used to define regressors within the framework of fMRI statistical analysis using a general linear model. Resulting fMRI clusters exhibiting the most significant responses were compared to the ones when defining regressors using standard manual classification of IED events. A presumed clinical reference was defined for each patient, based on seizure semiology and other available imaging techniques, and the level of spatial concordance with fMRI and ESI results was evaluated qualitatively at a sub-lobar level.

Results: From all eight patients, the automatic clustering algorithms detected 10 IED classes, for which the ESI location was found concordant with the presumed clinical reference in 6 out of 10 cases, and partially concordant in 2 out of 10 cases. Regarding corresponding fMRI results, fMRI analysis obtained for 7 out of 10 regressors defined using IED classes were found concordant with the presumed clinical reference, whereas no significant fMRI response was found for 3 out of 10 cases. Overall, considering either automatic or manual classification, we found an ESI localization and its corresponding most significant fMRI cluster to both be

concordant with the clinical reference for 6 out of 8 patients. Moreover, we showed that fMRI analyses obtained when using IED classes identified with the automatic clustering algorithm exhibited t-values similar overall to those obtained when using manual classification and larger t-values, when compared to random IED classifications.

Conclusions: This study showed that automatic clustering based on ESI, exhibited similar results to manual classification and better performance than random classification. Such technique offers a method to classify IED which is less subjective and less time-consuming for the epileptologist and therefore can help facilitating the process of EEG-fMRI analysis.

7.1 Introduction

For patients with drug-resistant focal epilepsy, surgery may be considered if the epileptogenic focus is precisely localized. Electrical source imaging (ESI) and simultaneous electroencephalography and functional magnetic resonance imaging (EEG-fMRI) are two neuroimaging techniques that may provide clinically relevant information on the epileptogenic focus, by localizing the generators of transient Interictal Epileptic Discharges (IEDs) (Pittau et al., 2014).

EEG-fMRI is a non-invasive technique that can measure the hemodynamic response elicited by the generation of IEDs (Mulert and Lemieux, 2010; Gotman and Pittau, 2011). fMRI is a whole-brain imaging technique that records the Blood Oxygen Level Dependent (BOLD) signal, which is sensitive to the local amount of deoxyhemoglobin (van Graan et al., 2015). In epilepsy, EEG, when recorded conjointly with fMRI, is usually used as a marker to detect IED events. The timing of the events is then convolved with the canonical hemodynamic response function, and then used as regressors in a general linear model (GLM) to detect the BOLD changes associated to these events. The regions exhibiting significant positive or negative BOLD responses are therefore related to the generation of epileptic discharges (Grova et al., 2008; Heers et al., 2014), their eventual propagation patterns (Vulliemoz et al., 2009) and remote influence, as for instance on the default mode network (Gotman et al., 2005). The region exhibiting the most significant BOLD cluster has been suggested to be a good indicator of the presumed epileptogenic focus (Heers et al., 2014; Khoo et al., 2017).

On the other hand, electrical source imaging (ESI) uses scalp EEG information to localize the underlying generators of the such bioelectrical activity recorded during epileptic events (He et al., 2018). Contrary to fMRI, ESI is a direct imaging technique of neuronal activity, but is mainly sensitive to sources located in the neocortex (Baillet et al., 2009). ESI was proven to be a reliable approach in terms of localization of the epileptogenic focus especially when considering source localization of IEDs (Brodbeck et al., 2011; Chowdhury et al., 2016,

2018; Mouthaan et al., 2019).

In general, both imaging techniques are performed during different sessions, where ESI was applied to EEG data acquired outside the scanner, in less difficult conditions. Most comparisons between ESI and EEG-fMRI results were notably reported from two separate acquisition sessions (Grova et al., 2008; Heers et al., 2014; Pittau et al., 2014; Lei et al., 2015). However, EEG recorded during an fMRI experiment can also be used for ESI, if a sufficient number of electrodes was used during the the EEG-fMRI recording and if special care was brought to clean the EEG data from MRI-related artifacts (Abreu et al., 2018a). A few studies have already pointed out the advantage of using both imaging techniques simultaneously in epilepsy (Centeno et al., 2017). Indeed, the concordance between both imaging techniques increases the accuracy of the prediction of the seizure outcome (Centeno et al., 2017). It was also shown that ESI was able to help distinguishing the epileptic discharge onset from the propagation pattern in fMRI (Vulliemoz et al., 2009; Groening et al., 2009). The detection of IEDs from scalp EEG data is a primordial step for the EEG-fMRI data analysis in epilepsy (Gotman and Pittau, 2011). However, a patient might exhibit different patterns of discharges and it is usually essential to classify IEDs into different categories for the EEG-fMRI data analysis (Gotman et al., 2004; Curtis et al., 2012). IEDs are often manually detected by expert epileptologists, using scalp EEG traces, and then classified into different types, based on the topography, the morphology of the EEG anomalies and their duration. fMRI analysis could then be performed considering one regressor for each IED type to determine one BOLD response per regressor, since the hemodynamic response might vary between each pattern of discharges and might involve different anatomical regions. Both spike detection and classification are operator-dependent and often offer poor reproducibility (Webber et al., 1993; Sharma et al., 2017). Moreover, inaccuracy in IED classification, as well as adding spurious IEDs or missing IEDs of interest, notably due to MR-related noise, can lead to errors during the estimation of the BOLD response (Flanagan et al., 2009). Indeed, grouping inconsistent IEDs together will decrease the statistical power of the GLM analysis since the events erroneously included in the same regressor should not correspond the same hemodynamic response. Therefore, one can expect that such inaccuracies of the GLM model might result in false positive BOLD responses, while reducing the sensitivity of the true response. This important issue may partly explain why fMRI responses to IEDs are often associated to a large number of significant BOLD clusters distant from the presumed focus (Heers et al., 2014). It is indeed not clear whether those distant BOLD responses could result from the propagation of EEG discharges (Vulliemoz et al., 2009), distant BOLD correlations (Gotman et al., 2005; Khoo et al., 2017) or false positive spurious detections. An automatic clustering of the IEDs called *wave_clus*, based on a selection of a few EEG channels, was

already used for EEG-fMRI analysis, and was shown to be a reliable alternative to manual classification (Pedreira et al., 2014; Sharma et al., 2017, 2019). However, this automatic IED classifier used only scalp traces and not ESI reconstructions. In this study, we hypothesize that source imaging could help distinguishing the different types of IEDs and therefore improve the IED classification required for fMRI analysis.

The purpose of this study was to present a reliable alternative to a manual classification, using a automatic clustering of IEDs using ESI results. We first proposed a method based on hierarchical clustering of the sources, using ESI results localized using the coherent Maximum on the Mean (cMEM) technique (Amblard et al., 2004; Chowdhury et al., 2013, 2016). We then applied our method on simultaneous EEG-fMRI data acquired from eight patients with focal epilepsy. We compared the accuracy of the fMRI statistical maps and ESI results by assessing their sublobar spatial concordance with a clinical reference localizing the presumed epileptogenic zone. We considered fMRI results obtained using either the standard manual classification or the automatic clustering of IEDs using the t-value of the most significant cluster (Khoo et al., 2017).

7.2 Material and Methods

7.2.1 Patient selection

The study was performed in agreement with the Helsinki Declaration of 1975 (and as revised in 1983), was approved by the Research Ethics Board of the Montreal Neurological Institute and a written informed consent was obtained from all participants. Eight patients with focal epilepsy were recruited (Table 7.1). Inclusion criteria were: (i) diagnosis of focal epilepsy; (ii) presence of frequent ($>$ 10 IEDs per hour) IEDs on telemetry; (iii) well-defined focus based on clinical history and seizure semiology, EEG features and anatomical MRI data.

7.2.2 Data acquisition

All acquisitions were conducted at the McConnell Brain Imaging Center of the Montreal Neurological Institute. High-density EEG data was recorded using a 256-electrode Philips Neuro system (Eugene, OR, USA) at a sampling rate of 1000 Hz. Electrocardiography was also recorded using two additional electrodes placed on the chest. For safety reasons allowing EEG recording inside the MRI, each electrode was equipped with an additional 10 kΩ resistance. We visually evaluated that good data quality was achieved by maintaining the EEG impedances below 70 kΩ as suggested by the manufacturer.

Table 7.1: Patient table. Abbreviations: L: left, R: right, mTLE: mesial temporal lobe epilepsy, TLE: temporal lobe epilepsy, FTLE: frontal temporal lobe epilepsy, P: parietal, F: frontal, T: temporal, P: parietal, O: Occipital, C: central, HME: hemimegalencephaly, FCD: focal cortical dysplasia, ACC: anterior cingulate cortex, H: heterotopia, AH: amygdalohippocampectomy

	Age/Sex	**Epilepsy syndrome**	**Topography of IEDs**	**MRI Lesion**	**Previous surgeries**	**Outcome**
1	31/F	L mTLE	L FT	None	*n/a*	*n/a*
2	38/M	R FTLE	1- bi F 2- L F 3- R F	R HME	1- R F 2- R FT 3- R F	Engel III
3	23/F	L FTLE	1- L F 2- bi F 3- L post. T	None	*n/a*	*n/a*
4	26/F	L FTLE	L FT	L ACC FCD	1- L ant. T 2- L ACC 3- L ACC	Engel IV
5	28/M	R TLE	1- R TP 2- R TPO	R T FCD	*n/a*	*n/a*
6	37/M	R FTLE	R FT	None	R F	Engel II
7	48/M	L TLE	L FT	L TO H	1- AH 2- L T	Engel IV
8	35/F	R P & R FTLE	1- R FT 2- R FCT	R P FCD	R P	Engel II

All MRI sequences used in this study were already reported in previous studies (Gotman and Pittau, 2011; Fahoum et al., 2013; Khoo et al., 2017). A T_1-weighed anatomical acquisition was obtained (1×1×1 mm^3, 192 sagittal slices, 256×256 matrix, TE = 2.98 ms, TR = 2.3 s, flip angle 9 °). The functional data was acquired in runs of 6 min using a T_2*-weighted echo-planar imaging sequence (3.7×3.7×3.7 mm^3 voxels, 33 slices, 64×64 matrix, TE = 25 ms, TR= 1.9 s, flip angle 90 s°). Patients were instructed not to move and to stay with eyes closed, resting during the acquisition.

7.2.3 EEG Preprocessing

MR-related artifacts (gradient and pulse artifacts) were corrected using averaged artifact subtraction method (Allen et al., 1998, 2000) using BrainVision BrainAnalyzer2 software (Brain Products, Munich, Germany). For some patients, Independent Component Analysis was used to remove remaining artifact residuals by manually discarding artifactual components based on their topographies and rhythmicity (Nakamura et al., 2006). A 1–70 Hz band-pass filter was then applied.

After preprocessing, EEG data was screened visually and marked by an expert epileptologist to detect epileptic events, considering a subset of 25 electrodes using a monopolar and bipolar montages (10-20 montage, plus F9, T9, P9, F10, T10, and P10), using the same number of electrodes as in previous EEG-fMRI reported studies from our group (Gotman and Pittau, 2011; Fahoum et al., 2013; Khoo et al., 2017).

7.2.4 Electrical source imaging

To perform ESI, only the first 6-min runs that contained a cumulative number of fewer than 300 IEDs were considered to reduce computation time, since our proposed method requires a pair-wise comparison between the sources of each single event. Each event was then segmented into a window of 2 s around the event and DC correction was applied, considering a baseline window from -1 s to -0.2 s. Electrodes located on the face and on the neck (76 channels) as well as any other potential noisy channels were excluded for further analysis. All the remaining electrodes were re-referenced to an average reference.

For each patient, a distance matrix between each event was calculated. The measured distance was the Euclidean distance of the spatial topography at the peak of the IED, using for each patient a subset of electrodes of interest (around 70 electrodes), i.e. the electrodes displaying the maximum amplitude at the peak of the average IED. Each IED was averaged with its four closest IEDs to increase signal-to-noise ratio (Hedrich et al., Under Review).

Each of these local averages were then considered for ESI, allowing an ideal trade-off between single event source localization and accurate localization at a good signal-to-noise ratio.

The source space consisted in a tessellated mesh of the cortical surface segmented based on the mid-line between gray-white matter interface and the pial surface, subsampled to around 8000 vertices, estimated using Freesurfer (Reuter et al., 2012) and Brainstorm software (Tadel et al., 2011). All dipolar sources in the distributed source model were oriented perpendicularly to the cortical surface.

EEG sensor positions were estimated using the Geodesic Photogrammetry System, which consists in a structure composed of 11 cameras, developed by Philips Neuro, and its dedicated software. The position of the electrodes was then coregistered to the scalp surface of the participant using a surface matching algorithm withing Brainstorm software

The forward model assessing the contribution of every dipolar source to EEG sensors was computed using the Boundary Element Method (BEM) proposed by Kybic et al. (2006). The gain matrix was calculated using a 3-layer BEM model consisting in the inner skull, outer skull and head surface (respective conductivity: 0.33 S/m, 0.0165 S/m, 0.33 S/m). The calculations were done using the OpenMEEG implementation (Gramfort et al., 2010) in Brainstorm software.

Source imaging was applied using coherent Maximum Entropy on the Mean (cMEM) (Amblard et al., 2004; Chowdhury et al., 2013) using a time window of 40 ms around the peak of each sub-averaged IED. The noise covariance was estimated using a time window of -1000 – -100 ms before the peak. cMEM is an empirical Bayesian approach developed in our laboratory which was carefully validated using simulations (Grova et al., 2006a; Chowdhury et al., 2016), evoked potentials (Hedrich et al., 2017, Under Review) and clinical data (Pellegrino et al., 2018; Chowdhury et al., 2018). The implementation of cMEM algorithm considered in this study is available as a plug-in in Brainstorm software and a tutorial describing its use is available on: http://neuroimage.usc.edu/brainstorm/Tutorials/TutBEst. For further methodological details on cMEM implementation and validation, the reader is referred to Chowdhury et al. (2013).

7.2.5 Automatic clustering of IEDs

For each patient, the Earth's mover distance (EMD) was used to perform a pairwise comparison of the source reconstructions of all the local subaverages. EMD was computed with ESI results at the peak of the discharge, defining a metric for the automatic IED clustering based on ESI results. EMD is a measure that was first used in image reconstruction (Pele and Werman, 2009; Rubner et al., 2000) but was also introduced in neurosciences for EEG/MEG

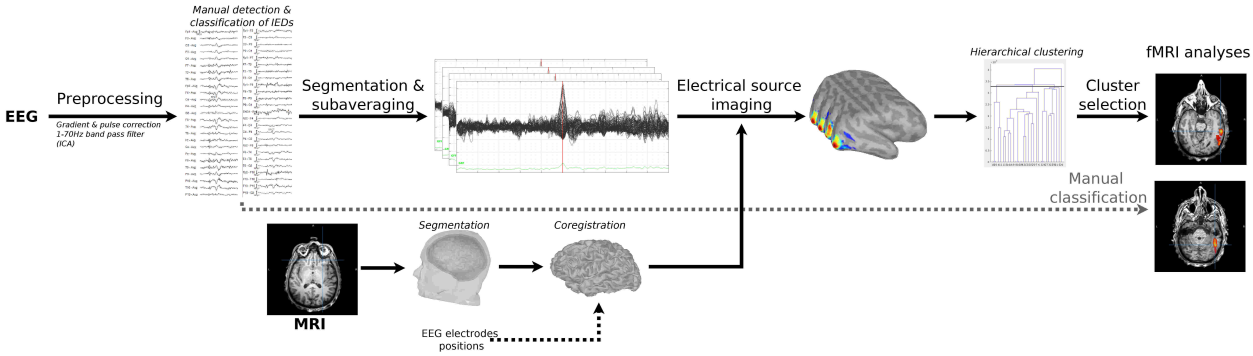

Figure 7.1: Diagram describing the method of this paper.

source reconstruction analyses in Haufe et al. (2008). In this measure, the source amplitude is considered as either a stack of earth for one source reconstruction, or a collection of holes for the other source. The EMD measures the least amount of work needed to fill the holes with earth, where the work is the product between the amount of earth which was transported and the ground distance covered. In our case, the ground distance was the geodesic distance along the cortical surface.

To measure EMD, source amplitudes below 10 % of the maximum were discarded and then the remaining amplitudes were normalized so that the sum of all amplitudes were the same, which is a prerequisite for the following algorithm. In these conditions, calculating EMD is similar to solving a transportation problem, that was solved using a least-cost algorithm (Klein, 1967). The least-cost algorithm for two amplitudes maps, one source $\boldsymbol{j}_s$ ("the stacks") and one target $\boldsymbol{j}_t$ ("the holes"), given the geodesic distance d, is computed as follows:

1. Set the cost c to 0

2. Select the dipolar sources with non-null amplitudes $(\hat{a}, \hat{b})$ with minimal distance:

$$(\hat{a}, \hat{b}) = \underset{(a,b)}{\arg\min}\, d(a, b), \text{ where } \boldsymbol{j}_s(\hat{a}) > 0 \text{ and } \boldsymbol{j}_t(\hat{b}) > 0 \tag{7.1}$$

   where $d(a, b)$ is the geodesic distance between the dipolar sources of indices a and b, or the Euclidean distance when a and b were not located in the same hemisphere.

3. Reduce as much amplitude as possible from the source and the target and add it to the cost:

$$\begin{aligned} m &= \min(\boldsymbol{j}_s(\hat{a}), \boldsymbol{j}_t(\hat{b})) \\ \boldsymbol{j}_s(\hat{a}) &\leftarrow \boldsymbol{j}_s(\hat{a}) - m \\ \boldsymbol{j}_t(\hat{b}) &\leftarrow \boldsymbol{j}_t(\hat{b}) - m \\ c &\leftarrow c + d(\hat{a}, \hat{b}) \times m \end{aligned} \tag{7.2}$$

4. Repeat from step 2 until $\boldsymbol{j}_s = \boldsymbol{j}_t = \mathbf{0}$

The EMD distance matrix was then used as a metric to perform a hierarchical clustering algorithm, similarly as in Chowdhury et al. (2018). Agglomerative hierarchical clustering was implemented using MATLAB R2019a "linkage" function, using the shortest distance to calculate distance between clusters. To determine the number of clusters, we used a visual inspection of a break in the evolution of the cluster linkage values, as recommended in Martinez and Martinez (2005). The clusters containing fewer than 5 events were discarded, and the others were used as regressors in the fMRI analysis.

7.2.6 fMRI analysis

The fMRI analysis was similar to previous studies (Khoo et al., 2017). Two fMRI analyses were considered, for the first one, the regressors were built from IED types that were classified manually. For the second analysis, we used our the IED types of our automatic clustering. Events with duration were manually classified but were not included in the automatic clustering algorithm. For the fMRI analysis, the events with duration, such as bursts of rhythmic activity or polyspikes, of a certain manual class were added to the automatic cluster whose cluster source average was closest to the manual class source average, since they were not suitable for standard ESI. For each IED class identified (manually or automatically), the corresponding regressor was obtained by convolving each event with four hemodynamic response function (HRFs) peaking at 3, 5, 7, and 9 seconds. The GLM analysis was performed with fMRIstat (Liao et al., 2002) to obtain a statistical t-maps. A combined t-map was created for each regressor by taking, at each voxel, the t-value with the highest absolute value from the four t-maps created with the four HRFs as described and evaluated in (Bagshaw et al., 2004). The combined map was first thresholded using an uncorrected $t > 3.1$ (or $t < -3.1$, i.e. $p < 0.001$), before correcting for multiple comparison with a topological false discovery rate (FDR) of 0.05.

7.2.7 Evaluation of clinical concordance

The ESI results and the most significant BOLD cluster provided by either the manual or the automatic IED classification were reported. The maximum of ESI was located in a sublobar atlas (see Figure 7.2), and was checked for concordance to the clinical reference. The presumed clinical reference was defined by patient history, semiology and other imaging techniques. Each result was characterized as **Concordant (C)**, when the maximum of the ESI map or the most significant BOLD cluster were located in the same sublobe of the

clinical reference; **partially Concordant (pC)**, if a secondary ESI local maximum or if any significant BOLD cluster was concordant with the clinical reference, or **Discordant (D)**.

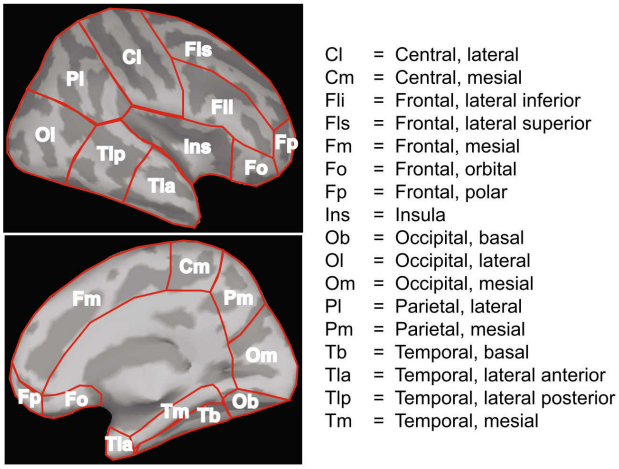

Figure 7.2: Sublobes used to determine concordance with the clinical reference.

To test whether the automatic clustering algorithm provided better statistical performance than chance, we additionally generated for each patient one hundred random IED clusterings. A random cluster was composed of the same number of IED clusters as the automatic clustering, with the same number of events in each cluster, but the composition of the IED cluster was randomly selected among all the marked events of the patient. Therefore, a similar number of events was discarded from fMRI analysis, both for the automatic and the random clustering (but not the same events were discarded in both conditions). The timing of IEDs corresponding to these random IED clusters were then used to build regressors for fMRI analysis. The t-values of the maximum BOLD cluster from all the 100 random clustering were reported and compared to the maximum t-value of the automatic clustering. To do so, we calculated how many random cluterings exhibited a higher t-value than the one obtained with the automatic clustering, and computed the maximum percentile of t-values larger than the t-value obtained by the automatic IED clustering.

The whole proposed methology is illustrated in Figure 7.1.

7.3 Results

7.3.1 Clinical relevance

The comparison between ESI and fMRI analysis results using the manual and automatic classification of the IEDs are summarized in Tables 7.2 and 7.3. The range of detected IED for the patients was between 18 and 282 (median: 58.5). Among the 8 patients, four of them had frontal-temporal lobe epilepsy, three of them had temporal lobe epilepsy, in which one had mesial temporal lobe epilepsy. The last patient, patient 8, had two focuses: one focus in the parietal lobe and one focus in the frontal-temporal lobe (See Table 7.1).

When considering manual IED classification (Table 7.2), 14 IED classes were found for the 8 patients resulting in 1.75 classes on average per patient. The corresponding ESI localization was found concordant with the estimated epileptogenic zone in 10 out of 14 of the IED classes, and partially concordant in 3 out of 14 cases. The fMRI most significant cluster was found concordant with the clinical reference in 7 out of the 14 IED classes, discordant for 1 out of 14 cases, and no significant clusters were found for 6 out of 14 cases. In 6 patients out of 8, at least one manual class was found concordant with the clinical reference in both ESI and fMRI BOLD.

Concerning the automatic classification, 10 IED classes were found resulting in 1.25 classes on average per patient. The corresponding ESI localization was concordant with the estimated epileptogenic zone in 6 out of 10 of the IED classes, and partially concordant in 3 out of 10 IED classes. The fMRI most significant cluster was found concordant with the clinical reference in 7 out of the 10 IED classes, and no significant cluster was found for 3 out of 10 cases. In 6 patients out of 8, at least one automatic IED class was found concordant or partially concordant with the clinical reference in both ESI and fMRI BOLD (For Patient 7 , the ESI results exhibiting a peak in RTla region were also partially concordant with the clinical reference, by exhibiting a secondary generator in the same LTla region found by fMRI analysis). The automatic clustering method discarded 2–26 events (2.4 % – 17.9 % of the total events for the patients). These discarded events were therefore not considered for further fMRI analysis. Those events were discarded because they were part of clusters with fewer than 5 events. With fewer IED events in the fMRI analysis, one could expect a decrease in the statistical power of the resulting BOLD clusters. We did not observe such an effect on statistical power in our analysis, since the maximum t-value of the BOLD clusters were similar between the analyses using the manual and the automatic classification algorithms. This might indicate that these discarded events did not negatively influence the fMRI results.

The relevance of the automatic clustering was further tested using random clusterings, using the same size of cluster than the automatic clustering. For each IED class of the

Table 7.2: Result table for manual IED classification. In the table are referred the estimated epilepsy syndrome, the number of IED classes identified by the epileptologist, the ESI focus with a color indicating the concordance with the clinical reference (Concordant, partially concordant and discordant) as well as the number of IED events (with or without duration) corresponding to each class. The location of the most significant BOLD cluster was also reported, with the same color code as the location of the ESI focus, as well as their most significant (maximum or minimum) *t*-values. The gray line indicated no significant cluster. L: left; R: right; bi: bilateral; mTLE: mesial temporal lobe epilepsy, TLE: temporal lobe epilepsy, FTLE: frontal temporal lobe epilepsy, P: parietal; the sublobar location acronyms are presented in Figure 7.2

Patient number	Epilepsy syndrome	Number of IED types	ESI focus	Number of IED events (+ events with duration)	Location of most significant BOLD cluster	Maximum *t*-value
1	L mTLE	1	bi Cl (**D**)	41+8	L hip (**C**)	6.25
2	R FTLE	3	L Fp (**pC**) / L Fp (**pC**) / R Fp (**C**)	14+0 / 2+0 / 2+0	— / — / —	*n.s.* / *n.s.* / *n.s.*
3	L FTLE	3	L Tla (**C**) / L Tla (**C**) / L Tla (**C**)	154+307 / 15+14 / 5+9	L Fp (**C**) / L Ins (**D**) / —	-23.44 / 8.43 / *n.s.*
4	L FTLE	1	L Tla (**C**)	54+4	L Ins (**C**)	7.86
5	R TLE	2	R Tla (**C**) / R Ol (**pC**)	149+31 / 97+5	R Tlp (**C**) / —	7.17 / *n.s.*
6	R FTLE	1	R Tlp (**C**)	182+64	R Tla (**C**)	7.53
7	L TLE	1	L Tlp (**C**)	32+11	L Tlp (**C**)	-6.03
8	R P & R FTLE	2	R Fo (**C**) / R Fo (**C**)	19+7 / 9+24	— / R Fo (**C**)	*n.s.* / 10.17

patients, the corresponding distribution of the *t*-value of the most significant BOLD cluster for the fMRI analysis of each random clustering is reported using boxplot representation in Figure 7.3. The actual maximum *t*-value of the most significant BOLD cluster of the fMRI analysesobtained with the automatic clustering technique was compared to those values (indicated as a dot Figure 7.3). In 6 out of 8 patients, in at least one of the IED clusters, the *t*-values obtained with the automatic clustering were higher than the third quartile of the *t*-values obtained with the random clusterings. In patient 2, significance of the fMRI maps was not obtained with the automatic classification, but was observed in 21 out of 100 random analyses, but none of them exhibited a fMRI BOLD response in concordance with the clinical reference. In two patients (Patients 5 and 8), two IED clusters were found by the automatic clustering algorithm. The fMRI analysis using the automatic IED clustering of the second cluster (containing fewer events than the first cluster) did not show any significant BOLD cluster and displayed a significant BOLD cluster for only 6 out of 100 random analyses for Patient 5, where only half of the 6 significant BOLD clusters were in concordance with the clinical reference, and for 2 out of 100 random analyses for Patient 8, showing no concordance with the clinical reference.

7.3.2 Representative cases

Patient 5 (Figure 7.4) is a 28 year old male with an extensive focal cortical dysplasia on the right temporal lobe, clearly identified on the anatomical MRI. Two types of IED events

Table 7.3: Result table for automatic IED clustering. In the table are referred the estimated epilepsy syndrome, the number of IED classes identified by the epileptologist, the ESI focus with a color indicated the concordance with the clinical reference (Concordant, partially concordant and discordant) as well as the number of IED events (with or without duration) corresponding to each class, and the number of discarded IED events. The location of the most significant BOLD cluster was also reported, with the same color code as the location of the ESI focus, as well as their most significant (maximum or minimum) t-values. The gray line indicated no significant cluster. L: left; R: right; bi: bilateral; mTLE: mesial temporal lobe epilepsy, TLE:temporal lobe epilepsy, FTLE: frontal temporal lobe epilepsy, P: parietal; the sublobar location acronyms are presented in Figure 7.2

Patient number	Epilepsy syndrome	Number of IED types	ESI focus	Number of IED events (+ events with duration)	Discarded events (% of events)	Location of most significant cluster	Maximum t-value
1	L mTLE	1	bi Cl (**D**)	39+8	2 (4.8%)	L hip (**C**)	6.25
2	R FTLE	1	L Fp (**pC**)	15+0	3 (16.7%)	—	*n.s.*
3	L FTLE	1	L Tla (**C**)	164+332	4 (2.4%)	L Fp (**C**)	-23.92
4	L FTLE	1	L Tla (**C**)	49+4	6 (10.9%)	L Ins (**C**)	8.69
5	R TLE	2	R Tla (**C**) / R Ol (**pC**)	121+31 / 99+5	26 (10.6%)	R Tlp (**C**) / —	6.98 / *n.s.*
6	R FTLE	1	R Tlp (**C**)	172+64	10 (5.5%)	R Tla (**C**)	7.60
7	L TLE	1	R Tla (**pC**)	27+11	5 (15.6%)	L Tla (**C**)	-5.67
8	R P & R FTLE	2	R Fo (**C**) / R Tlp (**C**)	15+24 / 8+7	5 (17.9%)	R Fo (**C**) / —	10.50 / *n.s.*

were visually identified by an expert epileptologist (H.M.K.). The first IED type consisted in right temporo-parietal (RTP) spikes and waves and polyspike complexes with a maximum amplitude on electrodes T4, T6, T10 and P10 on average montage. From the EEG signals of the patient, 180 RTP IED events were marked, among them 31 consisted in bursts of such discharges and were therefore marked with a duration, whereas 149 were marked as single event discharges consisting in one spike only (modeled as a Dirac for the GLM analysis). Only marked events with no duration were considered for ESI and then IED classification.

A second type of IED discharges consisted in right temporo-parieto-occipital spike and waves discharges, involving maximum amplitude on electrodes T6, P10 and O2. This type of events was named 'RTPO'. 102 of these IED events were marked, among them 5 were bursts marked with a duration.

Results for Patient 5 are presented in Figure 7.4. When considering manual classification of IEDs, ESI results of RTP events localized a generator in the right temporal lobe, with a maximum on the middle temporal gyrus. The corresponding fMRI analysis indicated a large activation cluster over the right temporal lobe, in complete agreement with ESI results and exhibiting a maximum t-value of 7.17. ESI results of RTPO events found a right lateral occipital generation, whereas the corresponding fMRI analysis did not exhibit any significant fMRI response after FDR correction.

Using hierarchical clustering of ESI results, the corresponding dendrogram was thresholded

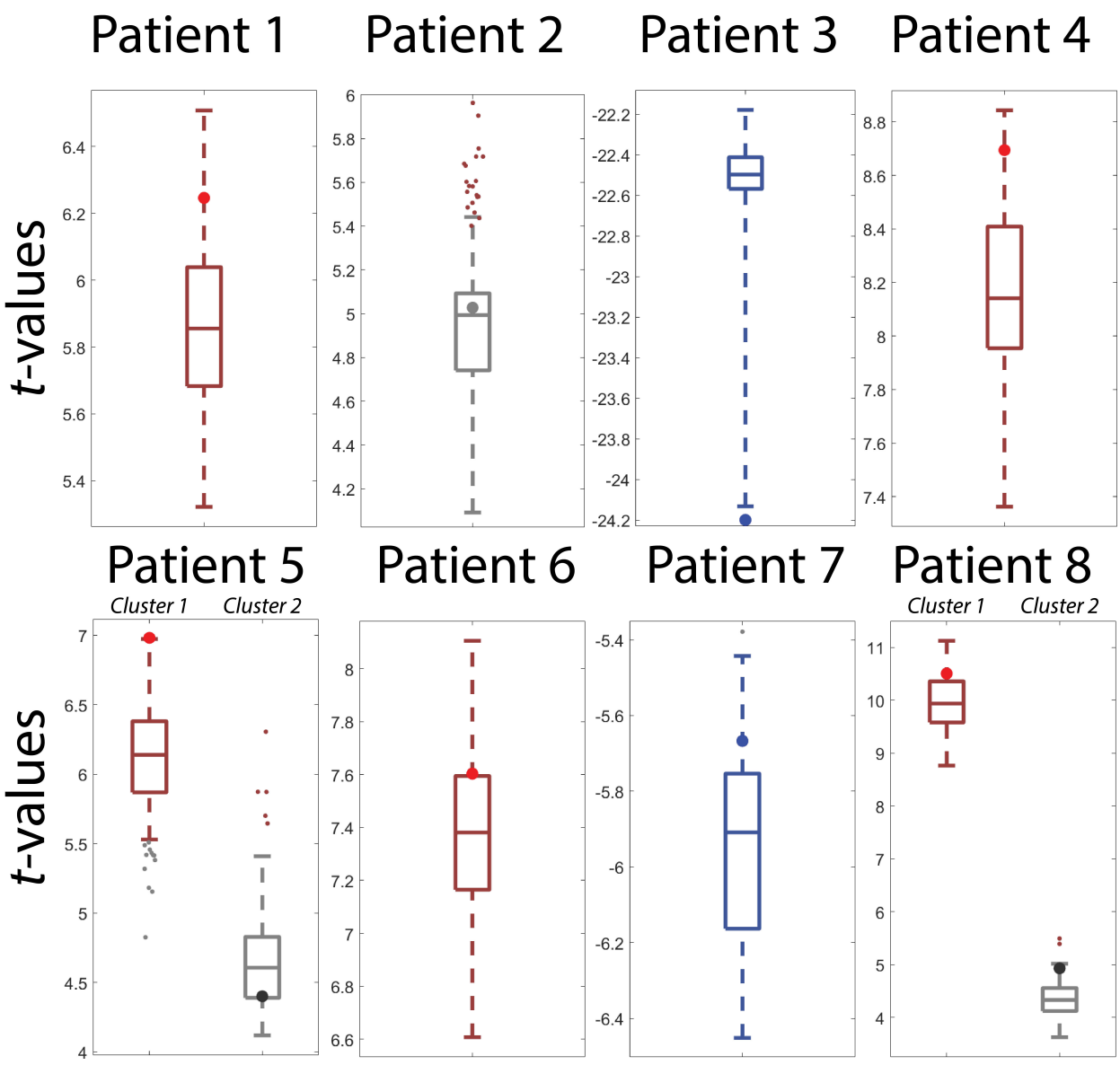

Figure 7.3: Distribution of the most significant t-values of fMRI analysis for all the 100 random clustering. Boxplot representation reporting the median value (middle line), the first and third quartiles (edges of the box) and the extrema (end of the dashed lines) of the t-value distribution. For each patient is also represented the maximum activation (red dot) or deactivation (blue dot) of the fMRI analysis of the automatic clustering. Non-significant t-values are colored in grey (level of significance: $p < 0.001$, FDR corrected). It is worth noting that the scale of t-values was different for each patient.

using the evolution of the cluster linkage values and obtained 22 clusters. Among them, only two large clusters were kept, since all the others were composed of fewer than 5 IED events, resulting in a total of 26 IED events further discarded from fMRI analysis. IED Class 1 obtained after hierarchical clustering of ESI results was composed of 121 events, among which

77 were previously manually classified as RTP and 44 as RTPO. Despite such a difference in classification, ESI results for this new automatic cluster corresponding to the RTP class were very similar to the manual class, exhibiting a right temporo-superior source. Therefore the events with duration corresponding to 'RTP' was attributed to this cluster.

The corresponding most significant fMRI cluster was located in the right temporal lobe with a maximum t-value of 6.98, very similar to the fMRI results obtained after manual classification of IEDs.

IED Class 2 obtained after hierarchical clustering of ESI results was composed of 99 events, among which among which 56 were previously manually classified as RTP and 43 as RTPO. Resulting ESI results for this class were localizing a right occipital lateral region very similar to the generator found when considering RTPO manually classified events. There were also 5 RTPO events with duration, for which ESI was not computed, those events were associated with this RTPO regressor for fMRI analysis. The fMRI analysis did not find any significant clusters.

When considering 100 random classifications consisting in 121 events for the first regressor and 99 for the second (total number of events: 220), none of the t-values obtained with the first regressor was as large as the one obtained in the first regressor using the automatic clustering, whereas only 6 out of 100 of the second regressor of the random analyses reached a significant level, in which only 3 of them were in agreement with the ESI.

Patient 8 (Figure 7.5) is a 35 year old female with a deep focal cortical dysplasia in the parietal region, associated with no IED manifestation on scalp EEG, and a diffuse lesion in the frontal-temporal lobe. Two types of IED events were visually identified. The first IED type consisted in right Fronto-temporal (RFT) spike and waves and polyspike complexes with a maximum amplitude on electrodes F8, T4, F10, and T10 on average montage. From the seven 6-minute runs selected for this study, 26 RFT IED events were marked, among them 7 consisted in bursts of such discharges and were therefore marked with a duration, whereas 19 were marked as single event discharges consisting in one spike only.

A second type of IED discharges consisted in right fronto-centro-temporal (RFCT) spike and waves discharges, involving maximum amplitude on electrodes F8, T4, F10, T10, and C4. 33 of these IED events were marked, among them 24 were bursts marked with a duration.

Results for Patient 8 are presented in Figure 7.5. When considering manual classification of IEDs, ESI results of RFT events localized a generator in the right orbito-frontal source. The corresponding fMRI analysis did not exhibit any significant fMRI response. ESI results of RFCT events found a similar source in right orbito-frontal source, whereas the corresponding fMRI analysis indicated a large activation cluster over the right orbito-frontal region, in

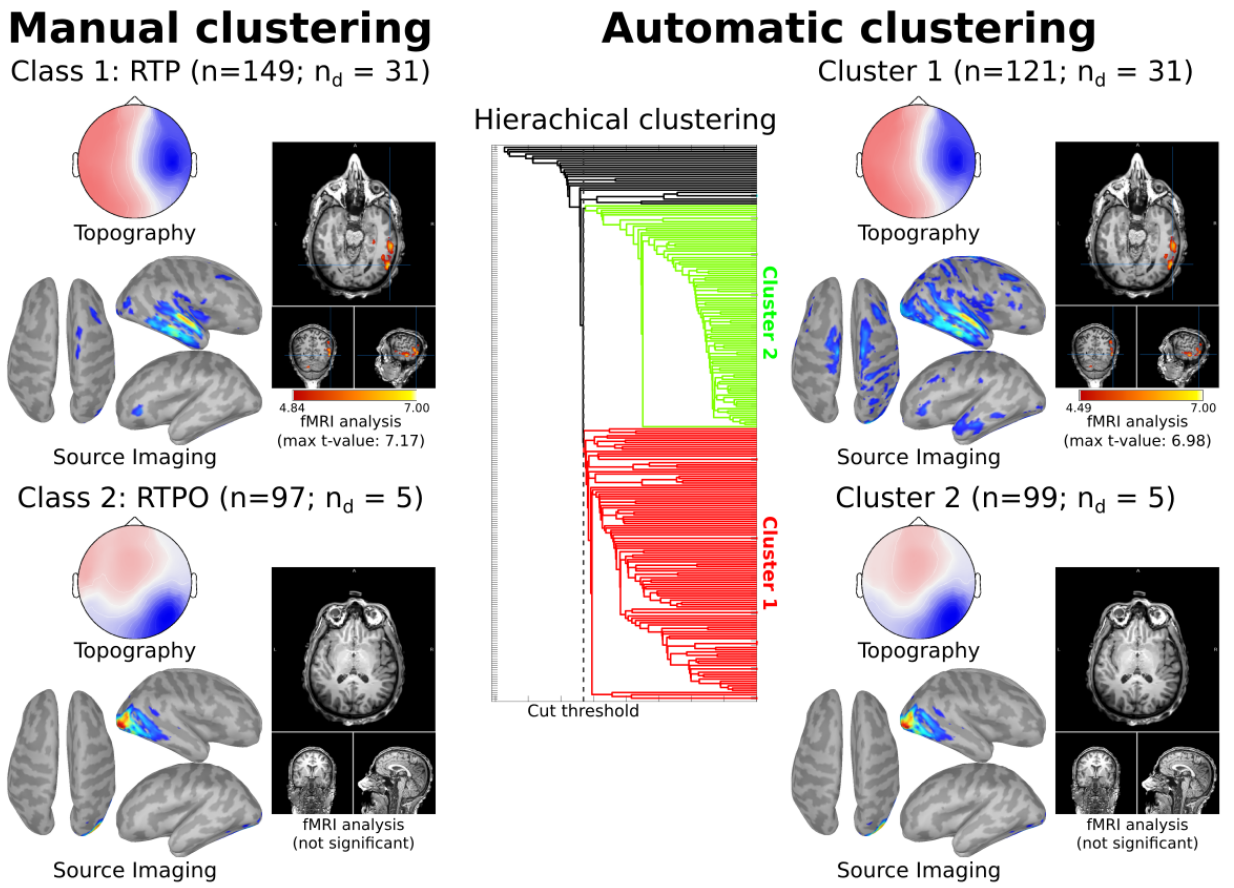

Figure 7.4: Illustration of Patient 5. The manual classifications contains two classes: RTP, composed $n = 149$ single IED events and $n_d = 31$ events with duration, and RTPO, composed of $n = 97$ single IED events and $n_d = 5$ events with duration. On the right hand side, the hierarchical clustering displays the dendrogram of all the single events, and the cut threshold. After thresholding, IED events belonging to IED clusters with fewer than 5 events were discarded (26 IED events in total). Two IED clusters contained more than 5 events and are shown on the right side: the first one containing $n = 121$, in which we added $n_d = 31$ events with duration, and the second with $n = 99$ in which we added $n_d = 5$ events with duration. For each class and IED cluster, the average topography and source imaging results using cMEM of the single events were presented, as well as the fMRI analysis using all $n + n_d$ events and centered on the most significant BOLD cluster. The source imaging map was thresholded so that only amplitudes higher than 10 % of the maximum were displayed. fMRI maps were threshold to reach a FDR of 0.05.

complete agreement with ESI results and exhibiting a maximum t-value of 10.17.

Using hierarchical clustering of ESI results, the corresponding dendrogram was thresholded using the evolution of the cluster linkage values and obtained 4 clusters. Among them, only two large clusters were kept, since the two others were composed of fewer than 5 IED events, resulting in a total of 5 IED events further discarded from fMRI analysis. IED Class 1 obtained after hierarchical clustering of ESI results was composed of 15 events, among which 10 were previously manually classified as RFT and 5 as RFCT. ESI results for this new

automatic cluster were very similar to the manual classes, exhibiting a right orbito-frontal source. This IED cluster contains the majority of the RFCT events and therefore the 24 events with duration corresponding to RFCT was attributed to this cluster.

The corresponding fMRI analysis exhibited the most significant BOLD cluster in the right orbito-frontal region with a maximum t-value of 10.50, very similar to the fMRI results obtained after the RFCT manual classification.

IED Class 2 obtained after hierarchical clustering of ESI results was composed of 8 events, among which 6 were previously manually classified as RFT and 2 as RFCT. Resulting ESI results for this class were localized in the right temporal region with a maximum value in the middle temporal gyrus and a secondary source in the right orbito-frontal region. There were also 5 RFT events with duration, those events were associated with this regressor for fMRI analysis. The fMRI analysis did not find any significant clusters.

When considering 100 random classifications consisting in 15 events for the first regressor and 8 for the second (total number of events: 23), t-values obtained in the first regressor of the automatic clustering was higher than the 85th percentile of the first regressor of the random analyses. No significant fMRI response was found for this second regressor of the random analyses, whereas only 2 out of 100 of the second regressor of the random analyses reached a significant level, in which none of them were in agreement with the ESI.

Patient 3 (Figure 7.6) is a 23 year old female with a large epileptogenic zone covering the frontal and the temporal lobe, as defined through intracranial EEG investigation, with no clear lesion seen on the MRI. Three types of IED events were visually identified. The first IED type consisted in spike and waves in the left frontal region (denoted 'F7F9Fp1'). 461 F7F9Fp1 IED events were marked, among them 307 consisted in bursts of such discharges and were therefore marked with a duration, whereas 154 were marked as single event discharges consisting in one spike only.

The second type of IED discharges consisted in bifrontal (denoted 'biF') spike and waves discharges. 29 of these IED events were marked, among them 14 were bursts marked with a duration.

The third type of IED discharges consisted in left temporal (denoted 'T5P9') spike and waves discharges. 14 of these IED events were marked, among them 9 were bursts marked with a duration.

Results for Patient 3 are presented in Figure 7.6. When considering manual classification of IEDs, ESI results of F7F9Fp1 events localized a generator in the left temporal lateral regions, whereas a secondary ESI generator covered a left frontal generator, in spatial agreement with fMRI results. The corresponding fMRI analysis exhibited a left frontal lobe deactivation with

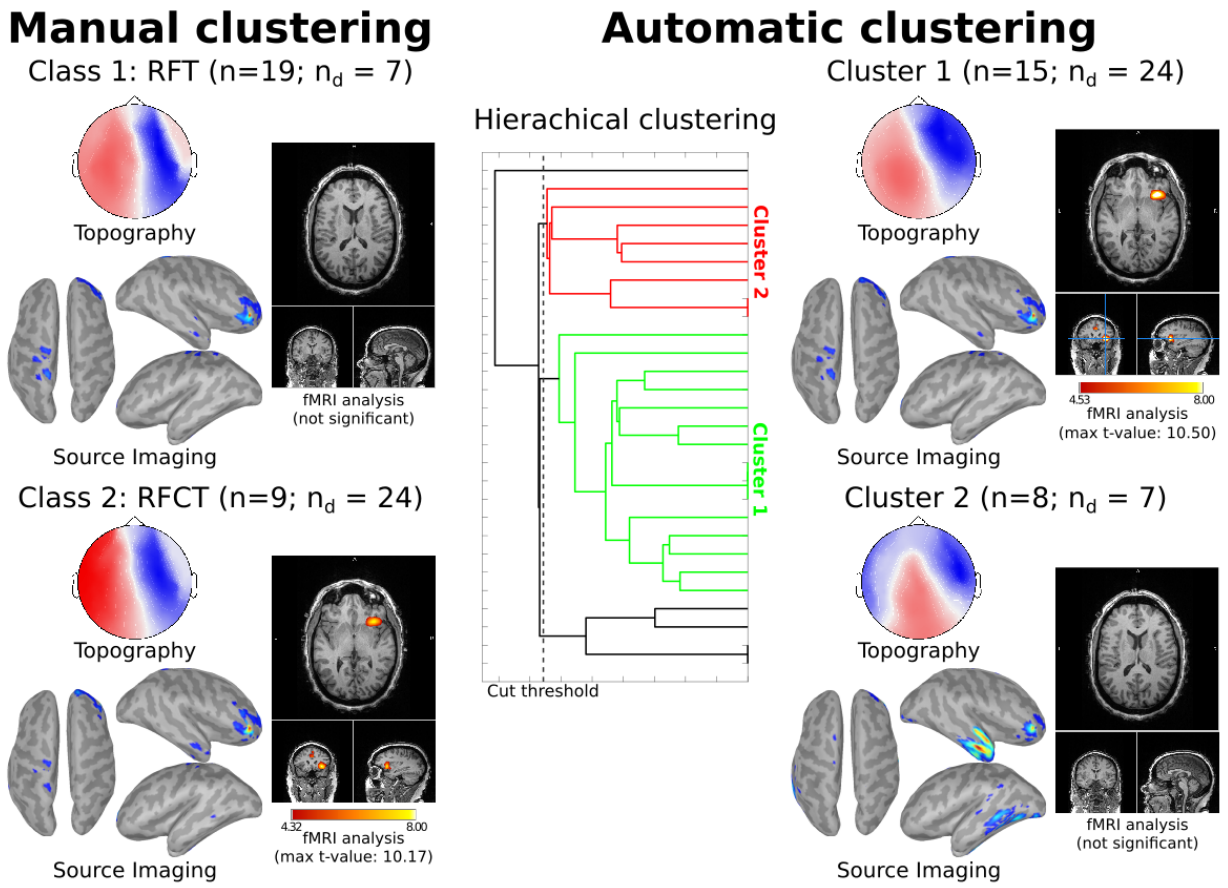

Figure 7.5: Illustration of Patient 8. The manual classifications contains two classes: RFT, composed $n = 19$ single IED events and $n_d = 7$ events with duration, and RFCT, composed of $n = 9$ single IED events and $n_d = 24$ events with duration. On the right hand side, the hierarchical clustering displays the dendrogram of all the single events, and the cut threshold. After thresholding, IED events belonging to IED clusters with fewer than 5 events were discarded (5 IED events in total). Two IED clusters contained more than 5 events and are shown on the right side: the first one containing $n = 15$, in which we added $n_d = 24$ events with duration, and the second with $n = 8$ in which we added $n_d = 7$ events with duration. For each class and IED cluster, the average topography and source imaging results using cMEM of the single events were presented, as well as the fMRI analysis using all $n + n_d$ events and centered on the most significant BOLD cluster. The source imaging map was thresholded so that only amplitudes higher than 10 % of the maximum were displayed. fMRI maps were threshold to reach a FDR of 0.05.

a minimum t-value of -23.44. ESI results of biF events found a similar source covering only the left temporal lobe, whereas the corresponding fMRI analysis showed a bilateral activation of the anterior frontal lobe, in discordance with the clinical reference with a maximum t-value of 8.43. ESI results of T5P9 events found a similar source in the left temporal lobe, whereas the corresponding fMRI analysis did not find any significant cluster.

Using hierarchical clustering of ESI results, the corresponding dendrogram was thresholded using the evolution of the cluster linkage values and obtained 7 clusters. Among them, only

one large cluster was kept, since the 6 others were composed of fewer than 5 IED events, resulting in a total of 9 IED events further discarded from fMRI analysis. The IED Class obtained after hierarchical clustering of ESI results was composed of 164 events, among which 145 were previously manually classified as F7F9Fp1, 14 as biF and 5 as T5P9. ESI results for this new automatic cluster were very similar to the manual classes, where the most significant BOLD response was found in the left temporal region. All the 332 events with duration marked for this patient were added to this cluster for the fMRI analysis.

The corresponding fMRI analysis exhibited the most significant BOLD cluster in the left frontal region with a minimum t-value of -23.92, very similar to the fMRI results obtained after the F7F9Fp1 manual classification for which this main deactivation was concordant with the secondary ESI source.

When considering 100 random classifications consisting in 164 events as regressor, the t-values obtained in the regressor of the automatic clustering was lower (i.e. more significant) than all the regressors obtained using random clusterings.

7.4 Discussion

The aim of this study was to introduce an automatic clustering technique of IEDs on EEG for the fMRI analysis in order to offer a less operator-dependent method than the standard manual classification. The method was based on the hierarchical clustering of ESI results at the peak of the IEDs, using the Earth Mover's Distance as source distance metric within a hierarchical clustering framework. The results of the automatic classification were compared to manual classification at the level of ESI cluster map and its contribution to the fMRI analysis. We also compared the fMRI results of the automatic clustering with random clustering, when considering cluster of the same size as for the automatic clustering, but with shuffled labels. In this study, 8 patients were analyzed, and we obtained overall similar results between the automatic and manual clustering. We could therefore conclude than our proposed automatic IED clustering provided similar results than the operator-dependent and time consuming manual classification. Moreover we also found that, based on the t-values of the most significant BOLD cluster, the automatic clustering performed better than random clustering.

To the best of our knowledge, automatic clustering of IED events was already proposed by only one group on EEG with 32 or 64 electrodes (Pedreira et al., 2014) and intracranial EEG (Sharma et al., 2017, 2019). In these studies, IED recordings at the sensor level were characterized by a wavelet-based technique in order to classify events based on their morphology, on some selected channels. This wavelet-based clustering method was denoted

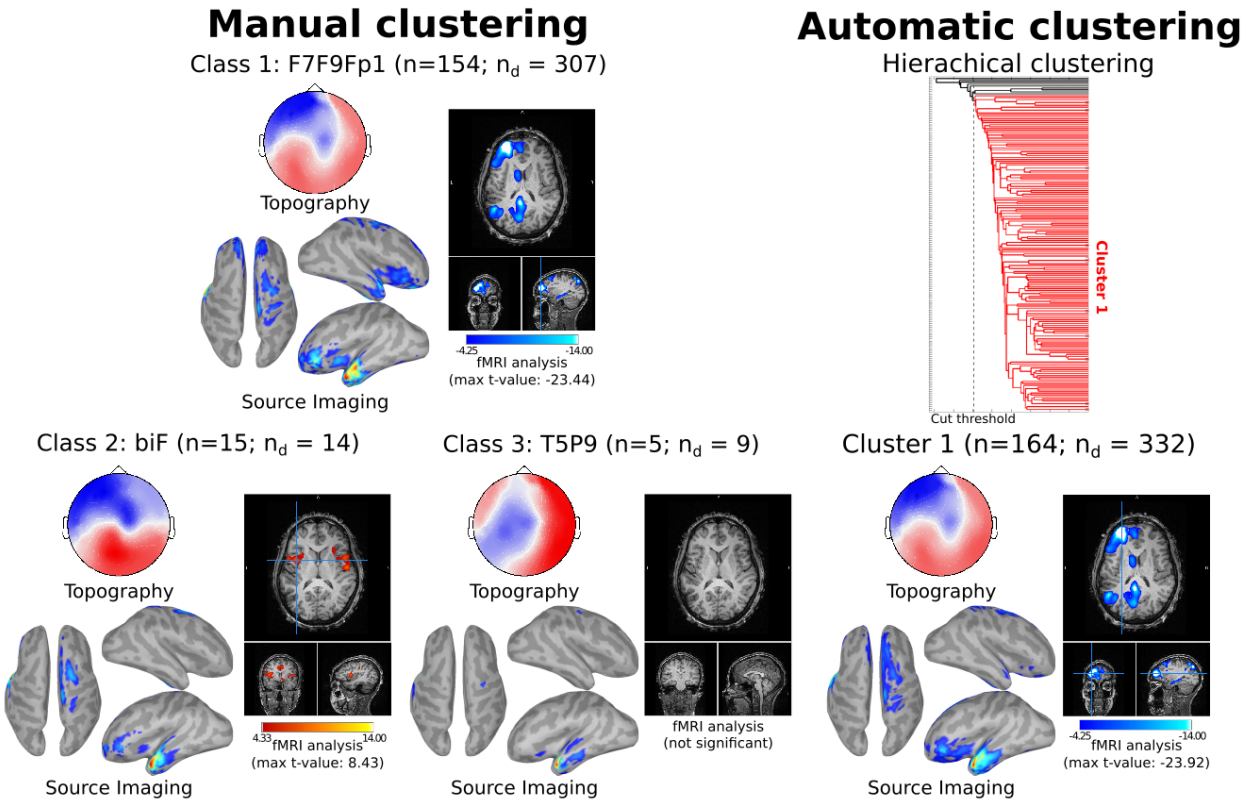

Figure 7.6: Illustration of Patient 3. The manual classifications contains three classes: F7F9Fp1, composed $n = 154$ single IED events and $n_d = 307$ events with duration; biF, composed of $n = 15$ single IED events and $n_d = 14$ events with duration, and T5P9, composed of $n = 5$ single IED events and $n_d = 9$ events with duration. On the right hand side, the hierarchical clustering displays the dendrogram of all the single events, and the cut threshold. After thresholding, IED events belonging to IED clusters with fewer than 5 events were discarded (10 IED events in total). Only one IED cluster contained more than 5 events and was shown on the right side: it contained $n = 164$, in which we added $n_d = 332$ events with duration. For each class and IED cluster, the average topography and source imaging results using cMEM of the single events were presented, as well as the fMRI analysis using all $n + n_d$ events and centered on the most significant BOLD cluster. The source imaging map was thresholded so that only amplitudes higher than 10 % of the maximum were displayed. fMRI maps were threshold to reach a FDR of 0.05.

wave_clus (Quian Quiroga et al., 2004). The results were validated using concordance between the clinical reference and the fMRI data analyses (Pedreira et al., 2014; Sharma et al., 2019) in comparison with manual classifications provided by several EEG reviewers (Sharma et al., 2017). From these studies, the authors showed using scalp EEG information that fMRI analyses using *wave_clus* was better than or similar to the manual clustering in most of the 8 studied patients (Pedreira et al., 2014) in terms of lobar concordance with the presumed epileptogenic zone. When considering intracranial EEG data acquired simultaneously with fMRI, the classification ability of *wave_clus* was tested on 5 patients and compared to

visual classifications made by 3 epileptologists, as quantified by the metric of "variation of information". the automatic classification variabity was found to fall within inter-reviewer agreement variability. Therefore the authors concluded that the automatic classification was indistinguishable from a visual classification (Sharma et al., 2017). Another study on intracranial EEG tested the concordance of the fMRI analysis based on manual and automatic classification with the resection zone of 8 patients who became seizure-free after surgery (Sharma et al., 2019). The authors found that BOLD maps for the automatic approach resulted in a larger proportion of BOLD clusters found in the vicinity of the resected area in four patients, a lower proportion in one patient, and the same proportion of concordant clusters for three remaining patients. *wave_ clus* is a technique exploiting the topography of IEDs at the EEG sensor level, using wavelet representation. The goal of our work is to test whether automatic classification using source imaging technique could be useful to guide fMRI analysis. The level of spatial agreement between the fMRI analysis obtained with the automatic clustering and the clinical reference was similar to our findings but their definition of concordance was less conservative than ours. Indeed, they used a threshold on the fMRI t-map so that $p < 0.001$, uncorrected from multiple comparison (Pedreira et al., 2014; Sharma et al., 2019), whereas we focused our analysis only on the cluster exhibiting the most significant BOLD response, as recommended by Khoo et al. (2017). Therefore we did not quantify the concordance of fMRI results for the secondary BOLD response, only the most significant response was taken into account in our sublobar concordance analysis. Moreover, the patient cohort used in both studies was different. The inclusion criteria in Pedreira et al. (2014) indicated that the patients should have at least 200 events to be selected, which was the case for only one in our patient cohort (Patient 5). Our patient cohort and the possibility for our automatic clustering technique to discard events are the possible reasons why our clustering algorithm seemed to reduce the number of clusters compared to the manual clustering. On the other hand, when using *wave_ clus*, automatic clustering had the tendency to rather increase the number of IED clusters.

The method we proposed here is based on source imaging using the cMEM technique. We have shown in our previous studies that cMEM was an excellent technique in terms of source localization of IEDs (Chowdhury et al., 2015, 2016; Pellegrino et al., 2018) and sensitivity to the spatial extent of the generators (Grova et al., 2006a; Chowdhury et al., 2013; Hedrich et al., 2017) and robustness to noisy data (Chowdhury et al., 2013; Hedrich et al., Under Review). This was the main reason why we chose cMEM as the source imaging technique to perform the automatic clustering technique. Moreover, it was proven that cMEM was a suitable technique to apply ESI on data recorded during an fMRI analysis (Hedrich et al., 2017, Under Review). In a previous study, we showed that scalp EEG signals were more

distorted by remaining high magnetic field related artifacts than ESI results (Hedrich et al., Under Review). Indeed, the SNR and the topography of the average evoked potential quality was decreased during a visual stimulation experiment. Similar performance of ESI results was found between the data recorded inside and outside the scanner. Based on this observation and the ability for cMEM to switch off inactive parcels and to reduce spurious activity, we hypothesized that IED clustering exploiting the sparsity property of cMEM sources would more likely be more discriminant than sensor-level IED clustering techniques, or source-level clustering techniques using MNE as a source localization technique This was the main reason why, in this study, the automatic classification of the IED inside the scanner was performed on ESI results and not on EEG signals. Further study would be needed to confirm the advantage of using cMEM source-based clustering techniques over sensor-based technique and other source localization methods, but fell outside the scope of the present study. However, in the same study, we also demonstrated that the signal-to-noise ratio of EEG data should be large enough to obtain reliable ESI results (Hedrich et al., Under Review). To do so, IED EEG data in this study was averaged with similar events to increase the signal-to-noise ratio. To reduce the uniformity of the EEG topographies due to averaging, each IED event was averaged with only the 4 closest IED events in terms of EEG topography of the peak.

The automatic clustering used in this study is very similar to the consensus map proposed by our group in Chowdhury et al. (2018). In this paper, we used a hierarchical clustering to gather source imaging results of the fusion between EEG and MEG single IED events. The source imaging cluster which was closest to the clinical reference was selected and considered as the consensus map. We found that for all the patients in this study, the consensus map corresponded to the cluster composed of the largest number of IEDs. The consensus map method was proposed because it was considered more reliable and robust than the global average of the sources, or the source imaging of the averaged IED events. For this study, hierarchical clustering was also used, but we considered another clustering metric, EMD, instead of the absolute correlation.

To the best of our knowledge, EMD was used in neuroimaging only once (Haufe et al., 2008) to compare magnetic source imaging results localization error. EMD was used because it provided "a meaningful measure for arbitrary types of source distributions" (Haufe et al., 2008). It is also worth noting that EMD is an important measure in image processing (Rubner et al., 2000; Pele and Werman, 2009). The important aspect of EMD is that it relies on the geodesic distance, which seems adequate for comparing source maps. Indeed if two sources were not concordant, EMD is sensitive to the geodesic distance between the sources; in other words, source maps showing discordant sources, but located in the same lobe would have a lower EMD than two source maps exhibiting sources which are located in remote

regions. For the calculation of EMD, a least-cost algorithm was used, which provides a fast but unoptimized estimation of EMD. The distances reported in this study were then overestimated. However, preliminary studies on several patients indicated such a bias did not have influence the overall clustering algorithm.

The purpose of our study was to automatically classify IEDs but not detecting them. Automatic detection of spikes is a challenging task which was already largely studied in the literature (See review in Hogan, 2011) but falls beyond the scope of this study. It has been shown that omitting true IED events and mixing true IED with non-epileptiform activity decreased the number of active voxels in the fMRI experiment (Flanagan et al., 2009). In our study, the automatic classification was able to discard events if they were too different from the other IED events in terms of EMD. On average for each patient, 10.0 % of the events were discarded without having any impact on the t-values of the fMRI analysis. From visual inspection, the events which were discarded presented a spurious source which was different from the other events.

Our study has some limitations which are worth mentioning. First of all, the events with duration were not taken into account in our classification method. This can be problematic for some patients who have numerous bursts of polyspikes, representing the majority of IED manifestations. However, source localization of epileptic events with duration is a difficult task, and the resulting source map might be different to the source imaging maps of the single events in terms of source distribution. This discrepancy can lead to the difficulty to classify events with duration along with single events, e.g. wrong classification and false rejection.

Whereas single spikes localizations of each event could still be considered within a burst of spikes with a specific duration, bursts of rhythmic activity are more complex to localize. However, bursts of rhythmic activity can also be successfully localized using different technique, such as wavelet-based MEM, which is an extension of MEM method applied after time frequency decomposition of the signals of interest (Lina et al., 2014). Consequently, strategies to take into account events with duration could be implemented in a future development of the presented automatic classification method, by focusing on the rhythmic activity of the events with duration (Pellegrino et al., 2016a; von Ellenrieder et al., 2016; Papadelis et al., 2016) or the localization of several single spikes within a burst. It is important to note here that the results presented here is simply a proof of concept of a new automatic IED clustering algorithm, and will need further investigation considering a larger cohort, and involving fewer complex cases.

The proposed automatic classification was based on the source localization results at the peak of the IEDs only. A future improvement of the classifier would be to take into account the potential propagation of the source, by using a time window instead of a single time

sample for the classification.

7.5 Conclusion

We have introduced a new automatic classification algorithm of epileptic events, based on ESI results, to guide fMRI analysis and applied this new methodology to the analysis of 8 patients who underwent simultaneous hdEEG-fMRI acquisition. The EEG-fMRI analysis using automatic classification overall exhibited fewer BOLD cluster with no significant response when compared to manual classification, therefore corresponding to an increase in fMRI sensitivity. On the other hand, specificity of fMRI analysis remained the same. In addition, we have shown that the automatic classification was better than random IED classification in terms of maximum t-values of the fMRI BOLD clusters. In summary, this new classification approach is a clinically useful tool that helps reducing subjectivity in the EEG-fMRI analysis during the presurgical evaluation of patients with focal epilepsy. This is an important finding allowing to consider a less operator-dependent approach for EEG-fMRI investigations in epilepsy.

CHAPTER 8

General discussion

8.1 Summary and limitations of main contributions

The objective of this PhD thesis was to assess the application and feasibility of ESI on hdEEG data recorded inside the MR scanner. To do so, we selected an ESI method developed in our laboratory, cMEM, and evaluated it in ideal conditions (Chapter 5). We then assessed its performance within a noisy MR environment using a visual paradigm (Chapter 6). Finally, we considered cMEM as a tool to classify interictal discharges to help the EEG-fMRI analysis of patients with epilepsy (Chapter 7).

In Chapter 5, the spatial resolution of several imaging methods was carefully evaluated using their resolution matrices (Hedrich et al., 2017). To do so, we used two metrics to measure their spatial properties: the dipole localization error, which is the distance between the estimated source and the simulated source, and the spatial dispersion, which quantifies the spatial spread around the simulated source. These metrics were used to measure two features of the resolution matrix, the point spread functions (PSF), i.e. the columns of the resolution matrix, assessing the solution of the source imaging method for the activation a single cortical dipole in ideal conditions, and crosstalk maps (CT), i.e. the rows of the resolution matrix, reflecting the influence a single dipolar source may have on the estimation of the generators in its neighborhood. We compared the resolution matrix metrics for two modalities, hdEEG and MEG using a similar number of sensors, and four source imaging techniques: cMEM, MNE and its noise-normalized variants, dSPM and sLORETA. Overall we found that DLE scores were similar for all source imaging techniques and for either PSF and CT maps, with the exception of sLORETA which was developed to have zero localization

error in PSF maps. cMEM outperformed the other source imaging techniques in terms of SD, both for PSF and CT maps. These findings indicated that all the tested source imaging techniques had the same level of localization bias, but that the spatial spread was smaller for cMEM, which made us conclude that cMEM had a better spatial resolution than the other tested techniques. Moreover, the performance of ESI was similar to the one of MSI. This is an important finding since it is the first time that ESI and MSI were compared by using a similar number of channels. The spatial resolution was further measured with an electrical median nerve experiment with five subjects. The estimated sources were compared to the hand region of the primary sensory cortex using DLE and SD. Since both metrics can be biased by remote sources, activity located far from the region of interest was discarded to calculate the metrics. A third metric, the ratio of spurious activity (RSA) was introduced to measure the influence of remote sources. The MNS data confirmed the analysis of the resolution matrix and the study on the RSA results indicated that cMEM was the source imaging technique with the lowest RSA scores, i.e. the method which was the most robust to noise. One of the limitations of the first manuscript was the fact that, since cMEM is not a linear technique, its resolution matrix did not exist. To overcome this issue, an approximation of the resolution matrix was constructed by concatenating all the measured point spread functions. Moreover, in ideal conditions, a generator composed of several dipolar sources is equal to the sum of the corresponding point spread functions. This property does not hold for cMEM but efforts were made to prove that the results found in focal generators could be extended to larger generators. The DLE and SD metrics here were calculated using Euclidean distance. The geodesic distance, i.e. the minimum distance following the cortical surface, was already used by our laboratory for the calculation of DLE (Grova et al., 2006a, 2008). In this manuscript, the Euclidean distance was preferred because it was more easily implementable. It is worth noting that the Euclidean distance and the geodesic distance were very similar measures when considering small distances from the expected generator, which was the case in this study. The results for DLE and SD were however reported using sub-millimetric precision, which was without doubt an overestimation of the precision of those metrics, given the resolution of the cortical mesh used in this study, where the mean distance between adjacent vertices was around 5 mm.

We can conclude from Chapter 5 that cMEM is a source imaging technique displaying an excellent spatial resolution. However, the results were collected in ideal condition, assuming no noise and no error in the forward model. Even if these findings were partly validated in real-life conditions with an experiment on somatosensory evoked responses in Chapter 5, we wanted to further understand the behavior of cMEM in a noisy environment. Because of this, the goal of Chapter 6 (Hedrich et al., Under Review) was to test the quality of

two ESI techniques (cMEM and MNE) on EEG data recorded in the MR scanner using a well-controlled visual stimulation paradigm. The artifacts created by the MRI environment were corrected using a software method: the average artifact correction (Allen et al., 1998, 2000). In this manuscript, the same visual stimulation experiment was performed twice, outside the scanner and then during an fMRI experiment. The quality of the EEG signal at the peak of the P100 visual potential obtained from the experiments was tested using two metrics: the SNR of the 02 channel, and the correlation of the topography with the topography of the evoked response of the group average (entitled Corr). Source imaging was then applied (using either cMEM or MNE) and three source metrics: DLE, SD and RSA, as defined in Chapter 5 (Hedrich et al., 2017), using an anatomical landmark as reference. To test the effect of the high-magnetic environment on EEG data and the source reconstruction at different SNR, the 5 metrics (SNR, Corr, DLE, SD and RSA) were calculated for different numbers of averaged evoked response (from 1 to 40). The results suggested that EEG data recorded inside the scanner had lower performance in terms of SNR and Corr, compared to data recorded outside. Concerning the quality of the source reconstruction however, no significant or low effect was observed for DLE and SD scores between the data recorded inside and outside the scanner. Conversely, RSA for cMEM was found significantly higher inside the scanner, indicating more spurious activity for source imaging results when recording during an EEG-fMRI experiment. These results indicated that the source imaging techniques were less affected by the MR-related noise, compared to the EEG signals itself. We concluded from these observations that source imaging inside the scanner was feasible. Moreover, cMEM was proven to have better performance in terms of SD and RSA when compared to MNE (the results in DLE were similar), indicating that cMEM could be a viable imaging technique for data recorded simultaneously with fMRI data. It is worth mentioning that one limitation of our proposed study could be the choice of the method used for MR-related artifacts correction. This is an important issue that was outside the scope of our proposed paper. It is important to note that MR-related artifacts mainly affect electrodes in the temporal regions. Therefore the choice of the right cleaning algorithm is less critical in our study since the artifacts have less influence on the accuracy of ESI for generators located in the occipital cortex, compared to other brain regions. In both Chapter 6 and 7, we considered the software-based method of Allen and colleagues (Allen et al., 1998, 2000) which has been validated multiple times and is still largely used today (Vanderperren et al., 2010; Masterton et al., 2007). Moreover, when artifacts were still present after this standard procedure, further cleaning was performed using independent component analysis (Nakamura et al., 2006; de Souza et al., 2013), albeit with the risk of reducing the quality of the data. In future experiments, it may be possible to use other artifact correction techniques to reduce distortion, such as such as hardware

techniques, e.g. the carbon wire loops (van der Meer et al., 2016b; Abreu et al., 2016) or other recordings to reduce the contribution of the artifacts on the EEG data (LeVan et al., 2013; Luo et al., 2014; Chowdhury et al., 2014). Finally, in this manuscript, it was difficult to measure the concordance between ESI reconstructions and fMRI analysis. As explained in the Discussion section of Chapter 6, the locations of the ESI reconstructions and the fMRI activation were different due to the visual stimulation protocol used in this paper. Even if assessing such multimodal concordance was not the main objective of the manuscript, it would have been interesting to compare the accuracy of the ESI results and the fMRI BOLD clusters, depending on the number of averaged trials. It has been shown that a block design of the same visual stimulation protocol offered an ESI source which was located in the same location as the fMRI activation Figure 6.7.

We have demonstrated in Chapters 5 and 6 that cMEM was a source imaging technique exhibiting an excellent spatial resolution (Hedrich et al., 2017), and that it was possible to obtain accurate ESI results with EEG data recorded during an fMRI acquisition (Hedrich et al., Under Review). These findings paved the way for the final project of this PhD thesis in Chapter 7 (Hedrich et al., In Preparation), which consisted of using ESI with cMEM to help the fMRI analysis on patients with epilepsy. In this last manuscript, we developed an automatic clustering technique that classified IEDs with their ESI results in order to improve the definition of IEDs regressors for the fMRI analysis. We aimed at improving the time-consuming and subjective process of IED classification to facilitate the EEG-fMRI analysis of patients with epilepsy. To do so, eight patients with focal epilepsy were recorded during a simultaneous high-density EEG and fMRI acquisition. After applying a standard denoising strategy, IEDs were detected and manually classified from EEG data by an expert epileptologist. Source imaging using cMEM was applied to each IED and an automatic clustering technique based on a hierarchical clustering was introduced. Our objective was to propose a new objective approach to classify IEDs in order to avoid the need for manual classification. The IED clusters obtained from both classification schemes (automatic and manual) were compared in terms of ESI localization. fMRI analyses were performed using the corresponding IED clusters as regressors. We then assessed sublobar concordance of ESI and fMRI results according to the clinical reference, defined by patient history, semiology and other imaging techniques. Overall, the results showed that the automatic clustering method provided fewer IED classes with similar ESI localizations and fewer BOLD clusters with no significant response corresponding to an increased in fMRI sensitivity, when compared to manual classification. We observed however no change for specificity. Moreover, we have shown that the automatic classification exhibited higher significant t-values for the resulting fMRI BOLD clusters when compared to EEG-fMRI analysis using a classification based on

IED random shuffling. These results indicate that our new classification approach could be used as a clinical tool that could help reduce subjectivity in the EEG-fMRI analysis during the pre-surgical evaluation of patients with focal epilepsy. There were a few limitations in this manuscript: first of all, we noticed that the SNR of non-averaged IEDs was too low to perform accurate ESI without averaging, when compared to IEDs acquired in less noisy conditions (Chowdhury et al., 2018). To overcome this issue, partial averages were considered, where IED were averaged to four other IEDs which were closer in terms of spatial topography at the peak. This subaveraging operator was performed to increase the SNR and produce an accurate ESI in order to obtain a reliable automatic clustering technique. Bursts of rhythmic activity and polyspikes were not included in the automatic clustering however, since specific ESI approaches should be used to localize these events, which was outside the scope of this study. This issue could have impacted our results since epileptic events with duration represented a large proportion of the marked events considered in fMRI analysis in some patients. Moreover, a clustering technique including a temporal component might be needed to differentiate different propagation patterns or the morphology of the IED. ESI was shown to be able to help distinguishing fMRI BOLD clusters corresponding to primary generators from the clusters related to propagation patterns (Vulliemoz et al., 2009; Tanaka et al., 2010). Indeed, it was shown that the generators of an epileptic discharge can propagated between the rising phase of the spike and its peak (Lantz et al., 2003b). Consequently, the future implementation of the IED classifier would include a time window including the rising slope of the spikes instead of only the peak of the spike, in order to distinguish different propagation patterns between IEDs and how different the corresponding fMRI regressors could be. Finally, given the low number of studied patients and the complexity of their epilepsy, these results would require further validation with a larger sample size.

8.2 Future directions

Throughout this PhD thesis, we validated the use of ESI inside the scanner and developed an automatic IED clustering technique based on ESI to assist fMRI analysis. This project paves the way towards better understanding of the understanding of the relationship between neuronal activity, recorded on EEG and localized with ESI, and the corresponding hemodynamic response, measured with fMRI. To do so, an interesting potential future study would be to test and compare findings obtained with ESI/fMRI data and different physiological models of neural generation of EEG signals (Garnier et al., 2016; Kameneva et al., 2017) and of neurovascular coupling (Mesmoudi et al., 2015; Blanchard et al., 2016; Mathias et al., 2017). The neural mass models aim to model the local field potentials coming from an assembly of

neurons (usually two populations of excitatory pyramidal cells, a inhibitory population of interneurons and, in recent studies, a population of astrocytes). Such modeling can enrich our understanding on brain mechanisms and are used to predict neuronal physiological and pathological behavior (Blanchard et al., 2016; Mathias et al., 2017). Similar models were used along with a physiological model of the neurovascular response to local field potential in order to simulate the BOLD response obtained in fMRI to a neuronal activity. The modeling community also proposed advanced models of neurovascular coupling (Mesmoudi et al., 2015; Blanchard et al., 2016; Mathias et al., 2017). The analysis of both ESI and fMRI from data acquired simultaneously offers the unique possibility to further understand neurovascular coupling mechanisms and therefore to confirm or invalidate predictions made by those models. The work done in this thesis, especially in Chapter 6, validated and introduced cMEM as an ESI technique suitable for performing a simultaneous and multimodal analysis of the neurovascular coupling that could assist further validation of those models.

As mentioned earlier in this thesis, special care needs to be taken to clean EEG signals from MR-related artifacts. In this thesis, EEG data were corrected from MR-related artifacts using a standard technique entitled Average Artifact Subtraction (AAS) (Allen et al., 1998, 2000), as mentioned in Chapter 3. Several other techniques have been proposed, discussed and compared in the literature (Vanderperren et al., 2010; Abreu et al., 2016). However, hardware-based solutions for artifacts removal seem to offer cleaner and more reliable results (van der Meer et al., 2016b; LeVan et al., 2013). In our group, recent investigations were made to include carbon wire loops to the high-density EEG systems to improve the artifact correction. Figure 8.1 is an illustration of our preliminary results with installing and testing the performance of artifact correction using the carbon wire loops (CWL). Five carbon wire loops were installed on a 256-electrode EEG net in order to measure the difference of potentials measures by the loops simultaneously with an EEG-fMRI analysis. The CWL are not sensitive to brain activity and record only MR-related artifacts. CWL signals were regressed out of the EEG signals using the technique proposed in van der Meer et al. (2016b). In these preliminary results illustrated in Figure 8.1, we have demonstrated that the data corrected using CWL signals seemed less distorted than when using the AAS technique. The power spectrum density of the EEG data corrected with the CWL seemed closer to the EEG recorded outside the scanner, when compared to the EEG data corrected with the AAS method.

The goal of this thesis was to obtain a good performance of ESI during an fMRI experiment. The ability of ESI obtained with hdEEG data to guide fMRI analysis was illustrated on patients with epilepsy, but the same framework could be extended to other neuroimaging applications. Indeed, analysis of ESI results and the automatic clustering technique could be of

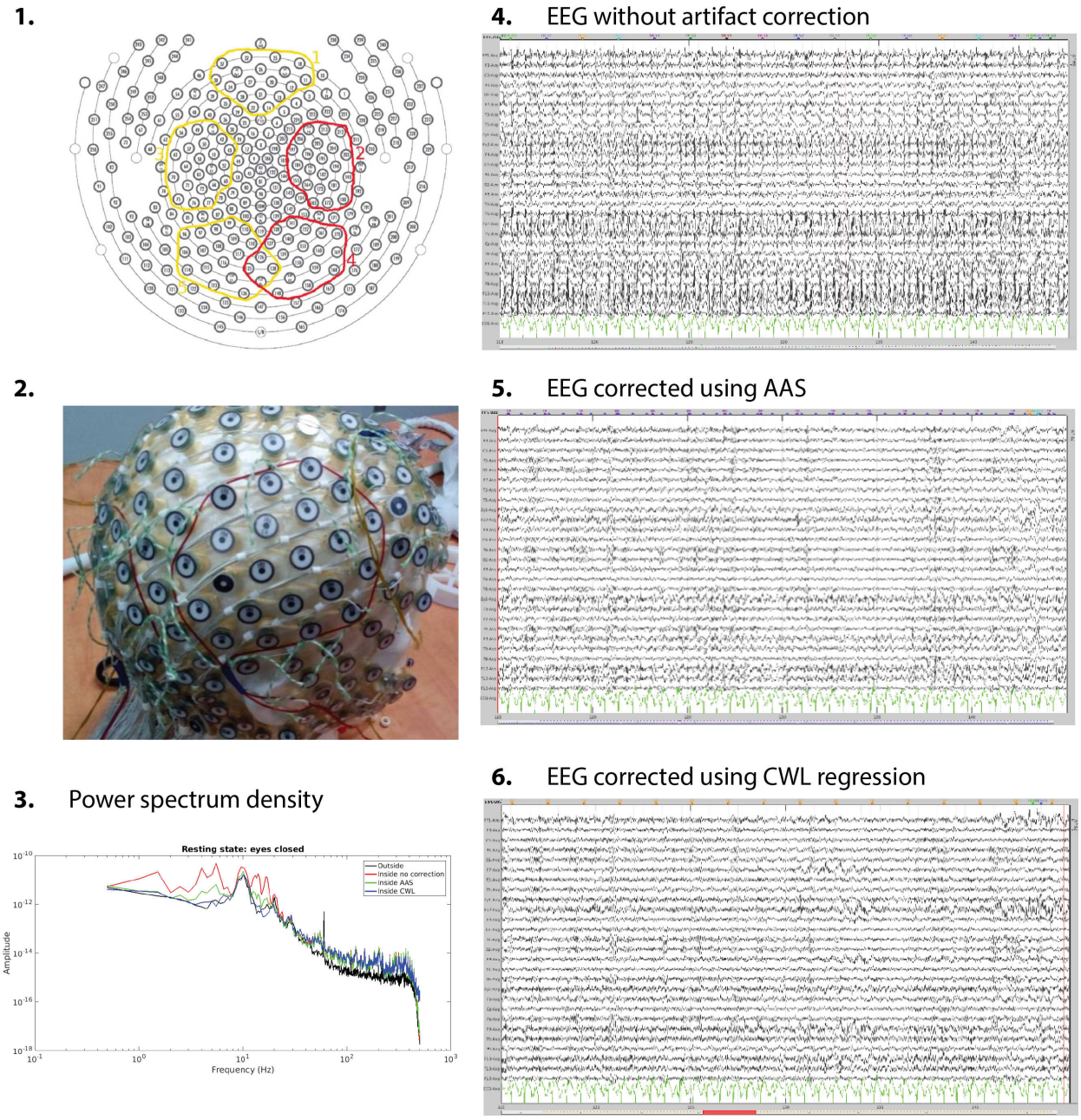

Figure 8.1: 1. Diagram illustrating the placement of the five carbon wire loops. **2.** Photograph of the EEG net with the carbon wire loops. **3.** Power spectrum density of EEG data during resting state when recording outside the MR scanner (**black**), inside without artifact correction (**red**), or with artifact correction using AAS (**green**) or CWL regression (**blue**). **4.** 7 seconds of EEG data during a resting state experiment during fMRI analysis without artifact correction. **5.** Same EEG segment, but with MR-related artifact correction using AAS. **6.** Same EEG segment, but with MR-related artifact correction using CWL regression.

great interest when studying the influence of sleep spindles discharges in sleep studies aiming at characterizing physiological and pathological processes associated with sleep. Spindles

are transient oscillations at 11–16 Hz occurring during the stages N2-N3 of non-rapid-eye-movement sleep (Berry et al., 2013). Spindles are often subcategorized into slow ($<$ 13 Hz) and fast ($\geq$ 13 Hz) spindles. Fast sleep spindles were shown to be involved in memory consolidation (Schabus et al., 2007), but also, as demonstrated recently by our group in an EEG-fMRI experiment, in declarative learning performance (Jegou et al., 2019). Another EEG study showed that memory consolidation was associated not only with spindles, but also with low- and high-frequency around the sleep spindles (Laventure et al., 2018). Such findings demonstrated that a characterization of sleep spindles using ESI alongside with fMRI could be useful to further understand the role of sleep spindles in memory consolidation and declarative memory.

cMEM was proven to be a source imaging technique that exhibits an excellent spatial resolution and is robust to noise. These properties could be of interest when considering ESI in other domains, notably in the context of resting-state functional connectivity Schölvinck et al. (2013). In Chapter 5, we have shown that cMEM was characterized by an excellent performance in terms of crosstalk maps. Crosstalk maps, which was related to source leakage, are measures which are important to control in order to avoid or reduce volume conduction errors when estimating the functional connectivity patterns. Moreover, the ability for cMEM to shut down parcel, when combined to effective hardware and software solutions to remove artifacts, would allow reducing the influence of spurious distant source from the measure of functional connectivity. Our group recently performed a study on functional connectivity using a wavelet-based MEM (wMEM), a time-frequency variant of cMEM, as the source imaging technique (Aydin et al., In Preparation). In this study, 13 patients performed simultaneous EEG/MEG acquisition before receiving surgery, in which 7 became seizure-free after surgery and 6 became non seizure-free. wMEM was able to discover a significant difference between the patients who were seizure-free and the patients who were not in terms of long-range functional connectivity in the alpha band. Seizure-free patients showed an isolated epileptic network characterized by weaker connections between the IED generator and the rest of the cortex when compared to connectivity patterns between the corresponding contralateral homologous region and the rest of the cortex. Conversely, non seizure-free patients were observed to have a stronger connectivity between the IED generator and the rest of the cortex, in comparison to the contralateral region and rest of the cortex. Connectivity in the alpha band was chosen because studies have found some correspondence between the alpha band fluctuations detected on MEG and the BOLD signals measured by fMRI (Hipp and Siegel, 2015; Brookes et al., 2005). However, one can only perform an indirect comparison since MEG and fMRI cannot be performed simultaneously. With the findings indicated by this thesis, it may be possible to use fMRI and ESI from hdEEG in healthy and pathological conditions to

further investigate the relationship between brain oscillations at different frequency bands and the corresponding hemodynamic response detected in fMRI.

8.3 Conclusion

The aim of this thesis was to test the concordance between ESI and fMRI results for the analysis of epileptic discharges. The emphasis was put on the choice of and challenges in selecting a suitable source imaging technique. An ESI and MSI framework was developed by our group, the MEM framework, and a data-driven prior model, cMEM was carefully validated as a suitable technique for simultaneous ESI-fMRI analysis. To do so, the intrinsic spatial resolution of cMEM was compared to traditional ESI/MSI techniques using their resolution matrices. We proved that cMEM had a better spatial resolution than the other standard approaches. However, EEG recorded during an fMRI analysis is affected by artifacts that may distort the signal: for this reason, we wanted to test the robustness of cMEM to MR-related noise. We compared the quality of cMEM applied on EEG data either acquired inside or outside an MR scanner, and we showed that even if the quality of the EEG signals were poorer inside the scanner, cMEM was able to perform as accurately in both conditions. We concluded that cMEM was an excellent candidate for an ESI technique to use during an EEG-fMRI analysis of patients with epilepsy. Based on this premise, we developed an automatic IED clustering using ESI results to improve the fMRI analysis process. We showed that the automatic clustering performed as well as a manual clustering, paving the way for a less operator-dependent and less time-consuming analysis of IEDs in an EEG-fMRI analysis. Overall, we demonstrated the feasibility of using ESI during an EEG-fMRI analysis and validated it in the context of patients with epilepsy. The possibility to obtain ESI results and fMRI BOLD responses at the same time could be of great interest in other fields, such as functional connectivity, in normal and pathological conditions.

Bibliography

D. F. Abbott, R. A. J. Masterton, J. S. Archer, S. W. Fleming, A. E. L. Warren, and G. D. Jackson. Constructing carbon fiber motion-detection loops for simultaneous EEG-fMRI. *Frontiers in Neurology*, 5(January):1–16, 2015.

C. Abdallah, L. G. Maillard, E. Rikir, J. Jonas, A. Thiriaux, M. Gavaret, F. Bartolomei, S. Colnat-Coulbois, J. P. Vignal, and L. Koessler. Localizing value of electrical source imaging: Frontal lobe, malformations of cortical development and negative MRI related epilepsies are the best candidates. *NeuroImage: Clinical*, 16(August):319–329, 2017.

R. Abreu, M. Leite, J. Jorge, F. Grouiller, W. van der Zwaag, A. Leal, and P. Figueiredo. Ballistocardiogram artifact correction taking into account physiological signal preservation in simultaneous EEG-fMRI. *NeuroImage*, 135:45–63, 2016.

R. Abreu, A. Leal, and P. Figueiredo. EEG-Informed fMRI: A Review of Data Analysis Methods. *Frontiers in Human Neuroscience*, 12(February):1–23, 2018a.

R. Abreu, A. Leal, F. Lopes da Silva, and P. Figueiredo. EEG synchronization measures predict epilepsy-related BOLD-fMRI fluctuations better than commonly used univariate metrics. *Clinical Neurophysiology*, 129(3):618–635, 2018b.

E. Adrian. Electrical Activity of the Nervous System. *Archives of Neurology and Psychiatry*, 32(6):1125–1136, 1934.

S. P. Ahlfors, J. Han, J. W. Belliveau, and M. S. Hämäläinen. Sensitivity of MEG and EEG to source orientation. *Brain topography*, 23(3):227–32, sep 2010.

S. P. Ahlfors, J. Han, F.-H. Lin, T. Witzel, W. John, M. S. Hämäläinen, E. Halgren, and J. Belliveau. Cancellation of EEG and MEG Signals Generated by Extended and Distributed Sources. *Human brain mapping*, 31(1):140–149, 2011.

A. Ahonen, M. Hämäläinen, M. Kajola, J. Knuutila, P. Laine, O. Lounasmaa, L. Parkkonen, J. Simola, and C. Tesche. 122-channel SQUID instrument for investigating the magnetic signals from the human brain. *Physica Scripta*, 198:198–205, 1993.

M. Akhtari, H. Bryant, A. N. Mamelak, E. Flynn, L. Heller, J. Shih, M. Mandelkern, A. Matlachov, D. M. Ranken, E. D. Best, M. DiMauro, R. Lee, and W. W. Sutherling. Conductivities of Three-Layer Live Human Skull. *Brain Topography*, 14(3):151–167, 2002.

G. Alarcon, C. N. Guy, C. D. Binnie, S. R. Walker, R. D. C. Elwes, and C. E. Polkey. Intracerebral propagation of interictal activity in partial epilepsy: implications for source localisation. *Journal of neurology, neurosurgery, and psychiatry*, 57(4):435–449, apr 1994.

P. J. Allen, G. Polizzi, K. Krakow, D. R. Fish, and L. Lemieux. Identification of EEG events in the MR scanner: the problem of pulse artifact and a method for its subtraction. *NeuroImage*, 8(3):229–239, oct 1998.

P. J. Allen, O. Josephs, and R. Turner. A method for removing imaging artifact from continuous EEG recorded during functional MRI. *NeuroImage*, 12(2):230–9, aug 2000.

T. Allison, G. McCarthy, M. Luby, A. Puce, and D. D. Spencer. Localization of functional regions of human mesial cortex by somatosensory evoked potential recording and by cortical stimulation. *Electroencephalography and clinical neurophysiology*, 4(1988):126–40, 1995.

C. Amblard, E. Lapalme, and J.-M. Lina. Biomagnetic source detection by maximum entropy and graphical models. *IEEE transactions on bio-medical engineering*, 51(3):427–42, mar 2004.

D. An, F. Fahoum, J. Hall, A. Olivier, J. Gotman, and F. Dubeau. Electroencephalography/functional magnetic resonance imaging responses help predict surgical outcome in focal epilepsy. *Epilepsia*, 54(12):2184–2194, 2013.

D. Arnstein, F. Cui, C. Keysers, N. M. Maurits, and V. Gazzola. -Suppression during Action Observation and Execution Correlates with BOLD in Dorsal Premotor, Inferior Parietal, and SI Cortices. *Journal of Neuroscience*, 31(40):14243–14249, 2011.

Ü. Aydin, J. Vorwerk, P. Küpper, M. Heers, H. Kugel, A. Galka, L. Hamid, J. Wellmer, C. Kellinghaus, S. Rampp, and C. H. Wolters. Combining EEG and MEG for the reconstruction of epileptic activity using a calibrated realistic volume conductor model. *PloS one*, 9(3):e93154, jan 2014.

Ü. Aydin, J. Vorwerk, M. Dümpelmann, P. Küpper, H. Kugel, M. Heers, J. Wellmer, C. Kellinghaus, J. Haueisen, S. Rampp, H. Stefan, and C. H. Wolters. Combined EEG/MEG Can Outperform Single Modality EEG or MEG Source Reconstruction in Presurgical Epilepsy Diagnosis. *PLoS ONE*, 10(3):1–29, 2015.

Ü. Aydin, G. Pellegrino, O. Bin Ka'b Ali, C. Abdallah, F. Dubeau, J.-M. Lina, E. Kobayashi, and C. Grova. Magnetoencephalography resting state connectivity in epilepsy predicts surgical outcome for individual patients . In Preparation.

F. Babiloni, D. Mattia, C. Babiloni, L. Astolfi, S. Salinari, A. Basilisco, P. M. Rossini, M. G. Marciani, and F. Cincotti. Multimodal integration of EEG, MEG and fMRI data for the solution of the neuroimage puzzle. *Magnetic Resonance Imaging*, 22(10 SPEC. ISS.): 1471–1476, 2004.

A. P. Bagshaw, Y. Aghakhani, C. G. Bénar, E. Kobayashi, C. Hawco, F. Dubeau, G. B. Pike, and J. Gotman. EEG-fMRI of focal epileptic spikes: Analysis with multiple haemodynamic functions and comparison with gadolinium-enhanced MR angiograms. *Human Brain Mapping*, 22(3):179–192, 2004.

A. P. Bagshaw, C. Hawco, C.-G. Bénar, E. Kobayashi, Y. Aghakhani, F. Dubeau, G. B. Pike, and J. Gotman. Analysis of the EEG-fMRI response to prolonged bursts of interictal epileptiform activity. *NeuroImage*, 24(4):1099–1112, feb 2005.

S. Baillet and L. Garnero. A Bayesian approach to introducing anatomo-functional priors in the EEG/MEG inverse problem. *IEEE Transactions on Biomedical Engineering*, 44(5): 374–385, 1997.

S. Baillet, J. C. Mosher, and R. M. Leahy. Electromagnetic brain mapping. *Human brain mapping*, 30(6):1753–7, jun 2009.

E. Balzamo, P. Marquis, P. Chauvel, and J. Régis. Short-latency components of evoked potentials to median nerve stimulation recorded by intracerebral electrodes in the human pre- and postcentral areas. *Clinical neurophysiology : official journal of the International Federation of Clinical Neurophysiology*, 115(7):1616–23, jul 2004.

C. Barba, M. Valeriani, G. Colicchio, and F. Mauguière. Short and middle-latency Median Nerve (MN) SEPs recorded by depth electrodes in human pre-SMA and SMA-proper. *Clinical neurophysiology : official journal of the International Federation of Clinical Neurophysiology*, 116(11):2664–74, nov 2005.

S. B. Baumann, D. R. Wozny, S. K. Kelly, and F. M. Meno. The electrical conductivity of human cerebrospinal fluid at body temperature. *IEEE Transactions on Biomedical Engineering*, 44(3):220–223, 1997.

S. Baxendale. Neuropsychological assessment in epilepsy. *Practical Neurology*, 18(1):43–48, 2018.

C.-G. Bénar, D. W. Gross, Y. Wang, V. Petre, B. Pike, F. Dubeau, and J. Gotman. The BOLD Response to Interictal Epileptiform Discharges. *NeuroImage*, 17(3):1182–1192, nov 2002.

C.-G. Benar, C. Grova, E. Kobayashi, A. P. Bagshaw, Y. Aghakhani, F. Dubeau, and J. Gotman. EEG-fMRI of epileptic spikes: concordance with EEG source localization and intracranial EEG. *NeuroImage*, 30(4):1161–70, may 2006.

C. G. Bénar, D. Schön, S. Grimault, B. Nazarian, B. Burle, M. Roth, J. M. Badier, P. Marquis, C. Liegeois-Chauvel, and J. L. Anton. Single-trial analysis of oddball event-related potentials in simultaneous EEG-fMRI. *Human Brain Mapping*, 28(7):602–613, 2007.

Y. Benjamini and Y. Hochberg. Controlling the false discovery rate: a practical and powerful approach to multiple testing. *Journal of the Royal Statistical Society. Series B ...*, 135(1): 22–6, jan 1995.

H. Berger. Über das Elektrenkephalogramm des Menschen. [On the human electroencephalogram] 1st edition. *Archiv für Psychiatrie*, 35(87):527–570, 1929.

H. Berger. Über das Elektrenkephalogramm des Menschen. [On the human electroencephalogram] 7th edition. *Archiv für Psychiatrie*, 35(100):301–320, 1933.

A. Bernasconi, N. Bernasconi, B. C. Bernhardt, and D. Schrader. Advances in MRI for 'cryptogenic' epilepsies. *Nature Reviews Neurology*, 7(2):99–108, 2011.

R. B. Berry, R. Brooks, C. E. Gamaldo, S. M. Harding, C. L. Marcus, and B. V. Vaughn. The AASM Manual for the Scoring of Sleep and Associated Events. Technical Report 9, American Academy of Sleep Medecine, 2013.

P. J. Besl and N. D. McKay. A Method for Registration of 3-D Shapes, 1992. ISSN 10066047.

C. E. Biazoli, M. Sturzbecher, T. P. White, H. H. Dos Santos Onias, K. C. Andrade, D. B. De Araujo, and J. R. Sato. Application of partial directed coherence to the analysis of resting-state EEG-fMRI data. *Brain Connectivity*, 3(6):563–568, 2013.

R. M. Birn, Z. S. Saad, and P. A. Bandettini. Spatial heterogeneity of the nonlinear dynamics in the FMRI BOLD response. *NeuroImage*, 14(4):817–826, 2001.

S. Blanchard, S. Saillet, A. Ivanov, P. Benquet, C. G. Bénar, M. Pélégrini-Issac, H. Benali, and F. Wendling. A new computational model for neuro-glio-vascular coupling: Astrocyte activation can explain cerebral blood flow nonlinear response to interictal events. *PLoS ONE*, 11(2):1–21, 2016.

E. Boto, S. S. Meyer, V. Shah, O. Alem, S. Knappe, P. Kruger, T. M. Fromhold, M. Lim, P. M. Glover, P. G. Morris, R. Bowtell, G. R. Barnes, and M. J. Brookes. A new generation of magnetoencephalography: Room temperature measurements using optically-pumped magnetometers. *NeuroImage*, 149(August 2016):404–414, 2017.

A. Boutin, B. Pinsard, A. Boré, J. Carrier, S. M. Fogel, and J. Doyon. Transient synchronization of hippocampo-striato-thalamo-cortical networks during sleep spindle oscillations induces motor memory consolidation. *NeuroImage*, 169(November 2017):419–430, 2018.

J. Britz, D. Van De Ville, and C. M. Michel. BOLD correlates of EEG topography reveal rapid resting-state network dynamics. *NeuroImage*, 52(4):1162–1170, 2010.

V. Brodbeck, L. Spinelli, A. M. Lascano, M. Wissmeier, M.-I. I. Vargas, S. Vulliemoz, C. Pollo, K. Schaller, C. M. Michel, and M. Seeck. Electroencephalographic source imaging: A prospective study of 152 operated epileptic patients. *Brain*, 134(Pt 10):2887–97, oct 2011.

M. J. Brookes, A. M. Gibson, S. D. Hall, P. L. Furlong, G. R. Barnes, A. Hillebrand, K. D. Singh, I. E. Holliday, S. T. Francis, and P. G. Morris. GLM-beamformer method demonstrates stationary field, alpha ERD and gamma ERS co-localisation with fMRI BOLD response in visual cortex. *NeuroImage*, 26(1):302–308, 2005.

M. J. Brookes, K. J. Mullinger, C. M. Stevenson, P. G. Morris, and R. Bowtell. Simultaneous EEG source localisation and artifact rejection during concurrent fMRI by means of spatial filtering. *NeuroImage*, 40(3):1090–1104, 2008.

R. B. Buxton. The elusive initial dip. *NeuroImage*, 13(6):953–958, 2001.

R. B. Buxton, E. C. Wong, and L. R. Frank. Dynamics of blood flow and oxygenation changes during brain activation: The balloon model. *Magnetic Resonance in Medicine*, 39 (6):855–864, 1998.

G. Buzsáki and A. Draguhn. Neuronal oscillations in cortical networks. *Science (New York, N.Y.)*, 304(5679):1926–9, jun 2004.

V. Calhoun, T. Adali, G. Pearlson, and K. Kiehl. Neuronal chronometry of target detection: Fusion of hemodynamic and event-related potential DATA. *2005 IEEE Workshop on Machine Learning for Signal Processing*, 30:239–244, 2005.

V. D. Calhoun, J. Liu, and T. Adali. A review of group ICA for fMRI data and ICA for joint inference of imaging, genetic, and ERP data. *NeuroImage*, 45(1 Suppl):163–172, 2009.

E. Carrette, M. Op De Beeck, M. Bourguignon, P. Boon, K. Vonck, B. Legros, S. Goldman, P. Van Bogaert, and X. De Tiège. Recording temporal lobe epileptic activity with MEG in a light-weight magnetic shield. *Seizure*, 20(5):414–418, 2011.

J. Castelhano, I. C. Duarte, M. Wibral, E. Rodriguez, and M. Castelo-Branco. The dual facet of gamma oscillations: Separate visual and decision making circuits as revealed by simultaneous EEG/fMRI. *Human Brain Mapping*, 35(10):5219–5235, 2014.

R. Caton. The electric currents of the brain. *British Medical Journal*, 2(1):278, 1875.

M. Centeno, T. M. Tierney, S. Perani, E. A. Shamshiri, K. St Pier, C. Wilkinson, D. Konn, S. Vulliemoz, F. Grouiller, L. Lemieux, R. M. Pressler, C. A. Clark, J. H. Cross, and D. W. Carmichael. Combined electroencephalography-functional magnetic resonance imaging and electrical source imaging improves localization of pediatric focal epilepsy. *Annals of Neurology*, 82(2):278–287, 2017.

G. E. Chatrian, E. Lettich, and P. L. Nelson. Ten Percent Electrode System for Topographic Studies of Spontaneous and Evoked EEG Activities. *American Journal of {EEG} Technology*, 25(2):83–92, jun 1985.

U. J. Chaudhary, J. S. Duncan, and L. Lemieux. Mapping hemodynamic correlates of seizures using fMRI: A review. *Human Brain Mapping*, 34(2):447–466, 2013.

A. Chilliat, S. Macmillan, P. Alken, C. Beggan, M. Nair, B. Hamilton, A. Woods, V. Ridley, S. Maus, and A. Thomson. The US / UK World Magnetic for 2015-2020. Technical report, NOAA National Geophysical Data Center, 2015.

M. E. H. Chowdhury, K. J. Mullinger, P. Glover, and R. Bowtell. Reference layer artefact subtraction (RLAS): A novel method of minimizing EEG artefacts during simultaneous fMRI. *NeuroImage*, 84:307–319, 2014.

M. E. H. Chowdhury, A. Khandakar, K. J. Mullinger, N. Al-Emadi, and R. Bowtell. Simultaneous EEG-fMRI: Evaluating the Effect of the EEG Cap-Cabling Configuration on the Gradient Artifact. *Frontiers in Neuroscience*, 13(July):1–15, 2019.

R. A. Chowdhury, I. Merlet, G. Birot, E. Kobayashi, A. Nica, A. Biraben, F. Wendling, J.-M. Lina, L. Albera, and C. Grova. Complex patterns of spatially extended generators of epileptic activity: Comparison of source localization methods cMEM and 4-ExSo-MUSIC on High Resolution EEG and MEG data. *NeuroImage*, 143:175–195, 2016.

R. A. Chowdhury, J. M. Lina, E. Kobayashi, and C. Grova. MEG Source Localization of Spatially Extended Generators of Epileptic Activity: Comparing Entropic and Hierarchical Bayesian Approaches. *PloS one*, 8(2):e55969, jan 2013.

R. A. Chowdhury, Y. Zerouali, T. Hedrich, M. Heers, E. Kobayashi, J.-M. Lina, and C. Grova. MEG – EEG Information Fusion and Electromagnetic Source Imaging : From Theory to Clinical Application in Epilepsy. *Brain Topography*, 28(6):785–812, 2015.

R. A. Chowdhury, G. Pellegrino, Ü. Aydin, J. M. Lina, F. Dubeau, E. Kobayashi, and C. Grova. Reproducibility of EEG-MEG fusion source analysis of interictal spikes: Relevance in presurgical evaluation of epilepsy. *Human Brain Mapping*, 39(2):880–901, 2018.

C. Christmann, C. Koeppe, D. F. Braus, M. Ruf, and H. Flor. A simultaneous EEG-fMRI study of painful electric stimulation. *NeuroImage*, 34(4):1428–1437, 2007.

C. J. S. Clarke and B. Janday. The solution of the biomagnetic inverse problem by maximum statistical entropy. *Inverse Problems*, 5(4):483–500, 1989.

A. Coenen, E. Fine, and O. Zayachkivska. Adolf beck: A forgotten pioneer in electroencephalography. *Journal of the History of the Neurosciences*, 23(3):276–286, 2014.

D. Cohen. Magnetoencephalography : Evidence of Magnetic Fields Produced by Alpha-Rhythm Currents. *Science*, 161(3843):784–786, 1968.

T. F. Collura. History and evolution of electroencephalographic instruments and techniques. *Journal of Clinical Neurophysiology*, 10(4):476–504, 1993.

B. Cottereau, J. Lorenceau, A. Gramfort, M. Clerc, B. Thirion, and S. Baillet. Phase delays within visual cortex shape the response to steady-state visual stimulation. *NeuroImage*, 54 (3):1919–1929, 2011.

B. N. Cuffin. A Comparison of Moving Dipole Inverse Solutions Using EEG's and MEG's. *IEEE Transactions on Biomedical Engineering*, BME-32(11):905–910, 1985.

M. D. Curtis, J. G. R. Jefferys, and M. Avoli. Interictal Epileptiform Discharges in Partial Epilepsy. Complex Neurobiological Mechanisms Based on Experimental and Clinical Evidence. In *Jasper's Basic Mechanisms of the Epilepsies*, pages 1–24. National Center for Biotechnology Information (US), 2012.

M. Czisch, R. Wehrle, C. Kaufmann, T. C. Wetter, F. Holsboer, T. Pollmächer, and D. P. Auer. Functional MRI during sleep: BOLD signal decreases and their electrophysiological correlates. *European Journal of Neuroscience*, 20(2):566–574, 2004.

A. M. Dale and M. I. Sereno. Improved localizadon of cortical activity by combining eeg and meg with mri cortical surface reconstruction: A linear approach. *Journal of Cognitive Neuroscience*, 1993.

A. M. Dale, A. Liu, B. R. Fischl, R. Buckner, J. W. Belliveau, J. D. Lewine, and E. Halgren. Dynamic statistical parametric neurotechnique mapping: combining fMRI and MEG for high-resolution imaging of cortical activity. *Neuron*, 26:55–67, 2000.

T. T. Dang-Vu. Functional Neuroimaging Insights into the Physiology of Human Sleep. *Sleep*, 33(12):1590–1603, 2010.

M. Dannhauer, B. Lanfer, C. H. Wolters, and T. R. Knösche. Modeling of the human skull in EEG source analysis. *Human Brain Mapping*, 32(9):1383–1399, 2011.

F. Darvas, D. Pantazis, E. Kucukaltun-Yildirim, and R. M. Leahy. Mapping human brain function with MEG and EEG: methods and validation. *NeuroImage*, 23 Suppl 1:S289–99, jan 2004.

J. Daunizeau, C. Grova, G. Marrelec, J. Mattout, S. Jbabdi, M. Pélégrini-Issac, J.-m. Lina, and H. Benali. Symmetrical event-related EEG/fMRI information fusion in a variational Bayesian framework. *NeuroImage*, 36(1):69–87, may 2007.

J. Daunizeau, H. Laufs, and K. J. Friston. EEG-fMRI information fusion: Biophysics and data analysis. In *EEG - fMRI: Physiological Basis, Technique, and Applications*, chapter 25, pages 511–526. Springer, 1 edition, 2010.

O. David and L. Garnero. Time-coherent expansion of MEG/EEG cortical sources. *NeuroImage*, 17(3):1277–1289, 2002.

H. Davis. *Crossroads on the Pathways to Discovery*, pages 311–321. Birkhäuser Boston, Boston, MA, 1992.

J. C. de Munck and M. J. Peters. A Fast Method to Compute the Potential in the Multisphere Model. *IEEE Transactions on Biomedical Engineering*, 40(11):1166–1174, 1993.

J. C. de Munck, S. I. Gonçalves, R. Mammoliti, R. M. Heethaar, and F. H. Lopes da Silva. Interactions between different EEG frequency bands and their effect on alpha-fMRI correlations. *NeuroImage*, 47(1):69–76, 2009.

J. C. De Munck, P. J. van Houdt, S. I. Gonçalves, E. Van Wegen, and P. P. W. Ossenblok. Novel artefact removal algorithms for co-registered EEG / fMRI based on selective averaging and subtraction. *NeuroImage*, 64:407–415, 2013.

A. C. de Souza, G. Fernandes Rodrigues, D. Callan, and H. C. Yehia. Analysis of the ballistocardiographic artifact removal in simultaneous EEG-fMRI recording using independent component analysis and coherence function. In *Telecommunications and Signal Processing (TSP), 2013 36th International Conference on*, pages 552–556, jul 2013.

J. De Tisi, G. S. Bell, J. L. Peacock, A. W. McEvoy, W. F. Harkness, J. W. Sander, and J. S. Duncan. The long-term outcome of adult epilepsy surgery, patterns of seizure remission, and relapse: A cohort study. *The Lancet*, 378(9800):1388–1395, 2011.

S. Debener, M. Ullsperger, M. Siegel, K. Fiehler, D. Y. von Cramon, and A. K. Engel. Trial-by-trial coupling of concurrent electroencephalogram and functional magnetic resonance imaging identifies the dynamics of performance monitoring. *The Journal of neuroscience*, 25(50):11730–11737, dec 2005.

R. Deichmann, U. Nöth, and N. Weiskopf. The Basics of Functional Magnetic Resonance Imaging. In *EEG - fMRI: Physiological Basis, Technique, and Applications*, chapter 3, pages 39–62. Springer, 2010.

G. Demoment. Image Reconstruction and Restoration: Overview of Common Estimation Structures and Problems. *IEEE Transactions on Acoustics, Speech, and Signal Processing*, 37(12):2024–2036, 1989.

F. Di Russo, A. Martínez, M. I. Sereno, S. Pitzalis, and S. A. Hillyard. Cortical sources of the early components of the visual evoked potential. *Human Brain Mapping*, 15(2):95–111, 2002.

F. Di Russo, S. Pitzalis, G. Spitoni, T. Aprile, F. Patria, D. Spinelli, and S. A. Hillyard. Identification of the neural sources of the pattern-reversal VEP. *NeuroImage*, 24(3):874–886, 2005.

L. Ding, C. Wilke, B. Xu, X. Xu, W. Van Drongelen, M. Kohrman, and B. He. EEG source imaging: Correlating source locations and extents with electrocorticography and surgical resections in epilepsy patients. *Journal of Clinical Neurophysiology*, 24(2):130–136, 2007.

F. H. Duffy, J. L. Burchfield, and C. T. Lombroso. Brain electrical activity mapping (BEAM): a method for extending the clinical use of EEG and evoked potential data. *Annals of Neurology*, 5, 1979.

J. S. Ebersole. EEG dipole modeling in complex partial epilepsy. *Brain Topography*, 4(2): 113–123, 1991.

J. S. Ebersole. Magnetoencephalography/magnetic source imaging in the assessment of patients with epilepsy. *Epilepsia*, 38 Suppl 4:S1–S5, 1997.

J. S. Ebersole and S. M. Ebersole. Combining MEG and EEG source modeling in epilepsy evaluations. *Journal of clinical neurophysiology : official publication of the American Electroencephalographic Society*, 27(6):360–371, 2010.

S. B. Eickhoff, C. Grefkes, G. R. Fink, and K. Zilles. Functional lateralization of face, hand, and trunk representation in anatomically defined human somatosensory areas. *Cerebral Cortex*, 18(12):2820–2830, dec 2008.

L. Elshoff, K. Groening, F. Grouiller, G. Wiegand, S. Wolff, C. Michel, U. Stephani, and M. Siniatchkin. The value of EEG-fMRI and EEG source analysis in the presurgical setup of children with refractory focal epilepsy. *Epilepsia*, 53(9):1597–1606, jul 2012.

J. J. Engel and T. A. Pedley. *Epilepsy: A Comprehensive Textbook*. Lippincott Williams & Wilkins (LWW), 2nd ed. edition, 2008.

F. Fahoum, R. Zelmann, L. Tyvaert, F. Dubeau, and J. Gotman. Epileptic Discharges Affect the Default Mode Network - fMRI and Intracerebral EEG Evidence. *PLoS ONE*, 8(6), 2013.

D. A. Feinberg and K. Setsompop. Ultra-Fast MRI of the Human Brain with Simultaneous Multi-Slice Imaging. *Journal of Magnetic Resonance*, 229:90–100, 2013.

W. Feindel. Brain physiology at the montreal neurological institute: Some historical highlights, 1992. ISSN 15371603.

S. Ferdowsi, S. Sanei, V. Abolghasemi, J. Nottage, and O. O'Daly. Removing Ballistocardiogram Artifact From EEG Using Short- and Long-Term Linear Predictor. *IEEE Trans Biomed Eng*, 60(7):1900–1911, jul 2013.

M. Fischer and H. Lowenback. Aktionsstrome des zentralnervensystems unter der einwikung von krampfgiften. I. Miteilung Strchnin und Pikrotoxin. *Arch Exp Pathol Pharmakol*, 1 (174):357–382, 1934.

B. Fischl. FreeSurfer. *NeuroImage*, 62(2):774–781, 2012.

R. Fisher and M. Saul. *Overview of epilepsy*. www.epilepsy.com, 2010.

R. S. Fisher, W. v. E. Boas, W. Blume, C. Elger, P. Genton, P. Lee, and J. Engel. Epileptic seizures and epilepsy: definitions proposed by the International League Against Epilepsy

(ILAE) and the International Bureau for Epilepsy (IBE). *Epilepsia*, 46(10):1698–9; author reply 1701–2, oct 2005.

R. S. Fisher, J. H. Cross, J. A. French, N. Higurashi, E. Hirsch, F. E. Jansen, L. Lagae, S. L. Moshé, J. Peltola, E. Roulet Perez, I. E. Scheffer, and S. M. Zuberi. Operational classification of seizure types by the International League Against Epilepsy: position paper of the ILAE Commission for Classification and Terminology. *Epilepsia*, 58(4):522–530, 2017.

D. Flanagan, D. F. Abbott, and G. D. Jackson. How wrong can we be? The effect of inaccurate mark-up of EEG/fMRI studies in epilepsy. *Clinical neurophysiology : official journal of the International Federation of Clinical Neurophysiology*, 120(9):1637–47, sep 2009.

E. Frank. Electric potential produced by two point current sources in a homogeneous conducting sphere. *Journal of Applied Physics*, 23(11):1225–1228, 1952.

B. Frauscher, F. Bartolomei, K. Kobayashi, J. Cimbalnik, M. A. van 't Klooster, S. Rampp, H. Otsubo, Y. Höller, J. Y. Wu, E. Asano, J. Engel, P. Kahane, J. Jacobs, and J. Gotman. High-frequency oscillations: The state of clinical research. *Epilepsia*, 58(8):1316–1329, 2017.

K. J. Friston, A. P. Holmes, J.-P. Worsley, C. D. Frith, and R. S. Frackowiak. Statistical parametric maps in functional imaging: a general linear approach. *Human Brain Mapping*, 2(081):189–210, 1995.

K. J. Friston, P. Fletcher, O. Josephs, A. Holmes, M. D. Rugg, and R. Turner. Event-related fMRI: characterizing differential responses. *NeuroImage*, 7(1):30–40, jan 1998.

K. J. Friston, A. Mechelli, R. Turner, and C. J. Price. Nonlinear responses in fMRI: the Balloon model, Volterra kernels, and other hemodynamics. *NeuroImage*, 12(4):466–77, oct 2000.

K. Friston, L. Harrison, J. Daunizeau, S. Kiebel, C. Phillips, N. Trujillo-Barreto, R. Henson, G. Flandin, and J. Mattout. Multiple sparse priors for the M/EEG inverse problem. *NeuroImage*, 39(3):1104–20, feb 2008.

D. Fuglø, H. Pedersen, E. Rostrup, A. E. Hansen, and H. B. Larsson. Correlation between single-trial visual evoked potentials and the blood oxygenation level dependent response in simultaneously recorded electroencephalography-functional magnetic resonance imaging. *Magnetic Resonance in Medicine*, 68(1):252–260, 2012.

A. Garnier, A. Vidal, and H. Benali. A Theoretical Study on the Role of Astrocytic Activity in Neuronal Hyperexcitability by a Novel Neuron-Glia Mass Model. *Journal of Mathematical Neuroscience*, 6(1):1–30, 2016.

M. Gavaret, J.-M. Badier, F. Bartolomei, C.-G. Bénar, and P. Chauvel. MEG and EEG sensitivity in a case of medial occipital epilepsy. *Brain topography*, 27(1):192–6, jan 2014.

F. A. Gibbs, H. Davis, and W. G. Lennox. The Electro-Encephalogram in Epilepsy and in Conditions of Impaired Consciousness. *Archives of Neurology and Psychiatry*, 34(6): 1134–1146, 1935.

G. H. Glover. Deconvolution of impulse response in event-related BOLD fMRI. *NeuroImage*, 9(4):416–429, 1999.

R. I. Goldman, J. M. Stern, J. J. Engel, and M. S. Cohen. Simultaneous EEG and fMRI of the alpha rhythm. *Neuroreport*, 13(18):2487–2492, 2002.

G. H. Golub, M. Heath, and G. Wahba. Generalized Cross-Validation as a Method for Choosing a Good Ridge Parameter. *Technometrics*, 21(2):215–223, 1979.

I. F. Gorodnitsky, J. S. George, and B. D. Rao. Neuromagnetic source imaging with FOCUSS: a recursive weighted minimum norm algorithm. *Electroencephalography and Clinical Neurophysiology*, 95(4):231–251, 1995.

J. Gotman, C. Grova, A. Bagshaw, E. Kobayashi, Y. Aghakhani, and F. Dubeau. Generalized epileptic discharges show thalamocortical activation and suspension of the default state of the brain. *Proceedings of the National Academy of Sciences of the United States of America*, 102(42):15236–40, 2005.

J. Gotman. Epileptic networks studied with EEG-fMRI. *Epilepsia*, 49 Suppl 3(0 3):42–51, jan 2008.

J. Gotman and F. Pittau. Combining EEG and fMRI in the study of epileptic discharges. *Epilepsia*, 52(Suppl. 4):38–42, 2011.

J. Gotman, C.-G. Benar, and F. Dubeau. Combining EEG and fMRI in Epilepsy: Methodological Challenges and Clinical Results. *Journal of Clinical Neurophysiology*, 21(4):229–240, jul 2004.

J. Gotman, E. Kobayashi, A. P. Bagshaw, C.-G. Bénar, and F. Dubeau. Combining EEG and fMRI: a multimodal tool for epilepsy research. *Journal of magnetic resonance imaging : JMRI*, 23(6):906–20, jun 2006.

A. Gramfort. *Mapping, timing and tracking cortical activations with MEG and EEG: Methods and application to human vision.* PhD thesis, INRIA Sophia Antipolis, 2009.

A. Gramfort, T. Papadopoulo, E. Olivi, and M. Clerc. OpenMEEG: opensource software for quasistatic bioelectromagnetics. *Biomedical engineering online*, 9:45, jan 2010.

A. Gramfort, M. Kowalski, and M. Hämäläinen. Mixed-norm estimates for the M/EEG inverse problem using accelerated gradient methods. *Phys Med Biol*, 57(7):1937–1961, 2012.

R. Grave de Peralta, O. Hauk, S. L. Gonzalez, R. G. D. Peralta, O. Hauk, and S. L. Gonzalez. The neuroelectromagnetic inverse problem and the zero dipole localization error. *Computational intelligence and neuroscience*, 2009:659247, jan 2009.

R. Grave De Peralta Menendez, O. Hauk, S. Gonzalez Andino, H. Vogt, and C. Michel. Linear inverse solutions with optimal resolution kernels applied to electromagnetic tomography. *Human brain mapping*, 5:454–467, 1997.

R. Grave de Peralta Menendez, S. G. Andino, G. Lantz, C. M. Michel, and T. Landis. Noninvasive localization of electromagnetic epileptic activity. I. Method descriptions and simulations. *Brain Topography*, 14(2):131–137, 2001.

J. J. Green, C. N. Boehler, K. C. Roberts, L. C. Chen, R. M. Krebs, A. W. Song, and M. G. Woldorff. Cortical and subcortical coordination of visual spatial attention revealed by simultaneous EEG-fMRI recording. *Journal of Neuroscience*, 37(33):7803–7810, 2017.

S. Grimault, S. Nolden, C. Lefebvre, F. Vachon, K. Hyde, I. Peretz, R. Zatorre, N. Robitaille, and P. Jolicoeur. Brain activity is related to individual differences in the number of items stored in auditory short-term memory for pitch: Evidence from magnetoencephalography. *NeuroImage*, 94:96–106, 2014.

K. Groening, V. Brodbeck, F. Moeller, S. Wolff, A. van Baalen, C. M. Michel, O. Jansen, R. Boor, G. Wiegand, U. Stephani, and M. Siniatchkin. Combination of EEG-fMRI and EEG source analysis improves interpretation of spike-associated activation networks in paediatric pharmacoresistant focal epilepsies. *NeuroImage*, 46(3):827–33, jul 2009.

J. Gross, J. Kujala, M. Hamalainen, L. Timmermann, A. Schnitzler, and R. Salmelin. Dynamic imaging of coherent sources: Studying neural interactions in the human brain. *Proceedings of the National Academy of Sciences of the United States of America*, 98(2):694–9, jan 2001.

J. Gross, S. Baillet, G. R. Barnes, R. N. Henson, A. Hillebrand, O. Jensen, K. Jerbi, V. Litvak, B. Maess, R. Oostenveld, L. Parkkonen, J. R. Taylor, V. van Wassenhove, M. Wibral, and J.-M. Schoffelen. Good practice for conducting and reporting MEG research. *NeuroImage*, 65:1–15, oct 2013.

F. Grouiller, L. Vercueil, A. Krainik, C. Segebarth, P. Kahane, and O. David. A comparative study of different artefact removal algorithms for EEG signals acquired during functional MRI. *NeuroImage*, 38(1):124–137, oct 2007.

F. Grouiller, R. C. Thornton, K. Groening, L. Spinelli, J. S. Duncan, K. Schaller, M. Siniatchkin, L. Lemieux, M. Seeck, C. M. Michel, and S. Vulliemoz. With or without spikes: Localization of focal epileptic activity by simultaneous electroencephalography and functional magnetic resonance imaging. *Brain*, 134(10):2867–2886, oct 2011.

C. Grova, J. Daunizeau, J.-M. Lina, C. G. Bénar, H. Benali, and J. Gotman. Evaluation of EEG localization methods using realistic simulations of interictal spikes. *NeuroImage*, 29 (3):734–53, feb 2006a.

C. Grova, S. Makni, G. Flandin, P. Ciuciu, J. Gotman, and J. B. Poline. Anatomically informed interpolation of fMRI data on the cortical surface. *NeuroImage*, 31(4):1475–1486, 2006b.

C. Grova, J. Daunizeau, E. Kobayashi, A. P. Bagshaw, J.-m. Lina, F. Dubeau, and J. Gotman. Concordance between distributed EEG source localization and simultaneous EEG-fMRI studies of epileptic spikes. *NeuroImage*, 39(2):755–74, jan 2008.

C. Grova, M. Aiguabella, R. Zelmann, J. M. Lina, J. A. Hall, and E. Kobayashi. Intracranial EEG potentials estimated from MEG sources: A new approach to correlate MEG and iEEG data in epilepsy. *Human Brain Mapping*, 37(5):1661–1683, 2016.

M. Günther. Perfusion Imaging. *Journal of Magnetic Resonance Imaging*, 40:269–279, 2014.

L. F. Haas. Hans Berger (1873-1941), Richard Caton (1842-1926), and electroencephalography. *Journal of Neurology, Neurosurgery & Psychiatry*, 74(1):9–9, 2003.

J. M. Habibabadi, M. Zare, and N. Tabrizi. The Role of Interictal Epileptiform Discharges in Epilepsy Surgery Outcome. *International Journal of Preventive Medicine*, 10(101), 2019.

H. Hallez, B. Vanrumste, R. Grech, J. Muscat, W. De Clercq, A. Vergult, Y. D'Asseler, K. P. Camilleri, S. G. Fabri, S. Van Huffel, and I. Lemahieu. Review on solving the forward problem in EEG source analysis. *Journal of NeuroEngineering and Rehabilitation*, 4, 2007.

M. Hämäläinen, R. Hari, R. J. Ilmoniemi, J. Knuutila, and O. V. Lounasmaa. Magnetoencephalography — theory, instrumentation, and applications to noninvasive studies of the working human brain. *Reviews of Modern Physics*, 65(2):413–497, 1993.

M. Hämäläinen and R. Ilmoniemi. Interpreting magnetic fields of the brain: minimum norm estimates. *Medical & biological engineering & Computing*, 32(1):35–42, 1994.

P. C. P. Hansen. Analysis of discrete ill-posed problems by means of the L-curve. *SIAM review*, 34(4):561–580, 1992.

K. Hara, F.-H. Lin, S. Camposano, D. M. Foxe, P. E. Grant, B. F. Bourgeois, S. P. Ahlfors, and S. M. Stufflebeam. Magnetoencephalographic mapping of interictal spike propagation: a technical and clinical report. *AJNR. American journal of neuroradiology*, 28(8):1486–8, sep 2007.

L. M. Harrison, W. Penny, J. Ashburner, N. Trujillo-Barreto, and K. J. Friston. Diffusion-based spatial priors for imaging. *NeuroImage*, 38(4):677–695, 2007.

M. Hassan, O. Dufor, I. Merlet, C. Berrou, and F. Wendling. EEG Source Connectivity Analysis: From Dense Array Recordings to Brain Networks. *PLoS ONE*, 9(8):e105041, 2014.

M. Hassan, I. Merlet, A. Mheich, A. Kabbara, A. Biraben, A. Nica, and F. Wendling. Identification of Interictal Epileptic Networks from Dense-EEG. *Brain Topography*, 30(1): 1–17, 2016.

J. Haueisen, C. Ramon, M. Eiselt, H. Brauer, and H. Nowak. Influence of tissue resistivities on neuromagnetic fields and electric potentials studied with a finite element model of the head. *IEEE Transactions on Biomedical Engineering*, 44(8):727–735, 1997.

M. Hauf, K. Jann, K. Schindler, O. Scheidegger, K. Meyer, C. Rummel, L. Mariani, T. Koenig, and R. Wiest. Localizing Seizure-Onset Zones in Presurgical Evaluation of Drug-Resistant Epilepsy by Electroencephalography/fMRI: Effectiveness of Alternative Thresholding Strategies. *American Journal of Neuroradiology*, 33(October):1818–1824, 2012.

S. Haufe, V. V. Nikulin, A. Ziehe, K.-R. Müller, and G. Nolte. Combining sparsity and rotational invariance in EEG/MEG source reconstruction. *NeuroImage*, 42(2):726–38, aug 2008.

O. Hauk and M. Stenroos. A framework for the design of flexible cross-talk functions for spatial filtering of EEG/MEG data: DeFleCT. *Human brain mapping*, 000, apr 2013.

O. Hauk, D. G. Wakeman, and R. Henson. Comparison of noise-normalized minimum norm estimates for MEG analysis using multiple resolution metrics. *NeuroImage*, 54(3):1966–74, feb 2011.

W. A. Hauser, J. F. Annegers, and L. T. Kurland. Prevalence of Epilepsy in Rochester, Minnesota: 1940–1980. *Epilepsia*, 32(4):429–445, 1991.

C. S. Hawco, A. P. Bagshaw, Y. Lu, F. Dubeau, and J. Gotman. BOLD changes occur prior to epileptic spikes seen on scalp EEG. *NeuroImage*, 35(4):1450–1458, 2007.

B. He, A. Sohrabpour, E. Brown, and Z. Liu. Electrophysiological Source Imaging: A Noninvasive Window to Brain Dynamics. *Annual Review of Biomedical Engineering*, 20(1): annurev–bioeng–062117–120853, 2018.

T. Hedrich, G. Pellegrino, E. Kobayashi, J. M. Lina, and C. Grova. Comparison of the spatial resolution of source imaging techniques in high-density EEG and MEG. *NeuroImage*, 157: 531–544, 2017.

T. Hedrich, H. M. Khoo, A. Koupparis, C. Abdallah, J. Gotman, and C. Grova. Automatic classification of interictal epileptic discharges based on electrical source imaging for the EEG-fMRI analysis of patients with focal epilepsy. In Preparation.

T. Hedrich, Ü. Aydin, S. Grimault, H. Benali, J.-M. Lina, and C. Grova. Effect of MR-related noise on the quality of electrical source imaging for simultaneous EEG-fMRI recordings. *Human Brain Mapping*, Under Review.

M. Heers, T. Hedrich, D. An, F. Dubeau, J. Gotman, C. Grova, and E. Kobayashi. Spatial correlation of hemodynamic changes related to interictal epileptic discharges with electric and magnetic source imaging. *Human Brain Mapping*, 35(9):4396–4414, feb 2014.

M. Heers, R. A. Chowdhury, T. Hedrich, F. Dubeau, J. A. Hall, J.-M. Lina, C. Grova, and E. Kobayashi. Localization Accuracy of Distributed Inverse Solutions for Electric and Magnetic Source Imaging of Interictal Epileptic Discharges in Patients with Focal Epilepsy. *Brain Topography*, 29(1):162–181, 2015.

R. N. Henson, J. Mattout, C. Phillips, and K. J. Friston. Selecting forward models for MEG source-reconstruction using model-evidence. *NeuroImage*, 46(1):168–176, may 2009.

R. N. Henson, C. J. Price, M. D. Rugg, R. Turner, and K. J. Friston. Detecting latency differences in event-related BOLD responses: Application to words versus nonwords and initial versus repeated face presentations. *NeuroImage*, 15(1):83–97, 2002.

J. F. Hipp and M. Siegel. BOLD fMRI correlation reflects frequency-specific neuronal correlation. *Current Biology*, 25(10):1368–1374, 2015.

R. Hoekema, G. H. Wieneke, F. S. Leijten, C. W. Van Veelen, P. C. Van Rijen, G. J. Huiskamp, J. Ansems, and A. C. Van Huffelen. Measurement of the conductivity of skull, temporarily removed during epilepsy surgery. *Brain Topography*, 16(1):29–38, 2003.

R. E. Hogan. Automated EEG detection algorithms and clinical semiology in epilepsy: Importance of correlations. *Epilepsy and Behavior*, 22(SUPPL. 1):S4, 2011.

R. D. Hoge, J. Atkinson, B. Gill, G. R. Crelier, S. Marrett, and G. B. Pike. Investigation of BOLD signal dependence on CBF and CMRO2: The deoxyhemoglobin dilution model. *NeuroImage*, 9(6 PART II):849–863, 1999.

M. X. Huang, J. C. Mosher, and R. M. Leahy. A sensor-weighted overlapping-sphere head model and exhaustive head model comparison for MEG. *Physics in Medicine and Biology*, 44(2):423–440, 1999.

A. Hyafil, A. L. Giraud, L. Fontolan, and B. Gutkin. Neural Cross-Frequency Coupling: Connecting Architectures, Mechanisms, and Functions. *Trends in Neurosciences*, 38(11): 725–740, 2015.

C. Iadecola. The Neurovascular Unit Coming of Age: A Journey through Neurovascular Coupling in Health and Disease. *Neuron*, 96(1):17–42, 2017.

J. R. Ives, S. Warach, F. Schmitt, R. R. Edelman, and D. L. Schomer. Monitoring the patient's EEG during echo planar MRI. *Electroencephalography and Clinical Neurophysiology*, 87(6): 417–420, 1993.

J. Jacobs, P. Levan, F. Moeller, R. Boor, U. Stephani, J. Gotman, and M. Siniatchkin. Hemodynamic changes preceding the interictal EEG spike in patients with focal epilepsy investigated using simultaneous EEG-fMRI. *NeuroImage*, 45(4):1220–31, may 2009.

H. Jasper. Report of committee on methods of clinical exam in EEG. *Electroencephalography & Clinical Neurophysiology*, 10(2):370–375, 1958.

A. Jegou, M. Schabus, O. Gosseries, B. Dahmen, G. Albouy, M. Desseilles, V. Sterpenich, C. Phillips, P. Maquet, C. Grova, and T. T. Dang-Vu. Cortical reactivations during sleep spindles following declarative learning. *NeuroImage*, 195(November 2018):104–112, 2019.

M. Jenkinson, P. Bannister, M. Brady, and S. Smith. Improved optimization for the robust and accurate linear registration and motion correction of brain images. *NeuroImage*, 17(2): 825–841, 2002.

J. Jorge, W. van der Zwaag, and P. Figueiredo. EEG-fMRI integration for the study of human brain function. *NeuroImage*, 102:24–34, 2013.

B. Josephson. Possible new effects in superconducive tunnelling. *Physics letters*, 1(7):251–253, 1962.

C. Juhász and H. T. Chugani. Imaging the epileptic brain with positron emission tomography. *Neuroimaging Clinics of North America*, 13(4):705–716, nov 2003.

V. Jurcak, D. Tsuzuki, and I. Dan. 10/20 , 10/10 , and 10/5 systems revisited: Their validity as relative head-surface-based positioning systems. *NeuroImage*, 34:1600–1611, 2007.

T. Kameneva, T. Ying, B. Guo, and D. R. Freestone. Neural mass models as a tool to investigate neural dynamics during seizures. *Journal of Computational Neuroscience*, 42 (2):203–215, 2017.

C. Kaufmann, R. Wehrle, T. C. Wetter, F. Holsboer, D. P. Auer, T. Pollmächer, and M. Czisch. Brain activation and hypothalamic functional connectivity during human non-rapid eye movement sleep: An EEG/fMRI study. *Brain*, 129(3):655–667, 2006.

T. Keränen, M. Sillanpää, and P. J. Riekkinen. Distribution of Seizure Types in an Epileptic Population. *Epilepsia*, 29(1):1–7, 1988.

H. M. Khoo, N. von Ellenrieder, N. Zazubovits, F. Dubeau, and J. Gotman. Epileptic networks in action: Synchrony between distant hemodynamic responses. *Annals of Neurology*, 82(1): 57–66, 2017.

S. J. Kiebel, J. Daunizeau, C. Phillips, and K. J. Friston. Variational Bayesian inversion of the equivalent current dipole model in EEG/MEG. *NeuroImage*, 39(2):728–741, 2008.

H.-c. C. Kim, S.-S. S. Yoo, and J.-h. H. Lee. Recursive approach of EEG-segment-based principal component analysis substantially reduces cryogenic pump artifacts in simultaneous EEG–fMRI data. *NeuroImage*, 104:437–451, 2015.

S. Klamer, A. Elshahabi, H. Lerche, C. Braun, M. Erb, K. Scheffler, and N. K. Focke. Differences Between MEG and High-Density EEG Source Localizations Using a Distributed Source Model in Comparison to fMRI. *Brain Topography*, 28(1):87–94, 2014.

M. Klein. A Primal Method for Minimal Cost Flows with Applications to the Assignment and Transportation Problems. *Management Science*, 14(3):205–220, 1967.

R. C. Knowlton and J. Shih. Magnetoencephalography in epilepsy. *Epilepsia*, 45 Suppl 4: 61–71, jan 2004.

R. C. Knowlton, R. Elgavish, J. Howell, J. Blount, J. G. Burneo, E. Faught, P. Kankirawatana, K. Riley, R. Morawetz, J. Worthington, and R. I. Kuzniecky. Magnetic source imaging versus intracranial electroencephalogram in epilepsy surgery: A prospective study. *Annals of Neurology*, 59(5):835–842, 2006.

R. C. Knowlton, S. N. Razdan, N. Limdi, R. A. Elgavish, J. Killen, J. Blount, J. G. Burneo, L. Ver Hoef, L. Paige, E. Faught, P. Kankirawatana, A. Bartolucci, K. Riley, and R. Kuzniecky. Effect of epilepsy magnetic source imaging on intracranial electrode placement. *Annals of Neurology*, 65(6):716–723, 2009.

M. G. Knyazeva, E. Fornari, R. Meuli, G. Innocenti, and P. Maeder. Imaging of a synchronous neuronal assembly in the human visual brain. *NeuroImage*, 29(2):593–604, 2006.

E. Kobayashi, A. P. Bagshaw, C. Grova, J. Gotman, and F. Dubeau. Grey matter heterotopia: What EEG-fMRI can tell us about epileptogenicity of neuronal migration disorders. *Brain*, 129(2):366–374, 2006.

L. Koessler, C. Benar, L. Maillard, J.-M. Badier, J. P. Vignal, F. Bartolomei, P. Chauvel, and M. Gavaret. Source localization of ictal epileptic activity investigated by high resolution EEG and validated by SEEG. *NeuroImage*, 51(2):642–653, jun 2010.

L. Koessler, T. Cecchin, S. Colnat-Coulbois, J. P. Vignal, J. Jonas, H. Vespignani, G. Ramantani, and L. G. Maillard. Catching the Invisible: Mesial Temporal Source Contribution to Simultaneous EEG and SEEG Recordings. *Brain Topography*, 28(1):5–20, 2014.

S. Kolind, L. Matthews, H. Johansen-Berg, M. I. Leite, S. C. Williams, S. Deoni, and J. Palace. Myelin water imaging reflects clinical variability in multiple sclerosis. *NeuroImage*, 60(1): 263–270, 2012.

M. Kottlow, K. Jann, T. Dierks, and T. Koenig. Increased phase synchronization during continuous face integration measured simultaneously with EEG and fMRI. *Clinical Neurophysiology*, 123(8):1536–1548, 2012.

K. Krakow, P. J. Allen, M. R. Symms, L. Lemieux, O. Josephs, and D. R. Fish. EEG recording during fMRI experiments: Image quality. *Human Brain Mapping*, 10(1):10–15, 2000.

C.-c. Kuo, P. Luu, K. K. Morgan, M. Dow, C. Davey, J. Song, A. D. Malony, and D. M. Tucker. Localizing Movement-Related Primary Sensorimotor Cortices with Multi-Band EEG Frequency Changes and Functional MRI. *PLoS ONE*, 9(11):e112103, 2014.

C.-C. Kuo, D. M. Tucker, P. Luu, K. Jenson, J. J. Tsai, J. G. Ojemann, and M. D. Holmes. EEG source imaging of epileptic activity at seizure onset. *Epilepsy Research*, 146(January): 160–171, 2018.

P. Kwan, A. Arzimanoglou, A. T. Berg, M. J. Brodie, W. A. Hauser, G. Mathern, S. L. Moshé, E. Perucca, S. Wiebe, and J. French. Definition of drug resistant epilepsy: Consensus proposal by the ad hoc Task Force of the ILAE Commission on Therapeutic Strategies. *Epilepsia*, 51(6):1069–1077, 2010.

K. K. Kwong, J. W. Belliveau, D. A. Chesler, I. E. Goldberg, R. M. Weisskoff, B. P. Poncelet, D. N. Kennedy, B. E. Hoppelt, M. S. Cohent, R. Turnert, H.-m. Cheng, T. J. Bradyt, and B. R. Rosent. Dynamic magnetic resonance imaging of human brain activity during primary sensory stimulation. *PNAS*, 89(June):5675–5679, 1992.

J. Kybic, M. Clerc, O. Faugeras, R. Keriven, and T. Papadopoulos. Generalized Head Models for MEG / EEG : BEM beyond Nested Volumes. *Physics in Medicine and Biology*, 2006.

Y. Lai, W. Van Drongelen, L. Ding, K. E. Hecox, V. L. Towle, D. M. Frim, and B. He. Estimation of in vivo human brain-to-skull conductivity ratio from simultaneous extra- and intra-cranial electrical potential recordings. *Clinical Neurophysiology*, 116(2):456–465, 2005.

G. Lantz, R. Grave de Peralta, L. Spinelli, M. Seeck, and C. M. Michel. Epileptic source localization with high density EEG: how many electrodes are needed? *Clinical neurophysiology : official journal of the International Federation of Clinical Neurophysiology*, 114(1): 63–9, jan 2003a.

G. Lantz, L. Spinelli, M. Seeck, R. Grave De Peralta Menendez, C. C. Sottas, and C. M. Michel. Propagation of interictal epileptiform activity can lead to erroneous source localizations: a 128-channel EEG mapping study. *Journal of clinical neurophysiology : official publication of the American Electroencephalographic Society*, 20(5):311–319, 2003b.

A. M. Lascano, T. Perneger, S. Vulliemoz, L. Spinelli, V. Garibotto, C. M. Korff, M. I. Vargas, C. M. Michel, and M. Seeck. Yield of MRI, high-density electric source imaging (HD-ESI), SPECT and PET in epilepsy surgery candidates. *Clinical Neurophysiology*, 127(1):150–155, 2015.

H. Laufs. Endogenous brain oscillations and related networks detected by surface EEG-combined fMRI. *Human Brain Mapping*, 29(7):762–769, 2008.

H. Laufs, U. Lengler, K. Hamandi, A. Kleinschmidt, and K. Krakow. Linking generalized spike-and-wave discharges and resting state brain activity by using EEG/fMRI in a patient with absence seizures. *Epilepsia*, 47(2):444–448, 2006.

P. C. Lauterbur. Magnetic Resonance Zeugmatography. *Pure and Applied Chemistry*, 40(1): 149–157, 1974.

S. Laventure, B. Pinsard, O. Lungu, J. Carrier, S. Fogel, H. Benali, J. M. Lina, A. Boutin, and J. Doyon. Beyond spindles: Interactions between sleep spindles and boundary frequencies during cued reactivation of motor memory representations. *Sleep*, 41(9):1–14, 2018.

X. Lei, D. Ostwald, J. Hu, C. Qiu, C. Porcaro, A. P. Bagshaw, and D. Yao. Multimodal functional network connectivity: An EEG-fMRI fusion in network space. *PLoS ONE*, 6(9), 2011.

X. Lei, T. Wu, and P. A. Valdes-Sosa. Incorporating priors for EEG source imaging and connectivity analysis. *Frontiers in neuroscience*, 9(August):284, 2015.

G. Leicht, S. Vauth, N. Polomac, C. Andreou, J. Rauh, M. Mußmann, A. Karow, and C. Mulert. EEG-Informed fMRI Reveals a Disturbed Gamma-Band-Specific Network in Subjects at High Risk for Psychosis. *Schizophrenia Bulletin*, 42(1):239–249, 2016.

F. S. Leijten and G. Huiskamp. Interictal electromagnetic source imaging in focal epilepsy: Practices, results and recommendations. *Current Opinion in Neurology*, 21(4):437–445, 2008.

L. Lemieux, A. Salek-Haddadi, O. Josephs, P. Allen, N. Toms, C. Scott, K. Krakow, R. Turner, and D. R. Fish. Event-related fMRI with simultaneous and continuous EEG: Description of the method and initial case report. *NeuroImage*, 14(3):780–787, 2001.

P. LeVan, L. Tyvaert, and J. Gotman. Modulation by EEG features of BOLD responses to interictal epileptiform discharges. *NeuroImage*, 50(1):15–26, 2010.

P. LeVan, J. Maclaren, M. Herbst, R. Sostheim, M. Zaitsev, and J. Hennig. Ballistocardiographic artifact removal from simultaneous EEG-fMRI using an optical motion-tracking system. *NeuroImage*, 75:1–11, jul 2013.

C. H. Liao, K. J. Worsley, J. B. Poline, J. A. Aston, G. H. Duncan, and A. C. Evans. Estimating the delay of the fMRI response. *NeuroImage*, 16(3 I):593–606, 2002.

R. P. Lim and I. Koktzoglou. Noncontrast Magnetic Resonance Angiography: Concepts and Clinical Applications. *Radiologic Clinics of North America*, 53(3):457–476, 2015.

F.-H. Lin, T. Witzel, S. P. Ahlfors, S. M. Stufflebeam, J. W. Belliveau, and M. S. Hämäläinen. Assessing and improving the spatial accuracy in MEG source localization by depth-weighted minimum-norm estimates. *NeuroImage*, 31(1):160–171, may 2006.

J. M. Lina, R. Chowdhury, E. Lemay, E. Kobayashi, and C. Grova. Wavelet-based localization of oscillatory sources from magnetoencephalography data. *IEEE Transactions on Biomedical Engineering*, 61(8):2350–2364, mar 2014.

M. A. Lindquist, J. Meng Log, L. Y. Atlas, and T. D. Wager. Modeling the Hemodynamic Response Function in fMRI: Efficiency, Bias and Mis-modeling. *Neuroimage*, 45(1 Suppl): S187–S199, 2009.

A. Liu, J. Belliveau, and A. Dale. Spatiotemporal imaging of human brain activity using functional MRI constrained magnetoencephalography data: Monte Carlo simulations. *Proceedings of the National Academy of Sciences*, 95:8945–8950, 1998.

A. K. Liu, A. M. Dale, and J. W. Belliveau. Monte Carlo simulation studies of EEG and MEG localization accuracy. *Human Brain Mapping*, 16(1):47–62, 2002.

N. K. Logothetis, J. Pauls, M. Augath, T. Trinath, and A. Oeltermann. Neurophysiological investigation of the basis of the fMRI signal. *Nature*, 412(6843):150–7, 2001.

H. O. Lüders, I. Najm, D. Nair, P. Widdess-Walsh, and W. Bingman. The epileptogenic zone: General principles. *Epileptic Disorders*, 8(SUPPL. 2):1–9, 2006.

M. Luessi, S. D. Babacan, R. Molina, J. R. Booth, and A. K. Katsaggelos. Bayesian symmetrical EEG/fMRI fusion with spatially adaptive priors. *NeuroImage*, 55(1):113–132, 2011.

Q. Luo, X. Huang, and G. H. Glover. Ballistocardiogram artifact removal with a reference layer and standard EEG cap. *Journal of Neuroscience Methods*, 233:137–149, 2014.

J. A. Maldjian, A. Gottschalk, R. S. Patel, J. a. Detre, and D. C. Alsop. The sensory somatotopic map of the human hand demonstrated at 4 Tesla. *NeuroImage*, 10(1):55–62, jul 1999.

H. Mandelkow, P. Halder, P. Boesiger, and D. Brandeis. Synchronization facilitates removal of MRI artefacts from concurrent EEG recordings and increases usable bandwidth. *NeuroImage*, 32(3):1120–1126, 2006.

J.-F. Mangin, V. Frouin, I. Bloch, J. Régis, and J. Lopez-Krahe. From 3D magnetic resonance images to structural representations of the cortex topography using topology preserving deformations. *Journal of Mathematical Imaging and Vision*, 5(4):297–318, 1995.

D. Mantini, M. G. Perrucci, C. Del Gratta, G. L. Romani, and M. Corbetta. Electrophysiological signature of brain resting state networks. *Proceedings of the National Academy of Sciences of the United States of America*, 104(32):13170–13175, 2007.

R. Marecek, M. Lamos, M. Mikl, M. Barton, J. Fajkus, I. Rektor, and M. Brazdil. What can be found in scalp EEG spectrum beyond common frequency bands. EEG-fMRI study. *Journal of Neural Engineering*, 13(4), 2016.

G. Marrelec, H. Benali, P. Ciuciu, M. Pélégrini-Issac, and J. B. Poline. Robust Bayesian estimation of the hemodynamic response function in event-related BOLD fMRI using basic physiological information. *Human Brain Mapping*, 19(1):1–17, 2003.

W. L. Martinez and A. R. Martinez. *Exploratory Data Analysis with MATLAB*. Chapman and Hall/CRC, 2005.

R. a. J. Masterton, D. F. Abbott, S. W. Fleming, and G. D. Jackson. Measurement and reduction of motion and ballistocardiogram artefacts from simultaneous EEG and fMRI recordings. *NeuroImage*, 37(1):202–211, 2007.

E. J. Mathias, M. J. Plank, and T. David. A model of neurovascular coupling and the BOLD response PART II. *Computer Methods in Biomechanics and Biomedical Engineering*, 20 (5):519–529, 2017.

J. Mattout, M. Plgrini-Issac, L. Garnero, and H. Benali. Multivariate source prelocalization (MSP): Use of functionally informed basis functions for better conditioning the MEG inverse problem. *NeuroImage*, 26(2):356–373, 2005.

S. D. Mayhew, K. J. Mullinger, D. Ostwald, C. Porcaro, R. Bowtell, A. P. Bagshaw, and S. T. Francis. Global signal modulation of single-trial fMRI response variability: Effect on positive vs negative BOLD response relationship. *NeuroImage*, 133:62–74, 2016.

S. D. Mayhew, S. G. Dirckx, R. K. Niazy, G. D. Iannetti, and R. G. Wise. EEG signatures of auditory activity correlate with simultaneously recorded fMRI responses in humans. *NeuroImage*, 49(1):849–864, 2010.

S. D. Mayhew, D. Ostwald, C. Porcaro, and A. P. Bagshaw. Spontaneous EEG alpha oscillation interacts with positive and negative BOLD responses in the visual-auditory cortices and default-mode network. *NeuroImage*, 76:362–372, 2013.

Y. Meir-Hasson, S. Kinreich, I. Podlipsky, T. Hendler, and N. Intrator. An EEG Finger-Print of fMRI deep regional activation. *NeuroImage*, 102(P1):128–141, 2014.

S. Mesmoudi, M. Rodic, C. Cioli, J. P. Cointet, T. Yarkoni, and Y. Burnod. LinkRbrain: Multi-scale data integrator of the brain. *Journal of Neuroscience Methods*, 241:44–52, 2015.

M. C. Meyer, E. S. B. Van Oort, and M. Barth. Electrophysiological correlation patterns of resting state networks in single subjects: A combined EEG-fMRI study. *Brain Topography*, 26(1):98–109, 2013.

R. Meyers, R. Hayne, and J. Knott. Electrical activity of the neonstriatum, paleostriatum and neighbouring structures in parkinsonism and hemiballismus. *Journal of neurology, neurosurgery, and psychiatry*, 12(2):111–123, 1949.

C. M. Michel and D. Brunet. EEG source imaging: A practical review of the analysis steps. *Frontiers in Neurology*, 10(APR), 2019.

C. M. Michel and T. Koenig. EEG microstates as a tool for studying the temporal dynamics of whole-brain neuronal networks: A review. *NeuroImage*, 180(May 2017):577–593, 2018.

C. M. Michel, M. M. Murray, G. Lantz, S. Gonzalez, L. Spinelli, and R. Grave de Peralta. EEG source imaging. *Clinical neurophysiology*, 115(10):2195–222, oct 2004.

L. Michels, K. Bucher, R. Lüchinger, P. Klaver, E. Martin, D. Jeanmonod, and D. Brandeis. Simultaneous EEG-fMRI during a working memory task: Modulations in low and high frequency bands. *PLoS ONE*, 5(4), 2010.

H. Mizuhara, L. Q. Wang, K. Kobayashi, and Y. Yamaguchi. Long-range EEG phase synchronization during an arithmetic task indexes a coherent cortical network simultaneously measured by fMRI. *NeuroImage*, 27(3):553–563, 2005.

S. Moeller, E. Yacoub, C. A. Olman, E. Auerbach, J. Strupp, N. Harel, and K. Ugurbil. Multiband Multislice GE-EPI at 7 Tesla, With 16-Fold Acceleration Using Partial Parallel Imaging With Application to High Spatial and Temporal Whole-Brain FMRI. *Magnetic Resonance in Medicine*, 63(5):1144–1153, 2010.

A. Molins, S. M. Stufflebeam, E. N. Brown, and M. S. Hämäläinen. Quantification of the benefit from integrating MEG and EEG data in minimum l2-norm estimation. *NeuroImage*, 42(3):1069–77, sep 2008.

M. M. Monti. Statistical analysis of fMRI time-series: A critical review of the GLM approach. *Frontiers in Human Neuroscience*, 5(MARCH):1–13, 2011.

V. A. Morozov. On the solution of functional equations by the method of regularization. *Dokl. Akad. Nauk SSSR*, 167(3):510–512, 1966.

J. C. Mosher, R. M. Leahy, and P. S. Lewis. {E}{E}{G} and {M}{E}{G}: forward solutions for inverse methods. *IEEE Trans Biomed Eng*, 46(3):245–259, mar 1999a.

J. C. Mosher and R. M. Leahy. Source localization using recursively applied and projected (RAP) music. *IEEE Transactions on Signal Processing*, 45(9):2405, 1997.

J. C. Mosher, P. S. Lewis, and R. M. Leahy. Multiple Dipole Modeling and Localization from Spatio-Temporal MEG Data. *IEEE Transactions on Biomedical Engineering*, 39(6): 541–557, 1992.

J. C. Mosher, S. Baillet, and R. M. Leahy. EEG source localization and imaging using multiple signal classification approaches. *Journal of Clinical Neurophysiology*, 16(3):225–238, 1999b.

B. E. Mouthaan, M. Rados, P. Boon, E. Carrette, B. Diehl, J. Jung, V. Kimiskidis, T. Kobulashvili, G. Kuchukhidze, P. G. Larsson, M. Leitinger, P. Ryvlin, F. Rugg-Gunn, M. Seeck, S. Vulliémoz, G. Huiskamp, F. S. Leijten, P. Van Eijsden, E. Trinka, and K. P. Braun. Diagnostic accuracy of interictal source imaging in presurgical epilepsy evaluation: A systematic review from the E-PILEPSY consortium. *Clinical Neurophysiology*, 130(5): 845–855, 2019.

C. Mulert and L. Lemieux. *EEG - fMRI: Physiological Basis, Technique, and Applications*. Springer, 2010.

K. J. Mullinger, S. D. Mayhew, A. P. Bagshaw, R. Bowtell, and S. T. Francis. Evidence that the negative BOLD response is neuronal in origin: a simultaneous EEG-BOLD-CBF study in humans. *NeuroImage*, 94:263–74, 2014.

K. Mullinger, S. Debener, R. Coxon, and R. Bowtell. Effects of simultaneous EEG recording on MRI data quality at 1.5, 3 and 7 tesla. *International Journal of Psychophysiology*, 67 (3):178–188, 2008a.

K. J. Mullinger, P. S. Morgan, and R. W. Bowtell. Improved artifact correction for combined electroencephalography/functional MRI by means of synchronization and use of vectorcardiogram recordings. *Journal of Magnetic Resonance Imaging*, 27(3):607–616, 2008b.

K. J. Mullinger, W. X. Yan, and R. Bowtell. Reducing the gradient artefact in simultaneous EEG-fMRI by adjusting the subject's axial position. *NeuroImage*, 54(3):1942–1950, 2011.

K. J. Mullinger, J. Havenhand, and R. Bowtell. Identifying the sources of the pulse artefact in EEG recordings made inside an MR scanner. *Neuroimage*, 71:75–83, may 2013a.

K. J. Mullinger, S. D. Mayhew, A. P. Bagshaw, R. Bowtell, and S. T. Francis. Poststimulus undershoots in cerebral blood flow and BOLD fMRI responses are modulated by poststimulus neuronal activity. *Proceedings of the National Academy of Sciences of the United States of America*, 110(33):13636–13641, 2013b.

T. Murta, L. Hu, T. M. Tierney, U. J. Chaudhary, M. C. Walker, D. W. Carmichael, P. Figueiredo, and L. Lemieux. A study of the electro-haemodynamic coupling using simultaneously acquired intracranial EEG and fMRI data in humans. *NeuroImage*, 142: 371–380, 2016.

T. Murta, U. J. Chaudhary, T. M. Tierney, A. Dias, M. Leite, D. W. Carmichael, P. Figueiredo, and L. Lemieux. Phase–amplitude coupling and the BOLD signal: A simultaneous intracranial EEG (icEEG) - fMRI study in humans performing a finger-tapping task. *NeuroImage*, 146:438–451, 2017.

T. Murta, M. Leite, D. W. Carmichael, P. Figueiredo, and L. Lemieux. Electrophysiological correlates of the BOLD signal for EEG-informed fMRI. *Human Brain Mapping*, 36(1): 391–414, 2015.

M. D. Mălîia, P. Meritam, M. Scherg, M. Fabricius, G. Rubboli, I. Mîndruţă, and S. Beniczky. Epileptiform discharge propagation: Analyzing spikes from the onset to the peak. *Clinical Neurophysiology*, 127(4):2127–2133, 2016.

M. Nakamura, S. Nishida, and H. Shibasaki. Evaluation Of The Signal-To-Noise Ratio For Average Evoked Potentials Contaminated By Colored Noise. *IFAC Proceedings Volumes*, 21(9):891–896, 1988.

W. Nakamura, K. Anami, T. Mori, O. Saitoh, A. Cichocki, and S.-i. I. Amari. Removal of ballistocardiogram artifacts from simultaneously recorded EEG and fMRI data using independent component analysis. *IEEE Transactions on Biomedical Engineering*, 53(7): 1294–308, jul 2006.

H. Nariai, S. A. Hussain, D. Bernardo, A. Fallah, K. K. Murata, J. C. Nguyen, R. R. Rajaraman, L. M. Rao, J. H. Matsumoto, J. T. Lerner, N. Salamon, D. Elashoff, R. Sankar, and J. Y. Wu. Clinical Neurophysiology Prospective observational study : Fast ripple localization delineates the epileptogenic zone. *Clinical Neurophysiology*, 130(11):2144–2152, 2019.

V. T. Nguyen and R. Cunnington. The superior temporal sulcus and the N170 during face processing: Single trial analysis of concurrent EEG-fMRI. *NeuroImage*, 86:492–502, 2014.

R. K. Niazy, C. F. Beckmann, G. D. Iannetti, J. M. Brady, and S. M. Smith. Removal of FMRI environment artifacts from EEG data using optimal basis sets. *NeuroImage*, 28(3): 720–37, nov 2005.

T. Nichols and S. Hayasaka. Controlling the familywise error rate in functional neuroimaging: a comparative review. *Statistical methods in medical research*, 12(5):419–446, oct 2003.

T. E. Nichols. Multiple testing corrections, nonparametric methods, and random field theory. *NeuroImage*, 62(2):811–815, 2012.

E. Niedermeyer. Historical Aspects. In *Electroencephalography : basic principles, clinical applications, and related fields*, chapter 1, pages 1–33. Lippincott Williams & Wilkins, 5 edition, 2005.

T. Nierhaus, C. Gundlach, D. Goltz, S. D. Thiel, B. Pleger, and A. Villringer. Internal ventilation system of MR scanners induces specific EEG artifact during simultaneous EEG-fMRI. *NeuroImage*, 74:70–76, 2013.

D. G. Nishimura. *Principles of Magnetic Resonance Imaging*. Stanford University, 2010.

S. Noachtar and J. Rémi. The role of EEG in epilepsy: a critical review. *Epilepsy & behavior : E&B*, 15(1):22–33, may 2009.

P. L. Nunez and R. B. Silberstein. On the relationship of synaptic activity to macroscopic measurements: Does co-registration of EEG with fMRI make sense? *Brain Topography*, 13 (2):79–96, 2000.

P. L. Nunez and R. Srinivasan. *Electric Fields of the Brain. The Neurophysics of EEG.* Oxford University Press, 2 edition, 2006.

J. V. Odom, M. Bach, C. Barber, M. Brigell, M. F. Marmor, A. P. Tormene, and G. E. Holder. Visual evoked potential standard (2004). *Documenta Ophthalmologica*, 108(1): 115–123, 2004.

S. Ogawa, T. M. Lee, A. R. Kay, and D. W. Tank. Brain magnetic resonance imaging with contrast dependent on blood oxygenation. *Proc. Natl. Acad. Sci. U.S.A.*, 87(24):9868–9872, dec 1990.

S. Ogawa, D. W. Tank, R. Menon, J. M. Ellermann, S. G. Kim, H. Merkle, K. Ugurbil, and W. David. Intrinsic signal changes accompanying sensory stimulation: functional brain mapping with magnetic resonance imaging. *Proceedings of the National Academy of Sciences*, 89(13):5951–5955, jul 1992.

M. Oishi, H. Otsubo, S. Kameyama, N. Morota, H. Masuda, M. Kitayama, and R. Tanaka. Epileptic spikes: magnetoencephalography versus simultaneous electrocorticography. *Epilepsia*, 43(11):1390–5, nov 2002.

D. Ostwald and A. P. Bagshaw. Information theoretic approaches to functional neuroimaging. *Magnetic Resonance Imaging*, 29(10):1417–1428, 2011.

D. Ostwald, C. Porcaro, and A. P. Bagshaw. An information theoretic approach to EEG-fMRI integration of visually evoked responses. *NeuroImage*, 49(1):498–516, 2010.

C. Papadelis, E. Tamilia, S. Stufflebeam, P. E. Grant, J. R. Madsen, P. L. Pearl, and N. Tanaka. Interictal High Frequency Oscillations Detected with Simultaneous Magnetoencephalography and Electroencephalography as Biomarker of Pediatric Epilepsy. *Journal of Visualized Experiments*, 1(118):1–13, 2016.

J. Parvizi and S. Kastner. Promises and limitations of human intracranial electroencephalography. *Nature Neuroscience*, 21(4):474–483, 2018.

R. D. Pascual-Marqui. Standardized low-resolution brain electromagnetic tomography (sLORETA): technical details. *Methods Find Exp Clin Pharmacol*, 24(Suppl D):5–12, 2002.

R. D. Pascual-Marqui, C. M. Michel, and D. Lehmann. Segmentation of brain electrical activity into microstates: model estimation and validation. *IEEE transactions on biomedical engineering*, 42(7):658–665, jul 1995.

C. Pedreira, A. E. Vaudano, R. C. Thornton, U. J. Chaudhary, S. Vulliemoz, H. Laufs, R. Rodionov, D. W. Carmichael, S. D. Lhatoo, M. Guye, R. Quian Quiroga, and L. Lemieux. Classification of EEG abnormalities in partial epilepsy with simultaneous EEG-fMRI recordings. *NeuroImage*, 99:461–476, 2014.

O. Pele and M. Werman. Fast and robust earth mover's distances. *IEEE 12th International Conference on Computer Vision*, pages 460–467, 2009.

G. Pellegrino, T. Hedrich, R. Chowdhury, J. A. Hall, J.-M. Lina, F. Dubeau, E. Kobayashi, and C. Grova. Source localization of the seizure onset zone from ictal EEG/MEG data. *Human brain mapping*, 2546(April):2528–2546, 2016a.

G. Pellegrino, A. Machado, N. von Ellenrieder, S. Watanabe, J. A. Hall, J. M. Lina, E. Kobayashi, and C. Grova. Hemodynamic response to interictal epileptiform discharges addressed by personalized EEG-fNIRS recordings. *Frontiers in Neuroscience*, 10(MAR), 2016b.

G. Pellegrino, T. Hedrich, R. A. Chowdhury, J. A. Hall, F. Dubeau, J. M. Lina, E. Kobayashi, and C. Grova. Clinical yield of magnetoencephalography distributed source imaging in epilepsy: A comparison with equivalent current dipole method. *Human Brain Mapping*, 39 (1):218–231, 2018.

A. A. Phillips, F. H. Chan, M. M. Z. Zheng, A. V. Krassioukov, and P. N. Ainslie. Neurovascular coupling in humans: Physiology, methodological advances and clinical implications. *Journal of Cerebral Blood Flow and Metabolism*, 36(4):647–664, 2015.

D. Picchioni, J. H. Duyn, and S. G. Horovitz. Sleep and the functional connectome. *NeuroImage*, 80:387–396, 2013.

P. Pinel, B. Thirion, S. Meriaux, A. Jobert, J. Serres, D. Le Bihan, J. B. Poline, and S. Dehaene. Fast reproducible identification and large-scale databasing of individual functional cognitive networks. *BMC Neuroscience*, 8(1):91, 2007.

F. Pittau, P. Levan, F. Moeller, T. Gholipour, C. Haegelen, R. Zelmann, F. Dubeau, and J. Gotman. Changes preceding interictal epileptic EEG abnormalities: Comparison between EEG/fMRI and intracerebral EEG. *Epilepsia*, 52(6):1120–1129, 2011.

F. Pittau, F. Dubeau, and J. Gotman. Contribution of EEG/fMRI to the definition of the epileptic focus. *Neurology*, 78:1479–1487, 2012.

F. Pittau, F. F. Grouiller, L. Spinelli, M. Seeck, C. M. Michel, and S. Vulliemoz. The role of functional neuroimaging in pre-surgical epilepsy evaluation. *Frontiers in Neurology*, 5 (March):1–16, jan 2014.

F. Pizzo, N. Roehri, S. Medina Villalon, A. Trébuchon, S. Chen, S. Lagarde, R. Carron, M. Gavaret, B. Giusiano, A. McGonigal, F. Bartolomei, J. M. Badier, and C. G. Bénar. Deep brain activities can be detected with magnetoencephalography. *Nature Communications*, 10(1):1–13, 2019.

R. Quian Quiroga, Z. Nadasdy, and Y. Ben-Shaul. Unsupervised Spike Detection and Sorting with Wavelets and Superparamagnetic Clustering. *Neural computation*, 16(5):1661–1687, 2004.

C. Ramon, P. Schimpf, J. Haueisen, M. Holmes, and A. Ishimaru. Role of soft bone, CSF and gray matter in EEG simulations. *Brain Topography*, 16(4):245–248, 2004.

S. Rampp, H. Stefan, X. Wu, M. Kaltenhauser, B. Maess, F. C. Schmitt, C. H. Wolters, H. Hamer, B. S. Kasper, S. Schwab, A. Doerfler, I. Blumcke, K. Rossler, and M. Buchfelder. Magnetoencephalography for epileptic focus localization in a series of 1000 cases. *Brain*, 0 (0):1–13, 2019.

M. Reuter, N. J. Schmansky, H. D. Rosas, and B. Fischl. Within-Subject Template Estimation for Unbiased Longitudinal Image Analysis. *NeuroImage*, 61(4):1402–1418, 2012.

P. A. Rinck. An Excursion into the History of Magnetic Resonance Imaging. In *Magnetic Resonance in Medicine. A critical Introduction*, pages 375–406. The Round Table Foundation, 2018. ISBN 9783746095189.

M. J. Rosa, J. Daunizeau, and K. J. Friston. EEG-fMRI Integration: a Critical Review of Biophysical Modeling and Data Analysis Approaches. *Journal of Integrative Neuroscience*, 09(04):453–476, 2010.

S. Rothlübbers, V. Relvas, A. Leal, T. Murta, L. Lemieux, and P. Figueiredo. Characterisation and Reduction of the EEG Artefact Caused by the Helium Cooling Pump in the MR Environment: Validation in Epilepsy Patient Data. *Brain topography*, 28(2):208–220, 2014.

Y. Rubner, C. Tomasi, and L. J. L. Guibas. The earth mover's distance as a metric for image retrieval. *International Journal of Computer Vision*, 40(2):99–121, 2000.

C. Rumeau, N. Tzourio, N. Murayama, P. Peretti-Viton, O. Levrier, M. Joliot, B. Mazoyer, and G. Salomon. Location of hand function in the sensorimotor cortex: MR and functional correlation. *American journal of neuroradiology*, 1994.

S. Rush and D. A. Driscoll. EEG Electrode Sensitivity—An Application of Reciprocity. *IEEE Transactions on Biomedical Engineering*, BME-16(1):15–22, 1969.

G. S. Russell, K. J. Eriksen, P. Poolman, P. Luu, D. M. Tucker, P. Poolman, P. Luu, and D. M. Tucker. Geodesic photogrammetry for localizing sensor positions in dense-array EEG. *Clinical Neurophysiology*, 116(5):1130–1140, 2005.

A. Salek-Haddadi, B. Diehl, K. Hamandi, M. Merschhemke, A. Liston, K. Friston, J. S. Duncan, D. R. Fish, and L. Lemieux. Hemodynamic correlates of epileptiform discharges: An EEG-fMRI study of 63 patients with focal epilepsy. *Brain Research*, 1088(1):148–166, 2006.

M. Schabus, T. T. Dang-Vu, G. Albouy, E. Balteau, M. Boly, J. Carrier, A. Darsaud, C. Degueldre, M. Desseilles, S. Gais, C. Phillips, G. Rauchs, C. Schnakers, V. Sterpenich, G. Vandewalle, A. Luxen, and P. Maquet. Hemodynamic Cerebral Correlates of Sleep Spindles During. *Proceedings of the National Academy of Sciences*, 104(32):13164–13169, 2007.

R. Scheeringa, P. Fries, K. M. Petersson, R. Oostenveld, I. Grothe, D. G. Norris, P. Hagoort, and M. C. Bastiaansen. Neuronal Dynamics Underlying High- and Low-Frequency EEG Oscillations Contribute Independently to the Human BOLD Signal. *Neuron*, 69(3):572–583, 2011.

R. Scheeringa, K. M. Petersson, A. Kleinschmidt, O. Jensen, and M. C. Bastiaansen. EEG Alpha Power Modulation of fMRI Resting-State Connectivity. *Brain Connectivity*, 2(5): 254–264, 2012.

E. Scheffer, S. Berkovic, G. Capovilla, M. B. Connolly, J. French, L. Guilhoto, E. Hirsch, S. Jain, G. W. Mathern, S. L. Moshé, D. R. Nordli, E. Perucca, and T. Tomson. Classificazione delle epilessie della International League Against Epilepsy : position paper della Commissione ILAE per la Classificazione e la Terminologia. *Epilepsia*, 58(4):512–521, 2017.

F. Schmitt, M. K. Stehling, and R. Turner. *Echo-Planar Imaging: Theory, Technique and Application*. Springer Science & Business Media, 2012.

J.-M. Schoffelen and J. Gross. Source connectivity analysis with MEG and EEG. *Human Brain Mapping*, 30(6):1857–1865, jun 2009.

M. L. Schölvinck, D. A. Leopold, M. J. Brookes, and P. H. Khader. The contribution of electrophysiology to functional connectivity mapping. *NeuroImage*, 80:297–306, 2013.

S. Schwab, T. Koenig, Y. Morishima, T. Dierks, A. Federspiel, and K. Jann. Discovering frequency sensitive thalamic nuclei from EEG microstate informed resting state fMRI. *NeuroImage*, 118:368–375, 2015.

F. Sharbrough, G. Chatrian, R. Lesser, H. Lüders, M. Nuwer, and T. Picton. American EEG society guidelines for standard electrode position nomenclature. *Journal of Nlinical Neurophysiologie*, 8(January 1991):200–202, 1991.

N. K. Sharma, C. Pedreira, M. Centeno, U. J. Chaudhary, T. Wehner, L. G. França, T. Yadee, T. Murta, M. Leite, S. B. Vos, S. Ourselin, B. Diehl, and L. Lemieux. A novel scheme for the validation of an automated classification method for epileptic spikes by comparison with multiple observers. *Clinical Neurophysiology*, 128(7):1246–1254, 2017.

N. K. Sharma, C. Pedreira, U. J. Chaudhary, M. Centeno, D. W. Carmichael, T. Yadee, T. Murta, B. Diehl, and L. Lemieux. BOLD mapping of human epileptic spikes recorded during simultaneous intracranial EEG-fMRI: The impact of automated spike classification. *NeuroImage*, 184(August 2018):981–992, 2019.

A. Shmuel. Locally Measured Neuronal Correlated of Functional MRI Signals. In C. Mulert and L. Lemieux, editors, *EEG-fMRI*, pages 63–82. Springer, 2010.

S. Shorvon. *Epilepsy*. OUP Oxford, 2009.

A. Sohrabpour, Y. Lu, P. Kankirawatana, J. Blount, H. Kim, and B. He. Effect of EEG electrode number on epileptic source localization in pediatric patients. *Clinical neurophysiology : official journal of the International Federation of Clinical Neurophysiology*, jul 2014.

Y. Song, R. A. Torres, S. Garcia, Y. Frometa, J. Bae, A. Deshmukh, W. C. Lin, Y. Zheng, and J. J. Riera. Dysfunction of neurovascular/metabolic coupling in chronic focal epilepsy. *IEEE Transactions on Biomedical Engineering*, 63(1):97–110, 2016.

R. C. Sotero and N. J. Trujillo-Barreto. Biophysical model for integrating neuronal activity, EEG, fMRI and metabolism. *NeuroImage*, 39(1):290–309, jan 2008.

G. S. Souza, B. D. Gomes, E. M. C. Lacerda, C. A. Saito, M. da Silva Filho, and L. C. L. Silveira. Contrast sensitivity of pattern transient VEP components: Contribution from M and P pathways. *Psychology and Neuroscience*, 6(2):191–198, 2013.

C. Stangor and J. Walinga. *Introduction to Psychology - 1st Canadian Edition*. BCcampus, 2017.

S. Sten, K. Lundengård, S. T. Witt, G. Cedersund, F. Elinder, and M. Engström. Neural inhibition can explain negative BOLD responses: A mechanistic modelling and fMRI study. *NeuroImage*, 158(July):219–231, 2017.

T. K. Stevens, J. R. Ives, L. M. Klassen, and R. Bartha. MR compatibility of EEG scalp electrodes at 4 tesla. *Journal of Magnetic Resonance Imaging*, 25(4):872–877, 2007.

C. Stippich. *Clinical functional MRI: Presurgical Functional Neuroimaging*. Springer Science & Business Media, 2007.

M. Strandberg, E. M. Larsson, S. Backman, and K. Kallen. Pre-surgical epilepsy evaluation using 3T MRI. Do surface coils provide additional information? *Epileptic Disord*, 10(2): 83–92, jun 2008.

W. W. Sutherling, A. N. Mamelak, D. Thyerlei, T. Maleeva, Y. Minazad, L. Philpott, and N. Lopez. Influence of magnetic source imaging for planning intracranial EEG in epilepsy. *Neurology*, 71(13):990–6, sep 2008.

F. Tadel, S. Baillet, J. C. Mosher, D. Pantazis, and R. M. Leahy. Brainstorm: a user-friendly application for MEG/EEG analysis. *Computational intelligence and neuroscience*, 2011: 879716, jan 2011.

N. Tanaka, M. S. Hämäläinen, S. P. Ahlfors, H. Liu, J. R. Madsen, B. F. Bourgeois, J. Woo, B. a. Dworetzky, J. W. Belliveau, S. M. Stuf, J. W. Lee, B. a. Dworetzky, J. W. Belliveau, and S. M. Stufflebeam. Propagation of epileptic spikes reconstructed from spatiotemporal magnetoencephalographic and electroencephalographic source analysis. *NeuroImage*, 50(1): 217–22, mar 2010.

J. X. Tao, M. Baldwin, S. Hawes-ebersole, and J. S. Ebersole. Cortical substrates of scalp EEG epileptiform discharges. *Journal of clinical neurophysiology : official publication of the American Electroencephalographic Society*, 24(2):96–100, apr 2007.

J. F. Téllez-Zenteno, R. Dhar, and S. Wiebe. Long-term seizure outcomes following epilepsy surgery: A systematic review and meta-analysis. *Brain*, 128(5):1188–1198, 2005.

J. F. Téllez-Zenteno, L. H. Ronquillo, F. Moien-Afshari, and S. Wiebe. Surgical outcomes in lesional and non-lesional epilepsy: A systematic review and meta-analysis. *Epilepsy Research*, 89(2-3):310–318, 2010.

R. Thornton, H. Laufs, R. Rodionov, S. Cannadathu, D. W. Carmichael, S. Vulliemoz, A. Salek-haddadi, A. W. McEvoy, S. M. Smith, S. Lhatoo, R. D. C. Elwes, M. Guye, M. C. Walker, L. Lemieux, and J. S. Duncan. EEG correlated functional MRI and postoperative outcome in focal epilepsy. *Journal of neurology, neurosurgery, and psychiatry*, 81(8):922–7, aug 2010.

B. I. Turetsky, J. Raz, and G. Fein. Noise and signal power and their effects on evoked potential estimation. *Electroencephalography and Clinical Neurophysiology*, 71:310–318, 1988.

L. Tyvaert, P. LeVan, C. Grova, F. Dubeau, and J. Gotman. Effects of fluctuating physiological rhythms during prolonged EEG-fMRI studies. *Clinical Neurophysiology*, 119(12):2762–2774, 2008.

M. Uji, R. Wilson, S. T. Francis, K. J. Mullinger, and S. D. Mayhew. Exploring the advantages of multiband fMRI with simultaneous EEG to investigate coupling between

gamma frequency neural activity and the BOLD response in humans. *Human Brain Mapping*, 39(4):1673–1687, 2018.

M. a. Uusitalo and R. J. Ilmoniemi. Signal-space projection method for separating MEG or EEG into components. *Medical & biological engineering & computing*, 35(2):135–140, mar 1997.

S. Vadera, L. Jehi, R. C. Burgess, K. Shea, A. V. Alexopoulos, J. Mosher, J. Gonzalez-Martinez, and W. Bingaman. Correlation between magnetoencephalography-based "clusterectomy" and postoperative seizure freedom. *Neurosurgical Focus*, 34(6):2–5, 2013.

P. A. Valdes-Sosa, J. M. Sanchez-Bornot, R. C. Sotero, Y. Iturria-Medina, Y. Aleman-Gomez, J. Bosch-Bayard, F. Carbonell, and T. Ozaki. Model driven EEG/fMRI fusion of brain oscillations. *Human Brain Mapping*, 30(9):2701–2721, 2009.

J. van der Meer, A. Pampel, E. van Someren, J. Ramautar, Y. van der Werf, G. Gomez-Herrero, J. Lepsien, L. Hellrung, H. Hinrichs, H. Möller, and M. Walter. "Eyes Open - Eyes Closed" EEG/fMRI data set including dedicated "Carbon Wire Loop" motion detection channels. *Data in Brief*, 7:990–994, 2016a.

J. N. van der Meer, A. Pampel, E. J. Van Someren, J. R. Ramautar, Y. D. van der Werf, G. Gomez-Herrero, J. Lepsien, L. Hellrung, H. Hinrichs, H. E. Möller, and M. Walter. Carbon-wire loop based artifact correction outperforms post-processing EEG/fMRI corrections-A validation of a real-time simultaneous EEG/fMRI correction method. *NeuroImage*, 125:880–894, 2016b.

L. A. van Graan, L. Lemieux, and U. J. Chaudhary. Methods and utility of EEG-fMRI in epilepsy. *Quantitative imaging in medicine and surgery*, 5(2):300–12, 2015.

P. van Mierlo, Y. Höller, N. K. Focke, and S. Vulliemoz. Network Perspectives on Epilepsy Using EEG/MEG Source Connectivity. *Frontiers in Neurology*, 10(July):1–13, 2019.

W. Van Paesschen, P. Dupont, S. Sunaert, K. Goffin, and K. Van Laere. The use of SPECT and PET in routine clinical practice in epilepsy. *Current Opinion in Neurology*, 20(2): 194–202, 2007.

B. D. Van Veen, W. van Drongelen, M. Yuchtman, and A. Suzuki. Localization of brain electrical activity via linearly constrained minimum variance spatial filtering. *IEEE transactions on bio-medical engineering*, 44(9):867–80, sep 1997.

K. Vanderperren, M. De Vos, J. R. Ramautar, N. Novitskiy, M. Mennes, S. Assecondi, B. Vanrumste, P. Stiers, B. R. H. Van Den Bergh, J. Wagemans, L. Lagae, S. Sunaert, and S. Van Huffel. Removal of BCG artifacts from EEG recordings inside the MR scanner : A comparison of methodological and validation-related aspects. *NeuroImage*, 50(3):920–934, 2010.

N. von Ellenrieder, L. Beltrachini, C. H. Muravchik, and J. Gotman. Extent of cortical generators visible on the scalp: Effect of a subdural grid. *NeuroImage*, 101:787–795, 2014.

N. von Ellenrieder, G. Pellegrino, T. Hedrich, J. Gotman, J.-M. Lina, C. Grova, and E. Kobayashi. Detection and Magnetic Source Imaging of Fast Oscillations (40–160 Hz) Recorded with Magnetoencephalography in Focal Epilepsy Patients. *Brain Topography*, 29(2):218–231, 2016.

J. Vorwerk, J. H. Cho, S. Rampp, H. Hamer, T. R. Knösche, and C. H. Wolters. A guideline for head volume conductor modeling in EEG and MEG. *NeuroImage*, 100:590–607, 2014.

J. Vorwerk, Ü. Aydin, C. H. Wolters, and C. R. Butson. Influence of head tissue conductivity uncertainties on EEG dipole reconstruction. *Frontiers in Neuroscience*, 13(JUN):1–17, 2019.

J. Vrba, K. Betts, M. Burbank, T. Cheung, A. A. Fife, P. R. Kubik, S. Lee, J. McCubbin, J. McKay, D. McKenzie, P. Spear, B. Taylor, M. Tillotson, D. Cheyne, and H. Weinberg. Whole Cortex, 64 Channel Squid Biomagnetometer System. *IEEE Transactions on Applied Superconductivity*, 3(1):1878–1882, 1993.

S. Vulliemoz, R. Thornton, R. Rodionov, D. Carmichael, M. Guye, S. Lhatoo, A. W. McEvoy, L. Spinelli, C. Michel, J. Duncan, and L. Lemieux. The spatio-temporal mapping of epileptic networks: Combination of EEG–fMRI and EEG source imaging. *NeuroImage*, 46 (3):834–843, jul 2009.

S. Vulliemoz, R. Rodionov, D. W. Carmichael, R. Thornton, M. Guye, S. D. Lhatoo, C. M. Michel, J. S. Duncan, and L. Lemieux. Continuous EEG source imaging enhances analysis of EEG-fMRI in focal epilepsy. *NeuroImage*, 49(4):3219–29, feb 2010a.

S. Vulliemoz, L. Lemieux, J. Daunizeau, C. M. Michel, and J. S. Duncan. The combination of EEG source imaging and EEG-correlated functional MRI to map epileptic networks. *Epilepsia*, 51(4):491–505, apr 2010b.

M. Wagner, M. Fuchs, H.-A. Wischmann, R. Drenckhahn, and T. Köhler. Smooth reconstruction of cortical sources from EEG or MEG recordings. *NeuroImage*, 3(3):S168, 1996.

X. Wan, J. Riera, K. Iwata, M. Takahashi, T. Wakabayashi, and R. Kawashima. The neural basis of the hemodynamic response nonlinearity in human primary visual cortex: Implications for neurovascular coupling mechanism. *NeuroImage*, 32(2):616–625, 2006.

J. P. Wansapura, S. K. Holland, R. S. Dunn, and W. S. Ball. NMR relaxation times in the human brain at 3.0 Tesla. *Journal of Magnetic Resonance Imaging*, 9(4):531–538, 1999.

W. Webber, B. Litt, R. P. Lesser, R. Fisher, and I. Bankman. Automatic EEG spike detection: what should the computer imitate? *Electroencephalography and Clinical Neurophysiology*, 87(6):364–373, dec 1993.

K. Wendel, O. Väisänen, J. Malmivuo, N. G. Gencer, B. Vanrumste, P. Durka, R. Magjarević, S. Supek, M. L. Pascu, H. Fontenelle, and R. Grave De Peralta Menendez. EEG/MEG source imaging: Methods, challenges, and open issues. *Computational Intelligence and Neuroscience*, 2009, 2009.

C. Whalen, E. L. Maclin, M. Fabiani, and G. Gratton. Validation of a method for coregistering scalp recording locations with 3D structural MR images. *Human Brain Mapping*, 29(11): 1288–1301, 2008.

K. Whittingstall, D. Wilson, M. Schmidt, and G. Stroink. Correspondence of visual evoked potentials with FMRI signals in human visual cortex. *Brain Topography*, 21(2):86–92, 2008.

S. Wiebe, D. R. Bellhouse, C. Fallahay, and M. Eliasziw. Burden of epilepsy: the Ontario Health Survey. *The Canadian journal of neurological sciences. Le journal canadien des sciences neurologiques*, 26(4):263–70, nov 1999.

R. Wilson, K. J. Mullinger, S. T. Francis, and S. D. Mayhew. The relationship between negative BOLD responses and ERS and ERD of alpha/beta oscillations in visual and motor cortex. *NeuroImage*, 199(June):635–650, 2019.

J. Wirsich, C. Bénar, J. P. Ranjeva, M. Descoins, E. Soulier, A. Le Troter, S. Confort-Gouny, C. Liégeois-Chauvel, and M. Guye. Single-trial EEG-informed fMRI reveals spatial dependency of BOLD signal on early and late IC-ERP amplitudes during face recognition. *NeuroImage*, 100:325–336, 2014.

C. H. Wolters. The Finite Element Method in EEG/MEG Source Analysis. *SIAM News*, 40 (2), 2007.

C. W. Woo, A. Krishnan, and T. D. Wager. Cluster-extent based thresholding in fMRI analyses: Pitfalls and recommendations. *NeuroImage*, 91:412–419, 2014.

C. C. Wood. Application of Dipole Localization Methods To Source Identification of Human Evoked Potentials. *Annals of the New York Academy of Sciences*, 338(1):139–155, 1982.

C. C. Wood, D. D. Spencer, T. Allison, G. McCarthy, P. Williamson, and K. R. Goffin. Localization of human sensorimotor cortex during surgery by cortical surface recording of somatosensory evoked potentials. *Journal of neurosurgery*, 68(1):99–111, jan 1988.

K. J. Worsley, S. Marrett, P. Neelin, A. C. Vandal, K. J. Friston, and A. C. Evans. A unified statistical approach for determining significant signals in images of cerebral activation. *Human brain mapping*, 4(1):58–73, jan 1996.

K. Worsley, C. Liao, J. Aston, V. Petre, G. Duncan, F. Morales, and A. Evans. A general statistical analysis for fMRI data. *Neuroimage*, 15(1):1–15, 2002.

W. Wu and K. L. Miller. Image formation in diffusion MRI: A review of recent technical developments. *Journal of Magnetic Resonance Imaging*, 46(3):646–662, 2017.

H. Xia, D. Ruan, and M. S. Cohen. Separation and reconstruction of BCG and EEG signals during continuous EEG and fMRI recordings. *Front Neurosci*, 8:163, 2014.

J. Xu, S. Mitra, C. Van Hoof, R. F. Yazicioglu, and K. A. Makinwa. Active Electrodes for Wearable EEG Acquisition: Review and Electronics Design Methodology. *IEEE Reviews in Biomedical Engineering*, 10:187–198, 2017.

W. X. Yan, K. J. Mullinger, G. B. Geirsdottir, and R. Bowtell. Physical modeling of pulse artefact sources in simultaneous EEG/fMRI. *Hum Brain Mapp*, 31(4):604–620, apr 2010.

L. Yang, Z. Liu, and B. He. EEG-fMRI reciprocal functional neuroimaging. *Clinical Neurophysiology*, 121(8):1240–1250, 2010.

D. Yao, Y. Qin, S. Hu, L. Dong, M. L. Bringas Vega, and P. A. Valdés Sosa. Which Reference Should We Use for EEG and ERP practice? *Brain Topography*, 32(4):530–549, 2019.

T. A. Yousry, U. D. Schmid, H. Alkadhi, D. Schmidt, A. Peraud, A. Buettner, and P. Winkler. Localization of the motor hand area to a knob on the precentral gyrus. A new landmark. *Brain : a journal of neurology*, 120(1):141–57, jan 1997.

H. Yuan, V. Zotev, R. Phillips, W. C. Drevets, and J. Bodurka. Spatiotemporal dynamics of the brain at rest - Exploring EEG microstates as electrophysiological signatures of BOLD resting state networks. *NeuroImage*, 60(4):2062–2072, 2012.

Y. Zerouali, J. M. Lina, Z. Sekerovic, J. Godbout, J. Dube, P. Jolicoeur, and J. Carrier. A time-frequency analysis of the dynamics of cortical networks of sleep spindles from MEG-EEG recordings. *Frontiers in Neuroscience*, 8(OCT):14–16, 2014.

Y. Zerouali, P. Pouliot, M. Robert, I. Mohamed, A. Bouthillier, F. F. Lesage, and D. K. Nguyen. Magnetoencephalographic signatures of insular epileptic spikes based on functional connectivity. *Human Brain Mapping*, 37(9):3250–3261, 2016.

J. Zhang, W. Liu, H. Chen, H. Xia, Z. Zhou, L. Wang, S. Mei, Q. Liu, and Y. Li. EEG-fMRI validation studies in comparison with icEEG: a review. *International journal of psychophysiology*, 84(3):233–9, jun 2012.

M. Zijlmans, G. M. Huiskamp, F. S. Leijten, W. M. Van der Meij, G. Wieneke, and A. C. Van Huffelen. Modality-specific spike identification in simultaneous magnetoencephalography/electroencephalography: A methodological approach. *Journal of Clinical Neurophysiology*, 19(3):183–191, 2002.

M. Zijlmans, G. Huiskamp, M. Hersevoort, J. H. Seppenwoolde, A. C. Van Huffelen, and F. S. Leijten. EEG-fMRI in the preoperative work-up for epilepsy surgery. *Brain*, 130(9): 2343–2353, 2007.